Natural convection adjacent to an inclined flat plate and in an attic space under various thermal forcing conditions

Thesis submitted by

Suvash Chandra SAHA, B.Sc., M.Sc.

in November 2008

for the degree of Doctor of Philosophy

in the School of Engineering

James Cook University

*This work is dedicated to
my parents, my wife, Mita
and
my baby, Adrita who was born in
during my PhD work.*

Statement of access

I, the undersigned, author of this work, understand that James Cook University will make this thesis available for use within the University Library and, via the Australian Digital Theses network, for use elsewhere.

I understand that, as an unpublished work, a thesis has significant protection under the Copyright Act and;

I do not wish to place any further restriction on access to this work.

_____   _____

      Signature   Date

Statement of sources declaration

I declare that this thesis is my own work and has not been submitted in any form for another degree or diploma at any university or other institution of tertiary education.

Information derived from the published or unpublished work of others has been acknowledged in the text and a list of references is given.

_____   _____

Signature   Date

Electronic copy

I, the undersigned, the author of this work, declare that the electronic copy of this thesis provided to the James Cook University Library is an accurate copy of the print thesis submitted, within the limits of the technology available.

_____   _____

Signature   Date

Acknowledgements

It would not be possible for me to complete this work without the support, encouragement and help from a number of people around me during my study at JCU. It is a great pleasure for me to express my sincere gratitude to all people who have helped me to reach this stage. First of all, I would like to thank my supervisors Professor John C. Patterson and Associate Professor Chengwang Lei for suggesting the original problem, their guidance and for many valuable discussions that we have had at weekly meetings throughout my candidature.

I am also grateful to the office staff, especially, Ms Helen Simpson, Ms Maxine Goulston and Ms Alison Ambrey for their official support and assistance with conference matters.

I am pleased to thank Dr. Feng Xu, who recently graduated from our research group. When I joined this group as a PhD student, I got many help from him about using Fluent and others. Thanks to Dr Tomasz Bednarz for his cordial help regarding some UDF writings for the simulations. Thanks to my office mates, Ms Yadan Mao and Mr. David Henderson. They gave me considerable assistance in some aspects when I really needed.

I am also pleased to thank the School of Engineering, James Cook University for providing me the scholarship during my study.

Finally, my sincere thanks go to my loving wife, Ms Mita Ghosh. Without her full support and consistent encouragement it would not be possible for me to finish my PhD. Also thanks to my family and my wife's family for their emotional support and patience to me. They have been waiting for the moment very patiently.

Abstract

The natural convection thermal boundary layer adjacent to an inclined flat plate and inclined walls of an attic space subject to instantaneous and ramp heating and cooling is investigated. Attention in this study has been given to fluid having a Prandtl number less than unity. A scaling analysis has been performed to describe the flow behaviour and heat transfer. Major scales quantifying the flow velocity, flow development time, heat transfer and the thermal and viscous boundary layer thicknesses at different stages of the flow development are established.

In Chapter 3, an investigation of the natural convection boundary layer adjacent to an inclined plate subject to sudden heating and a temperature boundary condition which follows a ramp function up until a specified time and then remains constant is reported. The development of the flow from start-up to a steady-state has been described based on scaling analyses and verified by numerical simulations. Different flow regimes based on the Rayleigh number are discussed with numerical results for both boundary conditions. For ramp heating, the boundary layer flow depends on the comparison of the time at which the ramp heating is completed and the time at which the boundary layer completes its growth. If the ramp time is long compared with the steady state time, the layer reaches a quasi steady mode in which the growth of the layer is governed solely by the thermal balance between convection and conduction. On the other hand, if the ramp is completed before the layer becomes steady; the subsequent growth is governed by the balance between buoyancy and inertia, as for the case of instantaneous heating.

In Chapter 4, the natural convection boundary layer adjacent to an inclined plate subject to sudden and ramp cooling boundary conditions is reported. It is found that the cold boundary layer adjacent to the plate is potentially unstable to a Rayleigh-Bénard instability if the Rayleigh number exceeds a certain critical value. A scaling relation for the onset of instability of the boundary layer is achieved. For the ramp cooling case, the onset of instability may set in at different stages of the boundary layer development. A proper identification of the time when the instability may set in is discussed. A numerical verification of the time for the onset of instability is presented in this chapter. Different flow regimes based on the stability of the boundary layer have also been discussed with numerical results.

In Chapters 5 and 6, a discussion of the fluid dynamics in the attic space is reported, focusing on its transient response to sudden changes of temperature along the two inclined walls. The transient behaviour of an attic space is relevant to our daily life. The sudden and ramp heating/cooling boundary conditions are applied on the sloping walls of the attic space. A theoretical understanding of the transient behaviour of the flow in the enclosure is performed through scaling analysis. A proper identification of the timescales, the velocity and the thickness relevant to the flow that develops inside the cavity makes it possible to predict theoretically the basic flow features that will survive once the thermal flow in the enclosure reaches a steady state. A time scale for the heating-up/cooling-down of the whole cavity together with the heat transfer scales through the inclined walls has also been obtained through scaling analysis. All scales are verified by the numerical simulations.

Further, a periodic temperature boundary condition is also considered in Chapter 7 to show the basic flow features in the attic space over diurnal cycles. The numerical results reveal that, during the daytime heating stage, the flow in the attic space is stratified; whereas at the night-time cooling stage, the flow becomes unstable. A symmetrical solution can be seen for relatively low Rayleigh numbers. However, as the Ra is gradually increased, a transition occurs at a critical value of Ra. Above this critical value, an asymmetrical solution exhibiting a pitchfork bifurcation arises at the night-time. It is also found that the calculated heat transfer rate at the night-time cooling stage is much higher than that during the daytime heating stage.

Table of contents

List of Figures

xvii

List of Tables

Nomenclature

A	h/l, slope of the plate/ aspect ratio of the cavity
a, b	coefficients of the discretized equation (2.26)
$\vec{A}_e$	surface area vector enclosing the control volume
c_p	specific heat capacity at a certain pressure
L	length of the plate, length of the sloping wall of the attic
l	half length of base of the attic, length of the horizontal projection of the plate
h	height of the plate/attic
h_{eff}	$q/\Delta T$, heat transfer coefficient
$F(\phi)$	function of ϕ
F_i	body force
F_x, F_y, F_z	components of the body force (in the x-, y- and z- directions)
g	acceleration due to gravity
k	thermal conductivity
Nu	$h_{eff}h/k$, Nusselt number
P	pressure
Pr	ν/κ, Prandtl number
q	$h_{\text{eff}}\Delta T$, convective heat flux through a boundary
Ra	$g\beta\Delta Th^3/(\kappa\nu)$, Rayleigh number
s_0, s_1	Series number of the control volume
T	temperature
T_A	$\Delta T/2$, amplitude of the diurnal temperature
t	time
t_s	steady state time
t_{sr}	quasi-steady time
t_p	ramp time
t_f	heating-up time for sudden heating
t_{fr}	heating-up time for ramp heating/cooling
t_{fc}	cooling-down time for sudden cooling
T_0	temperature on the bottom surface of the attic (Chapter 7)

T_c	cooling temperature
T_h	heating temperature
T_s	surface temperature condition
u, v	velocity components
u_s	steady state velocity
u_{sr}	quasi-steady velocity
$\vec{v}$	velocity vector
x, y, z	coordinates

Greek symbol

α	under-relaxation factor
β	thermal expansion coefficient
ΔT	temperature difference between hot or cold surface and the ambient
Δt	time step
$\Delta \phi$	variation of ϕ
δ_T	thickness of the thermal boundary layer
δ_{Ts}	steady state thickness of the thermal boundary layer
δ_{Tr}	thickness of the thermal boundary layer at quasi-steady time
δ_{Tq}	thickness of the thermal boundary layer at the quasi-steady stage
δ_p	thickness of the thermal boundary layer when the ramp is finished
ϕ	quantity in the general transport equation (2.18)
$\overline{\phi}_e$	average of ϕ on the edges
ϕ_{old}	value of ϕ in the previous iteration
Γ_ϕ	diffusion coefficient for ϕ in the general transport equation (2.18)
κ	thermal diffusivity
μ	dynamic viscosity
ρ	density
ν	μ/ρ, kinematic viscosity
ρ_0	density at the reference state

Subscript

e	edge of the control volume
i, j	tensor indices
n	normal to the edge
nb	number of edges enclosing the control volume

Superscript

n	time level

1 Introduction and literature review

1.1 Introduction

When heat is added to a fluid, most fluids expand at normal temperature, and thus changes its density. If the gravity is present this change in density will induce a change in the body forces, which may cause the fluid to move by itself without any externally imposed flow velocity. This is simply the phenomenon of natural convection, which is present everywhere in our daily experience: rising clouds of cigarettes, ripples of heat from a car's hood, thunderheads reaching into the stratosphere.

Buoyancy is a vertical force exerted on an object when it is immersed, partially or fully, in a fluid and strictly where the fluid is subject to a gravitational force but is not in free fall and its value is equal to the weight of the fluid displaced by the object. All objects that are surrounded by air or water on the surface of the Earth experience buoyancy to a certain degree. This buoyancy effect has influential implications in life. The natural convection currents encountered in the oceans, lakes, and the atmosphere owes their existence of buoyancy. Also light boats as well as heavy warships made of steel float on water because of buoyancy.

Natural convection flow is a leading mechanism of mass and heat transfer in many geophysical and technological phenomena. An understanding of such flows will improve predictions of the heat transfer rate and the development of effective methods for flow control. One can find a comprehensive discussion of the buoyancy-induced flows in Gebhart *et al.* (1988).

Natural convection adjacent to a thermal boundary is often idealized as a flow adjacent to a thermal infinite or semi-infinite flat plate. If the heated flat plate is horizontally placed, a typical natural convection phenomenon, Rayleigh Bénard convection, may arise. An extensive review of Rayleigh Bénard convection can be found in Bodenschartz *et al.* (2000). However, the Rayleigh Bénard instability can also be observed if the plate is inclined to the horizontal plane with a certain angle (see Sparrow and Husar 1969).

The main objective of this thesis is to investigate natural convection adjacent to the inclined walls of an attic space through scaling analysis. For a better understanding of the fluid flow and heat transfer adjacent to the inclined walls we consider an inclined

flat plate initially. Different inclinations of the plate and different aspect ratios of the attic space have been considered for this study. Comparatively a large number of studies on an inclined flat plate have been conducted previously both numerically and experimentally. However, very little attention has been given to the attic space problem although it has direct application in our daily life. A detailed literature review will be discussed in this chapter. .

1.1.1 Inclined flat plate

Both heating and cooling boundary conditions on the flat plate are considered with both sudden and ramp function temperature changes. A temperature boundary condition which follows a ramp function means that the temperature increases or decreases until a specified time (ramp time) and then remains constant. Therefore, there are four different boundary conditions of temperature that have been chosen for the study of an inclined flat plate. The subsequent development of the boundary layer has been distinguished and the scaling results of the transient, quasi-steady and steady state stage of the flow have been achieved. Schematics of the geometry and the thermal boundary layer development for heating and cooling temperature boundary conditions are shown in Figures 1.1a and 1.1b respectively.
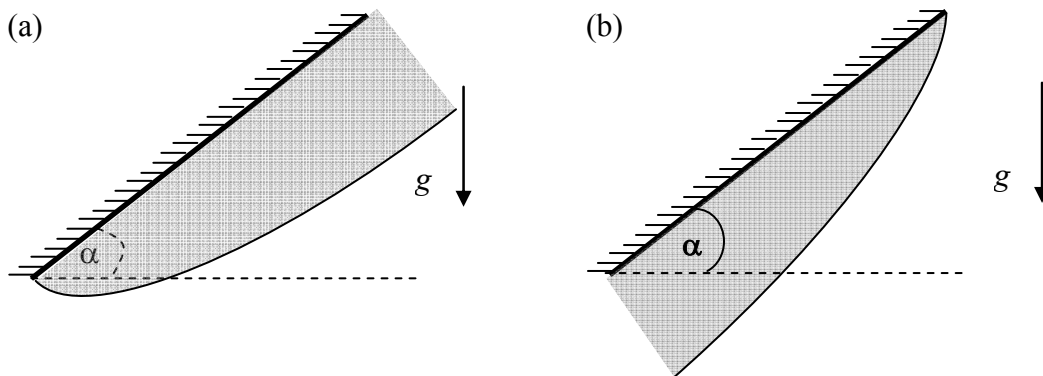
Figure 1.1 Schematic of the boundary layers adjacent to a (a) heated and a (b) cooled inclined flat plate.

1.1.2 Attic space

Similarly to the flat plate, the same set of temperature boundary conditions has been considered for the inclined walls of an attic space. In addition to these boundary conditions, a periodic thermal boundary condition, simulating the alternative night and

day conditions, has also been considered to show a more realistic situation in the attic space. An extensive scaling analysis has been performed for sudden and ramp heating/cooling boundary conditions. A schematic of the attic space boundary conditions is sketched in Figure 1.2. Here $2l$ is the total length of the base, h is the height of the cavity. On the sloping walls, a temperature boundary condition, T_s has been applied. T_s can be either sudden, ramp or periodic. For sudden and ramp heating/cooling boundary conditions, the bottom surface is kept adiabatic. However, for periodic boundary condition on the sloping wall the bottom surface has a fixed temperature, T_0. We applied a fixed temperature instead of adiabatic condition on the bottom surface to allow heat transfer through the ceiling. All boundaries are kept motionless and no slip.
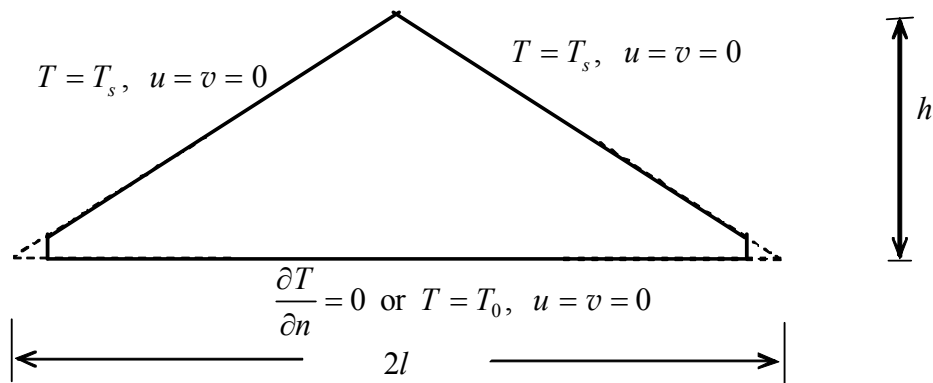
Figure 1.2 Schematic of the geometry and boundary conditions of the attic space.

1.2 Literature review

Buoyancy-induced fluid motions in cavities have been discussed widely because of the applications in nature and engineering. A large body of literature exists on the forms of internal and external forcing, various geometry shapes and temporal conditions (steady or unsteady) of the resulting flows. Especially for the classic cases of rectangular, cylindrical or other regular geometries, many authors have investigated imposed temperature or boundary heat fluxes. Reviews of these research can be found in Ostrach (1988) and Hyun (1994). The rectangular cavity is not an adequate model for many geophysical situations where a variable (or sloping) geometry has a significant effect on the system. However, the convective flows in triangular shaped enclosures have

received less attention than those in rectangular geometries, even though the topic has been of interest for more than two decades.

In previous studies of triangular geometries, researchers mainly focused on two applications. Firstly the fluid dynamics and heat transfer in an attic space with imposed temperature differences between the horizontal base and the sloping upper boundary have been studied by, for example, Poulikakos and Bejan (1983a; b), Salmun (1995a; b), Asan and Namli (2000). Secondly, the fluid dynamics and heat transfer in reservoir sidearms, seashores, lakes and other shallow water bodies with a sloping bottom have been studied by, for example, Horsch and Stefan (1988a; b); Horsch et al. (1994), Farrow and Patterson (1993a; b), Farrow and Patterson (1994); Lei and Patterson (2002a; b; c; 2003a; b; 2005) and Farrow (2004).

In the literature of fluid mechanics and heat transfer, several methodologies exist for developing some form of solution to complex problems. Among these, scale analysis or scaling is one of the simplest and most cost effective methods that can be applied as a first step in understanding the physics underlying the fluid flow and heat transfer issues. The results of scale analysis can serve as a guide for both experimental and numerical investigations. Therefore, scaling has been used by many researchers to investigate the transient flow development for different kinds of geometries and thermal forcing. This is a method for determining answers to concrete problems, such as the heat transfer rate in a configuration that is described completely. The results are accurate in an order-of-magnitude sense. The analysis is based on the conservation equations and all the initial and boundary conditions.

Patterson and Imberger (1980) carried out an extensive investigation by scale analysis of the transient behaviour that occurs when the two opposing vertical sidewalls of a two-dimensional rectangular cavity are impulsively heated and cooled by an equal amount. They devised a classification of the flow development through several transient flow regimes to one of three steady-state types of flow based on the relative values of the Rayleigh number Ra, the Prandtl number Pr (>1), and the aspect ratio A of the cavity. Patterson (1984) investigated the transient natural convection in a cavity driven by internal buoyancy sources and sinks distributed linearly in the horizontal direction and uniformly in the vertical direction using a scaling analysis and again found that there are a number of possible transient flow regimes. Schladow et al. (1989) conducted a series of two- and three-dimensional numerical simulations of transient

flow in a side-heated cavity, and their simulations generally agree with the results of the scaling arguments of Patterson and Imberger (1980).

Scaling analyses coupled with numerical simulations have been used in a variety of other geometries and thermal forcing. Recently Lin *et al.* (2008), Lin *et al.* (2007) and Lin and Armfield (2005a; b) investigated the transient processes in the cooling of an initially homogeneous fluid by natural convection in a vertical circular cylinder and in a rectangular container. The results show that vigorous flow activities are concentrated mainly in the vertical thermal boundary layer along the sidewall and in the horizontal region comprising the lower part of the domain where the cold intrusion flow is created. The transient flow patterns at the unsteady and quasi-steady stages were analysed, including the activities of the travelling waves in the vertical thermal boundary layer along the sidewall, the cold intrusion movements in the horizontal region, the stratification of the fluid, and the long-term behaviour beyond full stratification. Various scaling relations characterizing the flow evolution at these distinct development stages were developed by scaling analysis; these were then verified and quantified by extensive direct numerical simulations under different flow situations in terms of *Ra*, *Pr*, and *A*.

The majority of the past studies have focused on fluids with *Pr* > 1. Studies of natural convection flows with *Pr* < 1 resulting from the heating or cooling of vertical boundaries, especially those in which the long-term behaviour and the effect of *Pr* variation are examined, have been scarce.

To identify possible flow regimes of the unsteady natural convection flow in a small-slope shallow wedge induced by the absorption of solar radiation, Lei and Patterson (2002c) presented a scaling analysis and established relevant scales to quantify the flow properties in each flow regime. They classified the flow development broadly into one of three regimes: a conductive regime, a transitional regime and a convective regime, depending on the Rayleigh number.

Scaling analysis of the transient behavior of the flow in an attic space was conducted by Poulikakos and Bejan (1983a), valid for small aspect ratios, i.e $H/B \to 0$, where H and B are the attic height and length respectively. The transient phenomenon began with the sudden cooling of the upper sloped wall. It was noted that both walls developed thermal and viscous layers whose thicknesses increased towards steady state values. The authors mentioned that, by properly identifying the timescales of various features that develop inside the enclosures, it was possible to predict theoretically the

basic flow features that would endure in the steady state. Finally, they focused on a complete sequence of transient numerical simulations covering a range of controlling parameters including the Grashof number, the aspect ratio and the Prandtl number.

1.2.1 Natural convection adjacent to an inclined flat plate

Natural convection adjacent to an inclined flat plate has received less attention than the cases of vertical and horizontal plates. However, natural convection heat transfer from an inclined surface is very frequently encountered in engineering devices and the natural environment. Most of the previous works have been conducted by either numerical simulations or experimental observations. Theoretical or scaling analyses have not been employed for this type of problem, especially with regard to the transient flow behavior from start up, which is of great fundamental interest and has practical importance.

Jones (1973) studied free convection adjacent to a heated semi-infinite flat plate which is inclined at a small angle, α to the horizontal plane. Both positive and negative inclinations of the plate were considered for his studies. Positive values of the angle corresponded to cases in which the leading edge of the plate is its lowest point. It is noteworthy that near the leading edge of the plate the fluid absorbed insufficient heat for the buoyancy forces to be significant and therefore the flow is driven by a density variation. As the fluid moves over the plate and gains more heat from the plate by the conduction, the buoyancy forces become comparable with, and eventually dominate, the indirectly induced pressure gradient. For negative inclinations, although the pressure gradient associated with the indirect processes remains favourable, since the buoyancy forces now oppose the motion, finally the separation of the boundary layer from the plate occurs. For both positive and negative inclinations of the plate the author obtained a series of solutions, which is valid near the leading edge, using similarity variables. The solutions are then extended downstream beyond the range of applicability of the series by means of a step-by-step numerical method. In the case of $\alpha > 0$ the numerical solutions approach the asymptotic solution which is valid far downstream.

One of the important interests of this study is to find a time scale of the onset of instability of the boundary layer adjacent to the inclined flat plate and the sloping walls of the attic space. In the literature many researchers have conducted the instability analysis in the past. Sparrow and Husar (1969) were the first to prove experimentally the existence of longitudinal vortices in a natural convection flow along an inclined flat plate. The authors found that the wavelength of the vortices is nearly invariant with the angle of inclination of the plate, but varies inversely with the temperature difference between the plate and the ambient fluid. They also found that the onset of the vortices is moved downstream with the decreasing angle of inclination from the vertical plane and the decreasing temperature difference between the plate and the ambient fluid.

Lloyd and Sparrow (1970) made more quantitative measurements using the same experimental techniques as Sparrow and Husar (1969) used. They found a critical Rayleigh number (*Ra*) for the onset of instability at each angle of inclination, and compared their results with the results of previous investigations. However, these comparisons show a large scatter in the data because the earlier investigators were unaware of the presence of vortices, and it is not clear whether the critical *Ra* values found in the previous experiments indicated the onset or the breakup of the vortices. Lloyd and Sparrow (1970) also found that the vortices did not appear for angles from horizontal of more than 76°, and that the vortices coexisted with Tollmien-Schlichting wave instabilities between 73° and 76°. Lloyd (1974) studied the wavelength of the longitudinal vortices over an isothermal plate in water, using the same technique as that of Sparrow and Husar (1969). The author obtained a relation between the temperature differences and the spanwise wavelength, and confirmed that the wavelength is nearly invariant with the angle of inclination.

Cheng and Kim (1988) performed an experimental investigation of the vortices on an isothermal inclined plate using smoke visualization in air for low angles of inclination from the horizontal plane. Wavelengths and critical Rayleigh numbers for the onset of vortices were found and agreed qualitatively with the results of the previous studies. However, the angles studied were closer to the horizontal direction than those investigated in the earlier experiments, and so quantitative comparisons with the results of Lloyd (1974) are difficult.

An experimental investigation of the onset and wavelength of the vortices on a constant heat flux inclined plate has been performed by Shaukatullah and Gebhart

(1978). The authors measured local temperatures and velocities using thermocouples and constant temperature hot-film anemometers. A spanwise variation in fluid velocities was observed, indicating the presence of longitudinal vortices, and the onset and wavelength of these vortices were determined. In addition, growth rates were calculated from the temperature measurements. The effects of the angle of inclination and temperature difference on the onset locations and wavelengths of the vortices agree qualitatively with those of earlier investigations, but quantitative comparisons are not appropriate because of the different boundary conditions on the plate.

The onset of the vortices has been studied analytically, as well as experimentally, using linear stability theory by Haaland and Sparrow (1973). The authors performed a temporal linear stability analysis in which some non-parallel flow effects were taken into account and a numerical integration was performed. They determined that the parallel flow assumption does not lead to the correct behaviour at the outer edge of the boundary layer, and a modified parallel flow assumption allowing for the flow normal to the plate was used instead. A modified Reynolds number, R was introduced in place of the Rayleigh number, which has the advantage of providing critical values that are independent of the angle of inclination of the plate. The relation between the Reynolds number and the Grashof numbers is given by

$$Gr = \frac{R^4}{64}.$$

As was observed experimentally, the onset of instabilities is moved downstream with the decreasing angle from the vertical; however, the predicted onset occurs much farther upstream than that was observed experimentally by Lloyd and Sparrow (1970). Iyer and Kelly (1974) postulated that these experiments were not sensitive enough to detect the first instabilities predicted by theoretical analyses. Thus, using a spatial linear stability analysis with the parallel flow assumption, Iyer and Kelly (1974) examined the formation and growth of both wave instabilities and longitudinal vortices and attempted to find a correlation between experimental and theoretical results by finding the total amplification between the earliest disturbances and the observed disturbances. Chen and Tzuoo (1982) included the gravity component, which acts perpendicular to the plate in their temporal stability analysis. However, their results showed that the inclusion of the gravity component in the analysis did not change the predicted critical R significantly and the onset of the vortices was again predicted to occur far upstream of where it was observed experimentally by Lloyd and Sparrow (1970).

While most stability analyses deal with the onset of the vortices, another important feature of this flow is the pairing and breakup of the vortices. The photographs of Sparrow and Husar (1969) revealed that the longitudinal vortices merged and finally broke up at a downstream location; however, this transition had not been specifically studied in subsequent experiments. Chen *et al.* (1991) performed a temporal stability analysis that studied the locations of the onset and the merging and annihilation of the vortices, formulating the problem in the same manner as Haaland and Sparrow (1973). As in the case of onset, the merging and breakup of the vortices observed in the photographs of Sparrow and Husar (1969) occur much farther downstream than predicted by the stability analysis.

Zuercher *et al.* (1998) re-examined the formation and growth of the vortices experimentally. It differs from previous experiments in that it includes both visualization and velocity measurements of the flow, which allows the flow visualization to be correlated to the velocity field. In addition to investigating the streamwise location of the onset of the vortices, the authors also examined the locations of the merging and breakup of the vortices so that for the first time comparisons with the stability analysis of Chen *et al.* (1991) can be made. Finally, fluid velocity measurements were used to determine spatial instability growth rates by measuring the circulation in the vortices at successive streamwise locations. These results were compared with the calculations of Iyer and Kelly (1974).

1.2.2 Natural convection in an attic space

Heat transfer through the attic space into or out of buildings is an important issue for attic shaped houses in both hot and cold climates. One of the most important objectives for design and construction of houses is to provide thermal comfort for occupants. In the present energy-conscious society, it is also a requirement for houses to be energy efficient, i.e. the energy consumption for heating or air-conditioning must be minimized. Because of the relevance to these objectives, research related to the heat transfer in attics has been conducted for about three decades.

From the literature it is observed that two basic sets of temperature boundary conditions in the context of an attic have been considered previously: night-time or winter-time cooling (cold top and hot bottom) and day-time or summer-time heating

(hot top and cold bottom). Other topics related to the attic space have also been researched recently such as attics subject to localized heating, and attics filled with porous media.

1.2.2.1 Night-time boundary conditions

The night-time or winter-time boundary conditions mean the sloping walls of the attic are isothermally cooled and the bottom is heated. Flack (1980) adopted an isosceles triangle for his experimental model, and conducted flow visualizations and heat transfer measurements for the night-time conditions. From the temperature difference between the boundaries the author obtained heat transfer data and the motions of suspended particles were qualitatively observed. Also, the velocities at a few selected locations were measured using a laser velocimeter. The velocity measurements were made primarily to aid in the general understanding of the structure and direction of the flow. The author also showed the temperature profiles along the apparatus centerline. It was also found that initially, at low Rayleygh numbers, the flow remained laminar. However, as the Rayleigh number was increased, the flow eventually became turbulent. The author mentioned that four Bénard type convective cells were present in the laminar flow regime, but there was no mention of the development of the cellular flow pattern, or the relative positions of the cells.

The night-time attic problem was again investigated experimentally by Poulikakos and Bejan (1983b). In their study they modeled the enclosure as a right-angled triangle with an adiabatic vertical wall, which was half of a full attic space domain if the flow is assumed to be symmetric about the geometric mid plane. The focus of their investigation was on the flow regime with a Rayleigh number range 10^6 to 10^9, higher than considered previously. It was observed that the flow inside the enclosure was turbulent which was consistent with Flack (1980). Similarly, the authors showed a plot of the Nusselt number versus the Rayleigh number as a demonstration of heat transfer. To visualize the flow, the thymol blue pH indicator technique was used.

A fundamental study of the fluid dynamics inside an attic-shaped triangular enclosure at night-time was performed by Poulikakos and Bejan (1983a) with the assumption that the flow was symmetric about the center plane. The study was undertaken in three distinct parts. Firstly the flow and temperature fields in the cavity are determined theoretically on the basis of an asymptotic analysis which is valid for

shallow spaces i.e. $H/B \rightarrow 0$, where H and B are the attic height and length. They were able to show that in the $H/B \rightarrow 0$ limit the circulation consists of a single elongated cell driven by the cold upper wall. The net heat transfer in this limit is dominated by pure conduction. Secondly, scaling analysis examined the transient behaviour of the attic fluid. The transient phenomenon begins with the sudden cooling of the upper sloping wall. The authors mention that by properly identifying the timescales of various features that develop inside the enclosures, it is possible to predict theoretically the basic flow features that will endure in the steady state. Finally, they focused on a complete sequence of transient numerical simulations covering the ranges of parameters such as the Rayleigh number, aspect ratio and Prandtl number. The authors reported that the resulting flow patterns in the enclosure corresponded to a single convective cell, for the range of conditions considered.

Salmun (1995a) studied the problem of natural convection inside a two dimensional triangular geometry filled with air or water, with various aspect ratios and Rayleigh numbers ranging between 10^2 and 10^5. Following the earlier simulations, only half of the domain was examined. The center plane was insulated and this was thought to adequately model the entire domain. Numerical solutions of the time dependent problem were obtained using two different numerical techniques. The general flow structure corresponded to a single convective cell for low values of the *Ra* and to a multi-cellular regime for the high values of this parameter. The author disagreed with some results obtained by Poulikakos and Bejan (1983b) regarding the heat transfer mechanism. The problem regarding the stability of the single-cell steady state solution was re-examined by Salmun (1995b). The author used the same method that was developed by Farrow and Patterson (1993b). It is noted that the author attempted to present the results obtained from a linear stability analysis of the steady state asymptotic solution in a shallow triangular enclosure and to show that it is not stable to the type of instabilities expected in fluid layers heated differentially along horizontal boundaries.

Latter, an investigation to examine the details of the transition from single cell to multi cell flow was carried out by Asan and Namli (2001). The results of their study showed that both the height-base ratio and the Rayleigh number had a profound influence on the temperature and flow field. In addition, it was shown that as the aspect ratio decreases, the transition to multi cell flow takes place at higher Rayleigh numbers.

The results also showed that once a secondary cell began to form, it caused the primary cell to shift towards the plane of symmetry. However, since it was assumed that the plane of symmetry could be modeled as an adiabatic surface, the flow patterns obtained are comparable with those from works mentioned above.

Haese and Teubner (2002) investigated the phenomenon for a large-scale triangular enclosure for night-time or winter day conditions. The authors point out that for a realistic attic space, Rayleigh numbers as high as 10^{10} or 10^{11} would be encountered. This study focused on the existing building structure. It is interesting to note that, contrary to the previously mentioned work of Asan and Namli (2001), the authors of this study reported that the shift of multi cellular flow is accelerated by a decrease in the aspect ratio, for the same Rayleigh number. This is consistent with the results presented by Salmun (1995a), which indicated that the number of cells that developed, increased as the aspect ratio decreased.

The studies mentioned above assumed that the flow was symmetric about the centre plane. However, Holtzman *et al.* (2000) for the first time examined the validity of this assumption. The authors pointed out that at low *Ra*, symmetric solutions are obtained, indicating that a symmetry assumption is valid in agreement with the single cell solutions found in previous studies. However, as the Rayleigh number increases, a pitchfork bifurcation is observed in which two steady asymptotic mirror image solutions can be found. However, it was reported that only asymmetric solutions were stable beyond a critical Rayleigh number, if a finite perturbation was applied. To confirm the numerical predictions of the flow patterns and the existence of a symmetry-breaking bifurcation, a flow visualization study was conducted. The flow patterns were observed by slowly injecting smoke into the enclosure.

Transient thermal convection in an air-filled isosceles triangular cavity heated from below and cooled from above has been studied numerically by Ridouane and Campo (2006) for a fixed aspect ratio *A* = 0.5 over an extensive range of Rayleigh numbers. The authors applied a finite volume method for discretization of the governing conservation equations. The influence of *Ra* on the flow and temperature patterns is analyzed and discussed for two contrasting scenarios, which correspond to increasing and decreasing *Ra*. Two steady-state solutions were obtained numerically using appropriate initial perturbations. For increasing *Ra*, it is confirmed that the symmetric flow is achievable at relatively low *Ra* numbers. However, as *Ra* is continually increased, the symmetric plume breaks down and fades away. Thereafter, a

subcritical pitchfork bifurcation is created, giving rise to an anti-symmetric plume occurring at a critical Rayleigh number, $Ra=1.5\times10^5$. The evolution of the flow structure with time is studied in detail to illustrate how this physical transition manifests. The multiplicity of solutions is not a simple theoretical finding, because experimental evidence taken from the specialized literature supports it in a convincing manner. The existing ranges of these solutions are reported for both scenarios, i.e., increasing and decreasing *Ra*. The emergence of a hysteresis phenomenon is observed. This implies that the critical *Ra* characterizing the transition from a steady-state solution to another steady-state solution depends markedly on the scenario considered. In fact, when increasing *Ra*, this value is equivalent to $Ra=1.5\times10^5$, but when decreasing *Ra* this value decreases to $Ra=1.0\times10^4$. In the subinterval between these two critical values of *Ra*, both solutions are possible depending solely on the initial conditions. Quantitatively, for a fixed *Ra* in this subinterval, the difference in the mean Nusselt number between the symmetrical and the asymmetrical solutions is found to be about 1% – 3%.

Recently Lei and Patterson (2007) and Lei *et al.* (2008) studied both experimentally and numerically the natural convection flow in an isosceles triangular enclosure subject to abrupt heating from the base and simultaneous cooling from the inclined surfaces. The authors used water as the working fluid for flow visualization using a shadowgraph technique. A Finite Volume Method has been used for simulation by keeping a fixed aspect ratio $A = 0.5$, and a range of Rayleigh numbers is examined in the experiment. They classified the transient flow development in the enclosure into three distinct stages, an early stage, a transitional stage, and a steady or quasi-steady stage in both the experiments and numerical simulations. The early stage flow is characterized by the growth of thermal boundary layers adjacent to all the interior surfaces and the initiation of primary circulations. The transitional stage flow is characterized by the appearance of convective instabilities in the form of rising and sinking thermals and the formation of cellular flow structures. The steady-state flow at low Rayleigh numbers is characterized by symmetric flows about the geometric symmetry plane, and the quasi steady flow at relatively higher Rayleigh numbers is characterized by the pitchfork bifurcation, which results in alternative occurrence of convective instabilities from the two sides of the enclosure and the oscillation of the upwelling flow near the centre. They also established two important time scales from the numerical simulation; time scale for the onset of instability and the time scale for

the transition of the flow from symmetry to asymmetry due to the pitchfork bifurcation. All studies reported for the attic space problem are for the two dimensional domain. It is found that two dimensional simulations are good enough to characterize the flow.

1.2.2.2 Day-time boundary conditions

Unlike night-time conditions, the attic space problem under daytime conditions has received very limited attention. The boundary conditions for day-time or summer-time are that the sloping walls of the attic space are isothermally heated and the bottom surface is cooled. Flack (1980) first investigated the daytime boundary conditions on the triangular enclosures. The author found that under this conditions, the flow inside the enclosure remained laminar for Rayleigh numbers up to 4.9×10^7. It was found that the resulting heat transfer data could be correlated with heat fluxes calculated for one-dimensional conduction, suggesting that the heat transfer through the enclosure was dominated by conduction. Under the daytime conditions, the heat transfer rates and flow velocities were significantly lower than those under the night-time conditions. Latter Akinsete and Coleman (1982) numerically simulated the attic space with a hot upper sloping wall and cooled base. Their aim was to obtain previously unavailable heat transfer data, relevant to air conditioning calculations. This study considered only half of the domain. The authors considered two forms of heating on the hot wall including isothermal heating and constant heat flux heating. The calculated flow remained laminar in this study, which agrees with Flack (1980)'s experiment for daytime conditions.

With the continuation of the previous work for air conditioning calculation, Asan and Namli (2000) reported results for steady, laminar, two-dimensional natural convection in a pitched roof of triangular cross-section under the summer day boundary condition. The results showed that the height-to-base ratio has a profound influence on the temperature and flow field. On the other hand, the effect of Rayleigh number is not significant for $H/B <1$ and $Ra < 10^5$. For small Rayleigh numbers, two counter rotating vortices are present in the enclosure and the eye of the vortices is located at the center of the half of the cross-section. With the increase of the Rayleigh number, a secondary vortex developed and the newly develop secondary vortex pushes the eye of the primary vortex further towards the inclined wall. The transition from a two-vortex solution to a multiple vortex solution is dependent on the Rayleigh number and the

height-to-base ratio. It is noted that near the place of intersection of the cold horizontal wall and hot inclined wall a considerable proportion of the heat transfer across the base wall of the region takes place. The authors also showed the relationship between the mean Nusselt number, the Rayleigh number, and the height-to-base ratio.

1.2.2.3 Other boundary conditions

The effect of Prandtl number on natural convection in a right angled triangular enclosure with localized heating has been analyzed by Koca *et al.* (2007). In this study, the bottom wall of the triangular enclosure is partially heated while the inclined wall is maintained at a lower uniform temperature. The remaining walls were kept insulated. Various Prandtl numbers $(0.01 \leq Pr \leq 15)$ and Rayleigh numbers $(10^3 \leq Ra \leq 10^6)$ have been considered for computation with a range of heater locations and lengths. They observed that both flow fields and temperature fields are affected profoundly by the change of the Prandtl number, the location and the length of the heater as well as the Rayleigh number.

Varol *et al.* (2006a) studied the natural convection heat transfer numerically in a triangular enclosure with flush mounted heater on the vertical wall. The authors investigated the heat transfer as well as the steady state flow field for a range of Rayleigh numbers with a fixed Prandtl number. The authors also showed the effect of the variation of the size and the position of the heater and observed that the most important parameter on heat transfer and flow field is the position of the heater. A protruding heater which is located in a triangular enclosure has also been analysed by Varol *et al.* (2007c) numerically. The temperature on the inclined walls was considered lower than the heater and the rest of the bottom wall was kept adiabatic. They found that all parameters relevant to the geometrical dimensions of the heater were effective on the temperature distribution, flow field and heat transfer.

Natural convection of a triangular cavity filled with porous media was first investigated by Bejan and Poulikakos (1982). The authors studied analytically the natural convection in a wedge-shaped porous layer cooled from above and showed that the flow pattern can differ fundamentally from Bénard circulation encountered in constant-thickness horizontal layers. Recently Varol *et al.* (2006b; 2007a; b) and Varol *et al.* (2008) investigated the natural convection in porous triangular enclosures. They applied finite difference method to solve the governing equations which were written

using Darcy method. The effect of a range of aspect ratios and Rayleigh numbers on heat transfer and flow field is investigated.

Omri *et al.* (2005) examined the thermal exchange by natural convection and effects of buoyancy forces on flow structure. The authors revealed useful information on the sensitivity of the flow structure to the Rayleigh numbers and the tilt angle on the thermal exchange. They also found that many recirculation zones could occur in the core of the cavity. Recently, Basak *et al.* (2007) studied right-angled triangular enclosures with two cases; in one case the vertical wall is uniformly or linearly heated while the inclined wall is isothermal; and in the other case the configuration is opposite. They considered various values of the Rayleigh number and Prandtl number. It was noted that the average Nusselt number for the vertical wall is $2^{1/2}$ times that of the inclined wall.

1.3 Objectives and outline of the present study

From the above review it is clear that the understanding of the transient flow development and the heat transfer for the attic space problem is not complete and the realistic diurnal temporal effect on the attic shape roof is still unrevealed. Moreover, theoretical understanding of the flow adjacent to an inclined flat plate as well as in an attic space in the form of scaling analysis is almost absent in the literature. Therefore, the objectives of the present study are:

- To develop an understanding of the transient flow behaviour in the boundary layer adjacent to an inclined flat plate by scaling analysis.
- To quantify the onset of instability of the boundary layer when the plate is cooled and to describe some parameter regimes based on different stages of the flow development.
- To establish the heating-up and cooling-down time scales for an attic domain filled with a hot and cold fluid respectively. The corresponding heat transfer calculation for the sloping wall of the attic space is also an objective.
- To achieve an understanding of the flow development and heat transfer in an attic space subject to a realistic diurnal temperature boundary condition.

The outline of the thesis is illustrated in Figure 1.3. An introduction of this study has been given above along with a review of the related literature. A brief description of the numerical approach that has been employed in this investigation comprises Chapter 2. Based on the outline, the main body of this thesis consists of two parts; the inclined flat plate and the attic space, as illustrated in the figure below.
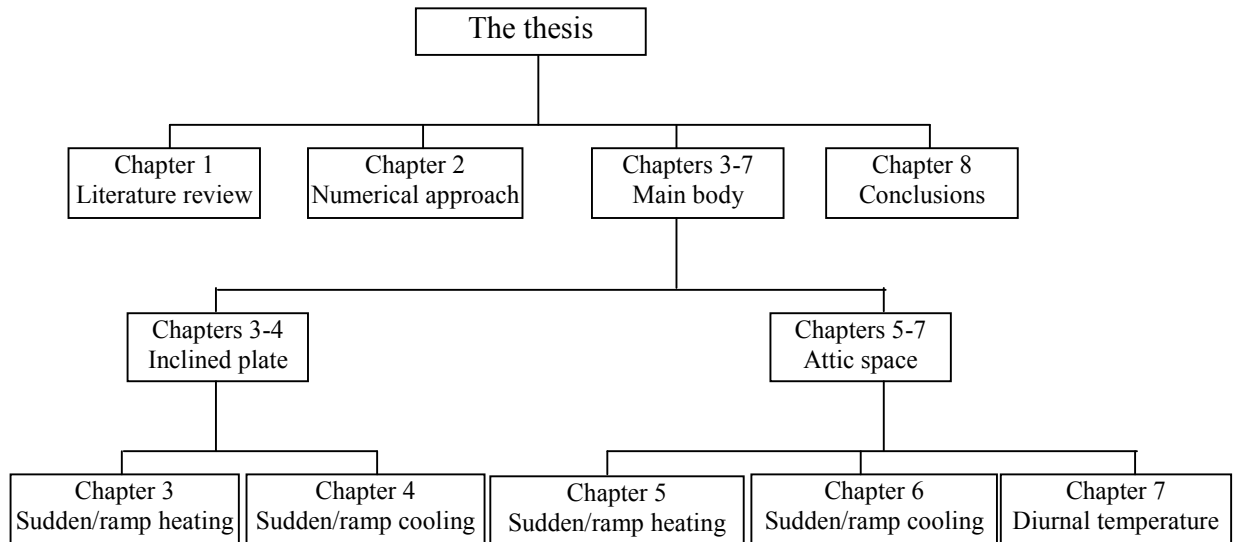
Figure 1.3 Outline of the thesis.

Natural convection boundary layer adjacent to an inclined flat plate due to sudden heating and ramp heating boundary conditions is discussed in Chapter 3. Scaling analyses of the transient flow development are established for both boundary conditions. Steady state scaling of the flow velocity, time and thickness has been developed for sudden heating. For the ramp heating boundary condition, several scaling relations are obtained with comparison of different time scales (ramp time and quasi-steady time).

Chapter 4 deals with the cooling boundary conditions. Sudden and ramp cooling boundary conditions are applied on the inclined plate. The boundary layer is potentially unstable if the Rayleigh number exceeds a certain critical value. A scaling prediction of the onset of instability is obtained for both boundary conditions. Different flow regimes based on the Rayleigh number are identified through scaling analysis for two different boundary conditions. Numerical simulations for a wide range of Rayleigh numbers and aspect ratios have been performed to verify the scaling results.

Chapter 5 and 6 consider the heating and cooling boundary conditions respectively for an attic space. Both sudden and ramp temperature boundary conditions are applied on the sloping walls of the attic space. Initially the boundary layer develops adjacent to the sloping wall. Latter, the hot or cold fluid ejected from the boundary layers eventually fills up the entire domain. The scaling results for heating-up or cooling-down for both sudden and ramp temperature boundary conditions are obtained. Moreover, the subsequent heat transfer scales during the heating-up or cooling-down stages are obtained. All scales are verified by numerical simulations.

Numerical simulations of natural convection of an attic space subject to diurnal temperature condition on the sloping walls have been investigated in Chapter 7. The effect of the aspect ratio and Rayleigh number on the flow field and heat transfer has been discussed in detail in this chapter. Furthermore, the formation of a pitchfork bifurcation of the flow at the symmetric line of the enclosure is also discussed. A comparison of the heat transfer during the day and night is also showed here. Chapter 8 summarizes the major findings of this study with suggestions for future studies.

2 Governing equations and numerical procedures

The governing equations describing natural convection adjacent to an inclined flat plate and in an attic space are presented and simplified in this chapter. The numerical procedures for solving the governing equations using FLUENT 6.2, a commercial Computational Fluid Dynamics (CFD) package, are also introduced. More details of the numerical procedures are available in the FLUENT User's Guide. The initial and boundary conditions as well as grid and time step dependence tests are not discussed in this chapter. Instead, they will be discussed in respective chapters.

2.1 Formulation

2.1.1 Governing equations

Natural convection adjacent to an inclined flat plate and in an attic space satisfies the conservation equations of mass, momentum and energy under the assumption of continuous media. The mathematical expressions of these conservation equations may be written together with the equation of state in Cartesian tensor notations as follows. The equation for conservation of mass, or continuity equation,

$$\frac{\partial \rho}{\partial t} + \frac{\partial(\rho u_j)}{\partial x_j} = 0,$$

(2.1)

Conservation of momentum based on Newton's second law,

$$\rho \frac{Du_i}{Dt} = -\frac{\partial p}{\partial x_i} + \rho F_i + \frac{\partial}{\partial x_j}\left[\mu\left(\frac{\partial u_i}{\partial x_j} + \frac{\partial u_j}{\partial x_i}\right)\right] - \frac{2}{3}\frac{\partial}{\partial x_i}\left(\mu \frac{\partial u_j}{\partial x_j}\right),$$

(2.2)

Conservation of energy equation,

$$\rho c_p \frac{DT}{Dt} = u_j \frac{\partial p}{\partial x_i} + \frac{\partial}{\partial x_j}\left(\kappa \frac{\partial T}{\partial x_j}\right) + \mu\left[\frac{\partial u_i}{\partial x_j}\left(\frac{\partial u_i}{\partial x_j} + \frac{\partial u_j}{\partial x_i}\right) - \frac{2}{3}\left(\frac{\partial u_j}{\partial x_j}\right)^2\right],$$

(2.3)

And the equation of state,

$$\rho = \rho(p,T),$$

(2.4)

In Equation (2.2), the body force F_i has three components: F_x, F_y and F_z in *x*-, *y*-, and *z*-directions respectively. In addition, *D/Dt* is a derivative operator defined as,

$$\frac{D}{Dt} = \frac{\partial}{\partial t} + u_j \frac{\partial}{\partial x_j},$$

(2.5)

2.1.2 Appropriate assumptions

The governing equations (2.1)-(2.3) are general forms of conservation equations, and may be simplified for particular problems such as the one considered in this study. Moreover, these equations are highly non-linear and coupled, and are very difficult to solve. Therefore, it is of significance to simplify these equations based on particular features such as follows so that numerical discretization and analyses can be easily performed.

For the transient natural convection adjacent to an inclined flat plate or an inclined wall of an attic space, it is understood that, when heat is added to the fluid, the fluid expands, and thus changes its density. If the gravity is present, this change in density induces a change in the body force, which may cause the fluid to move by itself without any externally imposed flow velocity. If the temperature difference between the walls and the ambient is not very large, the correlation between the density and the temperature may be considered as a linear relation. As a result, the equation of state (2.4) may be given by

$$\rho = \rho_0 \left[1 - \beta (T - T_0) \right],$$

(2.6)

where β is the thermal expansion coefficient. It is generally of an order of magnitude between 10^{-2} and 10^{-4} for different fluids (Ostrach (1964)).

The natural convection flows often involve a relatively small temperature difference and a low flow velocity, and thus an incompressible flow assumption is appropriate (see Batchelor (1954)). Accordingly, the continuity equation (2.1) may be simplified as follows,

$$\frac{\partial u_j}{\partial x_j} = 0.$$

(2.7)

The Boussinesq approximation is assumed for this problem, meaning that all fluid properties such as the viscosity and the thermal conductivity are treated as constants except the density in the buoyancy term. In the present study, a two dimensional coordinate system has been adopted, where the *x*-axis and the *y*-axis are

not parallel to the horizontal and the vertical respectively (see Figure 2.1). The inclination angle of the *x*-axis with the horizontal plane is θ. Therefore the effect of the gravitational acceleration on the flow field has two components; *x*-component ($g\sin\theta$) and *y*-component ($g\cos\theta$). Since there is no other volumetric force, the two components (F_x, F_y) of the body force in equation (2.2) may be written as

$$\rho F_x = -g\sin\theta(\rho - \rho_0).$$ (2.8)

and

$$\rho F_y = g\cos\theta(\rho - \rho_0).$$ (2.9)

Substituting Equation (2.6) to Equations (2.8) and (2.9) and applying the Boussinesq approximation we have

$$F_x = g\sin\theta\beta(T - T_0).$$ (2.10)

and

$$F_y = -g\cos\theta\beta(T - T_0).$$ (2.11)

Now equation (2.2) becomes after incorporating equations (2.7), (2.10) and (2.11)

$$\frac{Du_i}{Dt} = -\frac{1}{\rho}\frac{\partial p}{\partial x_i} + \nu\frac{\partial^2 u_i}{\partial x_j \partial x_j} \pm F_{x_i}.$$ (2.12)

Similarly, the energy equation can be simplified by assuming that the viscous energy dissipation and the pressure gradient associated with the incompressible assumption may be neglected if the velocity induced by the natural convection flow is lower. Therefore, the energy equation (2.3) can be simplified as

$$\frac{DT}{Dt} = \kappa\frac{\partial^2 T}{\partial x_j \partial x_j}.$$ (2.13)
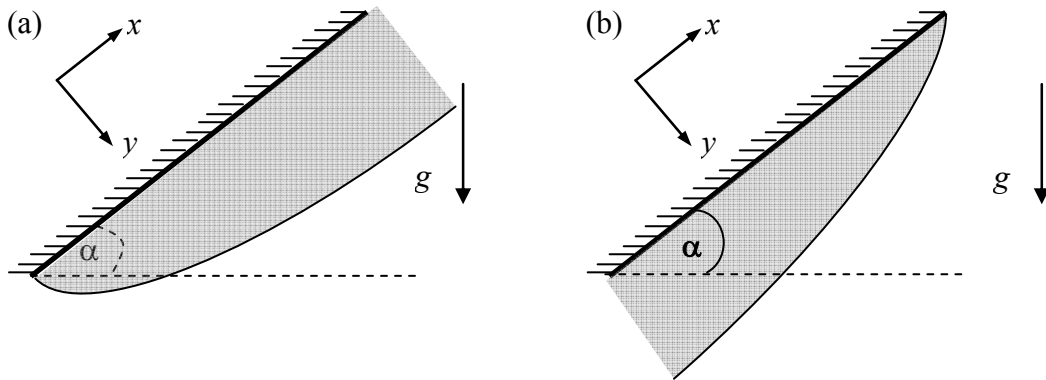
Figure 2.1 Schematic of the boundary layers adjacent to a (a) heated and a (b) cooled inclined flat plate.

The simplified continuity, momentum and energy equations of a *2D* model are expressed as follows:

$$\frac{\partial u}{\partial x} + \frac{\partial v}{\partial y} = 0 \tag{2.14}$$

$$\frac{\partial u}{\partial t} + u\frac{\partial u}{\partial x} + v\frac{\partial u}{\partial y} = -\frac{1}{\rho}\frac{\partial p}{\partial x} + \nu\left(\frac{\partial^2 u}{\partial x^2} + \frac{\partial^2 u}{\partial y^2}\right) + g\beta\sin\theta(T - T_0) \tag{2.15}$$

$$\frac{\partial v}{\partial t} + u\frac{\partial v}{\partial x} + v\frac{\partial v}{\partial y} = -\frac{1}{\rho}\frac{\partial p}{\partial y} + \nu\left(\frac{\partial^2 v}{\partial x^2} + \frac{\partial^2 v}{\partial y^2}\right) - g\beta\cos\theta(T - T_0) \tag{2.16}$$

$$\frac{\partial T}{\partial t} + u\frac{\partial T}{\partial x} + v\frac{\partial T}{\partial y} = \kappa\left(\frac{\partial^2 T}{\partial x^2} + \frac{\partial^2 T}{\partial y^2}\right) \tag{2.17}$$

The above set of governing equations has been successfully adopted in previous numerical simulations of natural convection in cavity (see e.g. Nateghi and Armfield (2004)). It is noted that in the case with a large temperature difference, the fluid does not satisfy the Boussinesq approximation, and thus cautions must be taken when adopting the above equations.

2.2 Numerical approach

The governing equations (2.14)-(2.17) are highly non-linear and coupled each other. Therefore it is impossible to get an analytical solution. Numerical methods can provide an approximate solution. The accuracy of the solution, however, depends on the adopted numerical scheme. In parallel with in-house CFD (Computational Fluid Dynamics) codes developed by researchers, there are a large number of commercially available CFD packages such as CFX, PHOENICS and FLUENT. These commercial packages are being improved day by day with the involvement of a large team of CFD specialists. From the above mentioned CFD packages, the FLUENT package has been chosen for the numerical simulations in this thesis. FLUENT is a Finite Volume based CFD package. It is one of the most widely used CFD packages.

2.2.1 Numerical Schemes

In this thesis, the Finite Volume scheme has been chosen to discretize the governing equations, with the QUICK scheme (see Leonard and Mokhtari 1990) approximating

the advection term. The diffusion terms are discretized using central-differencing with second order accurate. A second order implicit time-marching scheme has also been used for the unsteady term. Briefly, the control-volume-based technique:

- Divides the domain into discrete control volumes using a computational grid.
- Integrates the governing equations on the individual control volumes to construct algebraic equations for the discrete dependent variables such as velocities, pressure and temperature.
- Linearizes the discretized equations and solution of the resultant linear equation system to yield updated values of the dependent variables.
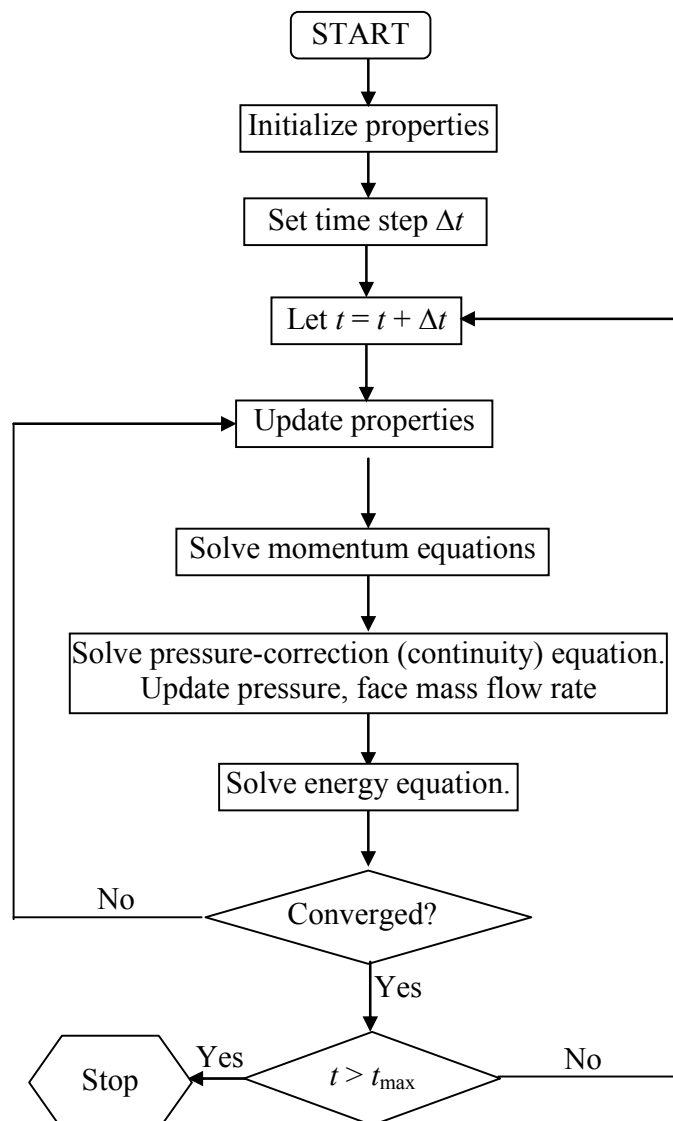
Figure 2.2 Flow chart of the SIMPLE method for transient flow.

The momentum and continuity equations are solved sequentially, in which the continuity equation appears as an equation of pressure correction although pressure

does not appear explicitly in the continuity equation for incompressible flows (i.e. the SIMPLE method). The numerical procedure of the SIMPLE method is shown in Figure 2.2.

Discretization of the governing equations can be illustrated most easily by considering the unsteady conservation equation for transport of a scalar quantity ϕ. This is demonstrated by the following equation written in integral form for an arbitrary control volume V as follows:

$$\int_V \frac{\partial \phi}{\partial t} dV + \oint \phi \vec{v}.d\vec{A}_e = \oint \Gamma_\phi \nabla \phi.d\vec{A}_e + \int_V S_\phi dV \qquad (2.18)$$

where

$\dfrac{\partial \phi}{\partial t}$ = conservative form of transient derivative of transported

variable, ϕ

$\vec{v}$ = velocity vector ($= u\hat{i} + v\hat{j}$ in 2D)

$\vec{A}$ = surface area vector

Γ_ϕ = diffusion coefficient for ϕ

$\nabla \phi$ = gradient of $\phi (=(\partial \phi / \partial x)\hat{i} + (\partial \phi / \partial y)\hat{j}$ in 2D)

S_ϕ = source of ϕ per unit volume

Equation (2.18) is applied to each control volume, or cell, in the computational domain. Discretization of Equation (2.18) on a given cell yields

$$\frac{\partial \phi}{\partial t} V + \sum_e^{nb} \phi_e \vec{v}_e.\vec{A}_e = \sum_e^{nb} \Gamma_\phi (\nabla \phi)_n.\vec{A}_e + S_\phi V \qquad (2.19)$$

where *nb* is the number of edges enclosing the control volume.
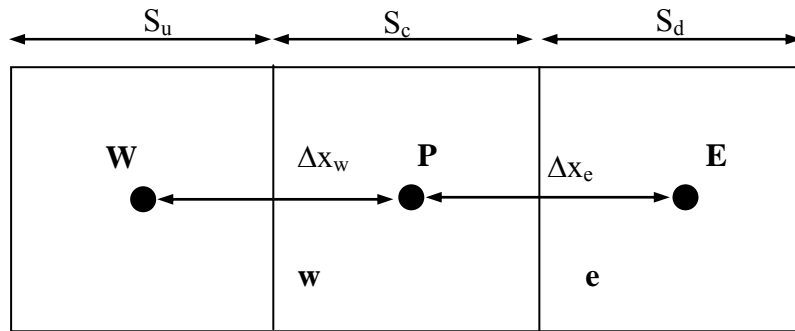
Figure 2.3 One-Dimensional Control Volume.

For quadrilateral meshes, where unique upstream and downstream faces and cells can be identified, the QUICK scheme (see Leonard and Mokhtari 1990) is adopted for computing a higher-order value of the convected variable ϕ at a face. QUICK-type schemes are based on a weighted average of second-order-upwind and central interpolations of the variable. For the face 'e' in Figure 2.3, if the flow is from left to right, such a value can be written as

$$\phi_e = \theta\left[\frac{S_d}{S_c + S_d}\phi_P + \frac{S_c}{S_c + S_d}\phi_E\right] + (1-\theta)\left[\frac{S_u + 2S_c}{S_u + S_c}\phi_P - \frac{S_c}{S_u + S_c}\phi_W\right] \qquad (2.20)$$

$\theta = 1$ in the above equation results in a central second-order interpolation while $\theta = 0$ yields a second-order upwind value. The traditional QUICK scheme is obtained by setting $\theta = 1/8$. The QUICK scheme is typically more accurate on structured grids aligned with the flow direction.

For transient simulations, the governing equations must be discretized in both space and time domains. The spatial discretization for the time-dependent equations is identical to the steady-state case. Temporal discretization involves the integration of every term in the differential equations over a time step Δt. The integration of transient terms is straightforward and a generic expression for the time evolution of a variable ϕ is given by

$$\frac{\partial \phi}{\partial t} = F(\phi) \qquad (2.21)$$

where the function $F(\phi)$ incorporates any spatial discretization. If the time derivative is discretized using backward differences, the first-order accurate temporal discretization is given by

$$\frac{\phi^{n+1} - \phi^n}{\Delta t} = F(\phi) \qquad (2.22)$$

and the second-order discretization is given by

$$\frac{3\phi^{n+1} - 4\phi^n + \phi^{n-1}}{2\Delta t} = F(\phi) \qquad (2.23)$$

Here, the implicit time integration is employed in order to evaluate $F(\phi)$ at a future time instance. An advantage of the implicit scheme is that it is unconditionally stable with respect to the time step. This implies that ϕ^{n+1} in a given cell is related to ϕ^{n+1} in a neighboring cells through $F(\phi^{n+1})$. This implicit equation can be solved by iterating the following equation

$$\phi^{n+1} = \frac{4}{3}\phi^n - \frac{1}{3}\phi^{n-1} + \frac{2}{3}\Delta t F(\phi^{n+1}) \tag{2.24}$$

The iteration terminates until a convergence criterion is met. The truncation error here is second-order with respect to the time step.

Because of the nonlinearity of Equations (2.14)-(2.17), it is necessary to control the change of ϕ. This is typically achieved by under-relaxation, which reduces the change of ϕ produced at the time of each iteration. In a simple form, the updated value of the variable ϕ within a cell depends upon the old value, ϕ_{old}, the computed change $\Delta\phi$ and the under-relaxation factor, α, as follows,

$$\phi = \phi_{old} + \alpha\Delta\phi \tag{2.25}$$

In the present study, the under-relaxation factors α are set to the default values in FLUENT, which are 0.3 for pressure, 0.7 for velocities and 1 for all other quantities.

2.2.2 Convergence criterion

For the efficiency and the success of iteration, convergence criteria control the iteration process. Therefore, selecting an appropriate convergence criterion is crucial for an iteration process.

In the present numerical solution using FLUENT 6.3.26, the residual sum for each of the conserved variables is computed and compared with the set convergence criterion. The iteration will continue until the sum of residuals drops bellow the set convergence criterion.

After discretization, the conservation equation for a general variable ϕ at a cell P can be written as

$$a_P\phi_P = \sum_{nb} a_{nb}\phi_{nb} + b \tag{2.26}$$

Here a_P is the center coefficient, a_{nb} are the influence coefficients for the neighboring cells, and b is the contribution of the constant part of the source term. The residual, R_ϕ may be defined as the imbalance in equation (2.26) summed over all the computational cells P (see Fluent User's Guide for details)

$$R_\phi = \frac{\sum_P \left| \sum_{nb} a_{nb}\phi_{nb} + b - a_P\phi_P \right|}{\sum_P |a_P\phi_P|} \tag{2.27}$$

For the momentum equations and energy equation, ϕ is replaced by u, v, or T respectively. For the continuity equation, the residual is defined by

$$R_c = \frac{\sum_P \left| \text{rate of mass creation in cell } P \right|}{\sum_{\text{Max in first five iterations}} \left| \text{rate of mass creation in cell } P \right|} \qquad (2.28)$$

Here, the denominator is the largest absolute value of the continuity residual in the first five iterations. The details of above convergence criteria can be found in the FLUENT User's Guide.

On a computer with infinite precision, these residuals will go to zero as the solution converges. On an actual computer, the residuals decay to some small value (round-off) and then stop changing (level out). For double precision computations, residuals can drop by up to twelve orders of magnitude (10^{-12}). In the present study double precision Fluent version is used and most of the numerical simulation 10^{-5} is adopted as the absolute convergence criteria of the continuity, *x*- and *y*-momentum and energy equations. Several tests were conducted for different convergence criteria from 10^{-3} to 10^{-8} and found that 10^{-5} is suitable for all simulation considered in this thesis.

2.3 Summary

In this chapter, the governing equations have been introduced and simplified for natural convection adjacent to an inclined plate and in an attic space. FLUENT package has been adopted for the numerical simulations of this problem with a finite volume method used to discretize the governing equations. SIMPLE scheme has been used to solve the linearized and discretized algebraic equations.

3 Natural convection boundary layer adjacent to an inclined flat plate subject to sudden and ramp heating

Scale analysis is a cost-effective way that can be applied as a first step in understanding the physics behind fluid flow and heat transfer issues. The results of scale analysis can serve as a guide for both experimental and numerical investigations. Therefore, scaling has been used by many researchers to investigate the transient flow development involving different kinds of geometry and thermal forcing. An extensive scaling analysis has been carried out by Patterson and Imberger (1980) for the transient flow behaviour that occurs when the two opposing vertical sidewalls of a two-dimensional rectangular cavity are impulsively heated and cooled by an equal amount. They devised a classification of the flow development through several transient flow regimes to one of three steady-state types of flow based on the relative values of the Rayleigh number, Ra, the Prandtl number, Pr, and the aspect ratio, A, of the cavity. Various scaling relations characterizing the flow evolution at distinct development stages were developed by scaling analysis.

In this chapter, scaling analysis will be carried out for the boundary layer development adjacent to an inclined flat plate for suddenly increased and linearly increasing (ramp) temperature boundary conditions. A series of numerical calculations has also been carried out for different parameters to verify the scaling predictions. Details of the numerical procedures can be found in the previous chapter (Chapter 2). However, the geometry, boundary conditions and grid and time step dependence tests are included in this chapter.

3.1 Problem formulation

Under consideration is the flow behaviour resulting from the heating of an initially motionless and isothermal Newtonian fluid with $Pr < 1$ by a heated flat plate. The physical system sketched in Figure 3.1 consists of an inclined flat plate ($CD = L$). We

extend both ends of the plate by a distance equal to its length and form a rectangular domain, which is filled with an initially stationary fluid at a temperature T_c. If we consider the plate as the hypotenuse of a right angled triangle then the altitude is h, the length of the base is l and the angle that the plate makes with the base is θ. Except for the plate (the section *CD* shown in Figure 3.1), all walls of the rectangular domain are assumed to be adiabatic, rigid and non-slip. Two heating boundary conditions are applied on the plate; sudden heating to a specified temperature which is then maintained, and heating by a linearly increasing temperature to a specified temperature over certain time (the ramp time) after which the temperature is maintained (the ramp function) . The ramp function is described in the scaling section in this chapter below.
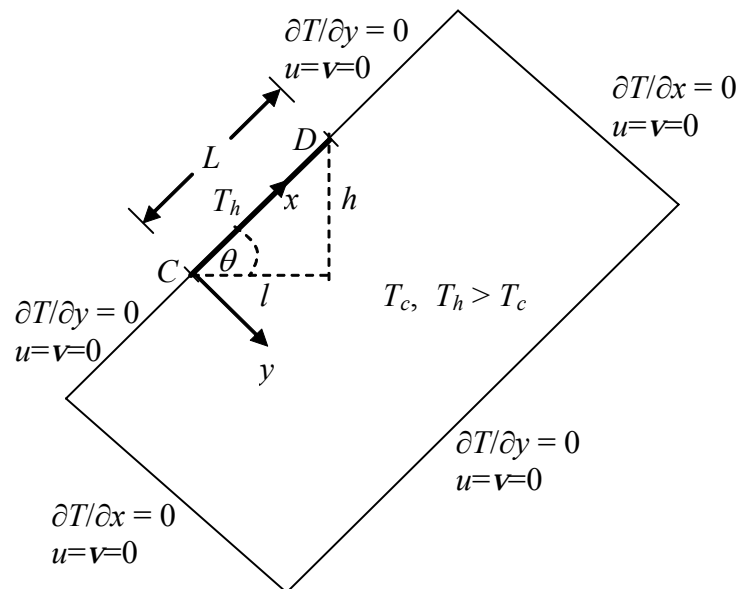
Figure 3.1 Schematic of the computational domain and boundary conditions.

3.2 Overview of the transient flow

As noted above, two thermal boundary conditions have been considered for the natural convection boundary layers adjacent to the inclined plate in this chapter.

The first case is the sudden heating boundary condition. The plate is suddenly heated to and thereafter maintained at a higher temperature T_h, whereas the ambient fluid has a lower temperature T_c.

(a)

(b)
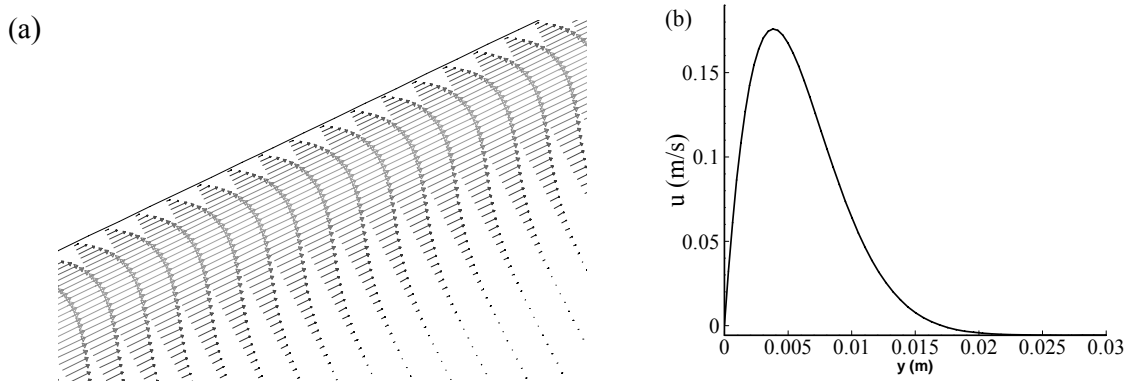
Figure 3.2 (a) Velocity vector and (b) velocity profile for $Ra = 3.00 \times 10^7$ with $Pr = 0.72$ and $A = 0.5$.

The characteristic velocity in this case is the maximum velocity parallel to the inclined plate. The velocity vector field in the region near the plate and the corresponding velocity profile along a line perpendicular to the plate at the mid point have been plotted in Figure 3.2 after initiation for a typical case. It is seen that the flow direction is approximately parallel to the heated plate.
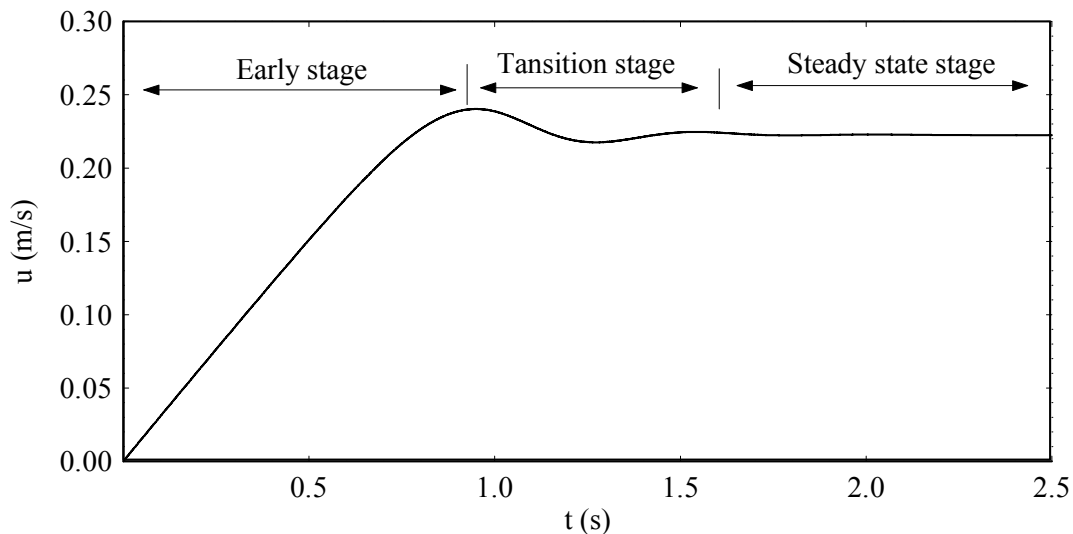
Figure 3.3 Time series of the maximum velocity parallel to the plate through the line perpendicular to its mid point for $Ra = 3.00 \times 10^7$, $A = 0.5$ and $Pr = 0.72$ for sudden heating.

Figure 3.3 shows a typical time series of the maximum velocity parallel to the plate for sudden heating, taken from the above-mentioned temperature profile at the mid point of the heated plate. Since the inclined plate is hot relative to the ambient fluid, the flow is laminar and stable so long as Ra is not too large. As a consequence, a

natural convection boundary layer develops adjacent to the hot inclined plate and continues to grow with increasing time. The development of the boundary layer can be described in three different stages (refer to Figure 3.3); namely, the early stage, transition stage and the steady state stage.
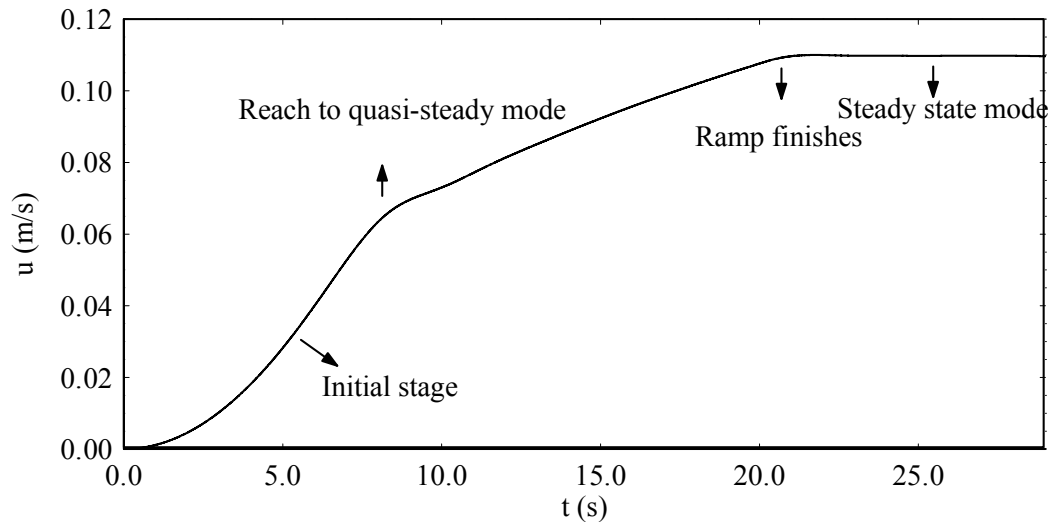
Figure 3.4 Time series of the maximum velocity parallel to the plate through the line perpendicular to its mid point for $Ra = 7.63 \times 10^6$, $A = 0.5$ and $Pr = 0.72$ for ramp heating.

The second case is an inclined plate subject to a temperature boundary condition which follows a linear function up until some specified time and then remains constant. The development of the thermal boundary layer flow depends on the comparison of the time at which the ramp heating finishes and the time at which the thermal boundary layer completes its growth. If the ramp time is long compared with the steady state time, the layer reaches a quasi-steady mode (see Figure 3.4). Further increase in the heat input simply accelerates the flow to maintain the proper thermal balance. The overall flow development for this case may be characterized as: the early stage, the quasi-steady stage and the steady state stage which can be clearly identified in Figure 3.4. On the other hand, if the ramp is completed before the layer becomes steady, the subsequent growth is the same as the case of sudden heating. What that means is that the boundary layer then grows as though the startup were instantaneous and eventually reaches a steady state, and thus there is no difference between the ramp and instantaneous start up cases (see Figure 3.5).
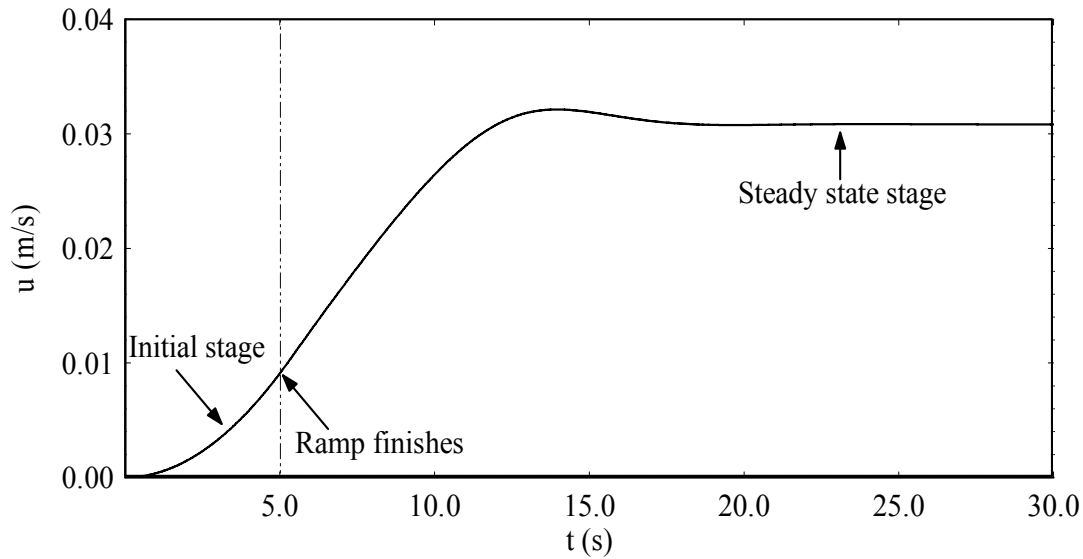
Figure 3.5 Time series of the maximum velocity parallel to the plate through the line perpendicular to its mid point $Ra = 6.11 \times 10^5$, $A = 0.5$ and $Pr = 0.72$ for ramp heating.

In the following sections, the detailed scaling analyses of the flow development for the two different thermal boundary conditions described above will be discussed. A grid and time step dependence test for numerical simulation will be described. To verify the scaling, a set of numerical results have been obtained for various parameters (Rayleigh numbers, *Ra*, aspect ratio, *A*) with a fixed Prandtl number, *Pr,* given the value for air.

3.3 Scaling for sudden heating

With the initiation of the flow, a thermal boundary layer develops adjacent to the heated inclined plate. The parameters characterizing the boundary layer development are predominantly the thermal boundary-layer thickness δ_T, the maximum velocity parallel to the plate u_s within the boundary layer, and the time t_s for the boundary layer to reach steady state.

3.3.1 Growth of the thermal boundary layer

As mentioned above, the sudden heating of the flat plate results in a thermal boundary layer developing adjacent to the inclined plate. We follow the arguments given by Patterson and Imberger (1980), appropriately modified for the inclined plate and the Prandtl number ($Pr < 1$).

The energy equation (2.15) indicates that since the fluid is initially motionless the heating effect of the plate will first diffuse into the fluid layer through pure conduction, resulting in a thermal boundary layer of thickness δ_T. Within the boundary layer, the dominant balance is between the unsteady and diffusion terms in the energy equation (2.15), that is,

$$\frac{\Delta T}{t} \sim \kappa \frac{\Delta T}{\delta_T^2},$$

which leads to a scale for the thickness of the thermal boundary layer

$$\delta_T \sim \kappa^{1/2} t^{1/2}. \tag{3.1}$$

This scaling is valid till the convection term becomes important.

The unsteady inertia term of the momentum equation (2.2) is $O(u/t)$, the viscous term $O(\nu u/\delta_T^2)$, and the advection term $O(u^2/L)$. The ratio of the advection term to the unsteady term is then $O(ut/L)$. For very small time $ut/L \ll 1$. Therefore the advection term is not significant for small time. The ratio of the unsteady to viscous term is $(u/t)/(\nu u/\delta_T^2) \sim \delta_T^2/(\nu t) \sim 1/Pr$, where $Pr = \nu/\kappa$. For $Pr \ll 1$ the viscous term is much smaller than the unsteady term, and therefore, the correct balance is between the unsteady term and buoyancy. However, for $Pr \gg 1$, the unsteady term is much smaller than the viscous term and the correct balance is between viscosity and buoyancy. If $Pr \sim O(1)$, then the unsteady and viscous terms are of the same order, and thus both terms need to be included in a balance with the buoyancy term. This balance was introduced by Lin *et al.* (2007).

The unsteady term is $O(u/t)$ and the viscous term is $O(Pru/t)$, so these two terms together are $O((1 + Pr)u/t)$. Now the balance in the inclined momentum equation is

$$(1+Pr)\frac{u}{t} \sim g\beta\Delta T \sin\theta. \tag{3.2}$$

Therefore $u \sim g\beta\sin\theta\Delta T t/(1+Pr)$. The inclination angle θ is related to the slope or aspect ratio A through $\sin\theta = A/(1+A^2)^{1/2}$. Hence (3.2) becomes

$$u \sim \frac{ARaPr}{(1+Pr)(1+A^2)^{1/2}} \left(\frac{t}{h^2/\kappa}\right)\left(\frac{\kappa}{h}\right), \tag{3.3}$$

where the Rayleigh number is defined as $Ra = g\beta\Delta T h^3/\nu\kappa$.

3.3.2 Steady state stage

As time passes, the thermal boundary layer thickness δ_T continues to grow until a balance between convection and conduction is reached. i.e.

$$u\frac{\Delta T}{L} \sim \kappa\frac{\Delta T}{\delta_T^2}$$

$$\Rightarrow \quad u \sim \frac{L}{t}. \tag{3.4}$$

Using the velocity scales (3.3) and (3.4) we conclude that the growth of the thermal boundary layer along the inclined plate ends at a time of the order t_s given by

$$\frac{ARaPr}{(1+Pr)(1+A^2)^{1/2}}\left(\frac{t_s}{h^2/\kappa}\right)\left(\frac{\kappa}{h}\right) \sim \frac{L}{t}$$

$$\Rightarrow t_s \sim \frac{(1+Pr)^{1/2}(1+A^2)^{1/2}}{ARa^{1/2}Pr^{1/2}}\left(\frac{h^2}{\kappa}\right). \tag{3.5}$$

The thickness of the thermal boundary layer along the plate at the steady state time, t_s is

$$\delta_T \sim \frac{h(1+Pr)^{1/4}(1+A^2)^{1/4}}{A^{1/2}Ra^{1/4}Pr^{1/4}}. \tag{3.6}$$

At the time when the thermal boundary layer reaches the steady state, the u velocity scale is

$$u_s \sim \frac{Ra^{1/2}Pr^{1/2}}{(1+Pr)^{1/2}}\left(\frac{\kappa}{h}\right). \tag{3.7}$$

The thermal boundary layer thickness at the steady state is shorter than the length of the plate if

$$\frac{\delta_T}{L} < 1.$$

This is equivalent to having

$$Ra > \frac{A^2(1+Pr)}{Pr(1+A^2)}. \tag{3.8}$$

Concurrently with the formation of a thermal boundary layer, a viscous boundary layer is developing. The thickness, δ_v of this viscous layer is a direct result of a balance between the viscous and inertia terms in the momentum equation,

$$\delta_v \sim (vt)^{1/2} \sim Pr^{1/2}\delta_T. \tag{3.9}$$

It is noted that for $Pr < 1$, the thickness of the viscous boundary layer is smaller than that of the thermal boundary layer. When the thermal layer has reached the steady state, the viscous layer has a thickness of the order

$$\delta_v \sim \frac{h\,Pr^{1/4}(1+Pr)^{1/4}\left(1+A^2\right)^{1/4}}{A^{1/2}Ra^{1/4}}. \tag{3.10}$$

3.3.3 Possible flow regimes

Based on the above scale analysis we may define some regimes of the flow development depending on the Rayleigh number. Since the viscous boundary layer is smaller than the thermal boundary layer for $Pr < 1$, the viscous layer is always embedded in the thermal boundary layer. We may classify the flow development as follows:

(i) If $Ra < A^2(1+Pr)/[Pr(1+A^2)]$, the thermal boundary layer has grown to a thickness greater than the length of the heated plate at the steady state.

(ii) If $Ra > A^2(1+Pr)/[Pr(1+A^2)]$, the thermal boundary layer thickness at the steady state is shorter than the length of the heated plate. That means the boundary layer flow becomes steady before the thickness reaches a length scale equivalent to the length of the heated plate. For sufficiently high Rayleigh numbers the flow may become turbulent, which is beyond the scope of this thesis.

3.4 Scaling for ramp heating

The flow behavior adjacent to an inclined plate subject to a ramp temperature boundary condition is considered for $Pr < 1$. Scaling analysis for this boundary condition is still absent in the literature. However, Patterson *et al.* (2008) has developed a scaling analysis for the ramp heating of a vertical flat plate with $Pr > 1$ and we follow that scaling here with $Pr < 1$. For this problem the physical system is the same as that for the sudden heating case which is depicted in Figure 3.1. The plate $CD = L$ is heated to T_h according to the following function.

$$T_h = \begin{cases} T_c & \text{if } t \leq 0; \\ T_c + \Delta T\left(t/t_p\right) & \text{if } 0 < t < t_p; \\ T_c + \Delta T & \text{if } t \geq t_p; \end{cases} \tag{3.11}$$

where $\Delta T = T_h - T_c$ and t_p is the time duration of ramp heating.

Initially the flow is motionless and isothermal. As soon as the above temperature, T_h applied on the plate, a thermal boundary layer develops adjacent to the

heated inclined plate. The subsequent flow development is described in the following sections.

3.4.1 Early stage

The start-up stage is initially dominated by heat transfer via conduction through the hot plate, resulting in a thermal boundary layer of a thickness δ_T. As mentioned earlier for the case of the sudden heating boundary condition, initially the boundary layer grows according to the scale $\kappa^{1/2}t^{1/2}$. Furthermore, for $Pr \sim O(1)$, the unsteady and viscous terms together (i.e. $(1+Pr)u/t$) balance the buoyancy term in the momentum equation;

$$(1+Pr)\frac{u}{t} \sim g\beta \sin \theta \Delta T \frac{t}{t_p}$$

$$\Rightarrow u \sim \frac{g\beta \sin \theta \Delta T t^2}{(1+Pr)t_p}. \qquad (3.12)$$

The above scale leads to the following velocity scale after substituting the Rayleigh number relation and the aspect ratio relation:

$$u_r \sim \frac{ARaPr}{(1+Pr)(1+A^2)^{1/2}} \left(\frac{t}{h^2/\kappa}\right)\left(\frac{t}{t_p}\right)\left(\frac{\kappa}{h}\right). \qquad (3.13)$$

This balance holds as long as $t < t_s$.

3.4.2 Quasi-steady state time

The boundary layer adjacent to the inclined plate continues to develop with the velocity scale defined in (3.13) and the thickness scale $\kappa^{1/2}t^{1/2}$ until the ramp finishes i.e. $t < t_p$ or until a balance between convection and conduction is reached at time t_{sr} determined below:

$$\frac{u}{L}\Delta T \frac{t_{sr}}{t_p} \sim \kappa \frac{\Delta T}{\delta_T^2} \frac{t_{sr}}{t_p}$$

$$\Rightarrow u \sim \frac{h}{At_{sr}\cos\theta}. \qquad (3.14)$$

Using the velocity scales (3.13) and (3.14) we conclude that the growth of the thermal boundary layer along the inclined wall ends at time t_{sr} when

$$\frac{ARaPr}{(1+Pr)(1+A^2)^{1/2}} \left(\frac{t_{sr}}{h^2/\kappa}\right)\left(\frac{t_{sr}}{t_p}\right)\left(\frac{\kappa}{h}\right) \sim \frac{h}{At_{sr}\cos\theta}$$

$$\Rightarrow t_{sr} \sim \frac{(1+Pr)^{1/3}(1+A^2)^{1/3}}{A^{2/3}Ra^{1/3}Pr^{1/3}}\left(\frac{t_p}{h^2/\kappa}\right)^{1/3}\left(\frac{h^2}{\kappa}\right). \tag{3.15}$$

so long as $t_{sr} < t_p$. This is the same as saying that

$$t_p > \frac{(1+Pr)^{1/2}(1+A^2)^{1/2}}{ARa^{1/2}Pr^{1/2}}\left(\frac{h^2}{\kappa}\right). \tag{3.16}$$

The right-hand side of (3.16) represents the steady state time scale for an instantaneous start up function (refer to 3.5). This means that if the ramp time is longer than the time it would take for the step function start up to reach a steady state boundary layer, then the boundary layer will have reached a convection-conduction balance before the ramp has finished.

The thickness of the thermal boundary layer along the plate at the time t_{sr} is

$$\Rightarrow \delta_{Tr} \sim \frac{h(1+Pr)^{1/6}(1+A^2)^{1/6}}{A^{1/3}(RaPr)^{1/6}}\left(\frac{t_p}{h^2/\kappa}\right)^{1/6}. \tag{3.17}$$

At the time when the plate boundary layer is steady, the u velocity scale is

$$u_{sr} \sim \frac{(RaPr)^{1/3}(1+A^2)^{1/6}}{A^{1/3}(1+Pr)^{1/3}}\left(\frac{h^2/\kappa}{t_p}\right)^{1/3}\left(\frac{\kappa}{h}\right). \tag{3.18}$$

On the other hand, if $t_p<(1+Pr)^{1/2}(1+A^2)^{1/2}h^2/[A(RaPr)^{1/2}\kappa]$, then $t_{sr}>t_p$ and the thermal boundary layer has not finished growing when the ramp finishes. At the time when the ramp is finished ($t = t_p$) the unsteady velocity scale in the boundary layer is obtained from (3.13) as

$$u \sim \frac{ARaPr}{(1+Pr)(1+A^2)^{1/2}}\left(\frac{t_p}{h^2/\kappa}\right)\left(\frac{\kappa}{h}\right),$$

which is identical to the unsteady velocity scale (3.3) for the case of sudden heating boundary condition at the same time. The subsequent development of the boundary layer for $t > t_p$ will follow the same thickness and velocity scales as those obtained for the sudden heating case until a steady state is reached. Hence there is no difference between the ramp and instantaneous start up cases after the ramp is finished.

3.4.3 Quasi-steady stage

For the case for which the steady state time is less than the ramp time, once the steady state time t_{sr} is reached, the boundary layer stops growing according to $\kappa^{1/2}t^{1/2}$ which is only valid for conductive boundary layers. The thermal boundary layer is in a quasi-

steady mode with convection balancing conduction. Further increase of the heat input simply accelerates the flow to maintain the proper thermal balance. For the ramp function startup, this means that

$$\frac{u}{L}\Delta T\frac{t_{sr}}{t_p} \sim \kappa\frac{\Delta T}{\delta_T^2}\frac{t_{sr}}{t_p}$$

$$\Rightarrow u \sim \frac{\kappa L}{\delta_T^2}. \tag{3.19}$$

At this time the unsteady term is not important because the ratio of the unsteady term to the viscous term is $O(\delta_T^2/(v\, t))$ and for large values of t, $\delta_T^2/(v\, t) \to 0$. Therefore, the viscous term balances the buoyancy term. Hence,

$$v\frac{u}{\delta_T^2} \sim g\beta\sin\theta\Delta T\frac{t}{t_p}$$

$$\Rightarrow \delta_T \sim \frac{h\left(1+A^2\right)^{1/4}}{A^{1/2}Ra^{1/4}}\left(\frac{t_p}{t}\right)^{1/4}. \tag{3.20}$$

From (3.19) the velocity scale in the quasi-steady mode becomes

$$u \sim Ra^{1/2}\left(\frac{\kappa}{h}\right)\left(\frac{t}{t_p}\right)^{1/2}. \tag{3.21}$$

Notice that the boundary layer thickness decreases beyond t_{sr}. This has to happen as the fluid is accelerating and is therefore more effective in convecting the heat away; the boundary layer has to contract so that conduction is increased to balance the increased convection.

In parallel with the formation of the thermal boundary layer for $t < t_{sr}$, a viscous boundary layer also appears adjacent to the inclined plate with a balance between the viscous and inertia terms of the momentum equation, i.e.

$$\delta_v \sim v^{1/2}t^{1/2} \sim Pr^{1/2}\delta_T \tag{3.22}$$

For $Pr < 1$, δ_v is smaller than δ_T, implying that the viscous boundary layer is always embedded within the thermal boundary layer. When the thermal layer has reached the quasi steady state (at t_{sr}), the viscous layer has a thickness of order

$$\delta_{vr} \sim \frac{h\, Pr^{1/3}\left(1+Pr\right)^{1/6}\left(1+A^2\right)^{1/6}}{A^{1/3}Ra^{1/6}}\left(\frac{t_p}{h^2/\kappa}\right)^{1/6}. \tag{3.23}$$

However as the temperature on the plate continues to increase for $t > t_{sr}$, the viscous boundary layer thickness after the quasi steady state is

$$\delta_v \sim \frac{hPr^{1/2}\left(1+A^2\right)^{1/4}}{A^{1/2}Ra^{1/4}}\left(\frac{t_p}{t}\right)^{1/4}. \tag{3.24}$$

Here it is also noted that the viscous boundary layer thickness also decreases after the time $t = t_{sr}$.

3.4.4 Possible flow regimes

Similarly to the sudden heating case we may also classify the flow development under the ramp heating boundary condition into different flow regimes. It is found in the scaling analysis that the flow development depends on two time scales: the ramp time and the quasi-steady time. Based on these two time scales we may classify the flow development as follows:

(i) If $Ra > (1+Pr)(1+A^2)h^4/[A^2Pr\kappa^2t_p^2]$, then the ramp time is longer than the quasi-steady time, and the flow becomes quasi-steady before the ramp is finished. Once conduction and convection are in balance, the thickness of the thermal boundary layer has reached a maximum.

If $Ra > A^4(1+Pr)\kappa\, t_p/[Prh^2(1+A^2)^2]$, then the thermal boundary layer thickness is shorter than the length of the heated plate. In this regime the flow is dominated by convection. The flow, however, may become turbulent for sufficiently high Rayleigh numbers. Turbulent analysis is out of the scope of this thesis.

(ii) If $Ra < (1+Pr)(1+A^2)h^4/[A^2Pr\kappa^2t_p^2]$, then the ramp time is shorter than the steady/quasi-steady time and the boundary layer has not finished growing when the ramp is finished. What that means is that the boundary layer then grows as though the start-up were instantaneous and reaches a steady state at t_s. Therefore, there is no difference between the ramp and instantaneous start up cases in this flow regime.

In the following sections, the above scaling relations are validated against the numerical simulation. However grid and time step dependence tests must first be performed to ensure the accuracy of the numerical results.

3.5 Grid and time step dependence tests

3.5.1 Grid generation

The resolution of the grid inside the computational domain plays an important role in the accuracy and the stability of numerical simulations. In some regions of the domain a significant number of meshes are required in order to resolve the true physical flow

features (e.g boundary layers). A poorly distributed mesh in a critical region could result in false results. Unfortunately, it is often difficult to determine the locations of significance before the calculation is actually carried out. However we may use our previous knowledge to locate the regions of large flow gradients. Although an increase of the grid resolution generally increases the numerical accuracy, it also requires significant computing resources for both calculation and post-processing. Therefore, it is necessary to compromise between the numerical accuracy and computing efficiency when considering the numerical grid.
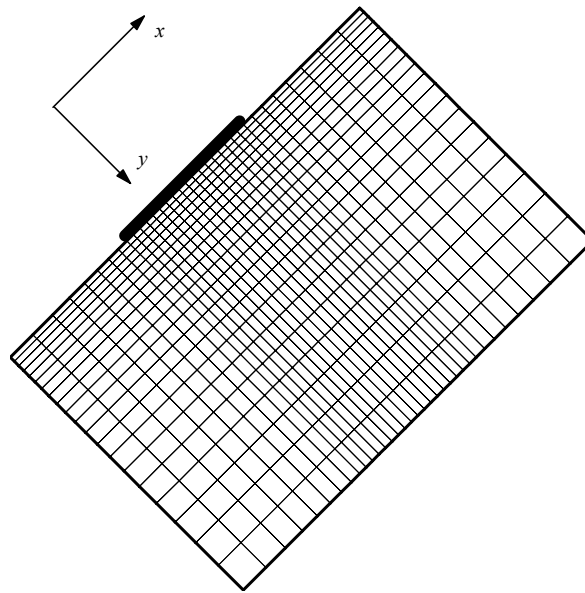
Figure 3.6 Grid distribution of the heated plate.

For natural convection adjacent to an inclined flat plate strong flows are present in the vicinity of the plate. Therefore, we need to distribute a non-uniform finer mesh near the plate when compared to other regions. We may use an expansion factor to distribute the non uniform mesh. However, the expanding factor of grid is usually limited in order to ensure that the solution is not degraded. A factor of up to 10% may be used according to Patterson and Armfield (1990).

Table 3.1 Grid parameter for $A = 0.5$ and 1.0.

Mesh size	Along *x*-axis			Along *y*-axis		Time
	Plate GN	Both side GN	EF	GN	EF	step
170×200	90	40	1.030	200	1.010	0.004
255×150	135	60	1.020	150	1.015	0.003
340×200	180	80	1.015	200	1.010	0.002
510×300	270	120	1.010	300	1.008	0.0015

Note: GN is Grid Number, EF is expansion factor.

The distribution of mesh tested is shown for three different aspect ratios in Tables 3.1 and 3.2. The grid distribution on the plate surface is uniform; however on the surface of the two extended sides of the plate an expansion factor has been used to form a non-uniform mesh. A non-uniform mesh has also been applied along the *y*-axis of the domain with finer mesh near the plate. A schematic of the grid distribution is shown in Figure 3.6.

Table 3.2 Grid parameter for $A = 0.1$.

Mesh size	Along *x*-axis			Along *y*-axis		Time
	Plate GN	Both side GN	EF	GN	EF	step
220×200	140	40	1.010	200	1.010	0.004
330×150	210	60	1.008	150	1.015	0.003
440×200	280	80	1.005	200	1.010	0.002
660×300	420	120	1.004	300	1.008	0.0015

3.5.2 Test results

Grid and time step dependence tests have been conducted based on the numerical procedures described earlier for the highest Rayleigh number case for both thermal forcing conditions (that is, sudden heating and ramp heating). It is expected that the mesh selected for the highest Rayleigh number will also be applicable for all lower Rayleigh numbers.

The time histories of the calculated maximum velocity parallel to the sloping wall for different aspect ratios with four different meshes are plotted in Figure 3.7 for the case of the sudden heating boundary condition. It is seen in the figure that all solutions indicate three stages of the flow development, an initial growth stage, a transitional stage and a steady state stage. In the initial growth stage, the four solutions follow each other closely (except the solution with a coarse mesh 330×150, which deviates slightly from the other three meshes for $A = 0.1$ in Figure 3.7a). The transitional stage is characterized by a single overshoot. The time to reach the steady state is around 0.8s, 1.5s and 6s for $A = 1.0, 0.5$ and 0.1 respectively.

(a)

(b)
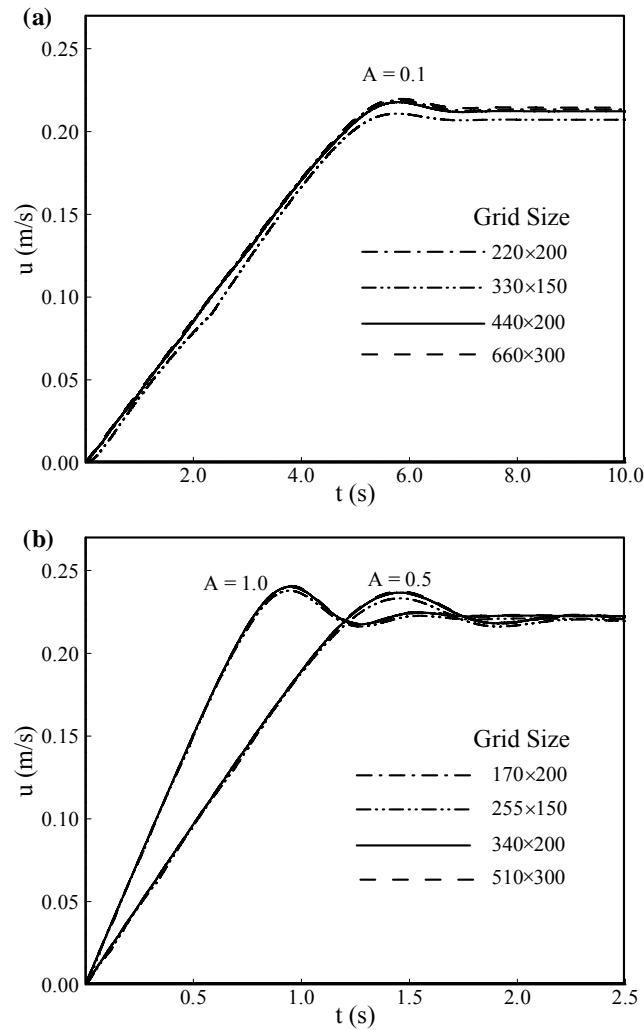
Figure 3.7 Time series of the maximum velocity for sudden heating with $Ra = 3.00 \times 10^7$ and $Pr = 0.72$. (a) $A = 0.1$ and (b) $A = 0.5$ and 1.0.

The maximum variation of the velocity between the coarsest and finest meshes for $A = 0.1$ is approximately 3.8%, and the maximum variation among the three fine meshes is only about 1.4%. The maximum variations of the velocity between the coarsest and finest meshes for $A = 0.5$ and 1.0 are 1.3% and 0.4% respectively. Therefore a fine mesh of 440×200 for $A = 0.1$ and a relatively coarse mesh 340×200 for $A = 1.0$ and 0.5 are adopted for the present simulations with a time step 0.002s.
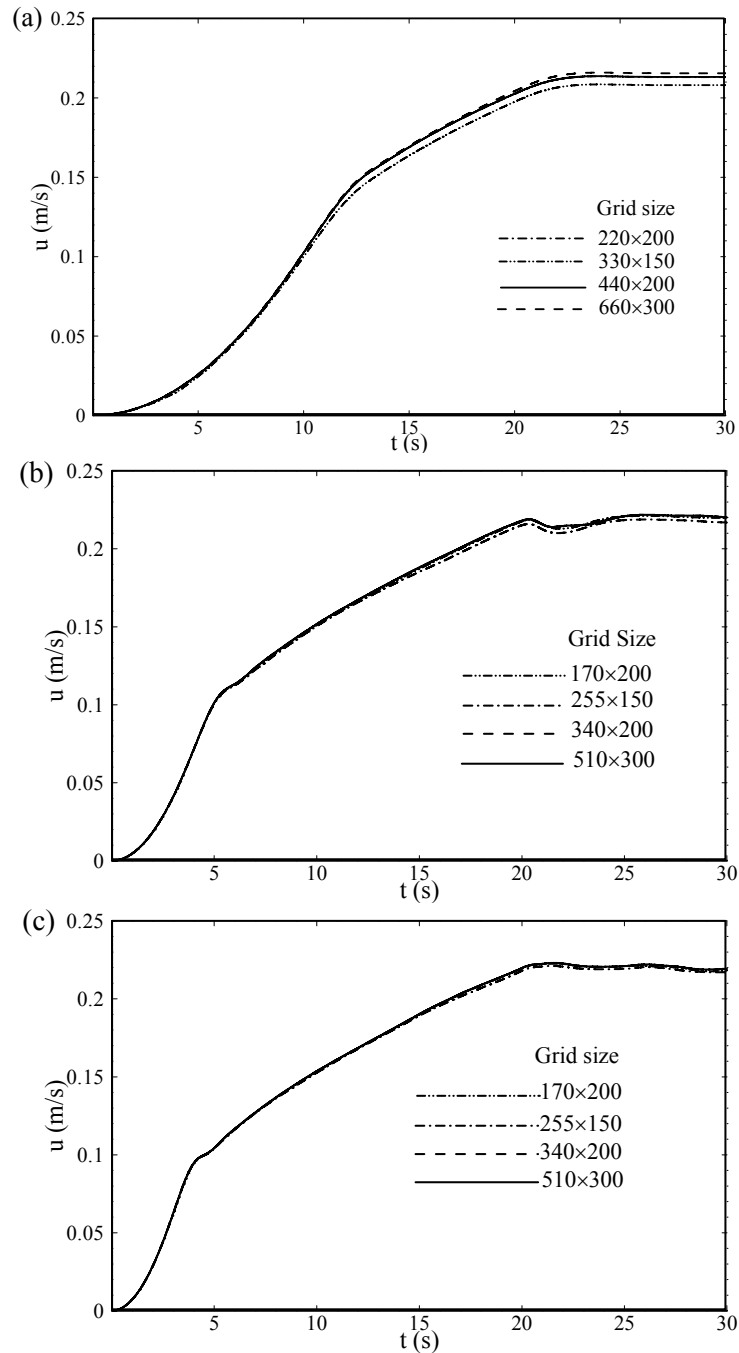
Figure 3.8 Time series of the maximum velocity for ramp heating with $Ra = 3.00 \times 10^7$ and $Pr = 0.72$. (a) $A = 0.1$, (b) $A = 0.5$ and (c) $A = 1.0$.

Mesh and time step dependence tests have also been conducted for the ramp heating boundary condition to ensure the accuracy of the numerical solutions. The same meshes as the sudden heating case have been considered here for three different aspect ratios.

Figure 3.8 shows the time series of the maximum velocity parallel to the inclined surface calculated along a line normal to the surface at the mid point of the

heated plate for three different aspect ratios for the ramp heating boundary condition for $Ra = 3.0 \times 10^7$ and $Pr = 0.72$. The ramp time has been set to 20s for all cases. As is mentioned in the scaling analysis, the ramp time may be longer or shorter than the steady state time for the boundary layer. If the ramp time is longer than the steady state time, then after the steady-state time the velocity continues to increase as the plate is still being heated. However, the growth rate of the velocity is reduced compared with that in the earlier phase. The two-stage growth of the velocity is clearly seen in the simulation results (see Figure 3.8). It is seen in this figure that at about 12s, 5.2s and 4s for $A = 0.1$, 0.5 and 1.0 respectively, the boundary layer becomes quasi steady. At $t = 20s$ the ramp finishes and the boundary layer becomes completely steady.

The maximum variation of the calculated maximum velocity between the coarsest and finest meshes for $A = 0.1$, 0.5 and 1.0 is 3.85%, 0.54% and 0.50% respectively. Therefore any of these meshes is appropriate for this simulation, and the mesh size 440×200 is adopted for $A = 0.1$ and 340×200 is adopted for $A = 0.5$ and 1.0 for the following simulations with the time step size 0.002s.

3.6 Flow development in different flow regimes for sudden heating

3.6.1 Conduction regime

The numerical results for a low Rayleigh number case are shown in Figure 3.9 with $Pr = 0.72$, $Ra = 10$ and $A = 0.5$. The temperature contours and streamlines at $t/t_s=2.4$ are plotted in Figures 3.9(a) and (b), respectively. The heated portion of the inclined plate has been marked at the time of post processing. This is also the case for subsequent Figures 3.10, 3.11, and 3.12. In this flow regime the thermal boundary layer eventually expands to the entire domain. Figure 3.9(c) shows the temperature profile which has been extracted along a line perpendicular to the plate at the mid point. The distance has been normalised by the length of the plate. It is seen in Figure 3.9(c) that the thickness of the thermal boundary layer is larger than $y/L = 1$. Therefore, the flow is dominated by conduction in this regime.

(a)

(b)

(c)

$\dfrac{\text{T-T}_c}{\Delta\text{T}}$

$\dfrac{\text{y}}{\text{L}}$
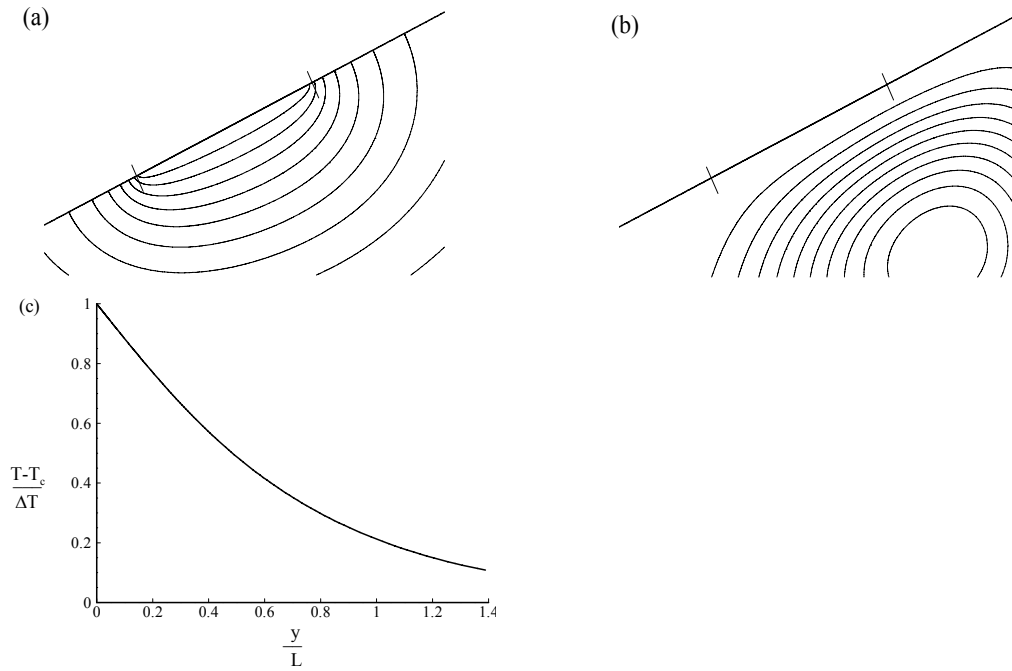
Figure 3.9 (a) Temperature contours, (b) streamlines and (c) temperature profiles along the line perpendicular to the plate at mid point of the boundary layer development for $Ra = 10$, $Pr = 0.72$ and $A = 0.5$ at $t/t_s = 2.4$.

3.6.2 Convection regime

The numerical results for a higher Rayleigh number with $Pr = 0.72$, $Ra = 2.58 \times 10^7$ and $A = 0.5$ at $t/t_s = 1.58$ are shown in Figure 3.10. The temperature contours are presented in Figure 3.10(a) and the streamlines are presented in Figure 3.10(b). We notice that convection increases significantly in this regime as the Rayleigh number increases. The temperature contours are very much concentrated in the thin thermal boundary layer near the inclined plate as the result of strong convection. A temperature profile along a line perpendicular to the plate at the mid point has been shown in Figure 3.10(c). The thermal boundary layer thickness can easily be deduced from this profile and is very small when compared to the length of the plate, supporting the strong convection effect in the heat transfer and fluid flow.
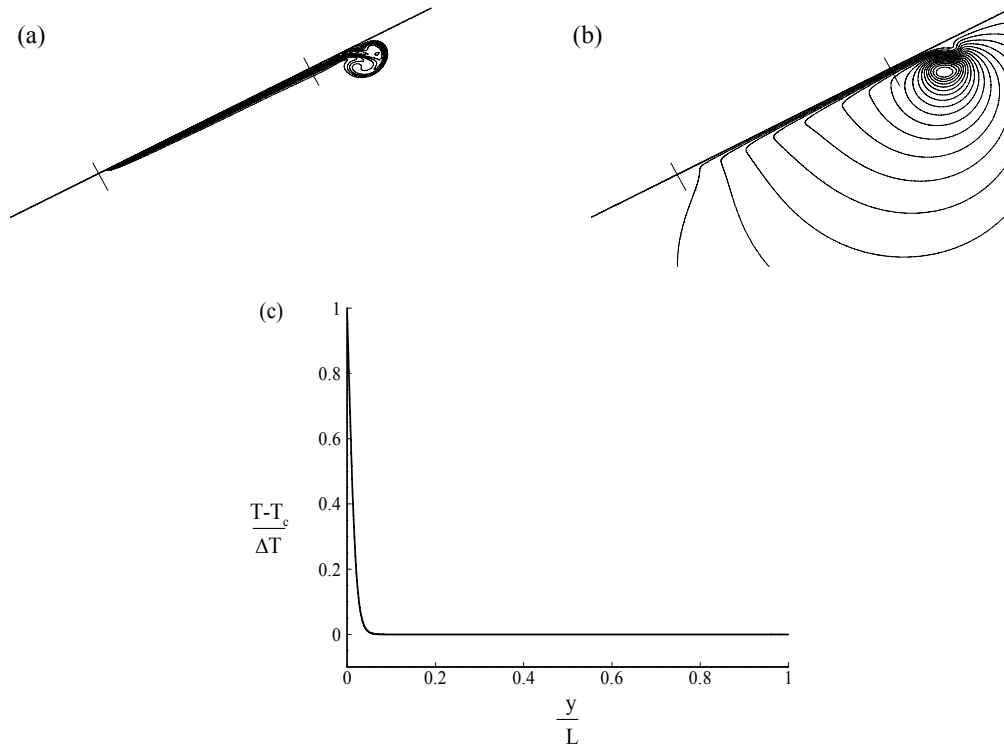
Figure 3.10 Temperature contours and streamlines of boundary layer development for $Ra = 2.58 \times 10^7$, $Pr = 0.72$ and $A = 0.5$ at $t/t_s = 1.58$.

3.7 Flow development in different regimes for ramp heating

3.7.1 Ramp time shorter than steady state time

Figure 3.11 shows the temperature contours, the streamlines and a temperature profile for $Pr = 0.72$, $Ra = 5$ and $A = 0.5$ at $t/t_{sr} = 2.77$ where the length of the ramp time is $t_p/t_{sr} = 0.042$. Figures 3.11(a) presents the temperature contours and Figure 3.11(b) presents the corresponding streamlines. For this regime the steady state time is larger than the ramp time. Therefore the flow behaviour at the steady state stage is identical to that for the sudden heating case. As soon as the heating starts, the thermal boundary layer expands outwards from the heated plate and eventually arrives at the opposite wall of the rectangular domain as time passes. A temperature profile has been shown in Figure 3.11(c) which is calculated along a line perpendicular to the plate at the mid point. The distance is normalised by the length of the plate. It is seen that the thickness of the

thermal boundary layer is larger than $y/L = 1$. Therefore, the flow is dominated by conduction in this regime.
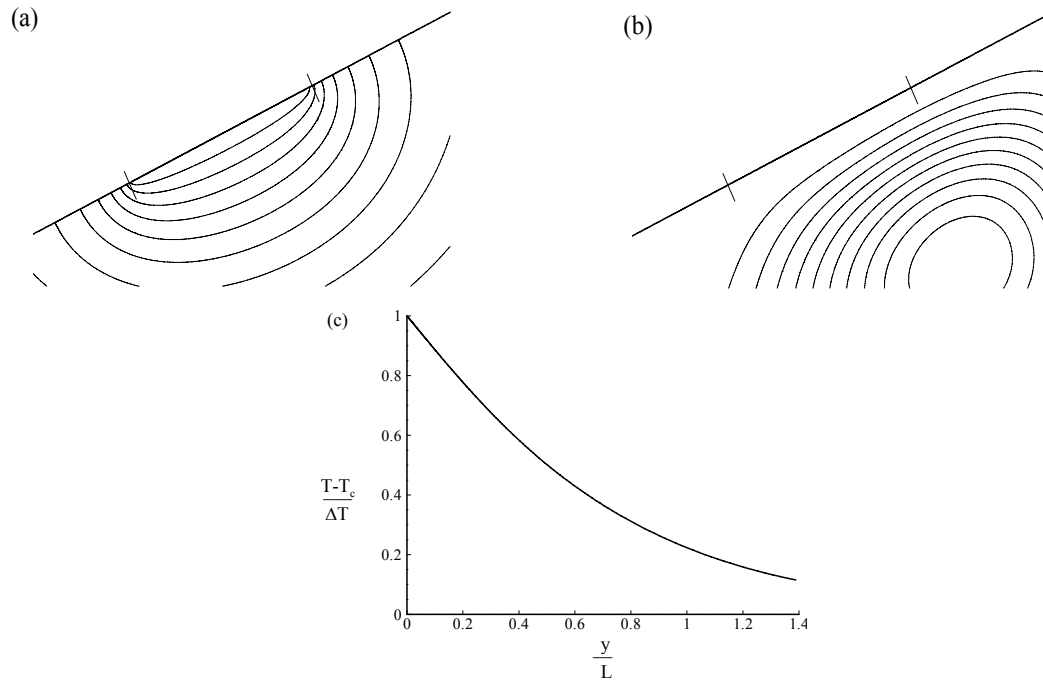
Figure 3.11 Temperature contours, (b) streamlines and (c) temperature profiles along the line perpendicular to the plate at mid point of the boundary layer development for $Ra = 5$, $Pr = 0.72$ and $A = 0.5$ at $t/t_s = 2.77$.

3.7.2 Ramp time longer than steady time

In this regime, the flow becomes quasi-steady state before the ramp is finished. As it is mentioned in the scaling development section, the boundary layer thickness decreases beyond the quasi-steady time, t_{sr}. A representative Rayleigh number of $Ra = 7.63 \times 10^6$ has been chosen to demonstrate the flow features in this flow regime. A time series of the maximum tangential flow velocity in the boundary layer obtained at this Rayleigh number has been presented in Figure 3.4, in which different stages of the flow development including the start up stage, the quasi-steady state and the steady state can be clearly identified. The corresponding temperature contours and streamlines are shown in Figure 3.12 at different times of the boundary layer development for an aspect ratio $A = 0.5$.
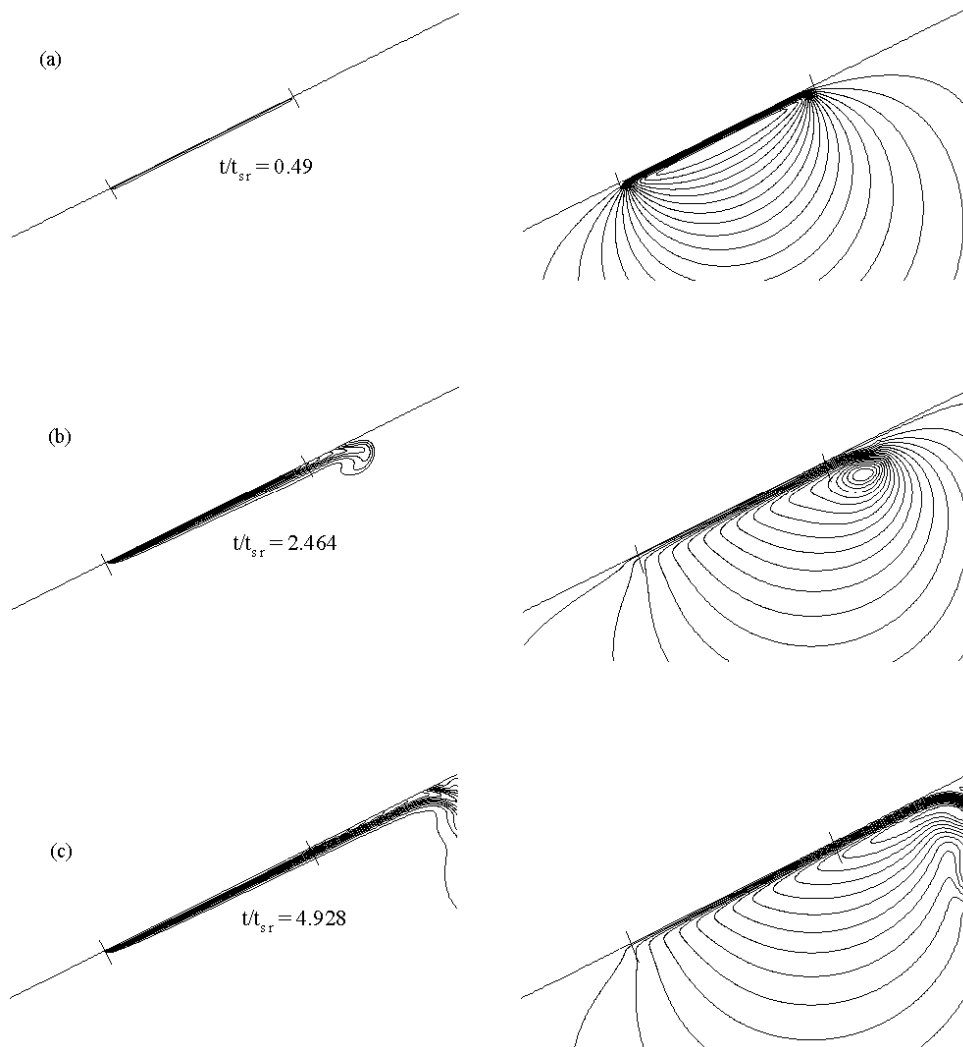
Figure 3.12 (a, b, c) Temperature contours (left) and the streamlines (right) for different times of boundary layer development (d) temperature profiles along a line perpendicular to the plate at mid point for $Ra = 7.63 \times 10^6$, $Pr = 0.72$ and $A = 0.5$.

We notice in Figure 3.12 that the boundary layer develops adjacent to the plate and moves upwards. The ramp time, selected for this problem, is $t_p/t_{sr} = 4.928$. The isotherms and streamlines in Figure 3.12(a) are at $t/t_{sr} = 0.49$, that is, before the flow becomes quasi-steady; those in Figure 3.12(b) are at $t/t_{sr} = 2.464$ when the flow is in quasi-steady mode; and those in Figure 3.12(c) are at the time when the ramp just finishes ($t/t_{sr} = 4.928$) and the flow is in a transitional stage from the quasi steady to the final steady state. We see from the start-up of the flow development to the steady state,

the boundary layer is not affected significantly by the adiabatic walls which are artificial boundaries for forming a closed computational domain.

Figure 3.13 shows the temperature profiles at two different times, t/t_{sr} = 2.464 and 4.928 respectively. At t/t_{sr} = 2.464 the flow just becomes quasi-steady (see figure 3.4) and at t/t_{sr} = 4.924, the ramp time finishes. It is seen in the temperature profiles that the thickness of the thermal boundary layer is smaller at the time 4.924 than that at 2.464. This supports the scaling relation (3.20) that the thermal boundary layer contracts beyond the quasi-steady time t_{sr}.
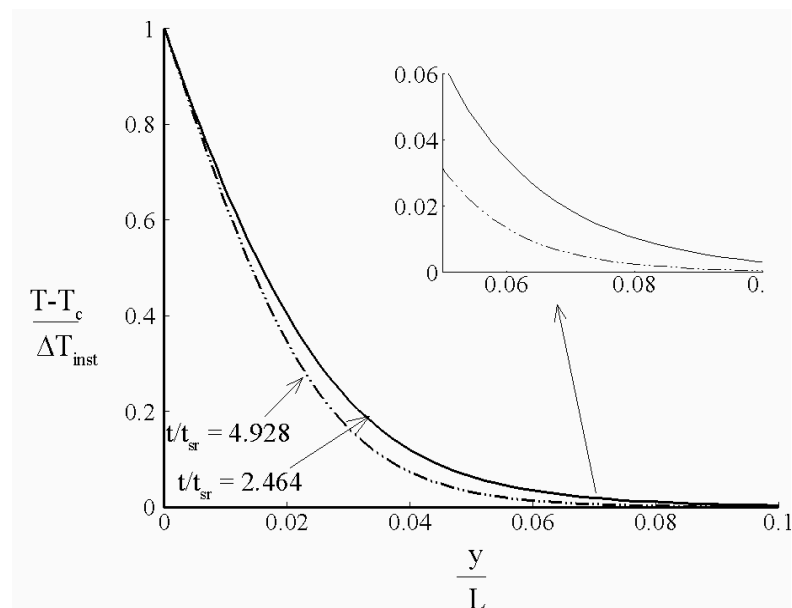
Figure 3.13 Temperature profiles along a line perpendicular to the plate at mid point for
$Ra = 7.63{\times}10^6$, $Pr = 0.72$ and $A = 0.5$.

3.8 Validation of selected scales

3.8.1 Scaling for sudden heating

The unsteady velocity scale (3.3), steady state time scale (3.5), steady state thermal layer thickness scale (3.6) and steady state velocity scale (3.7) of the boundary layer development for the case of sudden heating can be re-written in non-dimensional forms as

$$\frac{(1+Pr)(1+A^2)^{1/2}}{ARaPr}\left(\frac{u}{\kappa/h}\right) \sim \frac{t}{h^2/\kappa}. \tag{3.25}$$

$$\frac{t_s}{h^2/\kappa} \sim \frac{(1+Pr)^{1/2}(1+A^2)^{1/2}}{ARa^{1/2}Pr^{1/2}}. \tag{3.26}$$

$$\frac{\delta_T}{h} \sim \frac{(1+Pr)^{1/4}(1+A^2)^{1/4}}{A^{1/2}Ra^{1/4}Pr^{1/4}}. \tag{3.27}$$

$$\frac{u_s}{\kappa/h} \sim \frac{Ra^{1/2}Pr^{1/2}}{(1+Pr)^{1/2}}. \tag{3.28}$$

In Table 3.3, Runs 1-5 with $Ra = 3.00\times10^7$, 6.11×10^6, 2.58×10^6, 5.17×10^5 and 2.58×10^5 while keeping $A = 0.5$ and $Pr = 0.72$ unchanged have been carried out to show the dependence of the scaling relations on the Rayleigh number Ra; Runs 6-7 and 1 with $A = 1.0$, 0.1 and 0.5 respectively while keeping $Ra = 3.00\times10^7$ and $Pr = 0.72$ unchanged have been carried out to show the dependence on the slope of the inclination of the plate.

Table 3.3 Values of A, and Ra for 7 runs.

Runs	A	Ra
1	0.5	3.00×10^7
2	0.5	6.11×10^6
3	0.5	2.58×10^6
4	0.5	5.17×10^5
5	0.5	2.58×10^5
6	1.0	3.00×10^7
7	0.1	3.00×10^7

The velocity components and the temperature have been recorded at several locations along a line perpendicular to the plate at the mid point to obtain the velocity and temperature profiles along that line. The maximum velocity parallel to the plate, u_s has also been calculated from the velocity components and is used to verify the velocity scale relation.

The thermal boundary-layer thickness δ_T is determined as the perpendicular distance from the mid point of the heated wall to the location where the temperature difference between the fluid in the thermal boundary layer and the ambient drops to

$0.01(T_h - T_c)$. The steady state time, t_s for the boundary-layer development to reach the steady state is determined as the moment when the first trough appears in the time history of the maximum parallel velocity, u_s, which is calculated along the line perpendicular to the plate at the mid point (see Figure 3.1).

The unsteady velocity scale (3.25) has been plotted in Figure 3.14 for different parameters considered here, in which the *x*-axis is the normalised time and the *y*-axis includes the rest of the scale values. It is seen that all lines for different Rayleigh numbers and aspect ratios lie together initially on a straight line through the origin. This indicates that the scaling relation for the unsteady velocity is appropriate.
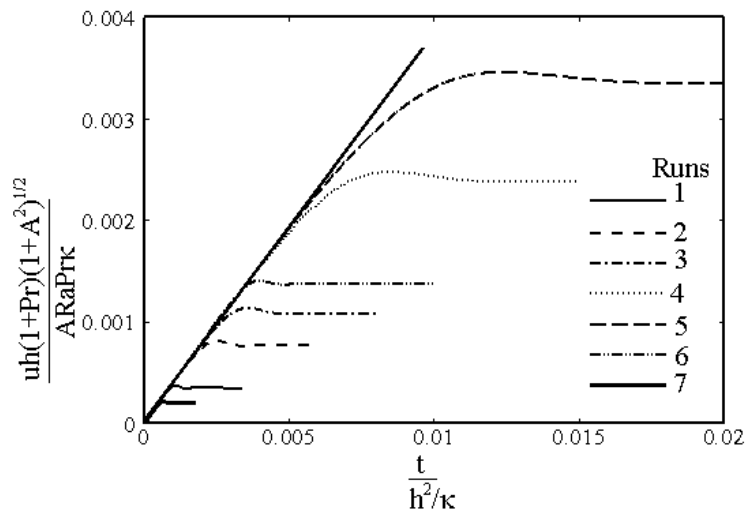
Figure 3.14 Normalised unsteady velocity against time for 7 runs.

Numerical results supporting the scaling laws for the steady state time, the steady-state thermal boundary layer thickness and the steady-state velocity parallel to the plate, (3.26), (3.27) and (3.28) respectively, are presented in Figure 3.15. It is found in the figure that the numerical results agree very well with these three scaling relations. For all the calculated cases, the numerical results fall approximately onto a straight line, which proves that the scaling relations (3.26), (3.27) and (3.28) properly describe the thermal boundary layer at the steady state.
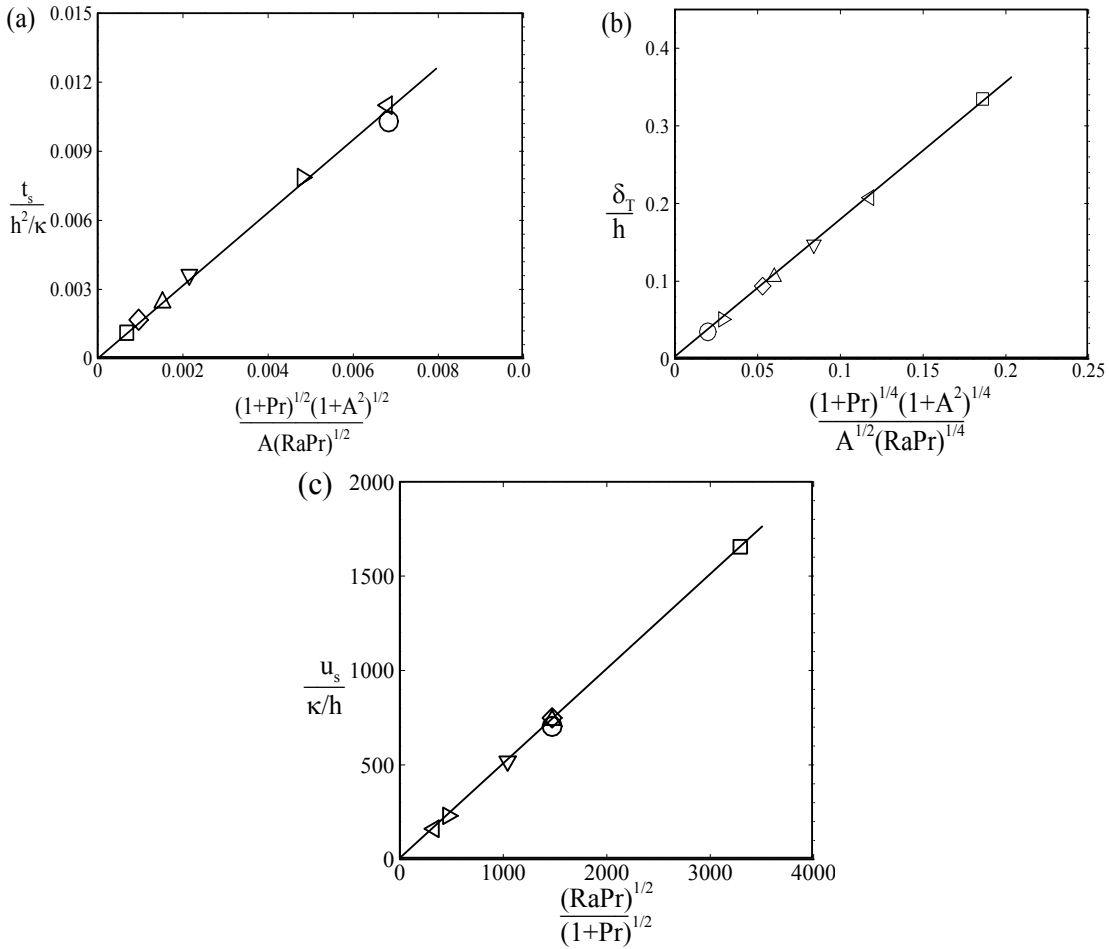
Figure 3.15 Numerically obtained values of the steady state (a) time, (b) thermal boundary layer thickness and (c) maximum velocity parallel to the plate at the mid point against corresponding scaling values, for all 7 runs. □, run 1; Δ, run 2; ∇, run 3; ▷, run 4; ◁, run 5; ◊, run 6, o, run 7. Solid line, linear fit.

The velocity and temperature profiles at $t/t_s = 3.0$ (when the flow is fully steady) are shown in Figure 3.16 for different Rayleigh numbers and aspect ratios. Figure 3.16(a) shows the raw data of the velocity along the line perpendicular to the plate at the mid point. In Figure 3.16(b), the velocity parallel to the plate has been normalized by its steady state scale (3.7) and the distance normalized by its viscous boundary layer thickness scale (3.10). Raw data of the temperature profiles is depicted in Figure 3.16(c) at the same time for various Rayleigh numbers and aspect ratios. In Figure 3.16(d), the temperature has been normalized by the maximum temperature difference (ΔT) and the distance normalized by the steady state thermal boundary layer thickness (3.6).

52
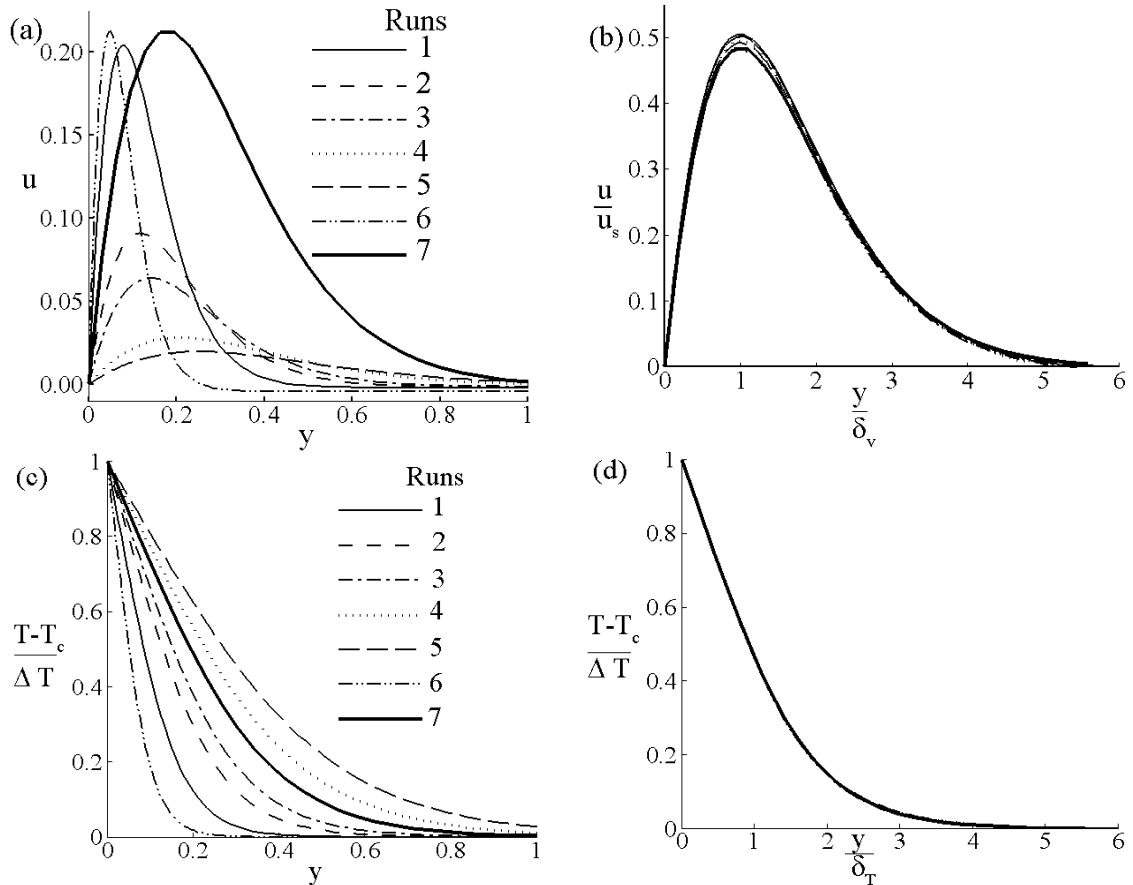
Figure 3.16 Velocity profiles (top) and temperature profiles (bottom) for 7 runs.

The scaling relations for the steady state velocity (3.7) and viscous boundary layer thickness (3.10) are seen to perform well for the velocity profiles. All profiles collapsing almost onto a single curve (see Figure 3.16b). The scaling relation for the thermal boundary layer thickness (3.6) also works very well as all temperature profiles for the different parameters fall together. Therefore the scaling, derived from the sudden heating boundary condition, has been verified by the numerical simulation.

3.8.2 Scaling for ramp heating

A total of nine simulations have been performed to verify the scaling relations derived from the ramp heating boundary condition. Table 3.4 shows the details of the flow parameters considered for this study. Here, Runs 1-7 with the same aspect ratio A = 0.5 and Prandtl number Pr = 0.72 but different Rayleigh numbers have been carried out to show the dependence of the scaling relations on the Rayleigh number Ra; and Runs 8-9 and 1 with A = 0.1, 1.0 and 0.5 respectively while keeping Pr = 0.72 and Ra =

3.00×10^7 unchanged have been carried out to show the dependence of the scaling relations on the aspect ratio *A*.

Table 3.4 Values of *A*, and *Ra* for 9 runs.

Runs	*A*	*Ra*
1	0.5	3.00×10^7
2	0.5	7.63×10^6
3	0.5	6.11×10^6
4	0.5	3.00×10^6
5	0.5	1.55×10^6
6	0.5	1.30×10^6
7	0.5	1.04×10^6
8	1.0	3.00×10^7
9	0.1	3.00×10^7

For this problem, the velocity parallel to the plate and the temperature have also been recorded at several locations along a line perpendicular to the plate at the mid point to obtain the velocity and temperature profiles. Moreover, the maximum velocity parallel to the plate has been calculated as the characteristic velocity (u_{sr}) of the boundary layer, which is used to verify the velocity scale relation.
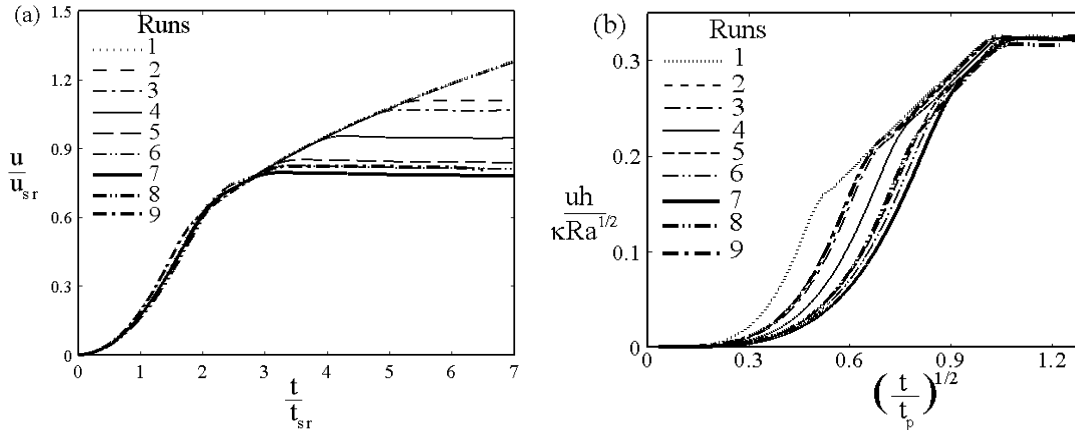
Figure 3.17 (a) Normalised velocity plotted against normalised time; (b) $uh/[\kappa Ra^{1/2}]$ plotted against $(t/t_p)^{1/2}$.

Figure 3.17(a) shows the time series of the maximum velocity parallel to the inclined plate at the mid point of the plate, where both the time and velocity are normalised with respect to their respective steady state scaling values. It is clear that

initially all lines collapse together; at about t/t_{sr} = 2.2 all curves bend together, indicating that at this time the flow reaches its quasi-steady mode. After that quasi-steady state time, all curves continue to follow the same trend until the ramp is finished at respective times. This confirms the scaling relations (3.15) and (3.18).
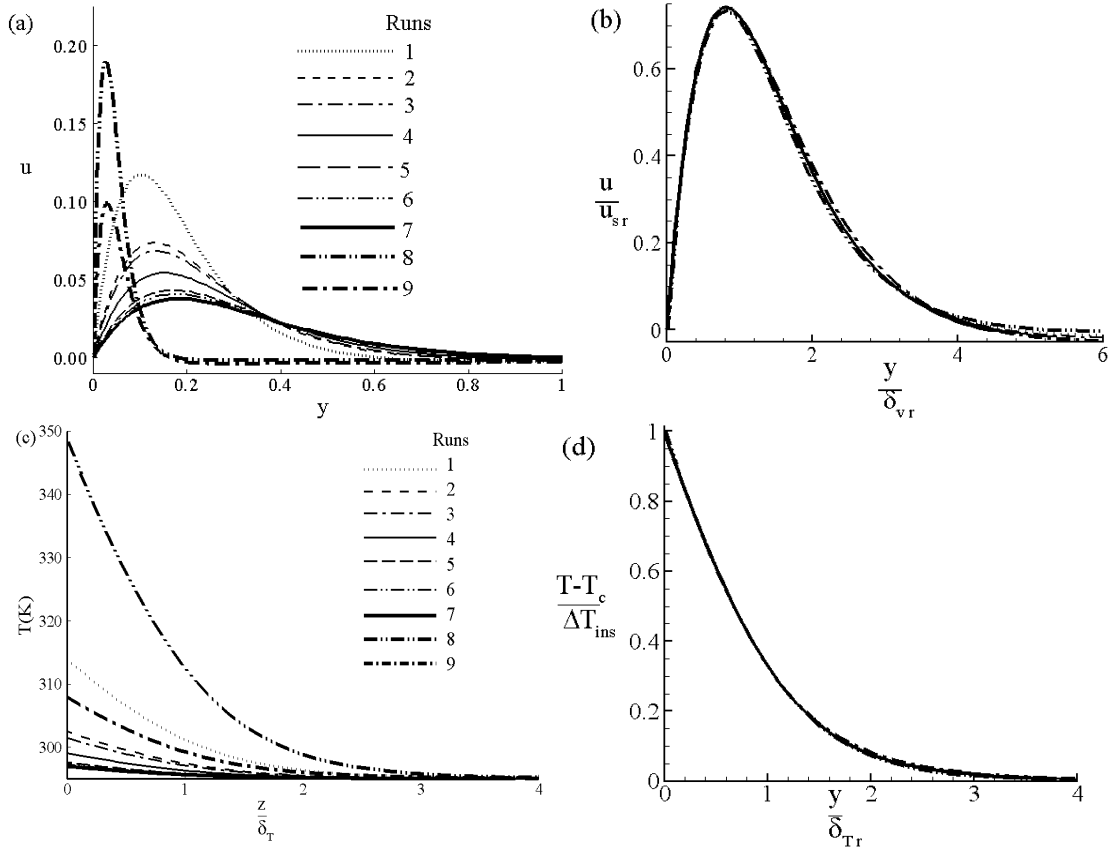
Figure 3.18 Velocity profiles (top) and temperature profiles (bottom) at t/t_{sr} = 2.6 for all runs.

To verify the scaling relation (3.21), $uh/\kappa Ra^{1/2}$ has been plotted against $(t/t_p)^{1/2}$ for different Rayleigh numbers and aspect ratios with Pr = 0.72 in Figure 3.17(b). This scaling is valid for $t > t_{sr}$. It is seen that all lines after the quasi-steady state time fall approximately onto a single line. However, those cases for which the quasi-steady time and the ramp time are very close deviate a little from others. It is seen that after t/t_p=1.0, when ramp time finishes, all lines for different parameters lie together and form a horizontal line which confirms the scaling relation (3.21).

Figure 3.18 shows the velocity and temperature profiles for different Rayleigh numbers and aspect ratios along the line perpendicular to the plate at the mid point at

time t/t_{sr} = 2.6, when the flow becomes quasi steady. Raw velocity profiles for different aspect ratios and Rayleigh numbers have been shown in Figure 3.18(a). In Figure 3.18(b), the velocity is normalized with respect to the quasi-steady state velocity scale (3.18) and the position is normalized with respect to the viscous boundary layer thickness scale (3.23). In Figure 3.18(c) the raw temperature has been plotted against the normalized position with respect to the quasi-steady state thermal layer thickness. The temperature on the inclined plate does not reach the maximum temperature at this time as the ramp has not yet finished. Moreover, the instantaneous temperature differences are not the same at this time for different Rayleigh numbers and aspect ratios. The position of the temperature profile in Figure (d) is also normalized by the quasi steady state thermal boundary layer thickness (3.17). However, the temperature is normalized by the instantaneous temperature difference (ΔT_{inst}).

It is seen in Figure 3.18(b) that all velocity profiles for different *Ra* and *A*, fall into a single curve. Therefore, the scaling relations (3.18) and (3.23) are appropriate representations of the velocity and thickness respectively of the boundary layer. The same scenario can be seen in the temperature profiles in Figure 3.18(d). All profiles fall onto a single line, confirming the scaling of the thermal boundary layer thickness (3.17).

3.9 Summary

Natural convection adjacent to a heated inclined flat plate is examined by scaling analysis and verified by numerical simulations for air (*Pr* = 0.72). It is found that the flow is mainly dominated by three distinct stages for the sudden heating boundary condition, i.e. the start-up stage, the transitional stage and the steady state stage. The scaling relations are formed based on the established characteristic flow parameters of the maximum velocity inside the boundary layer (u_s), the time for the boundary layer to reach the steady state (t_s) and the thermal (δ_T) and viscous (δ_v) boundary layer thickness. Through comparisons of those scaling assumptions with the numerical simulations, it is found that the scaling results agree very well with the numerical simulations. Hence the numerical results have confirmed the scaling relations which characterize the transient flow development.

A temperature boundary condition of a ramp function which is applied on the inclined plate has also been investigated for the same problem. The boundary layer

flow for this boundary condition depends on the comparison of the time at which the ramp heating is completed with the time at which the boundary layer completes its growth. If the ramp time is long compared with the steady state time, the thermal boundary layer reaches a quasi-steady mode in which the growth of the layer is governed by the thermal balance between convection and conduction. On the other hand, if the ramp is completed before the thermal boundary layer becomes steady, the subsequent growth is governed by the balance between buoyancy and inertia, as for the case of sudden heating. Several scaling relations have been established in this study, which include the maximum velocity parallel to the inclined plate inside the boundary layer (u_{sr}), the time for the boundary layer to reach the quasi-steady state (t_{sr}) and the thermal and viscous boundary layer thicknesses (δ_{Tr} and δ_v) for both quasi-steady and steady state mode. The comparisons between the scaling relations and the numerical simulations demonstrate that the scaling results agree very well with the numerical simulations.

4 Natural convection of an inclined flat plate subject to sudden and ramp cooling boundary conditions

The scaling analysis of a cooling boundary layer adjacent to an inclined flat plate is very similar to that for the heating boundary layer except for the formation of instability. It is seen in the previous chapter (Chapter 3) that the heated boundary layer is stable and laminar for relatively high Rayleigh numbers. However, in the cooling case, if the Rayleigh number exceeds a certain critical value, the boundary layer becomes unstable to the Rayleigh-Bénard instability. Sparrow and Husar (1969) and Lloyd (1974) were the first to prove experimentally the existence of longitudinal vortices in a natural convection flow along an inclined flat plate. For $Pr = 7.0$, they observed vortices over an isothermal plate for inclination angles of 73° or less from the horizontal plane and a two-dimensional wave structure for inclination angles of 76° or greater. Based on the local Rayleigh number, a scaling prediction for the onset of instability can be achieved.

A scaling analysis in a wedge subject to surface cooling has been investigated by Lei and Patterson (2005). In that study, the authors identified different flow regimes based on the Rayleigh number through scaling analysis for the boundary layer adjacent to the horizontal surface. They found that the flow is stable if the Rayleigh number is less than a critical value. However, the flow becomes unstable, characterised by plunging surface plumes, if the Rayleigh number exceeds that critical value. The same authors (Lei and Patterson (2002c) also carried out a scaling analysis in the wedge subject to radiative heating. In the latter case, the bottom inclined surface absorbs the residual radiation from the sun and re-emits the absorbed energy as a boundary heat flux. Therefore, a hot boundary layer develops adjacent to the sloping wall which is potentially unstable to the Rayleigh-Bénard instability for higher Rayleigh numbers. Similar to the cooling case, the authors also identified different flow regimes based on the Rayleigh numbers.

In this chapter, analytical and numerical models for suddenly decreased and linearly decreasing (ramp) temperature boundary conditions on an inclined flat plate are formulated. The aim is to formulate a model that will exhibit many of the characteristics of the flow adjacent the cooling plate which can be used to verify the scaling results derived from the governing equations with the specified model configuration and boundary conditions. A series of numerical calculations have been carried out for different parameter values to verify the scaling predictions. Details of the numerical procedures can be found in Chapter 2. However, the geometry, boundary conditions and grid and time step dependence tests specific to the present cases of sudden and ramp cooling of an inclined plate are shown in this chapter.
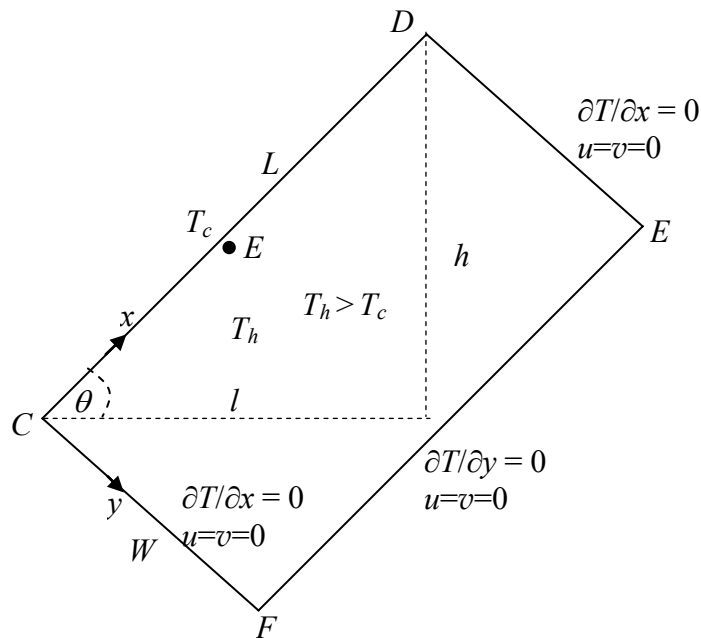
Figure 4.1 Schematic of the geometry and the coordinate system.

The flow adjacent to the inclined flat plate is modeled by the two dimensional flow of an initially stationary fluid contained in a rectangular domain *CDEF* shown in Figure 4.1. Unlike the heating case, we consider the full side of the rectangle, $CD = L$ as a cooled inclined flat plate. If the middle portion of the plate is cooled and the rest of the plate is adiabatic similarly to Chapter 3, then the leading edge triggers the instability for even very lower Rayleigh number. Initially the fluid temperature in the domain is T_h. If we consider the plate as the hypotenuse of a right angled triangle then the altitude is h, the length of base is l and the angle that the plate makes with the base is θ. Except

for the plate, all three other walls of the rectangle are assumed to be insulated, rigid and non-slip. Two cooling boundary conditions are applied on the plate; sudden cooling to a specified temperature which is then maintained, and cooling by a linearly decreasing temperature to a specified temperature over some time (the ramp time) after which the temperature is maintained (the ramp function).

4.1 Scaling analysis for sudden cooling

4.1.1 Thermal and viscous layer development

The instantaneous cooling on the flat plate triggers transient natural convection with a cold thermal boundary layer developing adjacent to the inclined plate. The thickness of the thermal boundary layer grows according to the scale $\kappa^{1/2}t^{1/2}$ as for the case for sudden heating (3.1) until there is a balance between conduction and convection in the energy equation (eqn 2.17). At the same time the velocity inside the boundary layer develops, governed by the balance of viscous and inertial terms with the buoyancy term in the inclined momentum equation (eqn 2.15). This unsteady velocity scale from (3.3) is

$$u \sim \frac{ARaPr}{(1+Pr)(1+A^2)^{1/2}} \left(\frac{t}{h^2/\kappa}\right)\left(\frac{\kappa}{h}\right).$$

$$(4.1)$$

This scale is valid until the time when conduction balances convection. Note that this boundary layer is potentially unstable at higher Rayleigh numbers.

The steady state scales of the boundary layer can be achieved by balancing the conduction and convection terms in the energy equation (eqn 2.17). The steady state scales of time (t_s), thickness (δ_T) and velocity (u_s) in the boundary layer from (3.5), (3.6) and (3.7) respectively are as follows,

$$t_s \sim \frac{(1+Pr)^{1/2}(1+A^2)^{1/2}}{ARa^{1/2}Pr^{1/2}}\left(\frac{h^2}{\kappa}\right),$$

$$(4.2)$$

$$\delta_T \sim \frac{h(1+Pr)^{1/4}(1+A^2)^{1/4}}{A^{1/2}Ra^{1/4}Pr^{1/4}},$$

$$(4.3)$$

and

$$u_s \sim \frac{Ra^{1/2}Pr^{1/2}}{(1+Pr)^{1/2}}\left(\frac{\kappa}{h}\right).$$

$$(4.4)$$

At the same time with the formation of the thermal boundary layer, a viscous boundary layer also develops as a direct result of a balance between the viscous and the inertia terms in the momentum equation which is,

$$\delta_v \sim \delta_T Pr^{1/2}. \tag{4.5}$$

The steady state scale of the viscous boundary layer can be achieved at the time when conduction balances convection in the energy equation,

$$\delta_v \sim \frac{h(1+Pr)^{1/4}(1+A^2)^{1/4}}{A^{1/2}Ra^{1/4}Pr^{1/4}}. \tag{4.6}$$

Like heating case, here it is also noted that for $Pr < 1$, the viscous boundary layer thickness is smaller than that of the thermal boundary layer.

4.1.2 Onset of the thermal layer instability

It is found in the literature (e.g. Chandrasekhar 1961; Drazin and Reid 1981) that the main characteristic parameter governing the stability property of a fluid layer cooled from above is the local Rayleigh number, *Ra*, which is defined by

$$Ra_L = \frac{g\beta\Delta T\delta_T^3}{\nu\kappa}, \tag{4.7}$$

where $\delta_{T,}$ is the thermal layer thickness, ΔT the temperature difference across the thermal boundary layer. Therefore, a critical Rayleigh number exists above which the instability will occur.

The critical Rayleigh number for the inclined plate can be derived directly from that of a differentially heated horizontal layer as suggested by Kurzweg (1970) and Chen and Pearlstein (1989). They established a relation between the critical Rayleigh number for the case of a differentially heated horizontal layer and an inclined plate layer, which is given by

$$Ra_c(\theta) = \frac{Ra_c(0^o)}{\cos\theta}, \tag{4.8}$$

where θ is the inclination angle of the plate with the horizontal plane and $Ra_c(\theta)$ and $Ra_c(0^o)$ are the critical Rayleigh numbers for the inclined and the horizontal fluid layers, respectively.

In the present case, the thermal boundary layer is bounded by a rigid surface of the plate and a cold air layer, which is equivalent to the free-rigid boundary configuration (see Chandrasekhar 1961; Drazin and Reid 1981; Lei and Patterson

2002c), for which $Ra_c(0^o) = 1101$. We will use this critical value and the angle of the inclined plate with the horizontal plane to calculate the critical Rayleigh number for the inclined thermal boundary layer in subsequent analyses and calculations.

The local Rayleigh number in the thermal boundary layer can now be calculated from (4.7), for which the thickness of the fluid layer is $\delta_T = \kappa^{1/2}t^{1/2}$. Applying this δ_T value to (4.7) the local Rayleigh number is given by.

$$Ra_L = Ra\left(\frac{t}{h^2/\kappa}\right)^{3/2}. \tag{4.9}$$

The instability will set in if $Ra_L \geq Ra_c$, where Ra_c is calculated from (4.8). From (4.9), a critical time scale for the onset of thermal layer instability at a given global Rayleigh number is obtained as

$$t_B = \left(\frac{Ra_c}{Ra}\right)^{2/3}\frac{h^2}{\kappa}, \tag{4.10}$$

where $Ra_c \approx 1106.5$, 1122.8 and 1230.9 for $A = 0.1$, $A = 0.2$ and $A = 0.5$ respectively. For $t < t_B$, the surface layer is stable, and for $t > t_B$, the instability will set in. The scale (4.10) indicates that the critical time for the onset of instability in the boundary layer increases as the Rayleigh number decreases. Theoretically, t_B approaches infinity if $Ra \rightarrow 0$. However, for Rayleigh numbers below a critical value the instability will never occur irrespective of the cooling time.

Two important time scales have been obtained from the above calculation; first, the time scale for the growth of the thermal boundary layer (t_s given by 4.2) and secondly, the time scale for the onset of convective instability (t_B given by 4.10). The ratio of these two times is

$$\frac{t_s}{t_B} = \left[\frac{(1+Pr)^3(1+A^2)^3 Ra}{Pr^3 A^6 Ra_c^4}\right]^{1/6}. \tag{4.11}$$

Therefore, for

$$Ra > \frac{Pr^3 A^6 Ra_c^4}{(1+Pr)^3(1+A^2)^3}, \tag{4.12}$$

$t_s > t_B$, and the instability will set in before the growth of the thermal boundary layer completes. On the other hand, if

$$Ra < \frac{Pr^3 A^6 Ra_c^4}{(1+Pr)^3(1+A^2)^3}, \tag{4.13}$$

$t_s < t_B$, the thermal boundary layer will reach its steady state before the instability sets in and an instability will not occur.

4.1.3 Possible flow regimes

The time scale for conduction across the full domain is the diffusion time, $t_c \sim h^2/\kappa$. A comparison of the three time scales t_c, t_s and t_B gives three possible regimes.

(i) If the diffusion time is shorter than the steady state time, i.e. $t_c < t_s$ then, $Ra < (1+Pr)(1+A^2)/[A^2 Pr]$ and $Ra < Ra_c$ and the flow is stable to the Rayleigh-Bénard instability. The thermal boundary layer grows slowly and exceeds the length of the plate before convection becomes important.

(ii) Again if $(1+Pr)(1+A^2)/[A^2 Pr] < Ra < (Pr^3 A^6 Ra_c^4)(1+Pr)^{-3}(1+A^2)^{-3}$. The flow is still stable to the Rayleigh-Bénard instability. A thermal boundary layer is established in the enclosure, and it reaches to the steady state at t_s.

(iii) If $Ra > (Pr^3 A^6 Ra_c^4)(1+Pr)^{-3}(1+A^2)^{-3}$ then the thermal boundary layer is unstable to the Rayleigh-Bénard instability. The instability sets in before the growth of the thermal boundary layer is completed.

There is also a regime at sufficiently high Rayleigh numbers, in which the thermal boundary layer becomes turbulent. This regime is not considered here.

4.2 Scaling analysis for ramp cooling

The boundary condition of the ramp temperature which is applied on the inclined plate, L in Figure 4.1 for the second case is given by

$$T_c = \begin{cases} T_h & \text{if } t \le 0; \\ T_h - \Delta T\left(t/t_p\right) & \text{if } 0 < t \le t_p; \\ T_h - \Delta T & \text{if } t > t_p; \end{cases} \qquad (3.14)$$

Initially the temperature on the plate and the ambient is the same. Then the temperature on the plate decreases linearly up to a specified time (t_p) and remains constant after that.

4.2.1 Thermal layer development

The start-up stage is initially dominated by heat transfer via conduction through the cold plate, resulting in a cold thermal boundary layer of a thickness $O(\delta_T)$. This layer grows according to $\kappa^{1/2}t^{1/2}$, which is obtained from a balance between the unsteady term

and the diffusion term in the energy equation (eqn. 2.17). The velocity inside the boundary layer increases with time according to the following velocity scale from (3.13)

$$u_r \sim \frac{ARaPr}{(1+Pr)(1+A^2)^{1/2}} \left(\frac{t}{h^2/\kappa}\right)\left(\frac{t}{t_p}\right)\left(\frac{\kappa}{h}\right). \tag{4.15}$$

This velocity scale is valid until the conduction balances convection (if the conduction and convection balance before the ramp is finished) or the ramp is finished (if the conduction and convection balance after the ramp is finished). The flow inside the boundary layer will be in a quasi-steady mode when conduction and convection balance at the time from (3.15)

$$t_{sr} \sim \frac{(1+Pr)^{1/3}(1+A^2)^{1/3}}{A^{2/3}Ra^{1/3}Pr^{1/3}} \left(\frac{t_p}{h^2/\kappa}\right)^{1/3}\left(\frac{h^2}{\kappa}\right), \tag{4.16}$$

so long as $t_{sr}<t_p$. As discussed in the previous chapter (chapter 3), if the quasi-steady state time is longer than the ramp time, then the steady state time is the same as the case of sudden cooling and there is no difference between ramp and instantaneous cooling at the later stage of the flow development after the ramp cooling is finished.

The thickness of the boundary layer along the plate and the velocity inside the boundary layer at the quasi-steady time respectively from (3.17) and (3.18) are

$$\delta_{Tr} \sim \frac{h(1+Pr)^{1/6}(1+A^2)^{1/6}}{A^{1/3}(RaPr)^{1/6}} \left(\frac{t_p}{h^2/\kappa}\right)^{1/6}, \tag{4.17}$$

and

$$u_{sr} \sim \frac{(RaPr)^{1/3}(1+A^2)^{1/6}}{A^{1/3}(1+Pr)^{1/3}} \left(\frac{h^2/\kappa}{t_p}\right)^{1/3}\left(\frac{\kappa}{h}\right). \tag{4.18}$$

Now if the quasi-steady state time is shorter than the ramp time then once t_{sr} is reached, the boundary layer stops growing according to $\kappa^{1/2}t^{1/2}$ which is valid only for conductive boundary layer. The thermal boundary layer is in a quasi-steady mode with convection balancing conduction. Further decrease of the heat simply accelerates the flow to maintain the proper thermal balance. Therefore, the thickness and the velocity scales at the quasi-steady mode are from (3.20) and (3.21)

$$\delta_{Tq} \sim \frac{h(1+A^2)^{1/4}}{A^{1/2}Ra^{1/4}} \left(\frac{t_p}{t}\right)^{1/4}, \tag{4.19}$$

and

$$u_q \sim Ra^{1/2}\left(\frac{\kappa}{h}\right)\left(\frac{t}{t_p}\right),\tag{4.20}$$

respectively.

The corresponding viscous boundary layer thickness prior to and at the quasi-steady time can be obtained and is given by

$$\delta_v \sim v^{1/2}t^{1/2} \sim Pr^{1/2}\delta_T,\tag{4.21}$$

and

$$\delta_{vr} \sim Pr^{1/3}\frac{h(1+Pr)^{1/6}(1+A^2)^{1/6}}{A^{1/3}Ra^{1/6}}\left(\frac{t_p}{h^2/\kappa}\right)^{1/6}.\tag{4.22}$$

However the temperature on the plate still decreases, therefore, the viscous boundary layer thickness after the quasi steady state is

$$\delta_{vq} \sim \frac{hPr^{1/2}(1+A^2)^{1/4}}{A^{1/2}Ra^{1/4}}\left(\frac{t_p}{t}\right)^{1/4}.\tag{4.23}$$

4.2.2 Onset of the thermal layer instability

The stability property of a fluid layer cooled from above is characterised by a local Rayleigh number, Ra_L, which is defined by (4.7). For the ramp cooling boundary condition the local Rayleigh number is calculated as

$$Ra_L = \frac{g\beta\Delta T(t/t_p)\delta_T^3}{v\kappa}.\tag{4.24}$$

Therefore, there exists a critical Rayleigh number for which the instability will occur. The critical Rayleigh number can be obtained from the relation (4.8).

From the above scaling analysis, it is found that the flow may become quasi-steady either before or after the ramp is finished.

For the case when the quasi-steady time is much shorter than the ramp time, the onset of instability may set in before or after the quasi-steady state but before the ramp is finished. If the instability sets in before the quasi-steady state, then the local Rayleigh number in the thermal boundary layer is calculated from (4.24), for which the thickness of the boundary layer develops according to $\delta_T \sim \kappa^{1/2}t^{1/2}$ and is given by

$$Ra_L = Ra\left(\frac{t}{t_p}\right)\left(\frac{t}{h^2/\kappa}\right)^{3/2}.\tag{4.25}$$

If $Ra_L \geq Ra_c$, where Ra_c is calculated in (4.8), the instability will set in. From (4.25), a critical time scale for the onset of thermal layer instability can be obtained as

$$t_{B1} = \left(\frac{Ra_c}{Ra} \frac{t_p}{h^2/\kappa} \right)^{2/5} \frac{h^2}{\kappa}, \tag{4.26}$$

so long as $t_{B1} < t_{sr}$. For $t < t_{B1} < t_{sr}$, the thermal boundary layer is stable. For $t > t_{B1}$, the instability will set in, and t_{sr} is irrelevant.

If the instability sets in after the quasi-steady state, then the local Rayleigh number in the thermal boundary layer is also calculated from (4.24), for which the thermal boundary layer thickness develops according to the scale (4.19). Therefore the local Rayleigh number is given by

$$Ra_L = \frac{Ra^{1/4}\left(1+A^2\right)^{3/4}}{A^{3/2}} \left(\frac{t}{t_p} \right)^{3/4}, \tag{4.27}$$

and the time scale for onset time of instability is

$$t_{B2} = \frac{Ra_c^4 A^6 t_p}{Ra\left(1+A^2\right)^3}, \tag{4.28}$$

so long as $t_{sr} < t_{B2} < t_p$.

As we discussed before, if the steady state time is longer than the ramp time then there is a mode where the flow develops as per the instantaneous case. Therefore, the instability may set in after or before the ramp is finished. If instability sets in before the ramp is finished then the scaling for the onset of instability is the same as (4.26). For the case when the instability sets in after the ramp is finished, the local Rayleigh number can be calculated from (4.7), for which the thermal boundary layer thickness develops according to $\delta_T = \kappa^{1/2}t^{1/2}$. As such the local Rayleigh number is given by,

$$Ra_L = Ra\left(\frac{t}{h^2/\kappa} \right)^{3/2}, \tag{4.29}$$

and the time scale for onset time of instability is

$$t_{B3} = \left(\frac{Ra_c}{Ra} \right)^{2/3} \frac{h^2}{\kappa}. \tag{4.30}$$

4.2.3 Possible flow regimes

If the quasi-steady time is shorter than the ramp time ($t_{sr} < t_p$), then the global Rayleigh number must satisfy the following condition:

$$Ra > \frac{(1+Pr)(1+A^2)}{A^2 Pr}\left(\frac{h^2/\kappa}{t_p}\right)^2,$$ (4.31)

and if the flow is stable until the ramp is finished then

$$\frac{(1+Pr)(1+A^2)}{A^2 Pr}\left(\frac{h^2/\kappa}{t_p}\right) < Ra < \frac{Ra_c^4 A^6}{(1+A^2)^3}.$$ (4.32)

However, if the instability happens after the quasi-steady state is reached but before the ramp is finished, the time scale for the onset of instability is (4.28), thus the global Rayleigh number is

$$\frac{Ra_c^4 A^6}{(1+A^2)^3} < Ra < \frac{Pr^5 A^{10} Ra_c^6}{(1+Pr)^5 (1+A^2)^5}\left(\frac{t_p}{h^2/\kappa}\right),$$ 4.33

and if the instability happens before the quasi-steady state then the global Rayleigh number is

$$Ra > \frac{Pr^5 A^{10} Ra_c^6}{(1+Pr)^5 (1+A^2)^5}\left(\frac{t_p}{h^2/\kappa}\right),$$ (4.34)

and if the steady state time is longer than the ramp time, then

$$Ra < \frac{(1+Pr)(1+A^2)}{A^2 Pr}\left(\frac{h^2/\kappa}{t_p}\right)^2.$$ (4.35)

If the instability sets in after the ramp is finished but before the steady state then

$$Ra_c < Ra < Ra_c \left(\frac{h^2/\kappa}{t_p}\right)^{3/2}.$$ (4.36)

However, the instability may set in before the ramp is finished when the ramp time is shorter than the steady time if

$$Ra_c \left(\frac{h^2/\kappa}{t_p}\right)^{3/2} < Ra < \frac{(1+Pr)(1+A^2)}{A^2 Pr}\left(\frac{h^2/\kappa}{t_p}\right)^2.$$ (4.37)

Based on the onset of instability, we may classify certain flow regimes based on the global Rayleigh number. The flow regimes for different Rayleigh numbers are tabulated in Tables 4.1 and 4.2.

Chapter 4

Table 4.1 Possible flow regimes for ramp cooling boundary condition for $t_{sr} > t_p$ or $Ra < (1+Pr)(1+A^2)h^4/[A^2 Pr\kappa^2 t_p^2]$.

$Ra < Ra_c$	$Ra_c < Ra < Ra_c[(h^2/\kappa)/t_p]^{3/2}$	$Ra_c[(h^2/\kappa)/t_p]^{3/2} < Ra < (1+Pr)(1+A^2)h^4/[A^2 Pr\kappa^2 t_p^2]$
Regime 1	*Regime* 2	*Regime* 3
The flow is stable to the Rayleigh-Bénard instability. The thermal boundary layer grows very slowly and exceeds the length of the plate before convection becomes important.	The flow is stable until the ramp is finished. However, it becomes unstable before the steady-state of the thermal boundary layer is reached.	The thermal boundary layer is unstable to the Rayleigh-Bénard instability before the ramp is finished.

Table 4.2 Possible flow regimes for ramp cooling boundary condition for $t_{sr} < t_p$ or $Ra > (1+Pr)(1+A^2)h^4/[A^2 Pr\kappa^2 t_p^2]$.

$(1+Pr)(1+A^2)h^4/[A^2 Pr\kappa^2 t_p^2] < Ra < Ra_c^4 A^6/(1+A^2)^3$	$Ra_c^4 A^6/(1+A^2)^3 < Ra < Pr^5 A^{10} Ra_c^6 t_p \kappa/[(1+Pr)^5(1+A^2)^5 h^2]$	$Ra > Pr^5 A^{10} Ra_c^6 t_p \kappa/[(1+Pr)^5(1+A^2)^5 h^2]$
Regime 4	*Regime* 5	*Regime* 6
The flow is stable to the Rayleigh-Bénard instability until the ramp is finished. The boundary layer reaches a quasi-steady state prior to the completion of the ramp time.	Again the thermal boundary layer reaches quasi-steady state with conduction convection balance. However, the flow becomes unstable to Rayleigh-Bénard instability in the quasi-steady state mode.	The thermal boundary layer is unstable to the Rayleigh-Bénard instability. The instability sets in before the growth of the thermal boundary layer completes.

In the following section, mesh and time step dependence tests will be carried for the accuracy of the numerical simulation. The numerical results will be used to verify the scaling relations derived above.

68

4.3 Grid and time step dependence test

The distribution of the mesh is shown for three different aspect ratios in Table 4.3. Grid distribution in the middle portion of the plate surface is uniformly distributed along the *x*-direction; however in the two end portions of the plate, an expansion factor has been used to construct non-uniform meshes. Non-uniform mesh has also been constructed along the *y*-direction of the domain with finer mesh near the plate. A schematic of grid distribution is shown in Figure 4.2
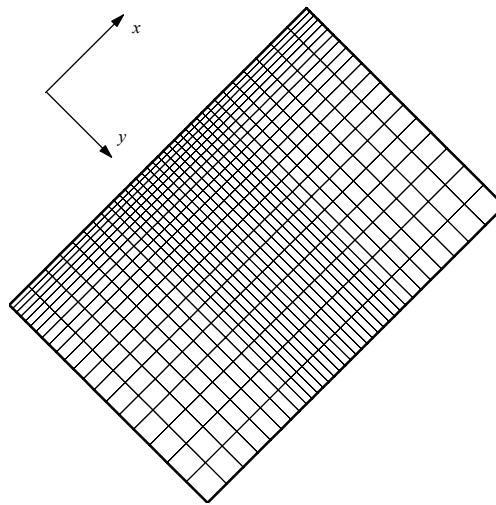
Figure 4.2 Schematics of grid distribution.

Table 4.3 Grid parameter.

Mesh size	Along the plate			Normal to the plate	
	Middle	Both side GN	EF	GN	EF
200×100	100	50	1.030	100	1.010
300×150	150	75	1.020	150	1.015
400×200	200	100	1.015	200	1.010
600×300	300	150	1.010	300	1.008

Note: GN=Grid Number, EF = Expansion Factor

Grid and time step dependence tests have been conducted for both the sudden and ramp cooling cases. The time steps have been chosen in such a way that the CFL (Courant-Freidrich-Lewy) number remains the same for all meshes. The maximum CFL number for A = 0.1, 0.2 and 0.5 are 2.54, 3.04 and 1.55 respectively. Four different mesh sizes, 200×100, 300×150, 400×200 and 600×300, have been considered for each aspect ratio. The computed time series of the temperature at a fixed point and

the standard deviation of temperature along a line parallel to the plate are shown in Figures 4.3 and 4.4 respectively as well as in Tables 4.4 and 4.5 respectively.

Table 4.4 Onset time of instability and the temperature at that time at a point, E for sudden cooling.

Mesh size	$A = 0.1$		$A = 0.2$		$A = 0.5$	
	t_B	T (at t=0.570s)	t_B	T (at t=0.718s)	t_B	T (at t=3.332s)
200×100	0.550s	291.898 K	0.715s	291.692 K	3.352s	290.798 K
300×150	0.510s	291.903 K	0.705s	291.697 K	3.348s	290.797 K
400×200	0.570s	291.909 K	0.718s	291.702 K	3.332s	290.797 K
600×300	0.562s	291.908 K	0.720s	291.699 K	3.342s	290.794 K

Table 4.5 Onset time of instability and the temperature at that time at a point, E for ramp cooling.

Mesh size	$A = 0.1$		$A = 0.2$		$A = 0.5$	
	t_B	T (at t=1.31s)	t_B	T (at t=4.21s)	t_B	T (at t=10.87s)
200×100	1.215s	299.494 K	3.58s	298.168 K	10.45s	295.028 K
300×150	1.251s	299.490 K	3.92s	298.177 K	10.65s	295.029 K
400×200	1.310s	299.496 K	4.21s	298.178 K	10.87s	295.030 K
600×300	1.321s	299.495 K	4.25s	298.176 K	10.92s	295.029 K

Calculated results of the grid dependence tests for the case of sudden cooling and ramp cooling boundary conditions are listed in Tables 4.4 and 4.5 respectively, which include the onset of instability and the temperature calculated at a point, E. The method of calculation of the onset of instability will be described in details in section 4.4. The temperature has been calculated at the time when the instability sets in. The variations of the onset time for the finest (600×300) and the second finest mesh (400×200) are less than 2% for all aspect ratios with the two different boundary conditions. However, the variations of the temperature among the four different meshes are very small (bellow 0.11%) for both boundary conditions and all aspect ratios. Therefore any one of the meshes can be selected for the simulations based on the temperature variation. However, based on the response of the onset of instability, either of the two finest meshes can be adopted.
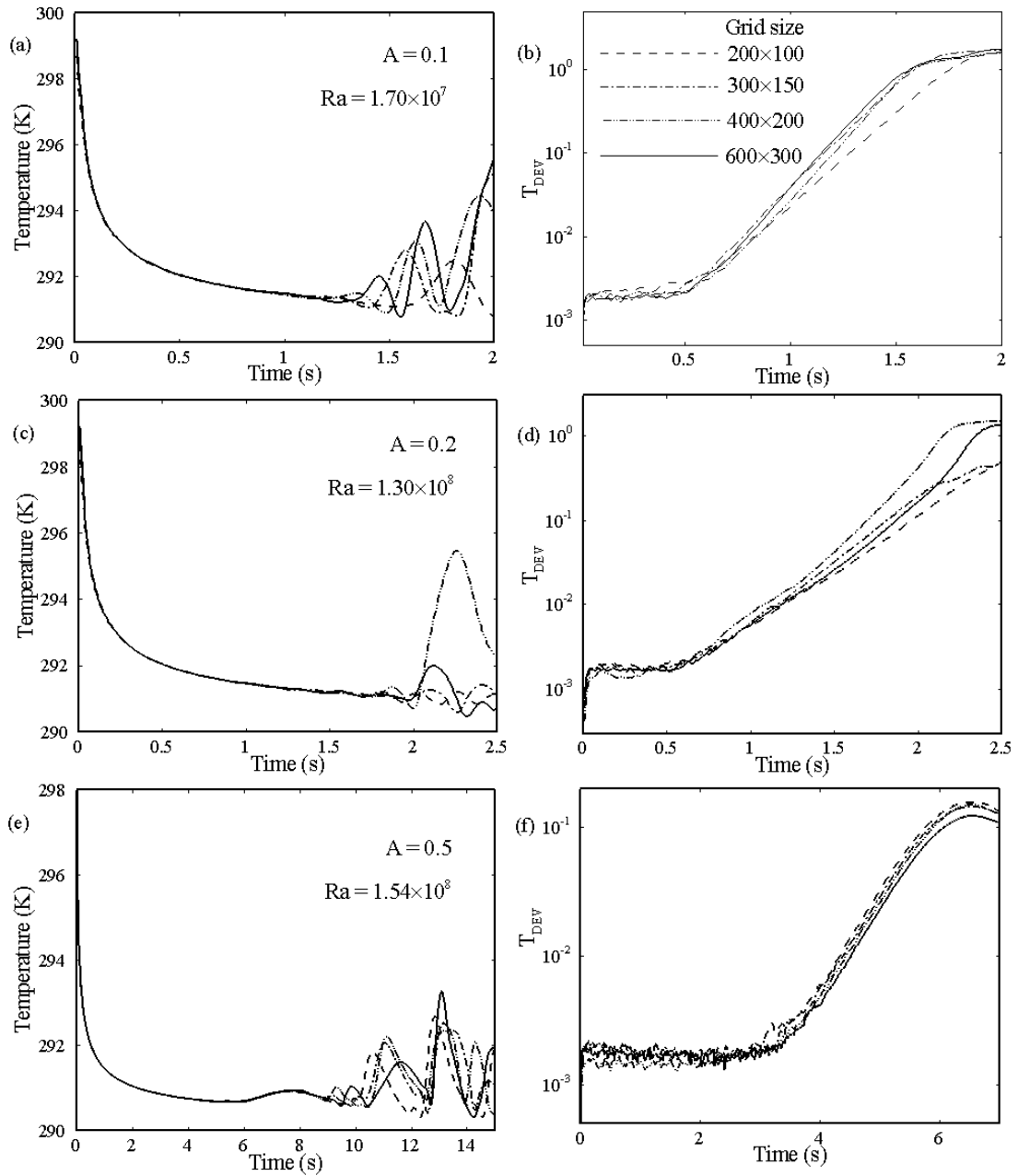
Figure 4.3 Time series of temperature (a, c, e) at a point (0.6*m*, 0.00121*m*) and the growth of the standard deviation of the temperature (b, d, f) for four different grids for the sudden cooling boundary condition.

Figure 4.3 plots the time series of the temperature at a point, *E* and the growth curves of the standard deviation of the temperature along a straight line which is parallel and very close (0.00121*m* far from the plate) to the plate for the sudden cooling boundary condition. The same unsteady calculation has also been performed for the case of ramp cooling boundary condition which is depicted in Figure 4.4. For both cases, instead of considering the straight line equal to the total length of the plate, we

choose to calculate the standard deviation in the middle portion (1/3 of the plate) of the plate to avoid the effect of two adiabatic end walls. Clearly, the predicted growth of the perturbation depends on the grid resolution. However, for the two finest grids (400×200 and 600×300), the dependency of the onset time of instability on the grid resolution is weak, consistent with the results shown in Tables 4.3 and 4.4.
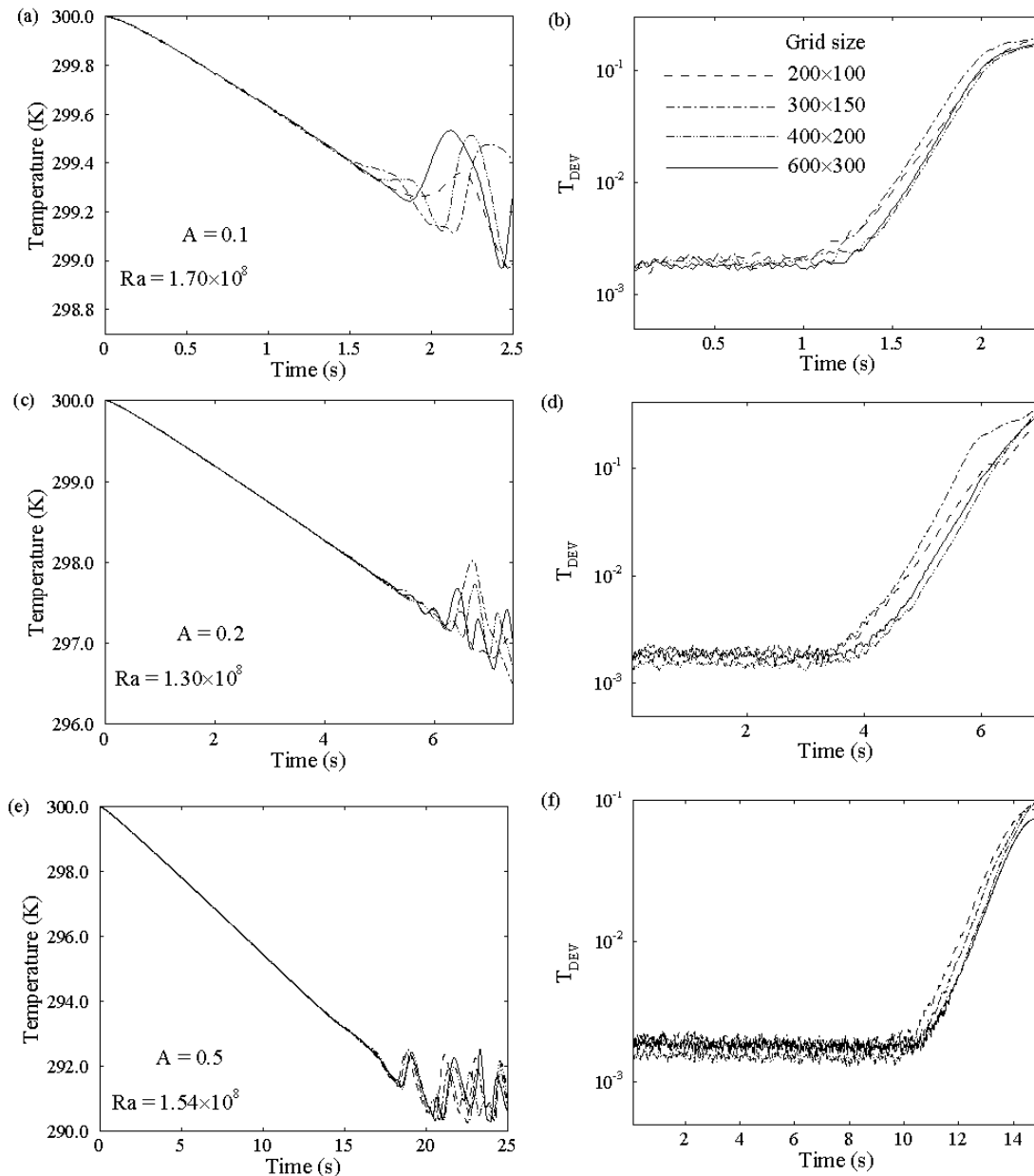
Figure 4.4 Time series of temperature (a, c, e) at a point (0.6*m*, 0.00121*m*) and the growth of the standard deviation of the temperature (b, d, f) for four different grids for ramp cooling boundary condition.

The time series of the temperature in both Figures 4.3 and 4.4 initially fall together for four different grid sizes of each aspect ratio. At the time when the instability sets in, the dependency of the temperature on the grid is negligible. However, after the instability sets in the temperature depends strongly on the mesh which can be seen in both boundary conditions and for all aspect ratios. Since the purpose of this study is to predict the onset of instability rather than resolving the details of the instability, either of the 400×200 and 600×300 meshes can be adopted to reproduce the basic features of the flow. Hence, a mesh size of 400×200 will provide adequate resolution for the present analysis and has been adopted for subsequent calculations.

4.4 Amplitude of the perturbation test

Since the two ends of the plate are connected with two adiabatic walls, some end effects are inevitable. To avoid the end-wall effects, we have calculated the standard deviation along a line parallel to the plate in the middle portion of the plate (1/3rd of the total length) which is very close to the plate. An artificial perturbation has also been continuously applied in time on the cold inclined plate, which is defined by

$$\hat{T} = \varepsilon[\text{rand}(0,1) - 0.5], \tag{4.38}$$

where ε specifies the intensity of the perturbation ($\varepsilon \ll 1$); rand (0, 1) generates random numbers between 0 and 1.

We first examine the system response to different perturbation amplitudes to ensure that the selected amplitude for this study is within the range in which the system response is linear. Three different values of the amplitude ($\varepsilon = 0.5\%$, 1.0% and 2.0% respectively) are calculated for the case of $Pr = 0.72$ and $Ra = 8.50 \times 10^6$.
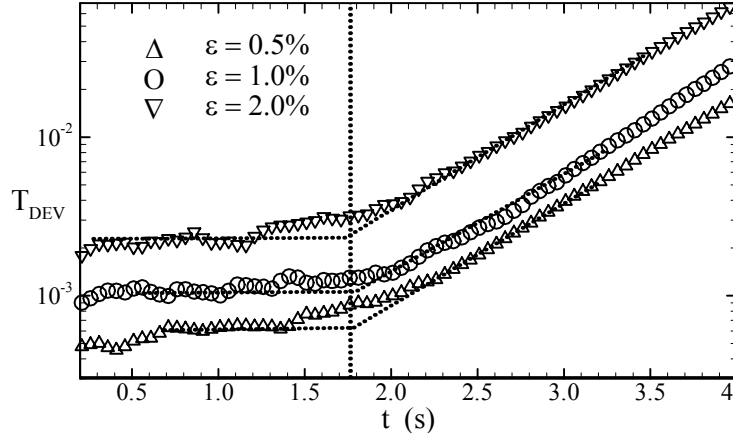
Figure 4.5 Growth of the standard deviation of the temperature for different amplitude of perturbation source for $Ra = 8.50 \times 10^6$.

Figure 4.5 shows the calculated results with different amplitudes of the perturbation source. The system response to perturbations, or the growth of perturbations, is indicated well by the time series of the standard deviation of temperature parallel to the plate. It is noted that the standard deviation is plotted on a logarithmic scale in this figure. As described by Lei and Patterson (2003a), each of the plots in Figure 4.5 can be divided into three regions in time: a constant-response region, an exponential-growth region, which is represented by the linearly increasing part of the curve, and a transitional region connecting the above two regions. In the constant-response region, the perturbation is not amplified, suggesting that the flow, and in particular the inclined thermal boundary layer, is stable, and the system response echoes the random perturbation.

The perturbation grows exponentially in the exponential-growth region with time, which is given by

$$T_{DEV} = a e^{c(t - t_B)}, \tag{4.39}$$

where T_{DEV} is the standard deviation of temperature along the line parallel and very close to the plate, a is the amplitude, c is the growth rate and t_B is the critical time for the onset of instability. The growth rate c then corresponds to the slope of the linearly increasing part in Figure 4.5, which can be determined accordingly. The critical time, t_B for the onset of the instability has been determined in Figure 4.5 as the intersection point between the constant-response curve and the exponential-growth curve (see Lei and Patterson 2003a). Note that the critical time is independent of the amplitude of the perturbation source.

74

In summary, within the range of parameters examined here, the variation of the perturbation amplitude does not change the stability properties of the flow (e.g. the critical time for the onset of instability), and the system response to perturbations is linear. Subsequent calculations will be conducted with a fixed perturbation amplitude of $\varepsilon = 1.0\%$.

4.5 Effect of plate length on transient flow

Figure 4.6 shows the temperature contours of inclined plates of three different lengths at the time 1000s for $A = 0.1$. The length of the plate of Figure 4.6(a) is 5.4m, (b) is 10.8m and (c) is 16.2m. All the physical fluid properties were kept the same for three geometries except the physical length of the plate. The Rayleigh numbers for (a), (b) and (c) are 7.74×10^4, 6.20×10^5 and 2.10×10^6 respectively. We see that a cold thermal boundary layer has been developed adjacent to the plate. It is also observed that there is an end effect at the top right corner of the enclosure for all three geometries. However, the middle portion of the plate is unaffected by that end effect.
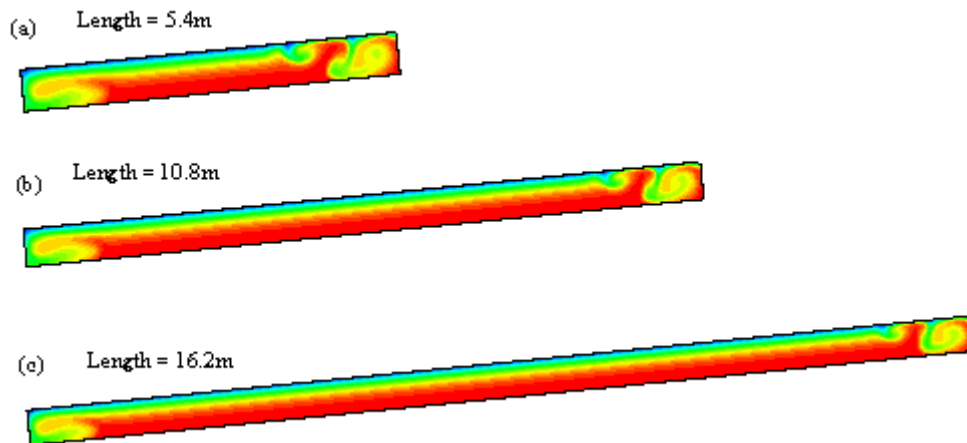
Figure 4.6 Temperature contours of the inclined plate with three different plate lengths.

Figure 4.7 shows the time series of the temperature at nine different positions along the plate which are taken at a distance of $W/4$ from the plate for $A = 0.1$. The length of the plate is 10.8m in Figure 4.7(a) and 16.2m in Figure 4.7(b). It is clear in Figure 4.7(a) that the onset of instability occurs almost at the same time (about at

1150s) at eight different positions. However, at the position 10*L*/12, which is the closest to the downstream region, the response is much earlier. This is due to the end effect. On the other hand, when the length is increased to 16.2*m* (see Figure 4.7b), the response of the onset of instability is at the same time at all nine different positions.
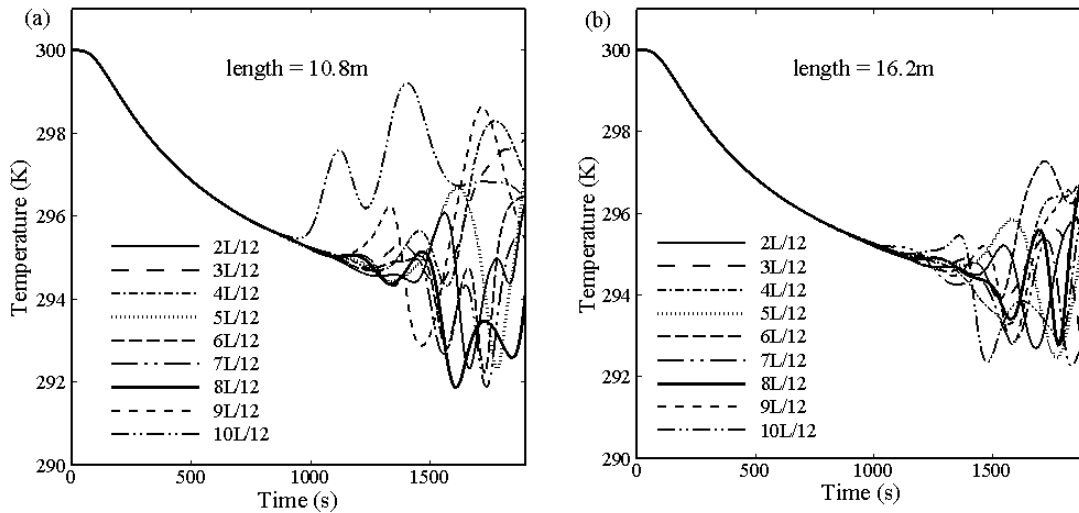
Figure 4.7 Time series of the temperature at different position of the plates of two different lengths which are *W*/4 distance far from the plate.

Time series of the temperature at the mid position of the plate and *W*/4 away from the plate obtained with the three different lengths of the plate are shown in Figure 4.8. It is noticed that the onset of instability for three different lengths is at the same time. However, for the smallest plate the response after the onset of instability is different from the other two. This may be attributed to the random nature of the instability in the form of sinking plumes which may happen at a random location. It is interesting to see that the time series of the temperature for the three different plate lengths fall together until the instability is set in. The reason for this can be explained by the scaling relations of transient velocity (4.1) and the unsteady thermal layer thickness ($\delta_T \sim \kappa^{1/2} t^{1/2}$), both of which are length independent.
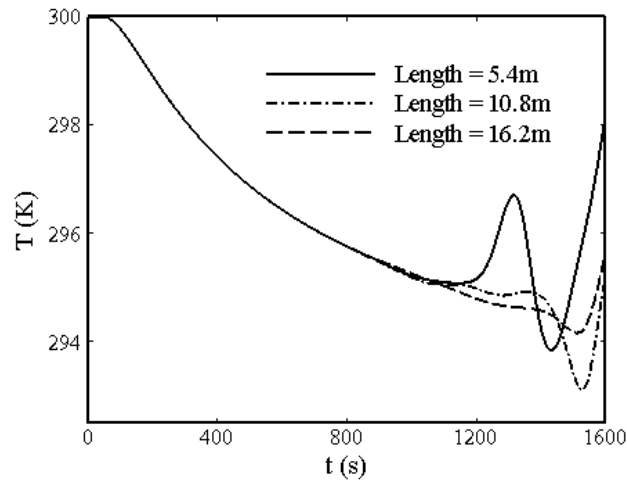
Figure 4.8 Time series of the temperature at the mid position of the plate and *W*/4 away from the plate.

Figure 4.9 shows the velocity profiles and the temperature profiles along the line perpendicular to the plate at midpoints for the three different plate lengths at the time *t* = 1000s. This is the time just before the instability sets in. It is seen in Figure 4.9(a) that the velocity profiles for the three different plate lengths fall almost onto a single profile which proves that the unsteady velocity does not depend on the plate length and confirms the scaling relation (4.1). The corresponding temperature profiles also fall onto a single profile as the thermal layer thickness increases according to $\kappa^{1/2}t^{1/2}$ at the transient stage. Therefore it does not depend on the plate length.
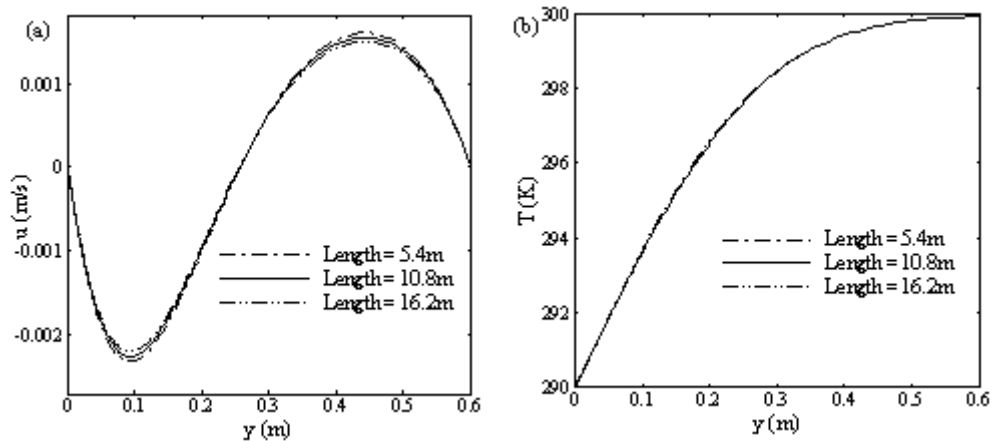
Figure 4.9 (a) velocity profiles and (b) temperature profiles along the line perpendicular to the plate at midpoints at time *t* = 1000s.

The time series of the thermal layer thickness at the mid position of two plates of different lengths are shown in Figure 4.10(a). The thickness has been calculated at the mid position of the plates as the distance from the plate to the position where the fluid temperature reaches $0.2(T_h - T_c)/\Delta T$. In Figure 4.10(b), the thickness is plotted with respect to $t^{1/2}$. Two lines initially fall together and make straight line which confirms the scaling relation $\delta_T \sim \kappa^{1/2} t^{1/2}$. However, at about 1150s, the instability sets in for both plates.
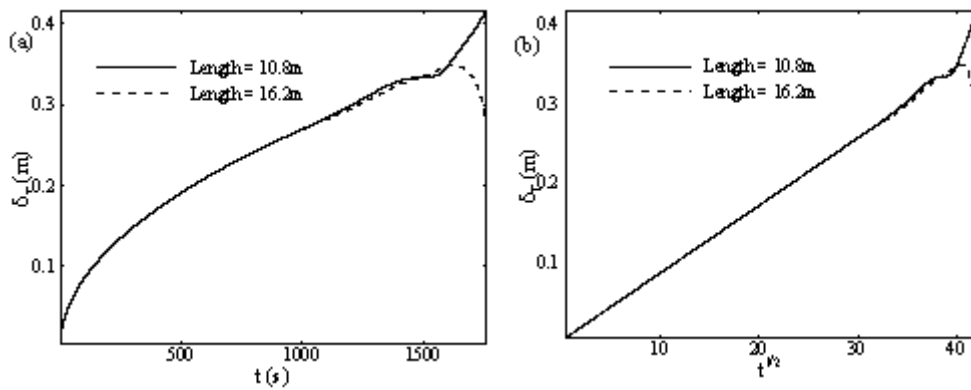
Figure 4.10 Time series of the thermal layer thickness at the mid position of the plates of two different lengths.

Temperature profiles at two different times are obtained with the 16.2-m long plate along five different perpendicular lines to the plate and depicted in Figure 4.11. Figure 4.11(a) represents the temperature profiles at $t = 600$s and Figure 4.11(b) shows the temperature profiles at $t = 1000$s. Both times are before the onset of instability. It is seen in both curves that all profiles at five different positions fall onto a single curve. Therefore, the thickness of the thermal layer is independent of the location along the plate.
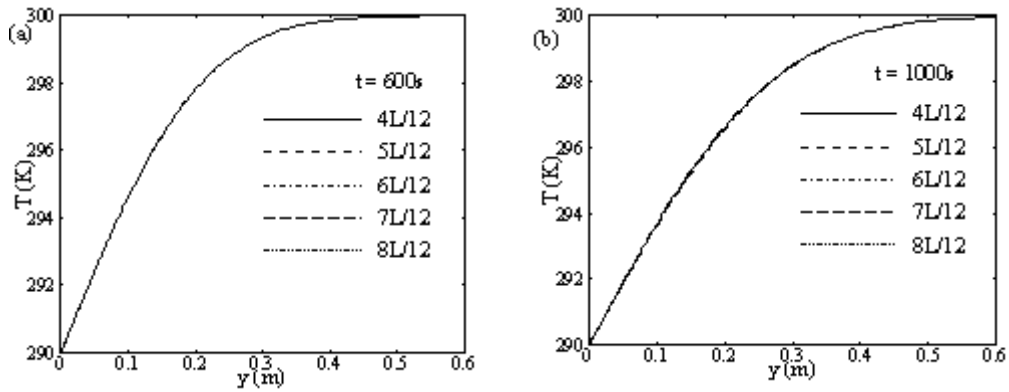
Figure 4.11 Temperature profiles at two different times of the plate (length = 16.2m) calculated along five different lines which are perpendicular to the plate.

4.6 Flow development in different regimes for sudden cooling

4.6.1 Conduction regime

Figure 4.12 presents the numerical results of a representative case in this low-Rayleigh number regime, $Ra < (1+Pr)(1+A^2)/(PrA^2)$ with $Pr = 0.72$, $Ra = 50$ and $A = 0.1$. The temperature contours and streamlines are plotted in Figures 4.12(a) and 4.12(b), respectively at time $t/t_s = 0.7$. The thermal boundary layer expands and exceeds the width of the domain and the steady state solution can not be reached. Since it is a closed domain with three adiabatic sides, the whole domain cools down with time. The streamlines typically show a single closed cell structure as it is a closed domain.
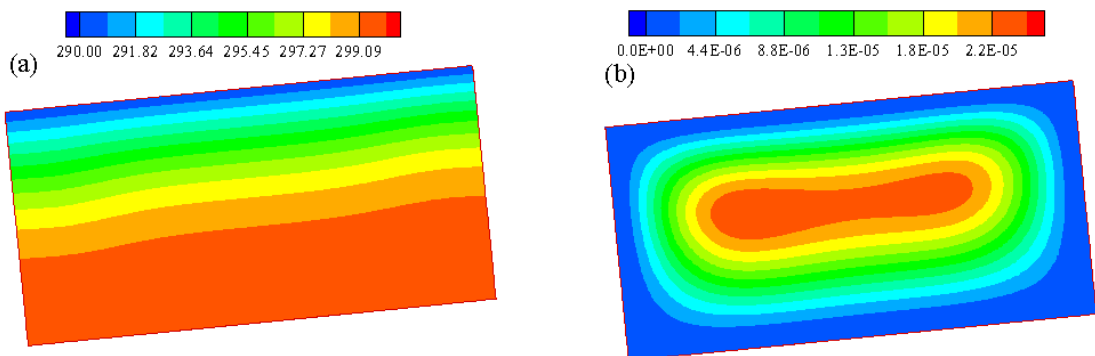
Figure 4.12 (a) Temperature contours and (b) streamlines for $Ra = 50$, $Pr = 0.72$ and $A = 0.1$ at $t/t_s = 0.7$.

4.6.2 Stable convection regime

Figure 4.13 presents the numerical results of a representative case in this flow regime, $(1+Pr)(1+A^2)/(A^2 Pr) < Ra < (Pr^3 A^6 Ra_c{}^4)(1+Pr)^{-3}(1+A^2)^{-3}$ with $Pr = 0.72$, $Ra = 8.5 \times 10^2$ and $A = 0.1$ at $t = t/t_s = 1.02$. Temperature contours are presented in Figures 4.13(a) and streamlines are in 4.13(b). In the isotherms we see that near the two ends of the plate there are some end effects. This is because of the presence of the two adiabatic walls at the ends of the plate. However, the middle portion of the plate is not affected by the end effects.
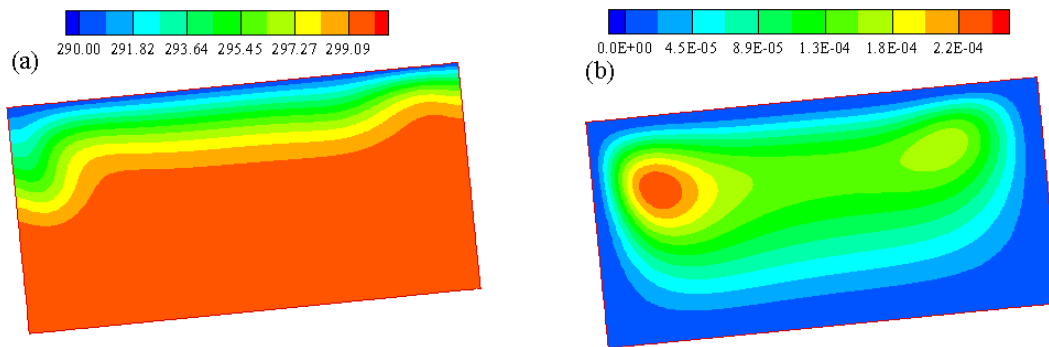
Figure 4.13 (a) Temperature contours and (b) streamlines for $Ra = 8.5 \times 10^2$, $Pr = 0.72$ and $A = 0.1$ at $t/t_s = 1.02$.

4.6.3 Unstable convection regime

This regime, $Ra > (Pr^3 A^6 Ra_c{}^4)(1+Pr)^{-3}(1+A^2)^{-3}$ is characterized by the presence of the Rayleigh Bénard instability in the form of sinking plumes. Figure 4.14 represents the isotherms and the streamlines for $Pr = 0.72$, $Ra = 1.70 \times 10^7$ and $A = 0.1$ at time $t/t_s = 1.22$ and $t/t_B = 2.88$ to demonstrate the features of this flow regime. In this regime, the boundary layer becomes unstable and forms sinking plumes adjacent to the cold plate before the steady state of the thermal boundary layer.
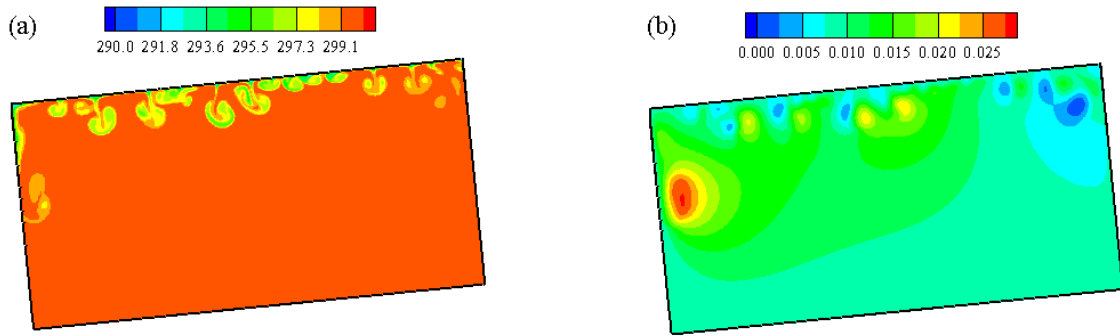
Figure 4.14 (a) Temperature contours and (b) streamlines for $Ra = 1.7 \times 10^7$, $Pr = 0.72$ and $A = 0.1$ at $t/t_s = 1.22$.

4.7 Flow development in different regimes for ramp cooling

4.7.1 Ramp time shorter than steady state time

Figure 4.15 shows the temperature contours and the streamlines (*Regime* 1) for $Pr = 0.72$, $Ra = 10$ and $A = 0.1$ at time $t/t_s = 0.22$, where $t_p/t_s = 4.35 \times 10^{-3}$. Figures 4.15(a) presents the temperature contours and Figure 4.15(b) presents the corresponding streamlines. In this regime the steady state time is longer than the ramp time. Therefore, the boundary layer grows according to the scale $\kappa^{1/2} t^{1/2}$ even after the ramp is finished. The thermal boundary layer expands and exceeds the length of the plate with time before the steady state of the boundary layer is reached. Since it is a closed domain with three adiabatic sides, the whole domain cools down with time. The streamlines typically show a single closed cell structure as it is a closed domain.
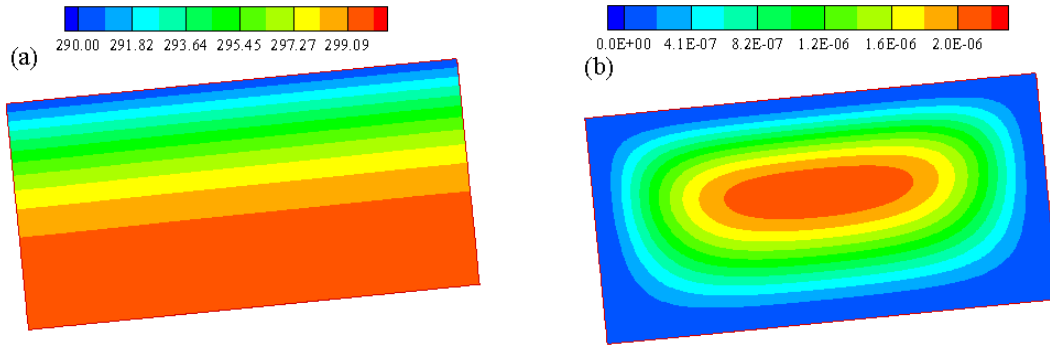
Figure 4.15 (a) Temperature contours and (b) streamlines for $Ra = 10$, $Pr = 0.72$ and A = 0.1 at $t/t_s = 0.22$.

Figure 4.16 represents the temperature contours and the streamlines for (*Regime* 2) $Pr = 0.72$, $Ra = 8.5 \times 10^4$ and $A = 0.1$ at time $t/t_s = 2.04$, where $t_p/t_s = 0.58$. Figures 4.15(a) presents the temperature contours and Figure 4.15(b) presents the corresponding streamlines. In this regime the thermal boundary layer becomes unstable to the Rayleigh-Bénard instability after the ramp is finished. The corresponding streamlines show a number of convective cells near the cooled plate. Since the two ends of the domain are not open, one larger cell forms inside the domain.
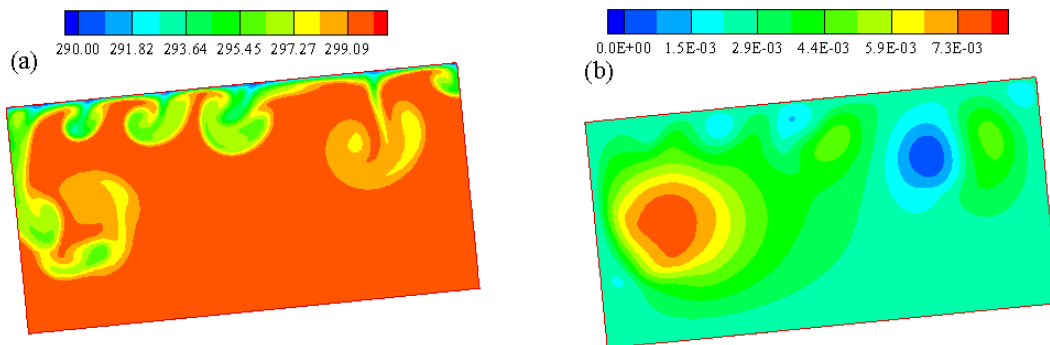
Figure 4.16 (a) Temperature contours and (b) streamlines for $Ra = 8.5 \times 10^4$, $Pr = 0.72$ and $A = 0.1$ at $t/t_s = 2.04$.

The numerical results for *Regime* 3 are presented in Figure 4.17. Figure 4.17 shows the temperature contours and the streamlines for $Pr = 0.72$, $Ra = 3.40 \times 10^5$ and A = 0.1 at time $t/t_s = 2.33$, where $t_p/t_s = 0.81$. The temperature contours and the corresponding streamlines are shown in Figures 4.17(a) and (b) respectively. In this

regime the instability sets in before the ramp is finished which is seen in the temperature contours. The corresponding streamlines show a number of convective cells near the cooled plate. Two larger cells appear inside the domain as two ends of the domain are adiabatic.
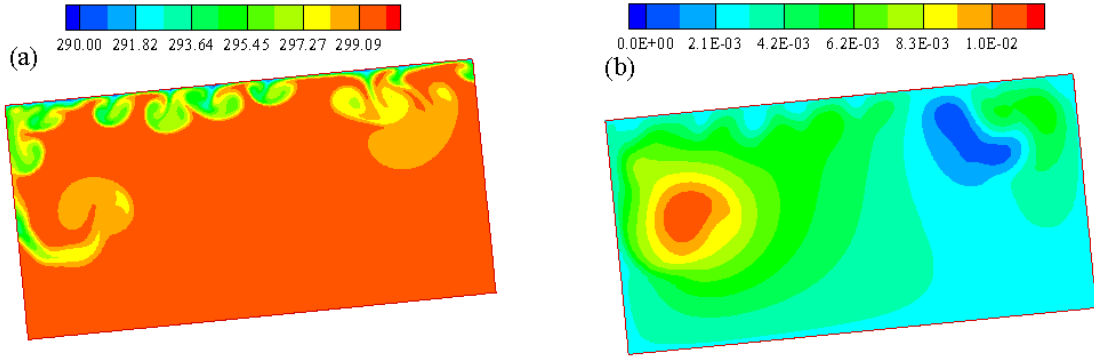
Figure 4.17 (a) Temperature contours and (b) streamlines for $Ra = 3.40 \times 10^5$, $Pr = 0.72$ and $A = 0.1$ at $t/t_s = 2.33$.

4.7.2 Ramp time longer than the quasi-steady time

A representative case in *Regime* 4 has been chosen as $Ra = 2.00 \times 10^3$, $Pr = 0.72$, $A = 0.1$, and $t_p/t_s = 1.05$. The temperature contours and streamlines are shown in Figure 4.18 for the above mentioned case at $t/t_{sr} = 1.05$. In this regime the flow is stable to the Rayleigh-Bénard instability until the ramp is finished. The boundary layer reaches a quasi-steady state prior to the completion of the ramp time. Since two ends of the plate have adiabatic walls, the boundary layer has an end effect (see Figure 4.18a). However, the middle portion of the boundary layer is unaffected. The corresponding streamlines show a big cell inside the enclosure (Figure 4.18b) with two small cells near two ends of the plate.
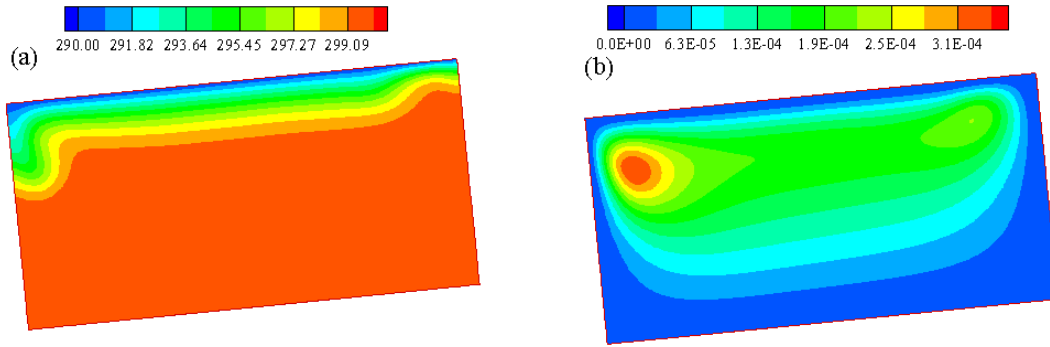
Figure 4.18 (a) Temperature contours and (b) streamlines for $Ra = 2.00 \times 10^3$, $Pr = 0.72$ and $A = 0.1$ at $t/t_{sr} = 1.05$.

The representative case in *Regime* 5 is chosen as $Ra = 1.35 \times 10^6$, $Pr = 0.72$, $A = 0.1$, and $t_p/t_s = 1.76$. The temperature contours and streamlines are shown in Figure 4.19 for the above mentioned case at $t/t_{sr} = 1.5$. In this regime the flow is stable initially and reaches to the quasi-steady state time. However, in the temperature contour (see Figure 4.19a) it is seen that the boundary layer becomes unstable in the quasi-steady mode as the plate is still cooling in the quasi-steady mode until the ramp is finished. The convective cells due to the Rayleigh-Bénard instability can be seen in the corresponding streamlines (Figure 4.19b).
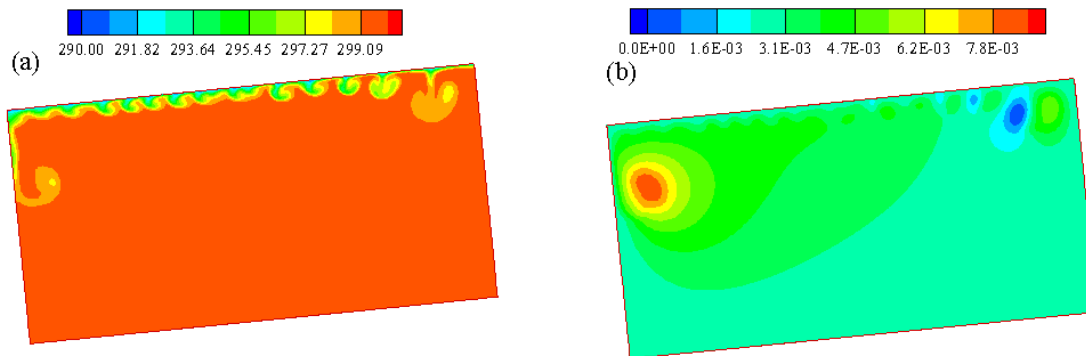
Figure 4.19 (a) Temperature contours and (b) streamlines for $Ra = 1.35 \times 10^6$, $Pr = 0.72$ and $A = 0.1$ at $t/t_{sr} = 1.5$.

On the other hand, the instability may set in before the flow becomes quasi-steady (*Regime* 6). Figure 4.20 represents the numerical results in this sub-regime at

t/t_{sr} = 0.81 for a case with t_p/t_{sr} = 4.10. The isotherms and streamlines for Ra = 1.70×10^7 and A = 0.1 with Pr = 0.72 are depicted in Figure 4.20(a) and 4.20(b) respectively. This regime is characterized by the presence of convective instability at the early stage of the flow development in a form of sinking plumes, as can be observed in Figure 4.20.
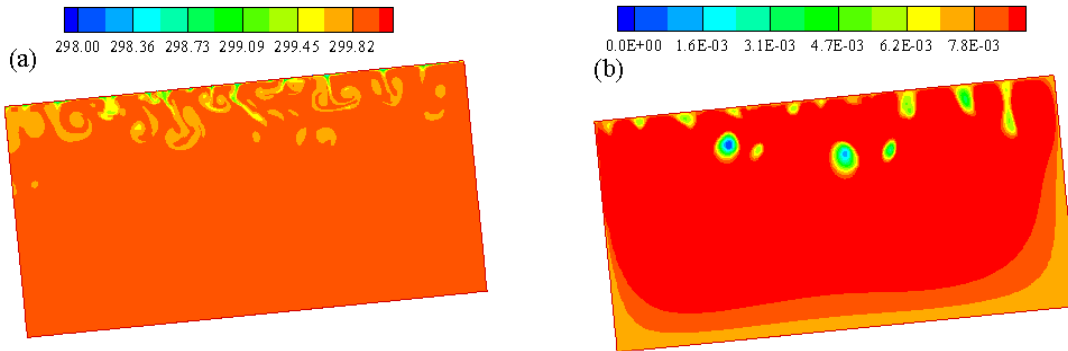
Figure 4.20 (a) Temperature contours and (b) streamlines for $Ra = 1.70 \times 10^7$, $Pr = 0.72$ and $A = 0.1$ at $t/t_{sr} = 0.81$.

4.8 Validation of selected scales

4.8.1 Sudden cooling

A total of 13 simulations have been performed to verify the scaling relations. These are listed in Table 4.6. Three aspect ratios, A = 0.1, 0.2 and 0.5 are considered to show the aspect ratio dependency of the scaling. For the aspect ratio A = 0.1, Rayleigh numbers in the range of $3.40 \times 10^3 < Ra < 1.70 \times 10^7$ are selected to verify the Rayleigh number dependency. For all simulations the Prandtl number has been fixed at 0.72 (air).

The flow velocity parallel to the inclined plate has been recorded at several locations along a line perpendicular to the plate at the mid point to obtain the velocity profile along that line. From this velocity profile, the maximum parallel velocity, u_s has been calculated and is used to verify the velocity scale relation.

Table 4.6 Values of *A*, and *Ra* for 13 runs.

Runs	A	Ra	Regimes
1	0.1	1.70×10^7	
2	0.1	2.81×10^6	
3	0.1	1.70×10^6	
4	0.1	1.70×10^5	
5	0.1	1.35×10^5	
6	0.1	8.50×10^4	*Unstable convection*
7	0.1	3.40×10^4	
8	0.1	1.70×10^4	
9	0.1	1.35×10^4	
10	0.2	1.30×10^8	
11	0.5	1.54×10^8	
12	0.1	8.50×10^2	*Stable convection*
13	0.1	50	*Conduction*

As soon as a cold temperature boundary condition is applied to the plate, a cold boundary layer starts to develop adjacent to the inclined plate. This boundary layer is potentially unstable to Rayleigh-Bénard instability if the Rayleigh number is higher than the critical Rayleigh number.
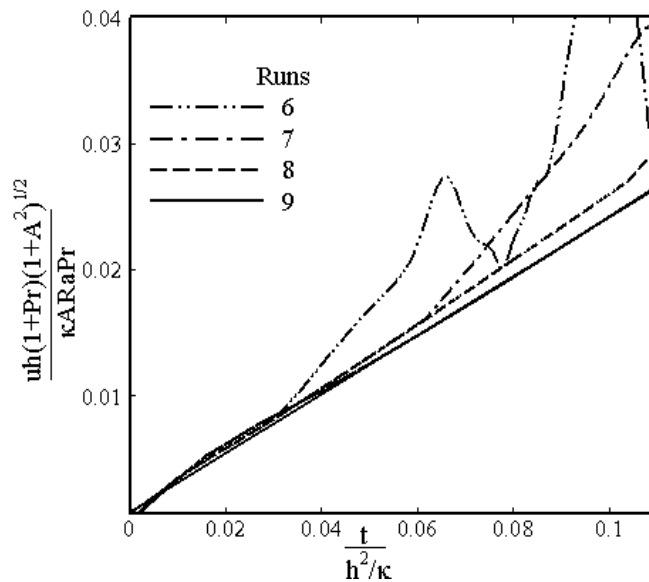
Figure 4.21 Normalised unsteady velocity against normalised time.

The unsteady velocity scale (4.1) is verified in Figure 4.21. The maximum velocity parallel to the surface has been calculated from the numerical simulation for different parameters considered here. Relatively smaller Rayleigh numbers have been chosen to verify the unsteady velocity scale to avoid complication caused by the instability in the early stage (runs 6 − 9). It is seen that all of the plots for different Rayleigh numbers lie together initially, forming a straight line through the origin, indicating that the scaling relation for the unsteady velocity (4.1) is valid for the cooling boundary layer. As we have seen for the case of sudden heating, this scaling is valid until the steady-state of the boundary layer is reached. However, in the selected Rayleigh number cases the flow is unstable to the Rayleigh-Bénard instability since the Rayleigh numbers are higher than the critical value corresponding to the aspect ratio. The deviation of the curves from the straight line in Figure 4.21 indicates the onset of instability.
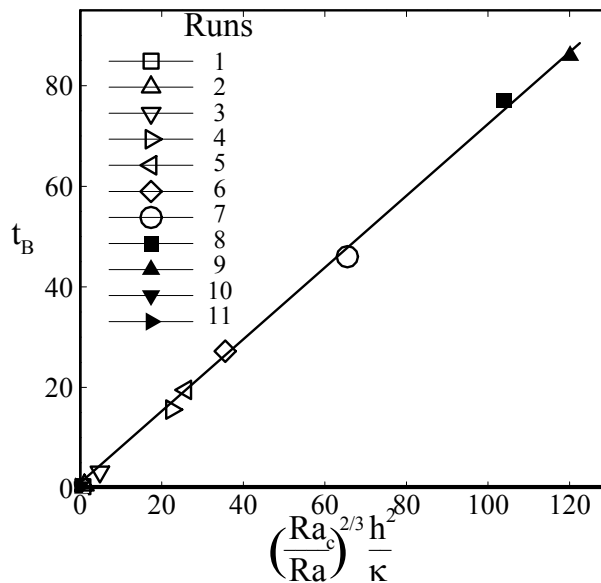
Figure 4.22 Numerically obtained onset time of instability against corresponding scaling values, for 11 runs; Solid line, linear fit.

For the sudden cooling boundary condition, as soon as the plate starts to cool, a cold boundary layer develops adjacent to the plate which is potentially unstable to the Rayleigh-Bénard instability. We calculate the onset time of instability for different Rayleigh numbers from the numerical simulations and compare it with the scaling results which have been depicted in Figure 4.22. The critical time, t_B for the onset of the instability from the numerical simulation has been determined as the intersection point

between the constant-response curve and the exponential-growth curve of the time series of standard deviation of the temperature which is shown previously in Figure 4.5. It is found that all calculated results fall onto a straight line. Therefore, the numerical results verify the scaling prediction (4.10).

4.8.2 Ramp cooling

Fourteen simulations of different Rayleigh numbers and aspect ratios with a fixed Prandtl number, which are shown in Table 4.7, have been performed to verify the scaling relations for different flow regimes under the ramp cooling condition. Based on the onset time of instability at different stages of flow development, there are four possible flow regimes. Runs 1-7 falls in the regime when the instability sets in before the quasi-steady state of the boundary layer is reached ($t_{B1} < t_{sr}$). Runs 8-10 falls into the regime when the instability sets in after the quasi-steady state but before the ramp is finished ($t_{sr} < t_{B2} < t_p$). Run 14 falls in the regime where the instability sets in before the ramp is finished in which the steady-state time is longer than the ramp time and runs 11-13 are in the regime when the instability sets after the ramp is finished ($t_{B3} > t_p$) for the case when the steady-state time is longer than the ramp time. For all the simulations the ramp time has been chosen to be 20s.

Table 4.7 Values of *A*, and *Ra* for 14 runs.

Runs	*A*	*Ra*	Regimes
1	0.1	1.70×10^8	
2	0.1	8.50×10^7	
3	0.1	3.40×10^7	
4	0.1	1.70×10^7	*Regime 6*
5	0.1	1.35×10^7	
6	0.1	8.50×10^6	
7	0.2	1.30×10^8	
8	0.1	2.88×10^6	
9	0.1	2.35×10^6	*Regime 5*
10	0.1	1.70×10^6	
11	0.1	1.70×10^5	
12	0.1	1.35×10^5	*Regime 2*
13	0.1	8.50×10^4	
14	0.5	1.54×10^8	*Regime 3*

Similarly to the sudden cooling case, the velocity parallel to the plate has been recorded at several locations along a line perpendicular to the plate at the mid point to obtain the velocity profile along that line. The maximum velocity parallel to the plate, u_s, is then calculated from the velocity profiles and used to verify the velocity scale relation.

The unsteady velocity scale (4.15) for ramp cooling boundary condition is verified in Figure 4.23. The maximum velocity parallel to the surface has been calculated from the numerical simulation for different parameters considered here. Relatively smaller Rayleigh numbers have been chosen to verify the unsteady velocity scale to avoid complication caused by the instability in the early stage. It is seen that all the plots for different Rayleigh numbers lie together initially, forming a straight line through the origin until the instability sets in for some Rayleigh numbers. This indicates that the scaling relation for unsteady velocity (4.15) is valid. Like the heating case (Chapter 3), this velocity scale is valid until the conduction and convection balance in the energy equation, provided that the flow remains stable for the cooling case. However, the flow for the cooling case is potentially unstable to the Rayleigh-Bénard instability if the Rayleigh number exceeds a critical value. The deviation of the curves from the straight line in Figure 4.23 indicates the onset of instability.
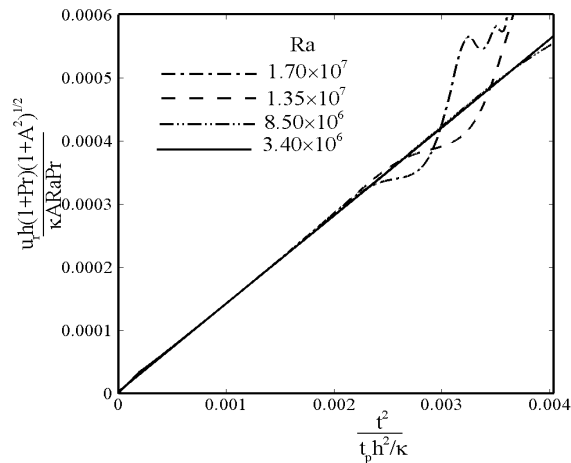
Figure 4.23 Normalised unsteady velocity against normalised time.

Figure 4.24 shows the comparison of the calculated critical time from the numerical simulation with the predicted critical time from the scaling analysis for different flow regimes. There are four possible scenarios based on the comparison of

three time scales, namely steady-state time, ramp time and the onset of instability time (see *Regimes* 2, 3, 5 and 6 in Table 4.1 and 4.2).
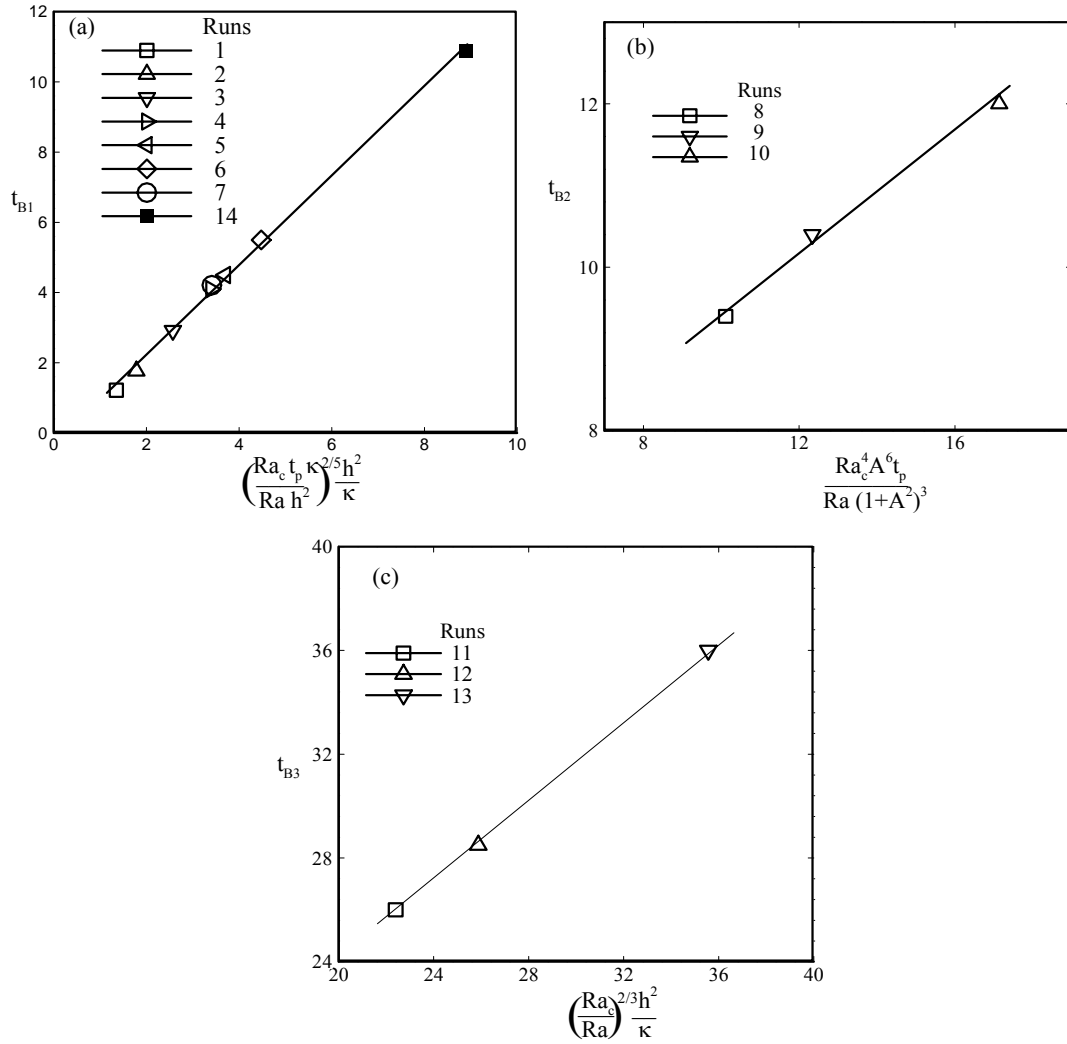
Figure 4.24 Numerically obtained onset time of instability against corresponding scaling values, for all runs. (a) $t_{B1} < t_{sr}$, (b) $t_{sr} < t_{B2} < t_p$, (c) $t_{B3} > t_p$.

Figure 4.24(a) shows the comparison of the calculated and predicted critical times in the case with the onset time shorter than the quasi-steady state time, which is shorter than the ramp time. This figure also includes the onset time of instability for the third scenario mention above (run 14). It is found in the figure that all values for different Rayleigh numbers and aspect ratios with a fixed Prandtl number fall onto a single straight line with the same order of magnitude. Therefore, the scaling relation (4.26) is verified. The second regime in which the instability sets in after the quasi-steady state has been shown in Figure 4.24(b). Again all results fall on a straight line

which confirms the scaling relation (4.28). Finally, the regime in which the instability sets in after the ramp is finished for the case with the steady state time longer than the ramp time is shown in Figure 4.24(c). Once again, all solutions fall onto a straight line. Therefore, the scale relation (4.30) is verified.

4.9 Summary

Natural convection adjacent to a cooled inclined flat plate is examined by scaling analysis and verified by numerical simulation for air ($Pr = 0.72$). Two types of cooling boundary condition are considered; sudden cooling and ramp cooling. For the sudden cooling boundary condition, as soon as the cold temperature is applied to the inclined plate, a cold boundary layer is formed. This boundary layer is potentially unstable to Rayleigh-Bénard instability. The scaling relations are formed based on the established characteristic flow parameters of the maximum velocity inside the boundary layer (u_s), the time for the boundary layer to reach the steady state (t_s), the thermal (δ_T) and viscous (δ_v) boundary layer thicknesses, and the onset time of instability (t_B). Through comparisons of these scaling predictions with the numerical simulations, it is found that the scaling relations agree very well with the numerical simulations. Hence the numerical results have confirmed the scaling relations which characterize the transient flow development under the sudden cooling condition.

Under the ramp cooling condition, the development of the boundary layer flow depends on the comparison of the time at which the ramp cooling is completed with the time at which the boundary layer completes its growth. As we know that the cold boundary layer is potentially unstable to the Rayleigh-Bénard instability, the instability may occur in different regimes, based on the global Rayleigh number. The instability may set in before the quasi-steady time, after the quasi-steady time or after the ramp is finished. Several scaling relations have been established in this case, which include the maximum velocity parallel to the inclined plate inside the boundary layer (u_{sr}), the time for the boundary layer to reach the quasi-steady state (t_{sr}), the thermal and viscous boundary layer thicknesses (δ_{Tr} and δ_v) for both quasi-steady and steady state modes, and the onset time of instability for four different regimes. The comparisons between the scaling relations and the numerical simulations demonstrate that the scaling results agree very well with the numerical simulations.

5 Natural convection in attics subject to sudden and ramp heating boundary conditions

The objective of this chapter is to understand the phenomenon of thermal convection in an attic or a wedge-shaped space, filled with a Newtonian fluid. The phenomenon of natural convection in spaces with perfectly parallel horizontal and vertical surfaces has received considerable attention because of its fundamental importance in geophysical fluid mechanics, solar-engineering applications, heat exchangers, buildings and thermal-insulation systems (see Ostrach 1972; Catton Catton 1979)**.** The attic or wedge geometry is of equal importance in all these applications, however, much less attention has been given to this geometry.

In this chapter, we investigate the fluid dynamics in the attic space, focusing on its transient response to sudden changes of temperature along two inclined walls. The transient behaviour of an attic space is relevant to our daily life. Certain periods of the day or night may be considered as having a constant ambient temperature (e.g. during 11am - 2pm or 11pm - 2am). However, at other times during the day or night the ambient temperature changes with time (e.g. between 5am - 9am or 5pm - 9pm). Based on these natural scenarios, we consider two cases in this chapter: one with sudden heating on the roof of the attic and the other with ramp heating under which the temperature on the roof follows a ramp function up until a specified temperature and then remains constant. A theoretical understanding of the transient behaviour of the flow in the enclosure is most valuable in a fundamental sense. Proper identification of the timescales relevant to various flow features that develop inside the cavity makes it possible to predict theoretically the basic flow features that will survive once the thermal flow in the enclosure reaches steady state.

The transient development of the flow in the attic space is described using scaling analysis for sudden heating as well as ramp heating boundary conditions in this chapter. These draw on the results of previous chapters. A time scale for the heating-up of the whole cavity together with the heat transfer through the inclined walls has also been predicted through scaling analysis. The scaling results have been verified with a

series of numerical simulation. Details of the numerical procedure can be found in Chapter 2. However, grid and time step dependence tests specific to the cases of sudden and ramp heating of an attic space are described in this chapter.

Under consideration is a triangular cavity of height h, half length of the base l, containing a Newtonian fluid with $Pr < 1$ which is initially at rest with a temperature T_c. At the time $t = 0$, two possible heating boundary conditions are considered on the inclined walls: sudden heating to a specified temperature which is then maintained; and heating by a linearly increasing temperature to a specified temperature over some time (the ramp time) after which the temperature is maintained (the ramp function). The ramp function is described in Chapter 3 (eqn 3.11). In order to avoid the singularities (if there is any) at the tips in the numerical simulation, the tips are cut off by 5% and at the cutting points (refer to Figure 5.1) rigid non-slip and adiabatic vertical walls are assumed. We anticipate that this modification of the geometry will not alter the overall flow development significantly.
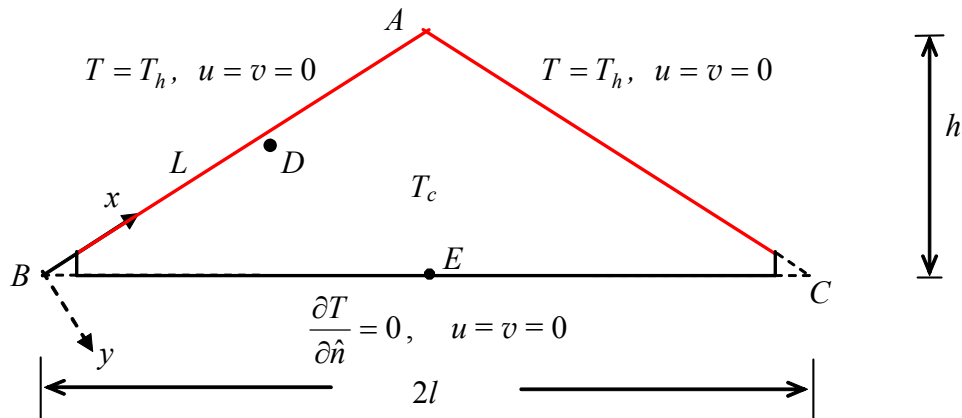
Figure 5.1 The schematic of the geometry and the coordinate system of $h/l = 0.5$.

5.1 Overview of the transient flow

As mentioned earlier, this chapter deals with two types of thermal boundary conditions applied to the inclined walls of an attic space. The first case is the sudden heating boundary condition. In this case, both inclined walls of the attic are suddenly heated to a temperature T_h, with $T_h > T_c$, where T_c is the initial fluid temperature inside the enclosure.
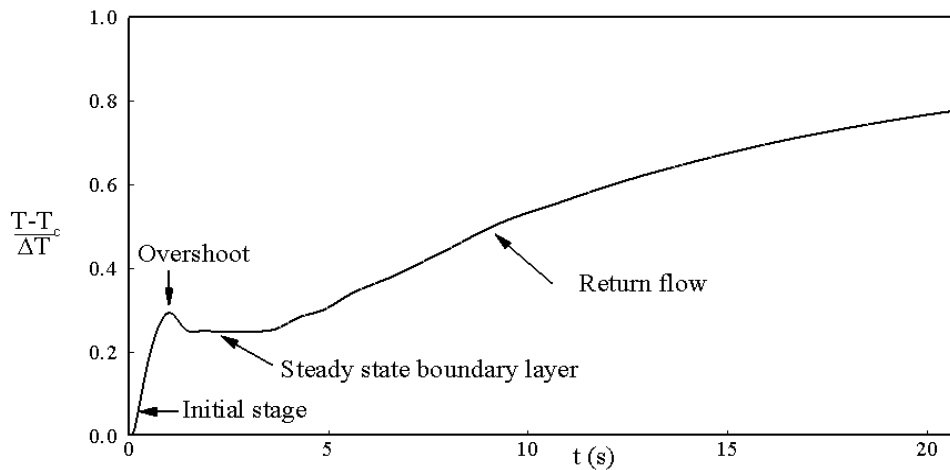
Figure 5.2 Time series of the temperature at *D* for *A* = 0.5 and *Ra* = 1.5×10^7.

Figure 5.2 shows a typical time series of temperature at the point *D* (marked in the enclosure) for *A* = 0.5 which is very close to the left inclined surface. Since the inclined wall (roof) is hot and the ambient is relatively cold, the flow is laminar and stable as long as the Rayleigh number is not too large. As a consequence, a stable thermal boundary layer develops adjacent to the hot inclined wall and continues to grow with time. The overall flow development in this case may be classified as: an initial stage, a transitional (overshoot) stage and a steady state stage of the boundary layer and a heating-up stage of the cavity. Since the bottom surface of the attic is adiabatic, the fluid inside the attic space will be heated up with time when the 'return flow' from the top reaches to the bottom surface. The detailed flow phenomena of these stages will be discussed in the scaling section.

The natural convection boundary layer adjacent to the inclined wall of an attic space subject to a ramp heating boundary condition is considered in the second case. Similarly, the overall flow development for this case may be characterized as: an early stage, a quasi-steady stage, a steady state stage of the thermal boundary layer, and a heating up stage of the cavity, all of which can be clearly identified in Figure 5.3. The boundary layer flow depends on the comparison of the time at which the ramp heating is completed and the time at which the thermal boundary layer completes its growth.

If the ramp time is longer than the steady state time, the boundary layer reaches a quasi-steady mode before the ramp finishes (see Figure 5.3). On the other hand, if the ramp is completed before the boundary layer becomes steady, the subsequent growth is the same as the case of instantaneous heating. It is noted that different stages for the

boundary layer development adjacent to an inclined plate have been shown in Chapter 3. However, heating-up stages in the attic space has been identified from the time series of temperature for both boundary conditions here in addition to other stages.
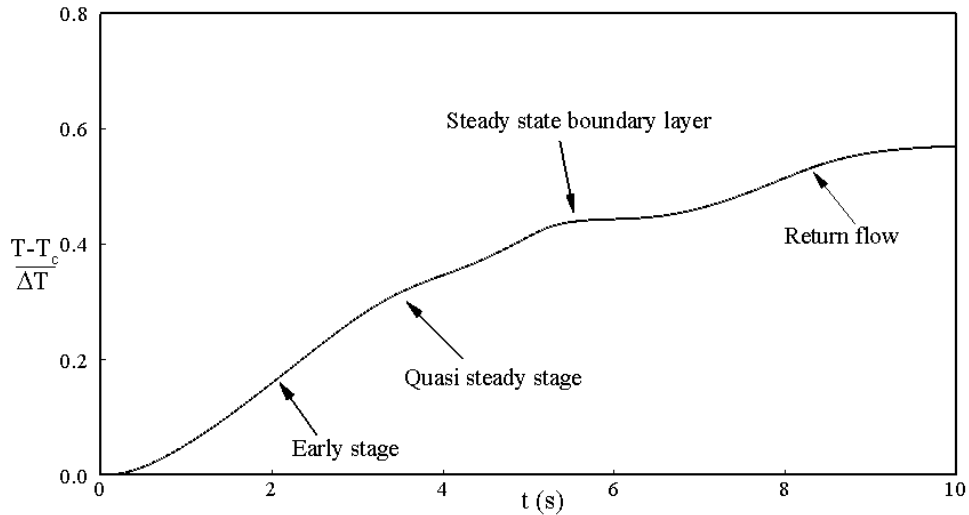
Figure 5.3 Time series of the temperature at the point, *D* for *A* = 1.0 and *Ra* = 3.0×10^6.

In the following sections, the details of the scaling analyses of the flow development, grid and time step dependency tests and the numerical verification of the scaling relations will be presented. The major findings are summarised at the end of this chapter.

5.2 Scaling analysis for sudden heating

In this section we focus on the flow which is dominated by two distinct stages of development, i.e. a boundary-layer development stage and a heating-up stage. The boundary layer development stage is the early stage of the flow development and the heating up stage is the stage when the cavity is filled with hot fluid.

The scaling results of the boundary layer development adjacent to the sloping walls of the attic space are identical to those obtained in Chapter 3 for the case of a heated inclined flat plate. Initially the thermal boundary layer adjacent to the sloping wall grows according to $\delta_T \sim \kappa^{1/2}t^{1/2}$. We see in Chapter 3 for the case of sudden heating boundary condition on the inclined flat plate that the transient velocity scale inside the boundary layer is given by (3.3) and is rewritten as

$$u \sim \frac{ARaPr}{(1+Pr)(1+A^2)^{1/2}} \left(\frac{t}{h^2/\kappa}\right)\left(\frac{\kappa}{h}\right),$$ (5.1)

and the steady state time, thickness and velocity scales from (3.5), (3.6) and (3.7) are respectively given by

$$t_s \sim \frac{(1+Pr)^{1/2}(1+A^2)^{1/2}}{ARa^{1/2}Pr^{1/2}}\left(\frac{h^2}{\kappa}\right),$$ (5.2)

$$\delta_T \sim \frac{h(1+Pr)^{1/4}(1+A^2)^{1/4}}{A^{1/2}Ra^{1/4}Pr^{1/4}},$$ (5.3)

and

$$u_s \sim \frac{Ra^{1/2}Pr^{1/2}}{(1+Pr)^{1/2}}\left(\frac{\kappa}{h}\right).$$ (5.4)

In addition to these scaling results the scaling for heat transfer through the inclined wall of the attic space at the steady state time, in the form of a Nusselt number, have been developed as follows

5.2.1 Heat transfer scales

The instantaneous local Nusselt number during the boundary-layer development stage can be calculated as

$$Nu \sim \frac{\left(\frac{\partial T}{\partial y}\right)}{\frac{\Delta T}{h}} \sim \frac{\Delta T}{\delta_T} \times \frac{h}{\Delta T} \sim \frac{h}{\delta_T} \sim \frac{h}{\kappa^{1/2}t^{1/2}}.$$ (5.5)

Using (3.5), the average steady-state Nusselt number for the boundary layer is given by

$$Nu_s \sim \frac{1}{L}\int_0^L Nudx \sim \frac{A^{1/2}Ra^{1/4}Pr^{1/4}}{(1+Pr)^{1/4}(1+A^2)^{1/4}}.$$ (5.6)

5.2.2 Heating up stage

Once the boundary layer is fully developed, the interior of the enclosure is gradually stratified by the hot fluid ejected from the boundary layer, starting from the top of the cavity, and this heating-up stage continues until the hot fluid layer from the top reaches the bottom surface. The appropriate parameters to characterize this heating-up stage are

the time, t_f for the fluid to be fully heated-up and the average Nusselt number on the heated wall.

Let us consider an arbitrary moment, t during the heating-up stage. At this moment, the fluid inside the enclosure can be assumed to consist of two layers with the location $x = x_i$ as the interface. The bottom layer is at the original temperature, T_c whereas the top layer is filled with the hot fluid discharged from the thermal boundary layer, the temperature of which is assumed to be the same as the wall temperature T_h.
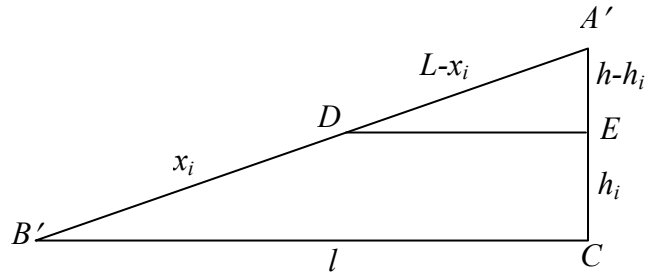
Figure 5.4 Schematic of heating-up process for sudden heating.

From $\Delta A'B'C$ and $\Delta A'DE$ in Figure 5.4, we have,

$$\frac{L - x_i}{L} = \frac{h - h_i}{h} \Rightarrow h - h_i = h\left(1 - \frac{x_i}{L}\right), \tag{5.7}$$

and

$$\frac{L}{L - x_i} = \frac{l}{DE} \Rightarrow DE = l\left(1 - \frac{x_i}{L}\right). \tag{5.8}$$

Therefore

$$\Delta A'DE = \frac{1}{2}hl\left(1 - \frac{x_i}{L}\right)^2 \sim \frac{h^2}{A}\left(1 - \frac{x_i}{L}\right)^2. \tag{5.9}$$

Suppose the total volume of the enclosure ABC is

$$V_{total} = \frac{1}{2}lh. \tag{5.10}$$

During the transient time the volume filed by the hot fluid is

$$V_{steady} \sim u_s \delta_T t_s, \tag{5.11}$$

which gives

$$V_{steady} \sim \frac{h^2 (1+Pr)^{1/4} (1+A^2)^{3/4}}{A^{3/2} Ra^{1/4} Pr^{1/4}}. \tag{5.12}$$

The ratio of the volumes

$$\frac{V_{steady}}{V_{total}} \sim \frac{(1+Pr)^{1/4} (1+A^2)^{3/4}}{A^{1/2} Ra^{1/4} Pr^{1/4}}. \tag{5.13}$$

It is estimated that the maximum ratio of the volume filled by hot fluid during the transient stage (from start-up to the steady state time) to the total volume of the enclosure is less than 0.095 over the ranges of *Ra*, *A* and other parameters considered here. Therefore, the filled volume at the transient stage is insignificant compared to the total volume and is neglected below.

From the mass conservation law

$$\frac{h^2}{A} \left(1 - \frac{x_i}{L}\right)^2 \sim u_s \delta_T t. \tag{5.14}$$

Now applying (3.6) and (3.7) in (5.14) we have,

$$\frac{h^2}{A} \left(1 - \frac{x_i}{L}\right)^2 \sim \frac{\kappa (1+A^2)^{1/4} Ra^{1/4} Pr^{1/4}}{(1+Pr)^{1/4} A^{1/2}} t$$

$$\Rightarrow x_i \sim L \left[1 - \frac{\kappa^{1/2} A^{1/4} Ra^{1/8} Pr^{1/8} (1+A^2)^{1/8}}{h (1+Pr)^{1/8}} t^{1/2} \right]. \tag{5.15}$$

The time when the whole enclosure is filled with hot fluid ($x_i \sim 0$) is obtained as

$$t_f \sim \frac{(1+Pr)^{1/4}}{A^{1/2} Ra^{1/4} Pr^{1/4} (1+A^2)^{1/4}} \left(\frac{h^2}{\kappa}\right). \tag{5.16}$$

Since only the lower part of the sloping wall contributes to the heat transfer at any given time, it is apparent from (5.2) that the instantaneous global Nusselt number, *Nu* at the heating up stage is,

$$Nu \sim \left(\frac{x_i}{L}\right) Nu_s. \tag{5.17}$$

Applying (5.15) and (5.16) in (5.17), we have

$$\frac{Nu}{Nu_s} \sim 1 - \frac{\kappa^{1/2} A^{1/4} Ra^{1/8} Pr^{1/8}}{h(1+Pr)^{1/8}} t^{1/2}$$

$$\Rightarrow \frac{Nu}{Nu_s} \sim 1 - \left(\frac{t}{t_f}\right)^{1/2}. \tag{5.18}$$

5.3 Scaling analysis for ramp heating

For the case with the ramp heating temperature boundary condition, a set of scaling results has been produced in Chapter 3 for an inclined thermal boundary layer. As soon as the heating boundary condition applied on the inclined wall, a thermal boundary layer starts to develop with the scale $\kappa^{1/2}t^{1/2}$. The transient velocity scale inside the boundary layer is given from (3.13) by

$$u_r \sim \frac{ARaPr}{(1+Pr)(1+A^2)^{1/2}}\left(\frac{t}{h^2/\kappa}\right)\left(\frac{t}{t_p}\right)\left(\frac{\kappa}{h}\right). \tag{5.19}$$

This scale is valid until the quasi-steady time if the ramp time is larger than the quasi-steady time or until the ramp is finished if the ramp time is shorter than the steady state time.

It is found in Chapter 3 for the case of inclined flat plate that the steady state scales for the ramp heating boundary condition of time, velocity and the boundary layer thickness are exactly the same as those for the sudden heating boundary condition if the ramp time is shorter than the steady state time. However, if the ramp time is longer than the quasi-steady time, then the quasi-steady time, the thermal layer thickness and velocity scales from (3.15), (3.17) and (3.18) are given respectively by

$$t_{sr} \sim \frac{(1+Pr)^{1/3}(1+A^2)^{1/3}}{A^{2/3}Ra^{1/3}Pr^{1/3}}\left(\frac{t_p}{h^2/\kappa}\right)^{1/3}\left(\frac{h^2}{\kappa}\right), \tag{5.20}$$

$$\delta_{Tr} \sim \frac{h(1+Pr)^{1/6}(1+A^2)^{1/6}}{A^{1/3}(RaPr)^{1/6}}\left(\frac{t_p}{h^2/\kappa}\right)^{1/6}, \tag{5.21}$$

and

$$u_{sr} \sim \frac{(RaPr)^{1/3}(1+A^2)^{1/6}}{A^{1/3}(1+Pr)^{1/3}}\left(\frac{h^2/\kappa}{t_p}\right)^{1/3}\left(\frac{\kappa}{h}\right). \tag{5.22}$$

After the quasi-steady time the thermal boundary layer develops according to the scale in the quasi-steady mode (from 3.20)

$$\delta_{Tq} \sim \frac{h(1+A^2)^{1/4}}{A^{1/2}Ra^{1/4}}\left(\frac{t_p}{t}\right)^{1/4}, \tag{5.23}$$

and the velocity grows according to the scale from (3.21)

$$u_q \sim Ra^{1/2}\left(\frac{\kappa}{h}\right)\left(\frac{t}{t_p}\right). \tag{5.24}$$

These two scales are valid until the ramp is finished. After the ramp is finished the boundary layer does not know that it comes from a ramp function. Note that the details of the development of these scales are described in Chapter 3.

In addition of those, for the attic space, a heat transfer scaling at different times of boundary layer development in a form of a Nusselt number has been developed as follows:

5.3.1 Heat transfer scaling for ramp heating

Since initially the temperature on the inclined wall is changing with time, the temperature difference between the wall and the interior is also changing with time up to the time when the ramp is finished. Therefore, the temperature difference is constant (maximum) after the ramp is finished. We may consider the maximum temperature difference or the transient temperature difference in the Nusselt number definition. Firstly, if we consider the temperature difference, ΔT as the maximum then the local Nusselt number on the inclined surface during the boundary-layer development stage is

$$Nu_X \sim \frac{\left(\dfrac{\partial T}{\partial y}\right)}{\dfrac{\Delta T}{h}} \sim \frac{\Delta T}{\delta_T} \times \frac{h}{\Delta T} \sim \frac{h}{\delta_T} \sim \frac{h}{\kappa^{1/2}t^{1/2}}. \tag{5.25}$$

Using (3.15), the average quasi-steady state Nusselt for the whole boundary layer is given by

$$Nu_{sr} \sim \frac{1}{L}\int_0^L Nu_X dx \sim \frac{A^{1/3}Ra^{1/6}Pr^{1/6}}{(1+Pr)^{1/6}(1+A^2)^{1/6}}\left(\frac{h^2/\kappa}{t_p}\right)^{1/6}. \tag{5.26}$$

After the quasi-steady state time, the boundary layer does not grow as $\kappa^{1/2}t^{1/2}$. It grows according to the scale (3.20). Therefore, the Nusselt number at the quasi-steady state mode is

$$Nu_h \sim \frac{A^{1/2}Ra^{1/4}}{(1+A^2)^{1/4}}\left(\frac{t}{t_p}\right)^{1/4}. \tag{5.27}$$

However, if we consider the instantaneous temperature difference then the local Nusselt number on the inclined surface during the boundary-layer development stage is

$$Nu_X \sim \frac{\left(\frac{\partial T}{\partial y}\right)}{\frac{\Delta T}{h}} \sim \frac{\Delta T t}{\delta_T t_p} \times \frac{h}{\Delta T} \sim \frac{ht}{\delta_T t_p} \sim \frac{ht^{1/2}}{\kappa^{1/2} t_p}. \tag{5.28}$$

At the quasi-steady state time predicted by (3.15), the local Nusselt number is

$$Nu_{ins} \sim \frac{1}{L} \int_0^L Nu_X \, dx \sim \frac{(1+Pr)^{1/6}(1+A^2)^{1/6}}{A^{1/3} Ra^{1/6} Pr^{1/6}} \left(\frac{h^2/\kappa}{t_p}\right)^{5/6}. \tag{5.29}$$

Similarly to (5.27), we may derive the Nusselt number at the quasi-steady state mode as

$$Nu_h \sim \frac{A^{1/2} Ra^{1/4}}{\left(1+A^2\right)^{1/4}} \left(\frac{t}{t_p}\right)^{5/4}. \tag{5.30}$$

5.3.2 Heating up scale of the entire cavity

Similar to the sudden heating case, once the boundary layer is fully developed by the ramp heating boundary condition, the fluid in the enclosure is gradually stratified by the hot fluid ejected from the boundary layer, starting from the top of the cavity, and this heating up stage continues until the whole body of fluid has the same temperature as that imposed on the incline walls of the attic space. The appropriate parameters characterizing this heating up stage are the time, t_f for the fluid to be fully heated up and the average Nusselt number on the heating wall.

Let us consider an arbitrary moment t during the heating up stage. At that moment, the fluid inside the enclosure is assumed to consist of two layers with the location $x = x_i$ as the interface. The bottom layer is at the original temperature, T_c, whereas the top layer is at the wall temperature T_h.
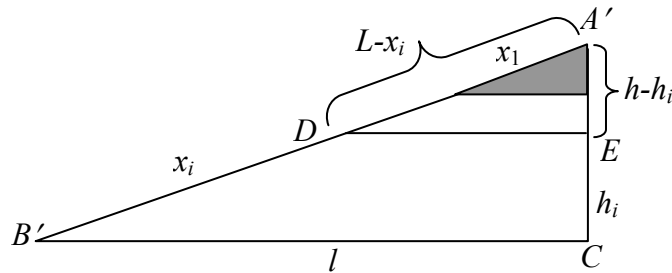
Figure 5.5 Schematic of heating-up process for ramp heating.

The total volume of the enclosure *A′B′C* is (Figure 5.5)

$$V_{\text{total}} = \frac{1}{2}lh. \tag{5.31}$$

During the transient time the volume filled by the hot fluid is

$$V_{\text{steady}} \sim u_{sr}\delta_{Tr}t_{sr}. \tag{5.32}$$

which gives

$$V_{\text{steady}} \sim \frac{h^2(1+Pr)^{1/6}(1+A^2)^{2/3}}{A^{4/3}Ra^{1/6}Pr^{1/6}}\left(\frac{t_p}{h^2/\kappa}\right)^{1/6}. \tag{5.33}$$

The ratio of the above two volumes is

$$\frac{V_{\text{steady}}}{V_{\text{total}}} \sim \frac{(1+Pr)^{1/6}(1+A^2)^{2/3}}{A^{1/3}Ra^{1/6}Pr^{1/6}}\left(\frac{t_p}{h^2/\kappa}\right)^{1/6}. \tag{5.34}$$

The maximum ratio of the volume filled with hot fluid at the transient stage to the total volume of the cavity is less than 0.08 for the ranges of *Ra*, *A* and other parameters considered here. Therefore, the quasi-steady time can be ignored for the calculation of the filling box time.

Suppose the ramp is finished when the interface is at $x = x_1$ measured from *A*, for the case when the ramp time is longer than the quasi-steady time ($t_p > t_{sr}$). Let us calculate the volume of the hot portion filled by the time $t = t_p$. The volume of the heated portion is

$$V_1 = \frac{1}{2}lh\left(\frac{x_1}{L}\right)^2. \tag{5.35}$$

The flux at the time $t = t_p$ is

$$u_q\delta_T t\Big|_{t=t_p} = \frac{\kappa A^{1/2}Ra^{1/4}(1+A^2)^{1/4}}{h^2}t_p. \tag{5.36}$$

Mass conservation then requires

$$\frac{1}{2}lh\left(\frac{x_1}{L}\right)^2 \sim \frac{\kappa Ra^{1/4}(1+A^2)^{1/4}}{A^{1/2}}t_p$$

$$\Rightarrow x_1 \sim L\left[\frac{\kappa A^{1/2}Ra^{1/4}(1+A^2)^{1/4}}{h^2}t_p\right]^{1/2}. \tag{5.37}$$

Therefore, the volume, V_1 is filled up with hot fluid by the time $t = t_p$. The rest of the volume will be filled up after the ramp is finished. At $t = t_p$ the thermal boundary layer thickness and the velocity scales from (5.23) and (5.24) respectively are

$$\delta_p \sim \frac{h(1+A^2)^{1/4}}{A^{1/2}Ra^{1/4}}, \tag{5.38}$$

and

$$u_p = Ra^{1/2}\left(\frac{\kappa}{h}\right). \tag{5.39}$$

The rest of the volume after ramp is finished is

$$\frac{1}{2}lh\left(1-\frac{x_i}{L}\right)^2 - \frac{1}{2}lh\left(\frac{x_1}{L}\right)^2 \sim \frac{A}{1+A^2}\left[(L-x_i)^2 - x_1^2\right].$$

Again from the mass conservation law we have

$$\frac{A}{1+A^2}\left[(L-x_i)^2 - x_1^2\right] \sim u_p\delta_p t. \tag{5.40}$$

Applying (5.38) and (5.39) we have,

$$\frac{A}{1+A^2}\left[(L-x_i)^2 - x_1^2\right] \sim \frac{\kappa Ra^{1/4}(1+A^2)^{1/4}}{A^{1/2}}t \tag{5.41}$$

$$\Rightarrow x_i \sim L - \left[x_1^2 + \frac{\kappa Ra^{1/4}(1+A^2)^{5/4}}{A^{3/2}}t\right]^{1/2}. \tag{5.42}$$

Recognizing that for $t = t_r$, $x_i = 0$, therefore,

$$t_r \sim \frac{\left[h^2(1+A^2) - A^2 x_1^2\right]}{A^{1/2}\kappa Ra^{1/4}(1+A^2)^{5/4}}, \tag{5.43}$$

where $L = (h/A)(1+A^2)^{1/2}$

However, if the enclosure is heated up before the ramp is finished then

$$\frac{h^2}{2A}\left(1-\frac{x_i}{L}\right)^2 \sim u_{sr}\delta_{sr}t. \tag{5.44}$$

Applying (5.22) and (5.21) we have,

$$\Rightarrow x_i \sim L\left[1 - \frac{\kappa^{5/12}(1+A^2)^{1/6}A^{1/6}(RaPr)^{1/12}}{h^{5/6}(1+Pr^2)^{1/12}t_p^{1/12}}t^{1/2}\right]. \tag{5.45}$$

And the heating-up time is then given by

$$t_{r'} \sim \frac{(1+Pr)^{1/6}t_p^{1/12}}{(1+A^2)^{1/3}A^{1/3}(RaPr)^{1/6}}\left(\frac{t_p}{h^2/\kappa}\right)^{1/6}\left(\frac{h^2}{\kappa}\right). \tag{5.46}$$

It is apparent from (5.26) that the instantaneous Nusselt number, *Nu* at the heating up stage is

$$Nu \sim \left(\frac{x_i}{L - x_1} \right) Nu_p. \qquad (5.47)$$

Using (5.42) and (5.43), we have

$$\frac{Nu}{Nu_p} \sim 1 - \left(\frac{t}{t_r} \right)^{1/2} \qquad for\ t > t_p, \qquad (5.48)$$

where Nu_p is the Nusselt number at the time, $t = t_p$

$$Nu_p \sim \frac{Ra^{1/4} A^{1/2}}{\left(1 + A^2 \right)^{1/4}}. \qquad (5.49)$$

In the following sections, the above scaling relations are validated against the numerical simulation. However grid and the time step dependence tests must first be performed to ensure the accuracy of the numerical results. Two-dimensional numerical simulations have been carried out in this study. For this purpose, an isosceles triangular domain is considered, and a Cartesian coordinate system is adopted, which is shown in Figure 5.1.

5.4 Grid and time step dependence test

An accurate and reliable numerical result depends on the resolution and distribution of the meshes inside the computational domain. In some regions in the domain we may need to distribute a significant number of meshes in order to resolve true physical flow features (e.g boundary layers). The results may be inaccurate if the mesh is not distributed properly or the number of mesh nodes inside the domain is insufficient. Unfortunately, it is difficult to accurately determine the locations of significance before the calculation is actually carried out, however we may use our previous knowledge to locate the regions of large flow gradients. Although an increase in the grid resolution will generally increase the numerical accuracy, it also increases the usage of computing resources for both calculation and post-processing. Therefore, it is necessary to compromise between the numerical accuracy and computing efficiency when considering the grid used for the simulations.

Since the thermal boundary layer develops adjacent to the inclined heated walls of the attic space and the gradients of all parameters are very strong near the two bottom tips, finer meshes need to be distributed near the walls and two bottom tips compared to other regions. An expansion factor may be adopted to distribute the non

uniform mesh. However, the expanding factor of grid is usually limited in order to ensure that the solution is not degraded. A factor of up to 10% may be used according to Patterson and Armfield (1990).
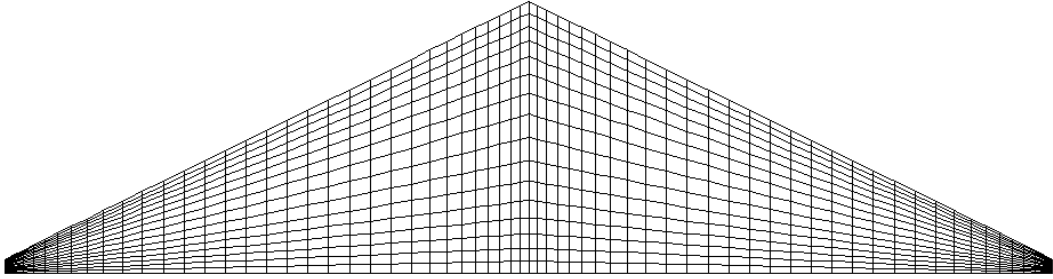
Figure 5.6 A sample mesh showing the major features of the non-uniform symmetric meshes adopted in this study.

The distribution of mesh has been shown for three different aspect ratios in Tables 5.1, 5.2 and 5.3. We divide the whole domain into two by the symmetry line. Then both left and right portions of the domain are again divided horizontally into three equal portions. The middle portion of the three sub region is mapped uniformly in the horizontal direction (see Figure 5.6), and the other two sub-regions are mapped non-uniformly in the horizontal direction. The symmetry line is mapped non-uniformly in the vertical direction with finer meshes near the bottom and apex. However, a uniform mesh has been distributed vertically on two bottom tips (tips are cut by 5%). A schematic of grid distribution has been shown in Figure 5.6.

The initial and boundary conditions for the numerical simulations are also specified as the air in the enclosure is initially motionless and isothermal with a uniform temperature of T_c. All the interior surfaces of the enclosure are assumed rigid and no slip.

Table 5.1 Grid distribution for aspect ratio 1.0.

Grid (H× L)	In the horizontal direction			In the vertical direction		Time step
	left(EF)	middle	right(EF)	bottom tip	symmetry line (EF)	
180 × 60	28(1.030)	34	28(1.02)	60	40(1.030)	0.004
270 × 90	42(1.025)	51	42(1.02)	90	60(1.025)	0.003
360 × 120	56(1.020)	68	56(1.02)	120	80(1.020)	0.002
540 × 180	84(1.016)	102	84(1.02)	180	120(1.016)	0.0015

EF: Expansion factor; H: horizontal grid; L: vertical grid

Table 5.2 Grid distribution for aspect ratio 0.5.

Grid (H× L)	In the horizontal direction			In the vertical direction		Time step
	left(EF)	middle	right(EF)	bottom tip	symmetry line (EF)	
160 × 40	25(1.030)	30	25(1.02)	40	40(1.030)	0.004
240 × 60	38(1.025)	44	38(1.02)	60	60(1.025)	0.003
320 × 80	50(1.020)	60	50(1.02)	80	80(1.020)	0.002
480 × 120	75(1.016)	90	75(1.02)	120	120(1.016)	0.0015

Table 5.3 Grid distribution for aspect ratio 0.2.

Grid (H× L)	In the horizontal direction			In the vertical direction		Time step
	left(EF)	middle	right(EF)	bottom tip	symmetry line (EF)	
180 × 45	30(1.030)	30	30(1.02)	45	45(1.030)	0.004
280 × 70	45(1.025)	50	45(1.02)	70	70(1.025)	0.003
360 × 90	60(1.020)	60	60(1.02)	90	90(1.020)	0.002
560 × 140	95(1.016)	90	95(1.02)	140	140(1.016)	0.0015

Grid and time step dependence tests have been conducted for the numerical procedures described earlier for the highest Rayleigh number case for both boundary conditions (sudden heating and ramp heating). It is expected that the mesh selected for the highest Rayleigh number will also be applicable for all lower Rayleigh numbers. The time steps have been chosen in such a way that the CFL (Courant-Freidrich-Lewy) number remains the same for all meshes.

Four different meshes for each aspect ratio, i.e. 180×60, 270×90, 360×120 and 540×180 for *A* = 1.0, 160×40, 240×60, 320×90 and 480×120 for *A* = 0.5 and 180×45, 280×70, 360×90 and 560×140 for *A* = 0.2 have been tested for the case of sudden heating boundary condition.

The time histories of the calculated maximum velocity parallel to the sloping wall for different slopes with the four different meshes are plotted in Figure 5.7 for the case of the sudden heating boundary condition. It is seen in the figure that all solutions indicate three stages of the flow development, an initial growth stage, a transitional

stage and a steady state stage. In the initial and steady state stage, the four solutions follow each other closely (except for the solution with the coarsest mesh 160×40 for A = 0.5, which deviates slightly from the other three meshes in Figure 5.7(b). The transitional stage is characterized by a single overshoot. The time to reach the steady state is around 2.0s, 1.3s and 6.5s for A = 1.0, 0.5 and 0.1 respectively. The maximum variation of the velocity between the coarsest and finest meshes for A = 0.5 is 5.35%. However, the maximum variation among the other three finer meshes is only 1.18%. The maximum variations of the velocity between the coarsest and finest meshes for A = 1.0 and 0.2 are 0.66% and 1.07% respectively. Accordingly, the mesh 320 × 90 for A = 0.5 and 360× 120 and 360× 90 for aspect ratios A = 1.0 and 0.2 respectively are adopted for the present simulations.

Mesh and time step dependence tests have also been conducted for the ramp heating boundary condition to ensure the accuracy of the numerical solutions. The same meshes as the sudden heating boundary condition have been considered here for three different aspect ratios.
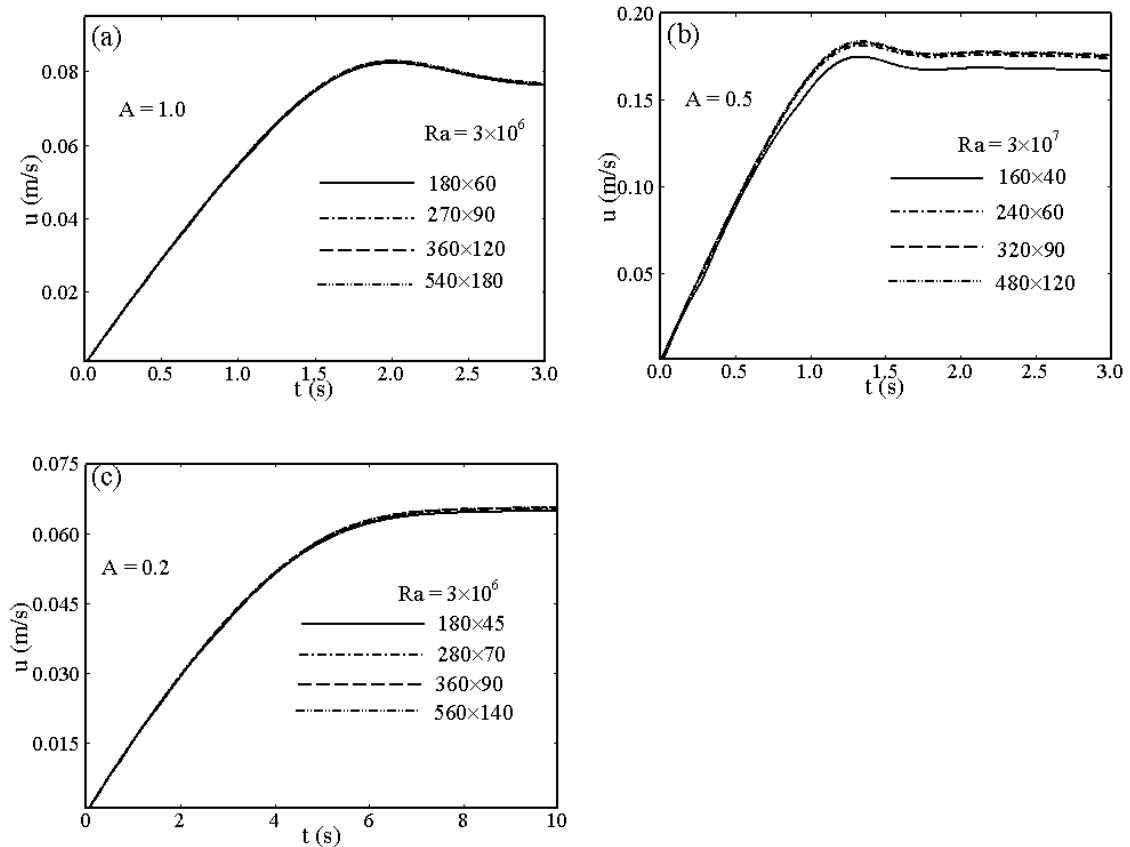
Figure 5.7 Maximum velocity parallel to the left inclined wall at its mid point of four
different meshes for each A = 1.0, 0.5 and 0.2 and Pr = 0.72 for sudden heating.
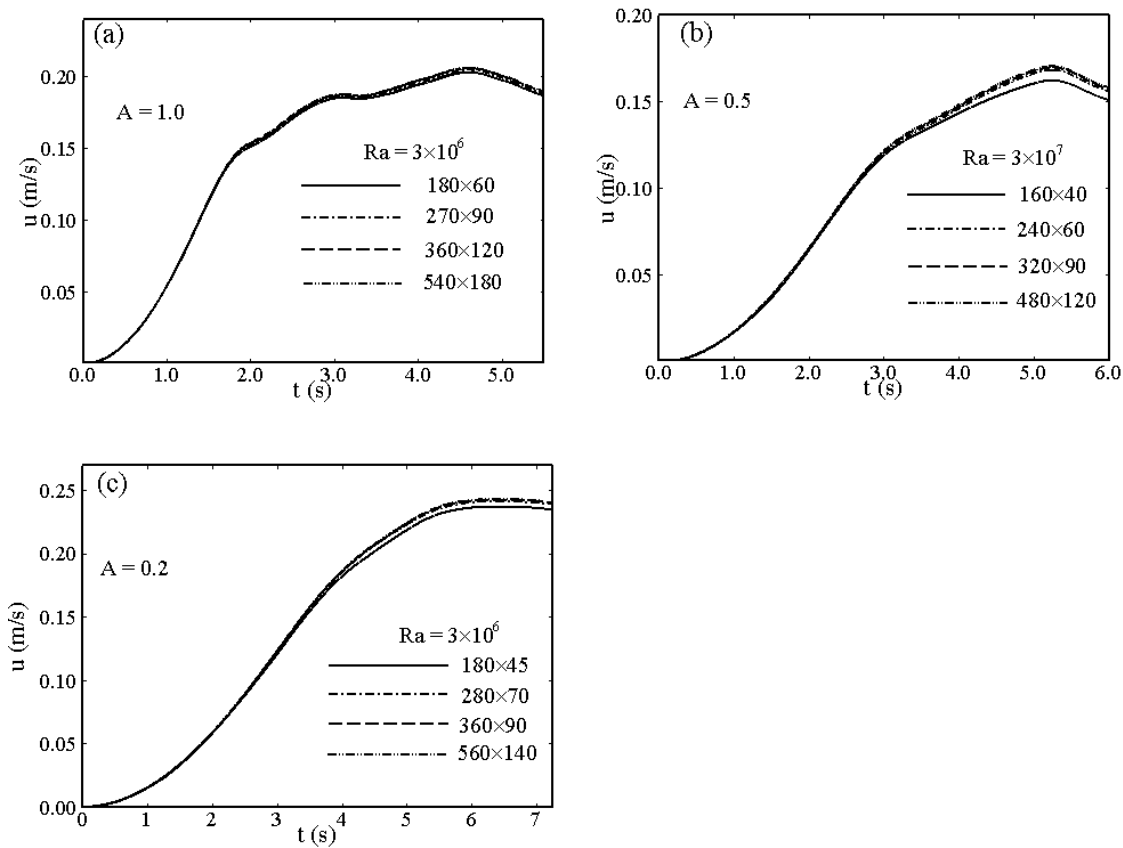
Figure 5.8 Maximum velocity parallel to the left inclined wall at its mid point of four different meshes for each *A* = 1.0, 0.5 and 0.2 and *Pr* = 0.72 for ramp heating.

Figure 5.8 shows the time series of the maximum velocity parallel to the inclined surface calculated on the line normal to the surface at the mid point for three different aspect ratios under the ramp heating boundary condition for *Pr* = 0.72. These velocities are calculated with four different meshes for each aspect ratio. The ramp time has been set to 5s for all the cases. As is mentioned in the scaling analysis, the ramp time may be either longer or shorter than the steady state time for the boundary layer. If the ramp time is longer than the quasi-steady time, then after the quasi-steady time the velocity continues to increase as the inclined wall is still being heated. However, the growth rate of the velocity is smaller than the velocity during the earlier phase. It is seen in this figure that at about 1.8s, 2.75s and 3.8s for *A* = 1.0, 0.5 and 0.2 respectively, the boundary layer becomes quasi-steady. However, the velocity still increases as the temperature on the wall is still increasing. At *t* = 5s, the ramp finishes and the boundary layer becomes completely steady. This scenario can be seen clearly for the inclined flat plate described in Chapter 3 (see Figure 3.4). However, as it is a

closed triangular domain, a return flow from the top breaks down the boundary layer as time passes.

The maximum variation of the velocity between the coarsest and finest meshes for *A* = 1.0 is 1.78%. The maximum variations of the velocity between the coarsest and finest meshes for *A* = 0.5 and 0.2 are 5.78% and 2.55% respectively. However, the maximum variations among the three fine meshes are 1.29% and 0.75% for *A*=0.5 and 0.2 respectively. Accordingly, the mesh size 360×120, 320×90 and 360×90 are adopted for *A* = 1.0, 0.5 and 0.2 respectively for the whole range of simulations.

Four different time steps have been tested along with the four different meshes for each aspect ratio (see Table 5.1, 5.2 and 5.3). The time step size 0.002s has been adopted for simulation for both sudden heating and ramp heating boundary condition. With the selected meshes and time steps, the maximum CFL numbers are 0.013, 0.14 and 0.14 for *A* = 0.2, 0.5 and 1.0 respectively at the steady stage.

5.5 Flow development in different regime for sudden heating

5.5.1 Conduction regime

The numerical results for a low Rayleigh number have been shown in Figure 5.9 with $Pr = 0.72$, $Ra = 10$ and $A = 0.5$ for the regime $Ra < (1+Pr)(1+A^2)/(A^2Pr)$. The temperature contours and streamlines at $t/t_s = 0.156$ are plotted in Figures 5.9(a) and 5.9(b), respectively. In this regime the thermal boundary layer expands to the entire domain. The minimum temperature in the domain is 298.94K. However, the initial temperature inside the domain was set to 295K. Therefore, the entire flow domain has been heated up and the thermal boundary layer is not distinct in this regime. Moreover, there is no steady state of the flow inside the cavity as it continues to be heated up as time passes and may become isothermal. There are two cells in the streamlines on both sides of the center line of the attic where the direction of the left cell is clockwise and the right cell is anti-clockwise.
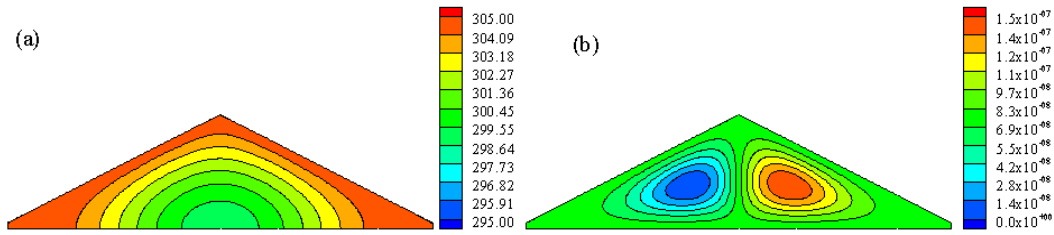
Figure 5.9 (a) temperature contours and (b) streamlines with *Pr* = 0.72, *Ra* = 10 and
A = 0.5.

5.5.2 Convection regime

The numerical results of a relatively high Rayleigh number for this regime with *Pr* = 0.72, *Ra* = 3.0 × 10^6 and *A* = 0.5 at *t*/*t*$_s$ = 7.0 are given in Figure 5.10 for the regime *Ra* > (1+*Pr*)(1+*A*^{2})/(*A*^{2}*Pr*). The temperature contours are presented in Figure 5.10(a) and the streamlines are presented in Figure 5.10(b). We notice that the convection increases significantly in this regime as the Rayleigh number increases. The steady state thermal boundary layers are distinct. The hot fluid travels through the boundary layers adjacent to both inclined walls and meet near the apex. The flow then has no other choice but to come downwards. However the interior temperature is lower than the temperature in the downward flow. Therefore, the hot fluid on top and the cold fluid in the interior form a horizontal stratification. This stratification process eventually heats up the entire cavity.
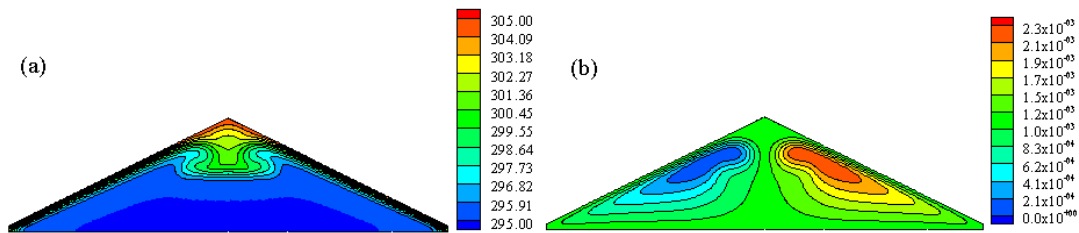
Figure 5.10 (a) temperature contours and (b) streamlines with *Pr* =0.72, *Ra* = 3.0 × 10^6
and *A* = 0.5.

5.6 Flow development in different regime for ramp heating

5.6.1 Ramp time shorter than steady time

Figure 5.11 shows the temperature contours and the streamlines for $Pr = 0.72$, $Ra = 5.0$ and $A = 0.5$ at time $t/t_s = 0.147$ for the regime $Ra < (1+Pr)(1+A^2)h^4/[A^2Pr\kappa^2 t_p^2]$. The ramp time for this case is $t_p/t_{sr} = 3.68\times10^{-3}$. Figures 5.11(a) presents the temperature contours and Figure 5.11(b) presents the corresponding streamlines. As soon as the heating starts the boundary layer develops and expands from the heated walls and reaches to the bottom surface. Two circular cells are seen in the streamlines (Figure 5.11b) with a clockwise circulation at the left side and an anti-clockwise circulation at the right side.
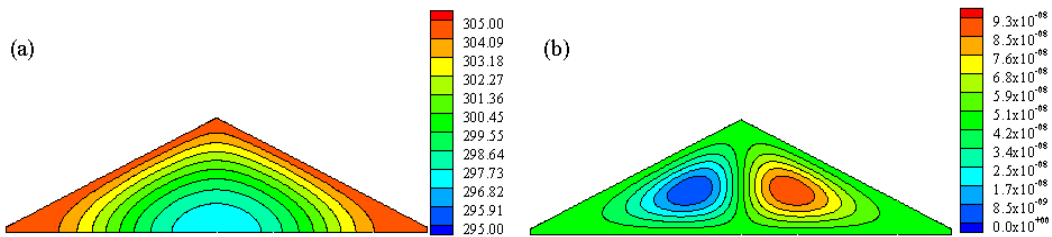
Figure 5.11 (a) temperature contours and (b) streamlines with $Pr = 0.72$, $Ra = 5.0$ and $A = 0.5$.

5.6.2 Ramp time longer than steady time

A representative Rayleigh number for this flow regime ($Ra > (1+Pr)(1+A^2)h^4/[A^2Pr\kappa^2 t_p^2]$) has been chosen as $Ra = 6.0\times10^6$. The temperature contours and the stream lines have been shown in Figure 5.12 at different times of the boundary layer development for aspect ratio $A = 0.5$. The ramp time, selected for this problem, is $t_p/t_{sr} = 1.57$.
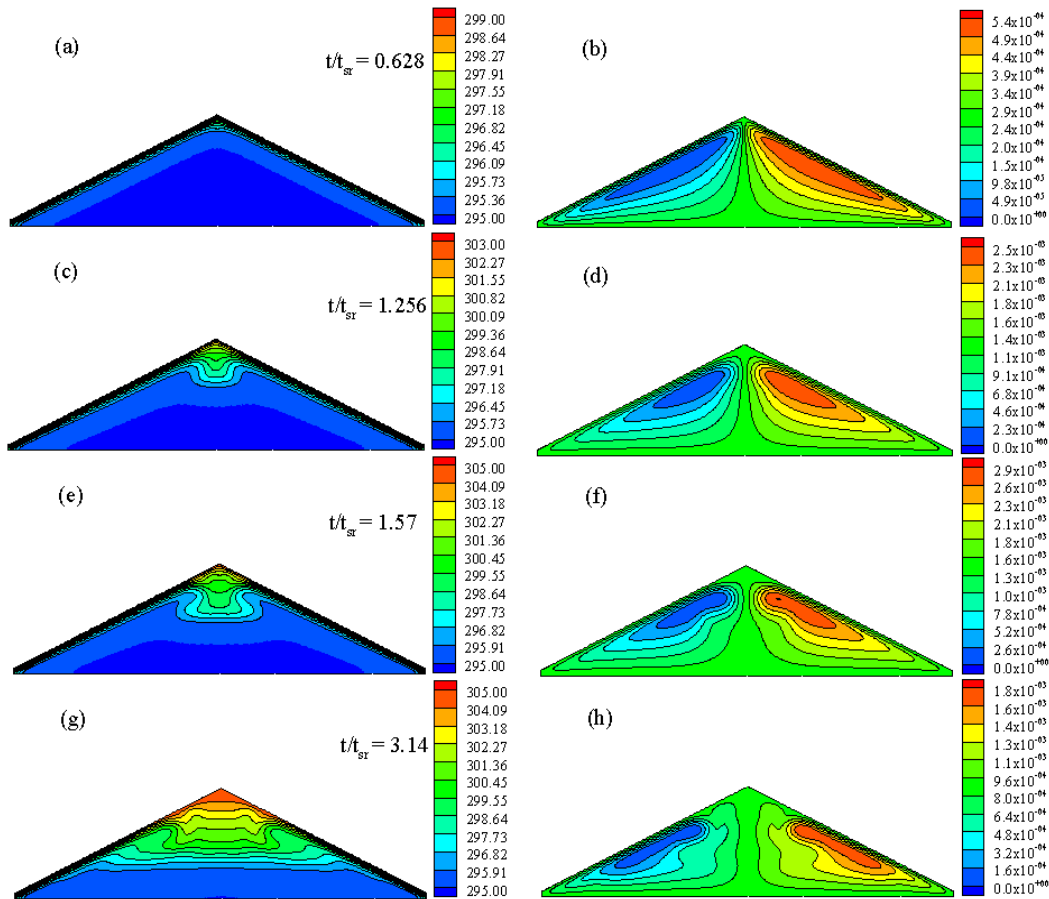
Figure 5.12 Temperature contours (a, c, e, g) and streamlines (b, d, f, h) with *Pr* =0.72, *Ra* = 6.0 × 10⁶ and *A* = 0.5 at different times.

The isotherms and stream lines of Figures 5.12(a, b) are at t/t_{sr} = 0.628, which is the time before the flow becomes quasi-steady; Figures 5.12(c, d) are at t/t_{sr} = 1.256, when the flow is in quasi-steady mode; Figures 5.12(e, f) are at the time when the ramp just finishes (t/t_{sr} = 1.57); and Figures 5.12(g, h) are at time after the ramp is finished (t/t_{sr} = 3.14). It is seen clearly from these figures that initially the boundary layer develops adjacent to the inclined walls of the cavity and moves upwards. However, as time passes, the top of the cavity gradually fills with hot fluid and becomes stratified, where the top portion fluid is hotter than the bottom portion. At the end the entire cavity has been heated up. It is noted that the typical situation of quasi-steady state and the finishing time of ramp can not be identified from these set of isotherms and streamlines.

5.7 Validation of selected scales

The flow features discussed theoretically above are verified on the basis of a complete series of numerical simulations. It is assumed that the fluid contained in the attic space is originally motionless and of a uniform temperature T_c. The cavity is heated from the top by means of sudden and ramp heating boundary conditions of the sloping wall. Throughout this simulation, the horizontal bottom wall is assumed to be adiabatic. The above scales have been developed with an assumption that the flow is symmetric along the symmetry center line of the cavity. Previous studies of attic space have revealed that the flow is indeed symmetric along the center line for the case of heating on the sloping walls.

The detailed validation of the boundary layer development has been discussed in chapter 3 (e.g. velocity scale, thickness scale etc). For brevity, those results are not repeated here. However, heat transfer scales together with steady state time scales have been verified in this chapter. Moreover, the heating-up time scale and the subsequent heat transfer scale at that time have also been verified.

5.7.1 Sudden heating

The heating-up time is determined by the heat flux through the natural convection boundary layer. The hot fluid moves upward along the boundary layers of both inclined walls and meets under the apex of the enclosure. Then it has no choice but to move downward right below the tip, forming a horizontal stratification. This stratified hot fluid fills the enclosure, ultimately reaching the bottom surface at which time the whole enclosure is filled with hot fluid.

Table 5.4 Values of *A* and *Ra* for six runs for sudden heating.

Runs	*A*	*Ra*
1	0.5	1.5×10^7
2	0.5	3.0×10^6
3	0.5	1.5×10^6
4	0.5	6.0×10^5
5	0.2	3.0×10^6
6	1.0	3.0×10^6

In Table 5.4, Runs 1-4 with $Ra = 1.5 \times 10^7$, 3.0×10^6, 1.5×10^6 and 6.0×10^5 while keeping $A = 0.5$ and $Pr = 0.72$ unchanged have been carried out to show the dependence of the scaling relations on the Rayleigh number, Ra; Runs 5-6 and 2 with $A = 0.2$, 1.0 and 0.5 respectively while keeping $Ra = 3.0 \times 10^6$ and $Pr = 0.72$ unchanged have been carried out to show the dependence on the slope of the inclination of the plate. All Rayleigh numbers considered here are in the convection regime.

Figure 5.13 Time series of the average Nusselt number calculated on the left inclined wall. (a) Plot of raw data; (b) Nusselt number versus normalized time; and (c) Normalized Nusselt number versus normalized time.

The numerical results showing the dependence of the instantaneous average Nusselt number Nu on Ra, and A at the boundary-layer development stage and at the heating-up stage are respectively presented in Figure 5.13 and Figure 5.14. Figure 5.13(a) shows the raw data of the time series of the Nusselt number which have been calculated from the left inclined wall of the cavity for different Rayleigh numbers and aspect ratios. It is found that the Nusselt number depends strongly on Ra and A. In

Figure 5.13(b), the time has been normalized with respect to the steady state time of the boundary layer development. We notice that the steady state of the Nusselt numbers fall on a vertical line (long dashed line), which validates the steady state time scale of the boundary layer development (5.2). The normalised Nusselt number with respect to its steady state value is plotted against normalized time with respect to the steady state time scale in Figure 5.13(c). As anticipated, all lines collapse together in one line which confirms the scaling relation (5.6) at the boundary-layer development stage.

The Nusselt number at the heating up time has been plotted in Figure 5.14. Again all lines collapse on a single line which validates the scaling relation (5.18) at the heating up stage. Note that the *x*-axis is on a log scale.
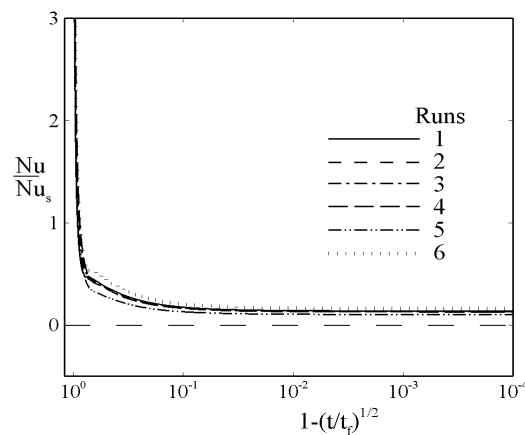
Figure 5.14 Time series of Nusselt number on the left inclined wall for heating-up

stage for sudden heating for six runs.

To verify the heating-up time scale, the temperature has been recorded at the mid point of the bottom surface, which is shown in Figure 5.15. Raw data of the time series of the temperature for different Rayleigh numbers and aspect ratios are plotted in Figure 5.15(a). It is anticipated that initially there is no response of the temperature at the middle point of the bottom surface. As soon as the hot fluid comes from the top and reaches the bottom, the temperature starts to increase. However, this response time is different for different *Ra* and *A*. In Figure 5.15(b), the time is normalised with respect to the heating-up time (5.16) and the temperature has been normalised by the temperature difference. We see that the temperature series response at the same time for different flow parameters. This confirms that the heating-up time scale (5.16) is accurate.

Figure 5.15 Time series of temperature recorded on the mid point of the bottom surface. (a) Plot of raw data; (b) Normalized temperature versus normalized time for sudden heating for six runs.

5.7.2 Ramp heating

Similarly to the sudden heating case, the heating-up time is also determined by the heat flux through the natural convection boundary layer for the ramp temperature boundary condition. Table 5.5 shows the full sets of flow cases considered for the numerical simulation. All Rayleigh numbers considered here are in the regime where the ramp time is longer than the quasi-steady time.

Table 5.5 Values of *A* and *Ra* for the six runs for ramp heating.

Runs	A	Ra
1	0.5	3.0×10^7
2	0.5	1.5×10^7
3	0.5	6.0×10^6
4	0.5	3.0×10^6
5	1.0	3.0×10^7
6	0.2	3.0×10^7

To demonstrate the dependency of the heat flux on time at various stages of boundary development stage, the time series of total heat flux on the left inclined surface of the attic space is plotted in Figure 5.16. It is seen in Figure 5.16(a) that heat flux increases with time and becomes quasi-steady state at about 2s. Since the surface is still receiving heat from the ramp temperature boundary condition, the heat flux increases until the ramp is finished. After the ramp finishes the heat flux suddenly drops and decreases as time increases. We have seen that the Nusselt number scale at the initial stage is the order of $O(t^{1/2})$ (see 5.14). Therefore, in Figure 5.16(b) the heat flux is plotted against $t^{1/2}$ and shows an initial linear growth. However, the Nusselt number scale after the quasi-steady state is of the order $O(t^{5/4})$ (see 5.16). To verify this scale, the heat flux in Figure 5.16(c) is plotted against $t^{5/4}$. The figure shows that after the quasi-steady state the heat flux show a linear growth until the ramp is finished.
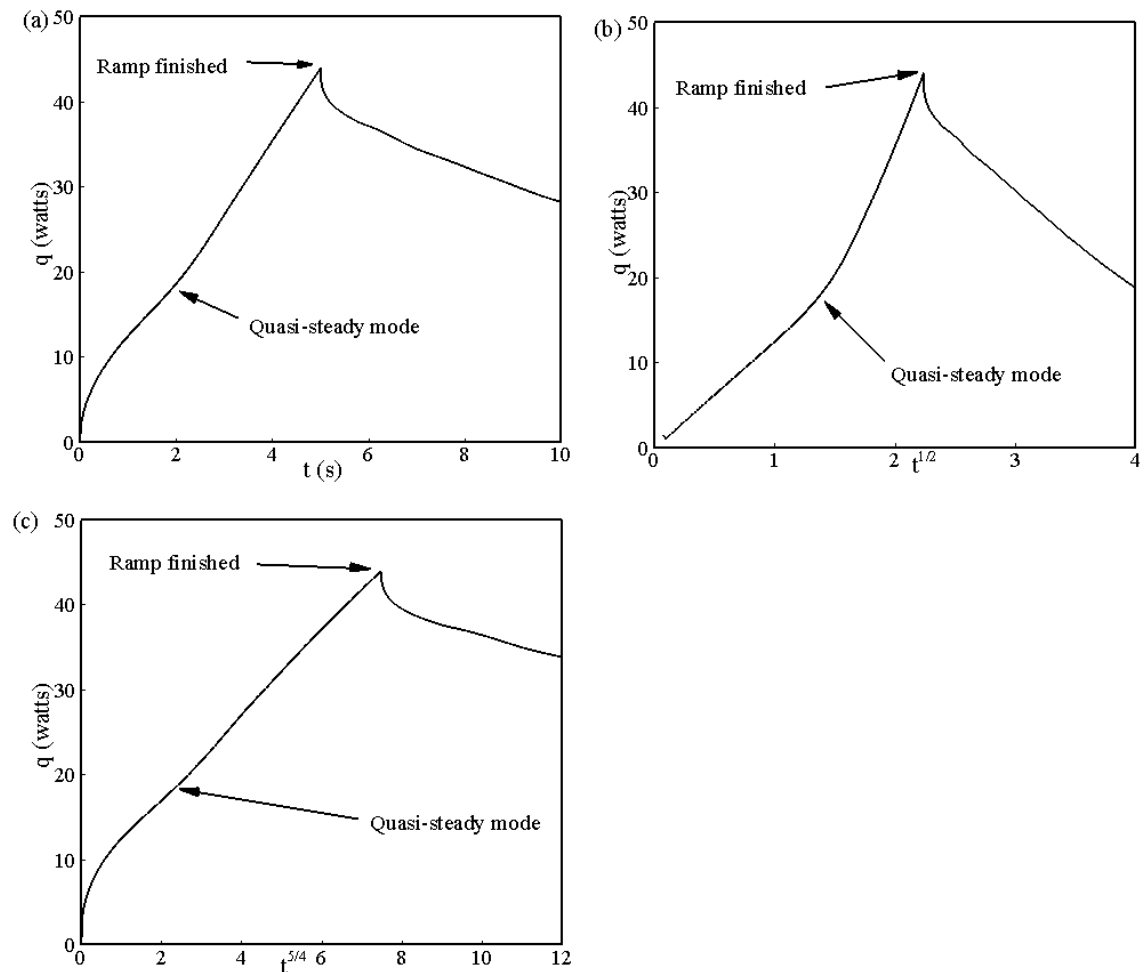
Figure 5.16 Time series of total heat flux on the left inclined surface for $Ra = 4.0 \times 10^7$, $A = 0.5$ and $Pr = 0.72$.

The numerical results showing the dependence of the average Nusselt number, *Nu* on *Ra,* and *A* at the boundary-layer development stage are presented in Figures 5.17 and 5.18. The Nusselt number has been calculated in two different ways; one with reference to the maximum temperature difference (see 5.26) and the other with reference to the instantaneous temperature difference (see 5.29). Figure 5.17(a) shows the raw data of the time series of the Nusselt number which has been calculated from the left inclined wall of the cavity using the maximum temperature difference (ΔT) for different Rayleigh numbers and aspect ratios. It is found the Nusselt number depends strongly on *Ra* and *A*. In Figure 5.17(b), the time has been normalized with respect to the quasi-steady time (5.20) and Nusselt number has been normalised by the scaling value (5.26). It is clear that all lines collapse together until the ramp is finished which validates the quasi-steady time (3.15) and Nusselt number (5.26) scales of the boundary-layer development stage.
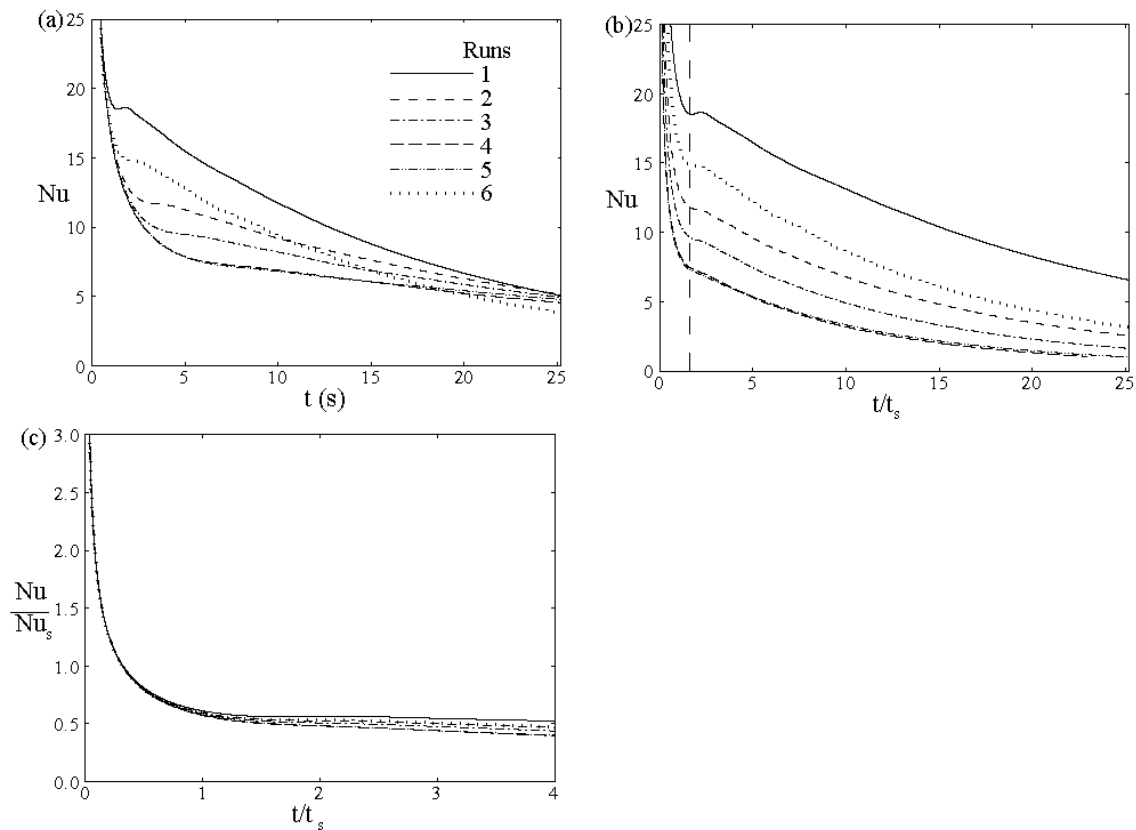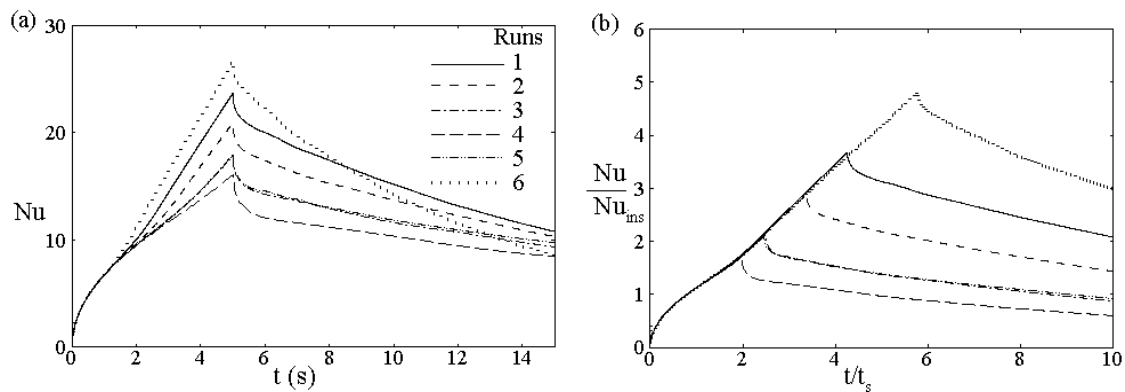

Figure 5.17 Time series of the average Nusselt number calculated on the left inclined wall. (a) Plot of raw data; (b) Normalized Nusselt number versus normalized time for ramp heating for six runs.

In Figure 5.18, the Nusselt number has been calculated using the instantaneous temperature difference ($\Delta T t/t_p$ for $t \leq t_p$). Raw data of the time series of the Nusselt number is plotted in Figure 5.18(a). It is seen that initially the Nusselt number approaches infinity and decreases sharply until the quasi-steady state time. After the quasi-steady state it increases very slowly until the ramp is finished. After the ramp finishes, the Nusselt number again decreases very fast. In Figure 5.18(b), the time has

been normalised by (5.20) and the Nusselt number by (5.29). Again all lines lie together until the ramp is finished, which confirms the scaling relation (5.20) and (5.29).
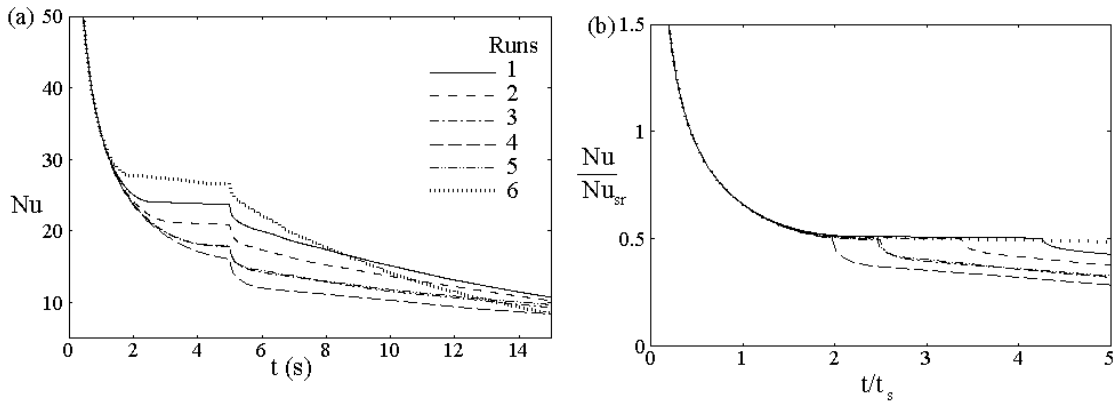
Figure 5.18 Time series of the average Nusselt number calculated on the left inclined wall. (a) Plot of raw data; (b) Normalized Nusselt number versus normalized time for ramp heating for six runs.

The Nusselt number at the heating-up time is plotted in Figure 5.19. Again all lines fall together in a line which validates the scaling relation (5.48) at the heating up stage. Note that the *x*-axis is on a log scale.
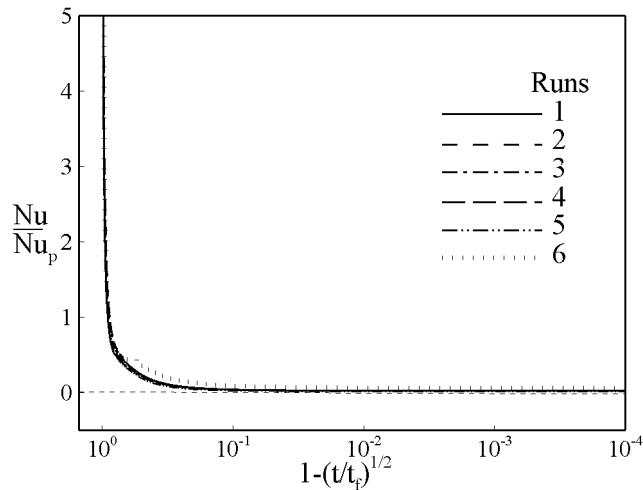
Figure 5.19 Normalized time series of Nusselt number at the heating up stage on the left inclined wall of the cavity for ramp heating for six runs.

To verify the heating-up time scale, the temperature has been recorded at the middle point of the bottom surface and plotted in Figure 5.20. Raw data of the time series of the temperature for different Rayleigh numbers and aspect ratios has been

shown in Figure 5.20(a). It is anticipated that initially there is no response of the temperature at the middle point of the bottom surface. As soon as the hot fluid comes from the top and reaches the bottom, the temperature starts to increase. However, this response time is different for different values of *Ra* and *A*. In Figure 5.20(b), the time is normalised with respect to the heating-up time (5.43) and the temperature has been normalised by the temperature difference. We see that the temperature starts to rise at the same time for different flow parameters. This confirms that the heating-up time scale (5.43) is accurate.
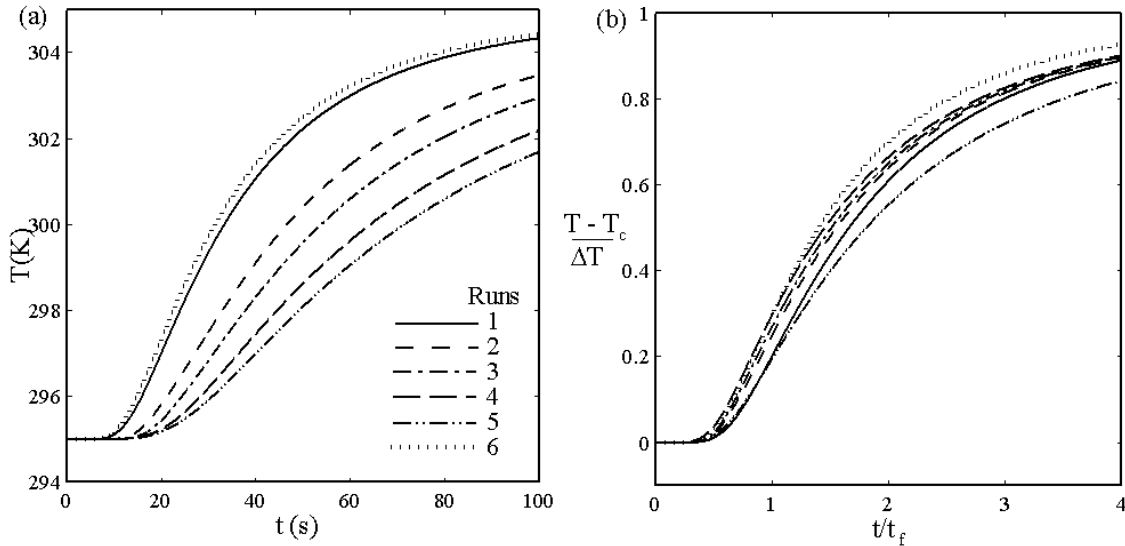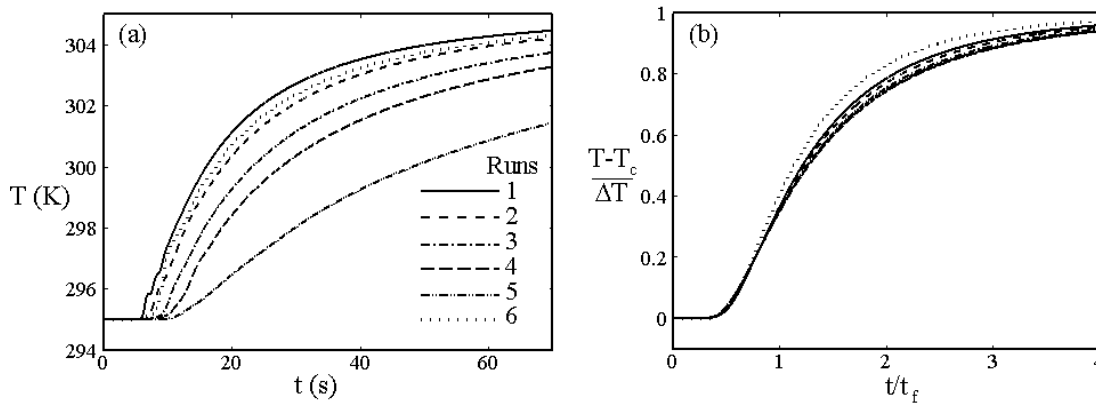

Figure 5.20 Time series of temperature recorded on the mid point of the bottom surface. (a) Plot of raw data; (b) Normalized temperature versus normalized time for ramp heating for six runs.

5.8 Summary

Natural convection adjacent to heated inclined walls of an attic space is examined by scaling analysis and the scales verified by numerical simulation for air (*Pr* = 0.72). It is found that the flow is mainly dominated by four distinct stages for the sudden heating boundary condition, i.e. start-up stage, transitional stage, steady state stage and heating-up stage. The scaling relations are formed based on the established characteristic flow parameters of the maximum velocity inside the boundary layer (u_s), the time for the boundary layer to reach the steady state (t_s), the thermal (δ_T) and viscous (δ_v) boundary layer thicknesses, Nusselt number scale (Nu_s), the heating up time (t_f) and the Nusselt number at the heating-up time. Moreover, some important regimes based on the

Rayleigh number have been established in this chapter. The scaling results agree very well with the numerical simulations.

Furthermore, a temperature boundary condition of a ramp function applied to the inclined walls has also been investigated. The boundary layer flow for this boundary condition depends on the comparison of the time at which the ramp heating is completed with the time at which the boundary layer completes its growth. If the ramp time is long compared with the steady state time, the thermal boundary layer reaches a quasi-steady mode in which the growth of the layer is governed by the thermal balance between convection and conduction. On the other hand, if the ramp is completed before the thermal boundary layer becomes steady, the subsequent growth is governed by the balance between buoyancy and inertia, as for the case of instantaneous heating. Several scaling relations have been established in this study, which include the maximum velocity parallel to the inclined plate inside the boundary layer (u_s), the time for the boundary layer to reach the quasi-steady state (t_{sr}) and the thermal and viscous boundary layer thicknesses (δ_{Tr} and δ_v), Nusselt number scale (Nu_{sr} and Nu_{ins}), the heating up time (t_f) and the Nusselt number at the heating-up time. Like the sudden heating case, some important flow regimes have been established for the ramp heating boundary condition. The scaling results agree very well with the numerical simulations. The comparisons between the scaling relationships and the numerical simulations demonstrate that the scaling results agree very well with the numerical simulations.

6 Natural convection in attics subject to sudden and ramp cooling boundary conditions

In this chapter, the transient natural convection flow in an attic space subject to cooling at the inclined surfaces is examined based on a scaling analysis. The transient phenomenon begins with either sudden or ramp cooling of the upper sloping walls. It is shown that thermal and viscous layers develop adjacent to both walls whose thicknesses increase towards steady-state values. However, these boundary layers are potentially unstable to Rayleigh-Bénard instability if the Rayleigh number exceeds certain critical Rayleigh value. Once the flow becomes unstable the scaling analysis can not be carried further except for providing a prediction of the onset of instability. For a Rayleigh number lower than the critical Rayleigh number, the scaling prediction is similar to that of the heating case.

Scaling analysis for an attic space subject to cooling at the inclined walls has been carried out by Poulikakos and Bejan (1983a). In that study, the working fluid in the attic space was assumed to be water ($Pr > 1$). The authors also assumed that the slope of the inclined wall was very small ($A \rightarrow 0$). However, in a practical situation, the aspect ratio of buildings varies roughly from 0.1 to 1.0. Moreover, numerical verification of the scaling prediction is absent in their work. Scaling analysis for the flow in a wedge with surface cooling has also been investigated by Lei and Patterson (2005) for a reservoir problem, in which case the cooled surface is horizontal. They identified several different regimes of flow development by scaling analysis.

The present chapter consists of two parts concerning an attic space subject to two types of boundary conditions: (i) a sudden cooling boundary condition and (ii) a ramp cooling boundary condition. In both cases the bottom boundary is kept adiabatic and the fluid inside the enclosure is initially isothermal and stationary. The flow response to the sudden and ramp cooling is investigated through combined scaling and numerical procedures. A series of numerical calculations has been carried out for a

range of parameter values to verify the scaling prediction. Details of the numerical procedures can be found in Chapter 2.
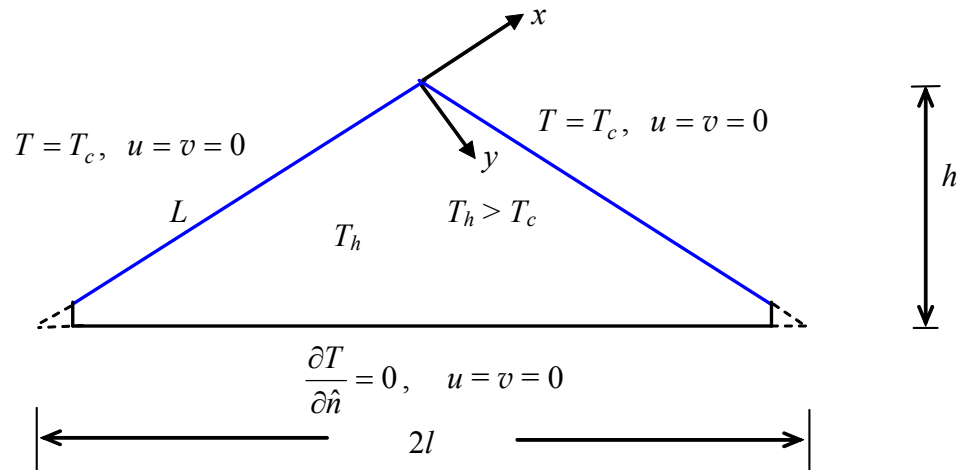
Figure 6.1 The schematic of the geometry and the coordinate system.

Under consideration is the flow behaviour resulting from the cooling of a Newtonian fluid with *Pr* < 1 in a two-dimensional triangular enclosure by unsteady natural convection due to an imposed sudden and ramp cooling temperature on the inclined walls. The physical system sketched in figure 6.1 consists of an enclosure which is filled with fluid having an initial temperature T_h. The height of the enclosure is *h* and the length of the half base is *l*. Therefore, the aspect ratio of the enclosure is $A = h/l$. The length of one sloping wall is $L (=(h/A)(1+A^2)^{1/2})$. At the time $t = 0$, the plate is cooled to T_c suddenly for the first case and over a ramp time, t_p for the second case and thereafter maintained at this temperature.

6.1 Scaling analysis for sudden cooling

Similarly to the heating case described in Chapter 5, the flow for the cooling case is also dominated by two distinct stages of development, i.e. a boundary-layer development stage and a cooling-down stage. The boundary layer development stage is the early stage of the flow development and the cooling-down stage is the stage when the whole cavity is filled with the cold fluid discharged from the boundary layer.

The detailed development of the scaling of the boundary layer for the sudden cooling boundary condition has been discussed in Chapter 4. Initially the thermal boundary layer adjacent to the sloping wall developed according to $\delta_T \sim \kappa^{1/2} t^{1/2}$. We see in Chapter 4 for the case of sudden cooling boundary condition on the inclined flat plate, the transient velocity scale inside the boundary layer is given by (4.1) as

$$u \sim \frac{ARaPr}{(1+Pr)(1+A^2)^{1/2}} \left(\frac{t}{h^2/\kappa}\right)\left(\frac{\kappa}{h}\right),$$
(6.1)

and the steady state time, thickness and velocity scales from (4.2), (4.3) and (4.4) are respectively given by

$$t_s \sim \frac{(1+Pr)^{1/2}(1+A^2)^{1/2}}{ARa^{1/2}Pr^{1/2}}\left(\frac{h^2}{\kappa}\right),$$
(6.2)

$$\delta_T \sim \frac{h(1+Pr)^{1/4}(1+A^2)^{1/4}}{A^{1/2}Ra^{1/4}Pr^{1/4}},$$
(6.3)

and

$$u_s \sim \frac{Ra^{1/2}Pr^{1/2}}{(1+Pr)^{1/2}}\left(\frac{\kappa}{h}\right).$$
(6.4)

The scaling results for heat transfer from the inclined wall of the attic space, measured by a Nusselt number, have been developed as follows.

6.1.1 Heat transfer scales

The instantaneous local Nusselt number on the inclined wall during the boundary layer development stage is given by

$$Nu \sim \frac{\left(\frac{\partial T}{\partial y}\right)_{y=0}}{\frac{\Delta T}{h}} \sim \frac{\Delta T}{\delta_T} \times \frac{h}{\Delta T} \sim \frac{h}{\delta_T} \sim \frac{h}{\kappa^{1/2}t^{1/2}}.$$
(6.5)

This scale is valid until the steady state of the boundary layer is reached. Once the boundary layer becomes steady then using (6.2), the average steady-state Nusselt number of the boundary layer adjacent to the cold inclined wall is given by

$$Nu_s \sim \frac{1}{L}\int_0^L Nudx \sim \frac{A^{1/2}Ra^{1/4}Pr^{1/4}}{(1+Pr)^{1/4}(1+A^2)^{1/4}}.$$
(6.6)

These scales are valid if the boundary layer remains stable.

6.1.2 Cooling down stage

As soon as the cooled temperature boundary condition is applied on the sloping wall, a cold boundary layer starts to develop adjacent to the wall. The cooled fluid inside the boundary layer then moves down the sloping wall with the velocity (6.1) and reaches the bottom tip of the cavity. After that the flow does not have any choice but to move horizontally adjacent to the bottom surface. As a result the interior of the enclosure is gradually filled by the cold fluid ejected from the boundary layer, starting from the bottom of the cavity, and this cooling-down stage continues until the whole cavity is filled with cold fluid. The appropriate parameters to characterize this cooling-down stage are the time t_{fc} for the enclosure to be filled with cooled fluid and the average Nusselt number calculated on the slopping wall.

Let us consider an arbitrary moment, t, during the cooling-down stage. At that moment, the fluid inside the enclosure can be assumed to consist of two layers with the location $x = x_i$ as the interface (see figure 6.2). The top fluid layer is at the initial temperature, T_h whereas the bottom layer has the wall temperature T_c.
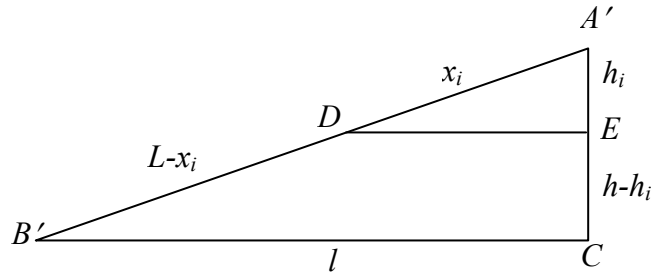
Figure 6.2 Schematic of cooling down process for sudden cooling.

From $\Delta A'B'C$ and $\Delta A'DE$ in figure 6.2, we have,

$$\frac{x_i}{L} = \frac{h_i}{h} \Rightarrow h_i = \frac{hx_i}{L},$$

(6.7)

and

$$\frac{L}{x_i} = \frac{l}{DE} \Rightarrow DE = \frac{lx_i}{L}.$$

(6.8)

Therefore, the area of $DB'CE$ is

$$\frac{1}{2}lh - \frac{1}{2}lh\frac{x_i^2}{L^2} \sim \frac{1}{2}lh\left(1 - \frac{x_i^2}{L^2}\right).$$

(6.9)

It is observed in Chapter 5, for the case of sudden heating boundary condition that the maximum ratio of the volume filled with heated fluid until the steady state time to the total volume is less than 0.095 for the range of *Ra*, *A* and other parameters considered. The same result can be found here for the sudden cooling boundary condition. Therefore, the filling volume at the transient stage is insignificant compared to the total volume.

From the mass conservation law

$$\frac{1}{2}lh\left(1-\frac{x_i^2}{L^2}\right) \sim u_s\delta_T t. \tag{6.10}$$

Applying (6.3) and (6.4) in (6.10) we have,

$$\frac{1}{2}lh\left(1-\frac{x_i^2}{L^2}\right) \sim \frac{\kappa\left(1+A^2\right)^{1/4}Ra^{1/4}Pr^{1/4}}{\left(1+Pr\right)^{1/4}A^{1/2}}t$$

$$\Rightarrow x_i \sim L\left[1-\frac{\kappa A^{1/2}Ra^{1/4}Pr^{1/4}\left(1+A^2\right)^{1/4}}{h^2\left(1+Pr\right)^{1/4}}t\right]^{1/2}. \tag{6.11}$$

The time when the whole enclosure is filled up with cold fluid from bottom ($x_i \sim 0$) is obtained as

$$t_{fc} \sim \frac{\left(1+Pr\right)^{1/4}}{A^{1/2}Ra^{1/4}Pr^{1/4}\left(1+A^2\right)^{1/4}}\left(\frac{h^2}{\kappa}\right). \tag{6.12}$$

Since only the upper part of the sloping wall contributes to the heat transfer during the filling up (or cooling down) process, it is apparent from (6.6) that the instantaneous Nusselt number, *Nu* at the cooling-down stage is

$$Nu \sim \left(\frac{x_i}{L}\right)Nu_s \tag{6.13}$$

Using (6.11) in (6.13), we have

$$\frac{Nu}{Nu_s} \sim \left[1-\frac{\kappa A^{1/2}Ra^{1/4}Pr^{1/4}\left(1+A^2\right)^{1/4}}{h^2\left(1+Pr\right)^{1/4}}t\right]^{1/2}$$

$$\Rightarrow \left(\frac{Nu}{Nu_s}\right)^2 \sim 1-\left(\frac{t}{t_{fc}}\right). \tag{6.14}$$

6.2 Scaling analysis for ramp cooling

For the case with the ramp cooling temperature boundary condition, a set of scaling results has also been produced in Chapter 4 for an inclined flat plate. As soon as the cooling boundary condition is applied on the inclined wall, a thermal boundary layer starts to develop according to the scale $\kappa^{1/2}t^{1/2}$. The transient velocity scale inside the boundary layer is given from (4.15) by

$$u_r \sim \frac{ARaPr}{(1+Pr)(1+A^2)^{1/2}}\left(\frac{t}{h^2/\kappa}\right)\left(\frac{t}{t_p}\right)\left(\frac{\kappa}{h}\right). \tag{6.15}$$

This scale is valid until the quasi-steady time if the ramp time is larger than the quasi-steady state time or until the ramp is finished if the ramp time is shorter than the steady state time.

It is found in Chapter 4 that, for the case of an inclined flat plate, the steady state scales of time, velocity and boundary layer thickness are exactly the same as those for the sudden cooling boundary condition if the ramp time is shorter than the steady state time. However, if the ramp time is longer than the quasi-steady time, then the quasi-steady time, the thermal layer thickness and velocity scales from (4.16), (4.17) and (4.18) are given respectively by

$$t_{sr} \sim \frac{(1+Pr)^{1/3}(1+A^2)^{1/3}}{A^{2/3}Ra^{1/3}Pr^{1/3}}\left(\frac{t_p}{h^2/\kappa}\right)^{1/3}\left(\frac{h^2}{\kappa}\right), \tag{6.16}$$

$$\delta_{Tr} \sim \frac{h(1+Pr)^{1/6}(1+A^2)^{1/6}}{A^{1/3}(RaPr)^{1/6}}\left(\frac{t_p}{h^2/\kappa}\right)^{1/6}, \tag{6.17}$$

and

$$u_{sr} \sim \frac{(RaPr)^{1/3}(1+A^2)^{1/6}}{A^{1/3}(1+Pr)^{1/3}}\left(\frac{h^2/\kappa}{t_p}\right)^{1/3}\left(\frac{\kappa}{h}\right). \tag{6.18}$$

After the quasi-steady time the thermal boundary layer develops according to the scale in the quasi-steady mode (from 4.19)

$$\delta_{Tq} \sim \frac{h(1+A^2)^{1/4}}{A^{1/2}Ra^{1/4}}\left(\frac{t_p}{t}\right)^{1/4}, \tag{6.19}$$

and the velocity scale from (4.20) is

$$u_q \sim Ra^{1/2}\left(\frac{\kappa}{h}\right)\left(\frac{t}{t_p}\right). \tag{6.20}$$

These two scales are valid until the ramp is finished. After the ramp is finished the boundary layer does not know whether it comes from a ramp function or not. Note that the details of the development of these scales have been described in Chapter 4.

In addition to those scales described in Chapter 4, for the attic space, a heat transfer scaling at different times of the boundary layer development in a form of a Nusselt number has been developed in the following section.

6.2.1 Heat transfer scale

Initially the temperature on the inclined wall decreases with time whereas the temperature inside the cavity is fixed (T_h). Therefore, the temperature difference between the wall and the interior increases with time ($\Delta Tt/t_p$) until the ramp is finished. However, the temperature on the wall becomes constant when the ramp is finished and at that time the temperature difference is the maximum. Based on these instantaneous temperature differences we may define the local Nusselt number on the inclined surface during the boundary-layer development stage as;

$$Nu_X \sim \frac{\left(\dfrac{\partial T}{\partial y}\right)_{y=0}}{\dfrac{\Delta T}{h}} \sim \frac{\Delta Tt}{\delta_T t_p} \times \frac{h}{\Delta T} \sim \frac{ht}{\delta_T t_p} \sim \frac{ht^{1/2}}{\kappa^{1/2} t_p}. \tag{6.21}$$

This Nusselt number scale is valid until the quasi-steady time if the ramp time is longer than the quasi-steady time or until the ramp is finished if the ramp time is shorter than the steady state time. For the first situation, when the ramp time is longer than the quasi-steady time, using (6.16) the average quasi-steady Nusselt number on the sloping boundary layer is given by

$$Nu_s \sim \frac{1}{L}\int_0^L Nu_X dx \sim \frac{(1+Pr)^{1/6}\left(1+A^2\right)^{1/6}}{A^{1/3} Ra^{1/6} Pr^{1/6}}\left(\frac{h^2/\kappa}{t_p}\right)^{5/6}. \tag{6.22}$$

After the quasi-steady state the thermal layer thickness does not grow according to $\kappa^{1/2} t^{1/2}$. Instead, it grows according to the scale (6.19). Therefore, the Nusselt number in the quasi-steady mode is

$$Nu_h \sim \frac{A^{1/2} Ra^{1/4}}{\left(1 + A^2\right)^{1/4}} \left(\frac{t}{t_p}\right)^{5/4} . \tag{6.23}$$

For the situation when the ramp time is shorter than the steady state time, the thermal boundary layer grows according to $\kappa^{1/2} t^{1/2}$ before the steady state time and the Nusselt number scale at the steady state time is the same as (6.2) which is the Nusselt number for the case of instantaneous temperature boundary condition. These scales are valid so long as the boundary layer remains stable.

6.2.2 Cooling down stage

Similar to the sudden cooling case, once the boundary layer is fully developed by the ramp cooling boundary condition, the fluid in the enclosure is gradually stratified by the cold fluid ejected from the boundary layer, starting from the bottom of the cavity, and this cooling-down stage continues until the whole body of fluid has the same temperature as that imposed on the inclined walls of the attic space. The appropriate parameters characterizing this cooling-down stage include the time, t_{fr} for the fluid to be fully cooled down and the average Nusselt number on the cooled wall.
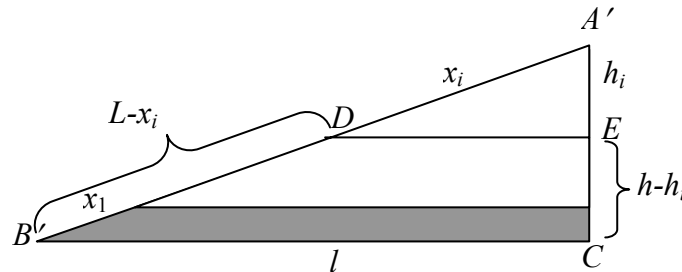
Figure 6.3 Schematic of cooling down process for ramp cooling.

Let us consider any specific moment t during the cooling-down stage when the fluid inside the container can be assumed to consist of two layers with the location $x = x_i$ as the interface (see figure 6.3). The top layer is at the initial temperature, T_h, whereas the bottom layer has the wall temperature T_c.

As it is discussed in Chapter 5 that the maximum ratio of the volume filled with heated fluid during the quasi-steady time to the total volume is less than 0.08 for the range of Ra, A and other parameters considered. The same result can be obtained for the

case of ramp cooling boundary condition. Therefore, the volume filled by the cold fluid during the transient stage may be ignored when calculating the filling box time.

Suppose the ramp is finished when the interface is at $x = x_1$ (x_1 measured from B'), for the case when the ramp time is longer than the quasi-steady time ($t_p > t_{sr}$). Let us calculate the volume (V_1) of the cooled portion filled by the time $t = t_p$. Therefore, the volume of the cooled portion is

$$V_1 = \frac{1}{2}lh\left[1-\left(1-\frac{x_1}{L}\right)^2\right]. \tag{6.24}$$

The flux at time $t = t_p$ is

$$u_q\delta_{Tq}t\Big|_{t=t_p} = \frac{\kappa A^{1/2}Ra^{1/4}\left(1+A^2\right)^{1/4}}{h^2}t_p. \tag{6.25}$$

Mass conservation then requires

$$\frac{1}{2}lh\left[1-\left(1-\frac{x_1}{L}\right)^2\right] \sim \frac{\kappa Ra^{1/4}\left(1+A^2\right)^{1/4}}{A^{1/2}}t_p.$$

$$\Rightarrow x_1 \sim L\left[1-\left(1-\frac{\kappa A^{1/2}Ra^{1/4}\left(1+A^2\right)^{1/4}}{h^2}t_p\right)^{1/2}\right]. \tag{6.26}$$

Therefore, the volume of the enclosure filled with cold fluid is V_1. The rest of the volume will be filled-up after the ramp is finished. At $t = t_p$ the thermal boundary layer thickness and the velocity scales from (6.19) and (6.20) respectively are

$$\delta_p \sim \frac{h\left(1+A^2\right)^{1/4}}{A^{1/2}Ra^{1/4}}, \tag{6.27}$$

and

$$u_p = Ra^{1/2}\left(\frac{\kappa}{h}\right). \tag{6.28}$$

The rest of the volume after ramp is finished is

$$\frac{1}{2}lh\left(1-\frac{x_i^2}{L^2}\right) - \frac{1}{2}lh\left[1-\left(\frac{L-x_1}{L}\right)^2\right] \sim \frac{A}{1+A^2}\left[(L-x_1)^2 - x_i^2\right].$$

Again from the mass conservation law we have

$$\frac{A}{1+A^2}\left[(L-x_1)^2 - x_i^2\right] \sim u_p\delta_p t. \tag{6.29}$$

Applying (6.27) and (6.28) we have,

$$\frac{A}{1+A^2}\left[(L-x_1)^2 - x_i^2\right] \sim \frac{\kappa Ra^{1/4}\left(1+A^2\right)^{1/4}}{A^{1/2}} t \tag{6.30}$$

$$\Rightarrow x_i \sim \left[(L-x_1)^2 - \frac{\kappa Ra^{1/4}\left(1+A^2\right)^{5/4}}{A^{3/2}} t\right]^{1/2}. \tag{6.31}$$

Recognizing that for $t = t_{fr}$, $x_i = 0$, therefore,

$$t_{fr} \sim \frac{\left[h\left(1+A^2\right)^{1/2} - Ax_1\right]^2}{A^{1/2}\kappa Ra^{1/4}\left(1+A^2\right)^{5/4}}, \tag{6.32}$$

where $L = (h/A)(1+A^2)^{1/2}$

If $t_p > h^2/[\kappa A^{1/2}Ra^{1/4}(1+A^2)^{1/4}]$ (see 6.26) the cavity will be filled up with cold fluid discharged from the boundary layer before the end of the ramp. Therefore, using the velocity and the thermal layer thickness scale from the quasi-steady mode the mass conservation law is

$$\frac{h^2}{2A}\left(1 - \frac{x_i^2}{L^2}\right) \sim u_q \delta_{Tq} t. \tag{6.33}$$

Using (6.19) and (6.20), the cooling-down time is

$$t_{fq} \sim \frac{h^{8/7} t_p^{3/7}}{\kappa^{4/7} Ra^{1/7} A^{2/7}\left(1+A^2\right)^{1/7}}. \tag{6.34}$$

For the case when the ramp time is shorter than the steady state time, the filling box time is the same as that obtained for sudden cooling boundary condition.

Since only the upper part of the sloping wall contributes to the heat transfer at any given time, it is apparent from (6.22) that the Nusselt number, Nu at the cooling-down stage is

$$Nu \sim \left(\frac{x_i}{L-x_1}\right) Nu_p. \tag{6.35}$$

Using (6.31), we have

$$\left(\frac{Nu}{Nu_p}\right)^2 \sim 1 - \left(\frac{t}{t_{fr}}\right), \tag{6.36}$$

where Nu_p is the Nusselt number at the time, $t = t_p$, and

$$Nu_p \sim \frac{Ra^{1/4} A^{1/2}}{\left(1+A^2\right)^{1/4}}. \tag{6.37}$$

If the cooling down time is less than the ramp time but greater than the quasi-steady time then the Nusselt number is given by

$$Nu \sim \left(\frac{x_i}{L} \right) Nu_s, \tag{6.38}$$

which is

$$\left(\frac{Nu}{Nu_s} \right)^2 \sim 1 - \left(\frac{t}{t_{fq}} \right). \tag{6.39}$$

In the following section, mesh and time step dependence tests will be carried to ensure the accuracy of the numerical simulations. The numerical results will be used to verify the scaling relations derived above.

6.3 Grid and time step dependence test

The distribution of the computational mesh in the enclosure for three different aspect ratios has been shown in Chapter 5. Mesh and time step dependence tests for sudden and ramp cooling boundary conditions have been conducted here. Two different mesh sizes, 180×60 and 270×90 for $A = 1.0$, three different mesh sizes, 160×40, 240×60 and 320×80, for $A = 0.5$ and three different meshes sizes, 180×45, 280×70 and 360×90, for $A = 0.2$, have been tested for each case of sudden and ramp cooling boundary conditions.
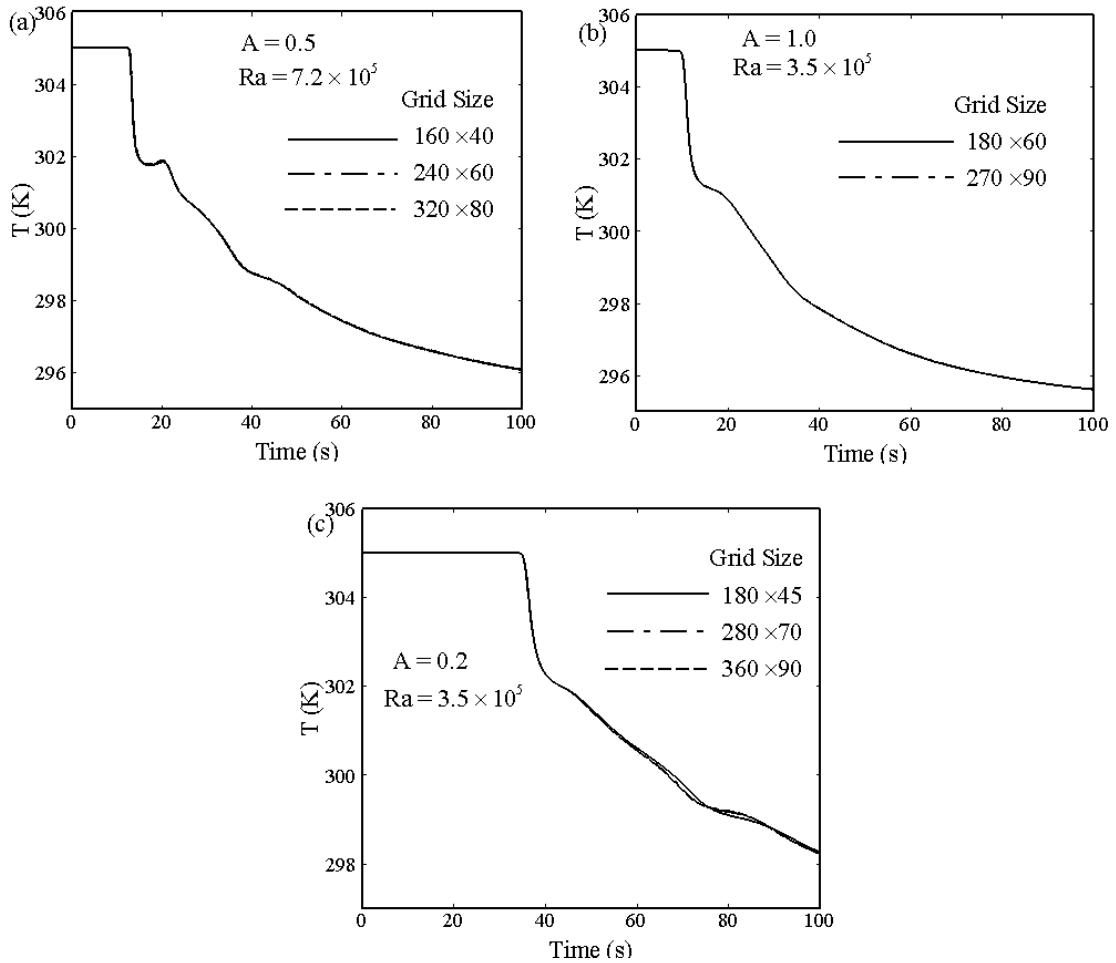
Figure 6.4 Time series of temperature at the mid point of the symmetry center line for different grids for sudden cooling boundary condition.

Figures 6.4 and 6.5 plot the time series of the temperature at the middle point of the symmetry centre line for the case of sudden and ramp cooling boundary conditions respectively. It is seen from both figures that the calculated numerical results are not grid sensitive. The maximum variation is less than 2% for all cases considered here. Therefore, even the coarsest mesh will be able to provide the basic flow features for three different aspect ratios. However, 270×90, 320×80 and 360×90 meshes have been adopted for A = 1.0, 0.5 and 0.2 respectively with a time step 0.002 for all aspect ratios.
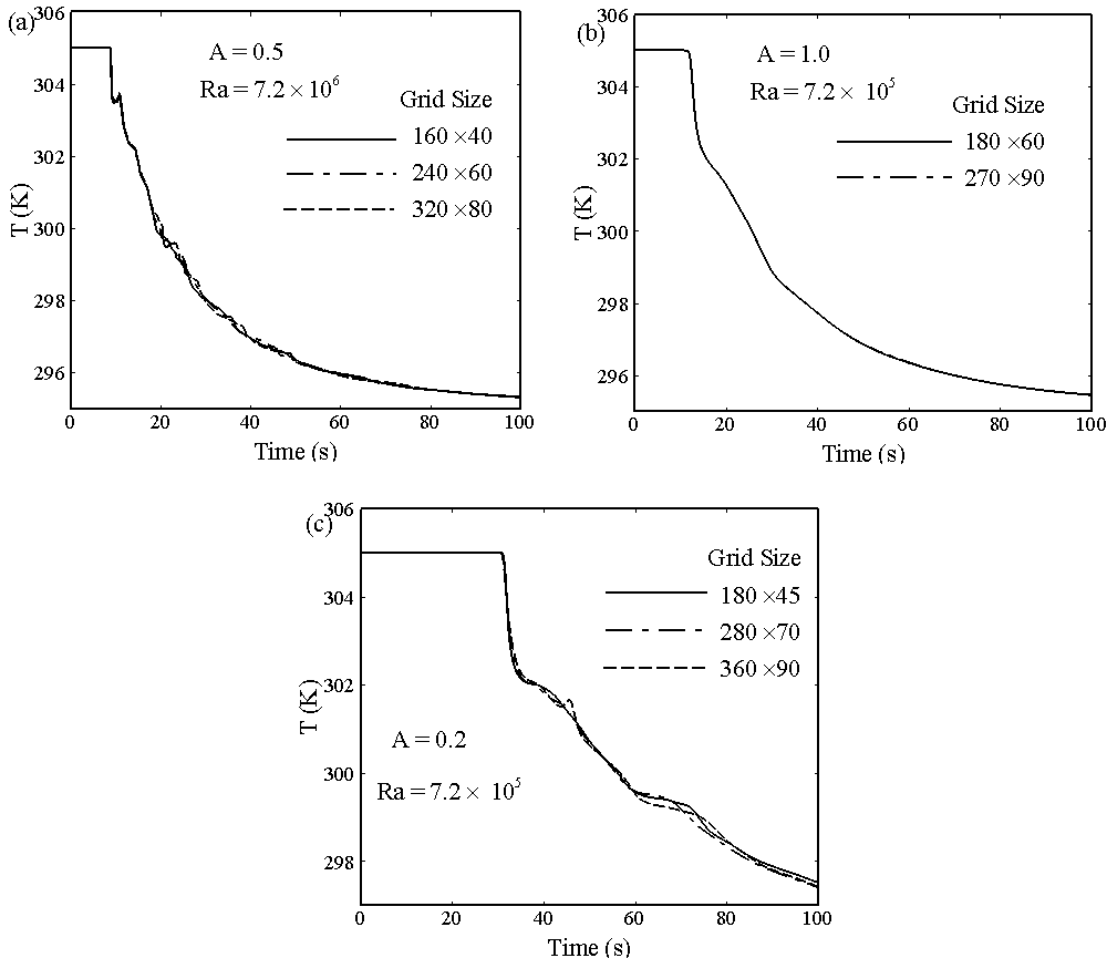
Figure 6.5 Time series of temperature at the mid point of the symmetry center line for different grids for ramp cooling boundary condition.

6.4 Flow development in different regimes for sudden cooling

Several possible flow regimes based on the Rayleigh number have been established in Chapter 4 for the case of sudden cooling boundary condition on the inclined flat plate. The same flow regimes can also be identified for the attic space problem. A brief discussion of those flow regimes with numerical results are presented as follows:

6.4.1 Conduction regime

Figure 6.6 presents the numerical results for the low-Rayleigh number regime, $Ra < (1+Pr)(1+A^2)/(A^2Pr)$ with $Pr = 0.72$, $Ra = 50$ and $A = 0.5$. The temperature contours and streamlines are plotted in figures 6.6(a) and 6.6(b), respectively at time t/t_s

= 0.25. In this regime the cold thermal boundary layer is stable and expands to the entire domain. The maximum temperature in the domain is 299K. However, the initial temperature inside the domain was set to 305K. The temperature profile has been extracted along a line perpendicular to the inclined wall at the mid point and shown in Figure 6.6(c). It is seen in figure 6.6 (c) that the thickness of the thermal boundary layer is larger than the perpendicular distance from the mid point of the left inclined wall to the bottom surface. Therefore, the flow is dominated by conduction in this regime. Moreover, there is no steady state of the flow inside the cavity as it continues to be cooled-down as time progresses. There are two symmetric cells in the streamlines where the direction of the left cell is anti-clockwise and the right cell is clockwise.
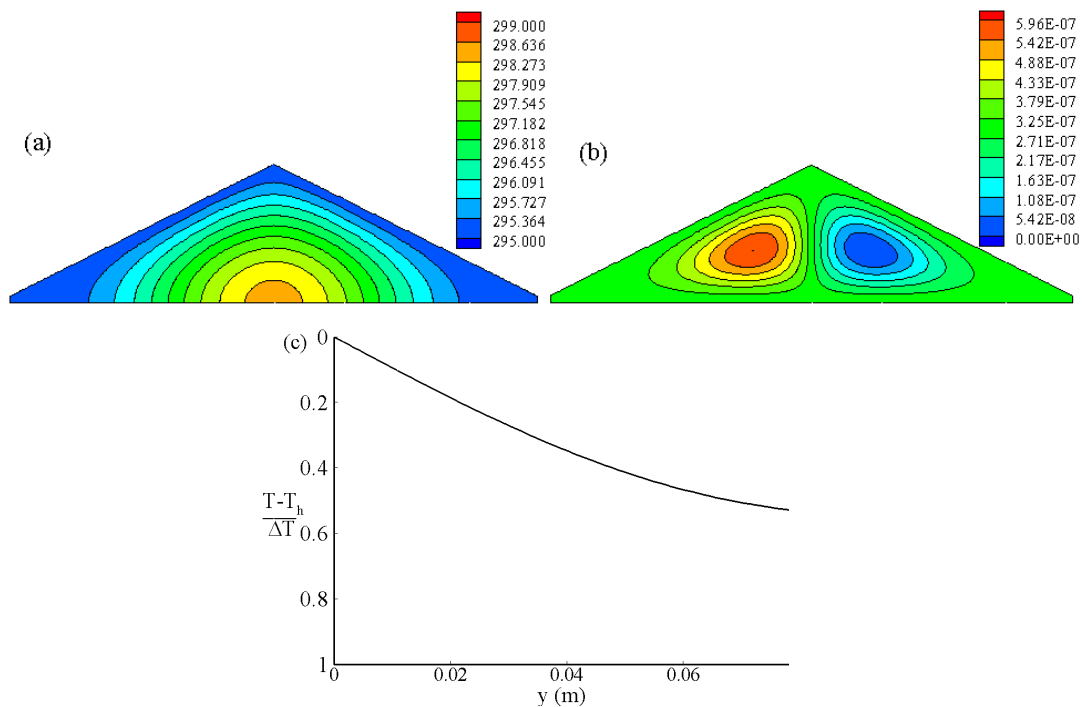
Figure 6.6 (a) temperature contours and (b) streamlines (c) temperature profile along the line perpendicular to the inclined wall at mid point with Pr = 0.72, Ra = 50 and A = 0.5.

6.4.2 Stable convection regime

Figure 6.7 presents the numerical results of a representative case in this flow regime, $(1+Pr)(1+A^2)/(A^2Pr) < Ra < (Pr^3A^6Ra_c^4)(1+Pr)^{-3}(1+A^2)^{-3}$ with $Pr = 0.72$, $Ra = 3.6 \times 10^4$ and $A = 0.5$ at $t/t_s = 1.6$. Temperature contours are presented in Figures 6.7(a) and streamlines are in Figure 6.7(b). The stable boundary layer becomes steady before the whole cavity is cooled down. The cold fluid travels through the boundary layers

adjacent to both inclined walls and meets the bottom adiabatic surface. The flow then has no other choice but to move to the interior of the cavity along the bottom surface.
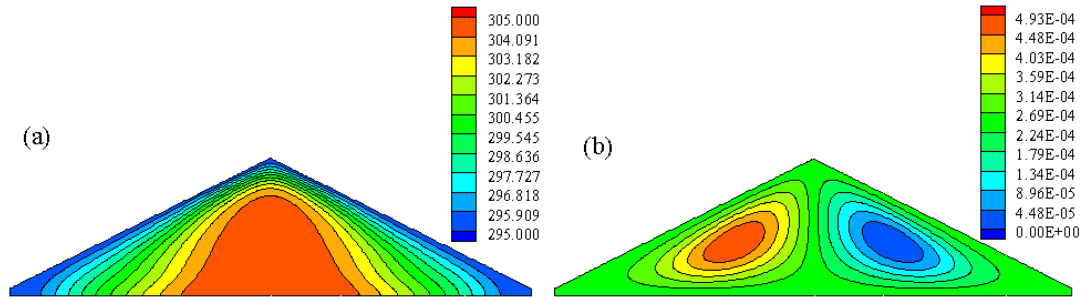
Figure 6.7 (a) temperature contours and (b) streamlines with $Pr = 0.72$, $Ra = 3.6 \times 10^4$ and $A = 0.5$.

6.4.3 Unstable convection regime

This flow regime, $Ra > (Pr^3 A^6 Ra_c{}^4)(1+Pr)^{-3}(1+A^2)^{-3}$ is characterized by the presence of convective instability in a form of sinking plumes. Figure 6.8 represents the isotherms and the streamlines for $Pr = 0.72$, $Ra = 7.2 \times 10^6$ and $A = 0.2$ at $t/t_s = 1.5$ to demonstrate the features of this flow regime. The plumes are formed in the cooling boundary layer. The cold fluid inside the boundary layer travels adjacent to the inclined wall and reaches the bottom tip. Then it changes its direction and moves to the interior of the cavity along the adiabatic bottom surface. Three convective cells on both sides of the symmetry line are observed in the streamlines at this particular time (Figure 6.8b).
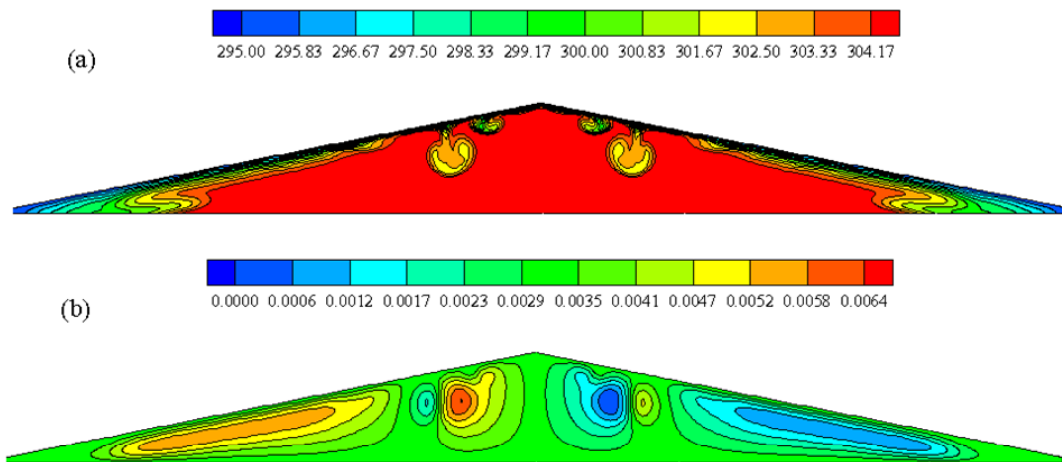
Figure 6.8 (a) temperature contours and (b) streamlines with $Pr = 0.72$, $Ra = 7.2 \times 10^6$ and $A = 0.2$ at $t/t_s = 1.5$.

6.5 Flow development in different regimes for ramp cooling

As it is discussed in Chapter 4 there are six possible flow regimes of the boundary layer development for ramp cooling boundary condition, it is also possible here to describe those regimes for the attic space problem. However, for brevity, only two main flow regimes have been explained in the following subsection.

6.5.1 Ramp time shorter than steady state time

Figure 6.9 shows the temperature contours and the streamlines for $Pr = 0.72$, $Ra = 7.2 \times 10^4$ and $A = 0.5$ at $t/t_s = 4.4$ for the regime $Ra < (1+Pr)(1+A^2)h^4/[A^2Pr\kappa^2 t_p^2]$. The ramp time has been set to 10s. In this regime the steady state time is longer than the ramp time. Therefore, the boundary layer grows according to the scale $\kappa^{1/2}t^{1/2}$ even after the ramp is finished. The thermal boundary layer becomes unstable or remains stable depending on the Rayleigh numbers. For the typical Rayleigh number considered here, the boundary layer is stable to the Rayleigh-Bénard instability. Figure 6.9(a) presents the temperature contours and Figure 6.9(b) presents the corresponding streamlines. A cold boundary layer develops adjacent to the sloping wall, reaches the bottom tip and moves to the interior of the cavity along the bottom adiabatic surface. Two intrusion boundary layers from two sides of the symmetry line meet at the mid point of the bottom surface and move upward. The corresponding streamlines show two symmetric convective cells.
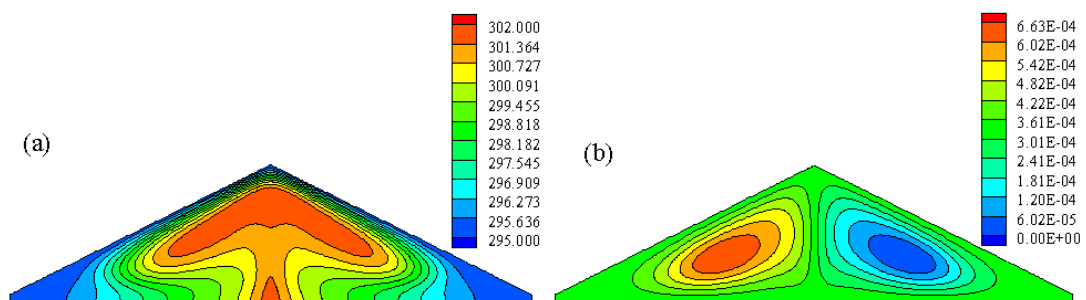
Figure 6.9 (a) Temperature contours and (b) streamlines for $Ra = 7.2 \times 10^4$, $Pr = 0.72$ and $A = 0.5$.

6.5.2 Ramp time longer than the steady state time

A representative Rayleigh case for this flow regime has been chosen as $Ra = 3.6 \times 10^6$, and $Pr = 0.72$ with $A = 0.2$. The temperature contours and streamlines are shown in Figure 6.10 for this case at $t/t_{sr} = 1.2$. The ramp time is 10s. In this regime the flow may be stable and reaches the quasi-steady mode. Since the plate is still cooling in the quasi-steady mode, the boundary layer may become unstable before the ramp is finished. On the other hand, the instability may set in before the flow becomes quasi-steady. For this typical Rayleigh number ($Ra = 3.6 \times 10^6$) the boundary layer becomes unstable before it reaches quasi-steady state. A number of sinking plumes appeared in the cold boundary layer adjacent to the sloping walls. The corresponding streamlines shows a number of convective cells on both sides of the symmetry line.
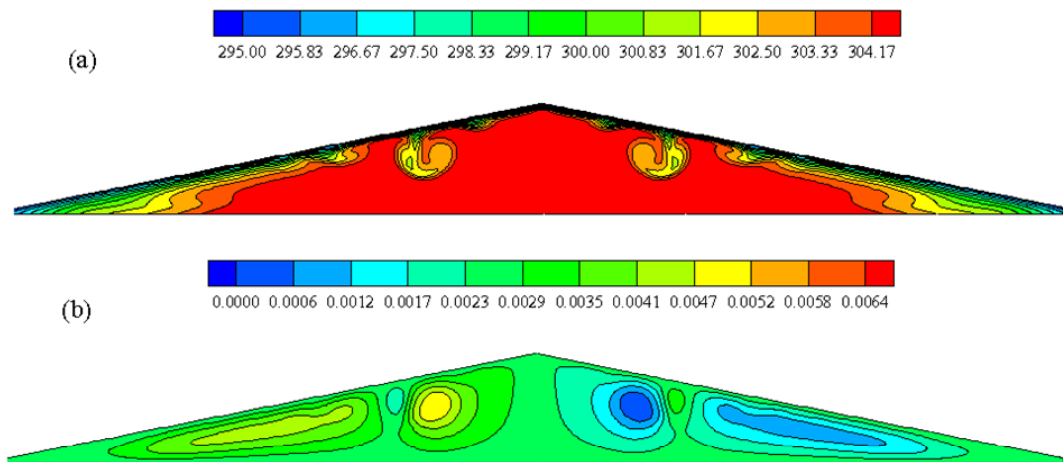
Figure 6.10 (a) Temperature contours and (b) streamlines for $Ra = 3.6 \times 10^6$, $Pr = 0.72$ and $A = 0.2$.

6.6 Validation of selected scales

The flow features discussed above are verified on the basis of a series of numerical simulations. The above scales have been developed with an assumption that the flow is symmetric along the symmetry center line of the cavity.

The detailed validation of the boundary layer development has been discussed in Chapter 4 (e.g. velocity scale, thickness scale, onset of instability etc). For brevity, those results are not repeated here. However, the heat transfer scales together with steady state time scale have been verified in this chapter. Moreover, the cooling-down

time scale and the subsequent heat transfer scale at that time have also been verified for both boundary conditions below.

6.6.1 Sudden cooling

The cooling-down time is determined by the heat flux through the natural convection boundary layer. The cold fluid moves downward through the boundary layer of both inclined walls. When the cold fluid reaches to the bottom tips then it has no choice but to move horizontally adjacent to the bottom surface. Once the boundary layer is fully developed, the fluid in the container is gradually stratified by the cold fluid ejected from the boundary layers, starting from the bottom of the container, and this cooling-down stage continues until the whole body of fluid becomes cold. However, for higher Rayleigh numbers the boundary layer may become unstable.

Table 6.1 Values of *A* and *Ra* for six runs for sudden cooling.

Runs	***A***	***Ra***
1	0.5	7.2×10^5
2	0.5	3.6×10^5
3	0.5	2.2×10^5
4	0.5	7.2×10^4
5	0.2	3.6×10^5
6	1.0	3.6×10^5

In Table 6.1, Runs 1-4 with $Ra = 7.2 \times 10^5$, 3.6×10^5, 2.2×10^5 and 7.2×10^4 while keeping $A = 0.5$ and $Pr = 0.72$ unchanged have been carried out to show the dependence of the scaling relations on the Rayleigh number; Runs 5-6 and 2 with $A = 0.2$, 1.0 and 0.5 respectively while keeping $Ra = 3.6 \times 10^5$ and $Pr = 0.72$ unchanged have been carried out to show the dependence on the slope of the inclination of the sloping walls. All Rayleigh numbers considered here are in the unstable convection regime.

The numerical results showing the dependence of the instantaneous average Nusselt number *Nu* on *Ra* and *A* at the boundary-layer development stage and at the cooling-down stage are presented in Figure 6.11. Figure 6.11(a) shows the raw data of the time series of the Nusselt number which have been calculated from the left inclined

wall of the cavity for different Rayleigh numbers and aspect ratios. It is found that the Nusselt number depends significantly on *Ra* and *A*. In Figure 6.11(b), the time has been normalized with respect to the steady-state time (6.2) of the boundary layer development and the Nusselt number has been normalized with respect to its steady-state value (6.6). As anticipated, all lines collapse together in one line which confirms the scaling relations of (6.2) and (6.6) at the boundary-layer development stage. The Nusselt number for the cooling-down stage has been plotted in Figure 6.11(c). Again all lines fall together in a line which validates the scaling relation (6.14) at the cooling-down stage. Note that the *x*-axis is plotted on a log scale.
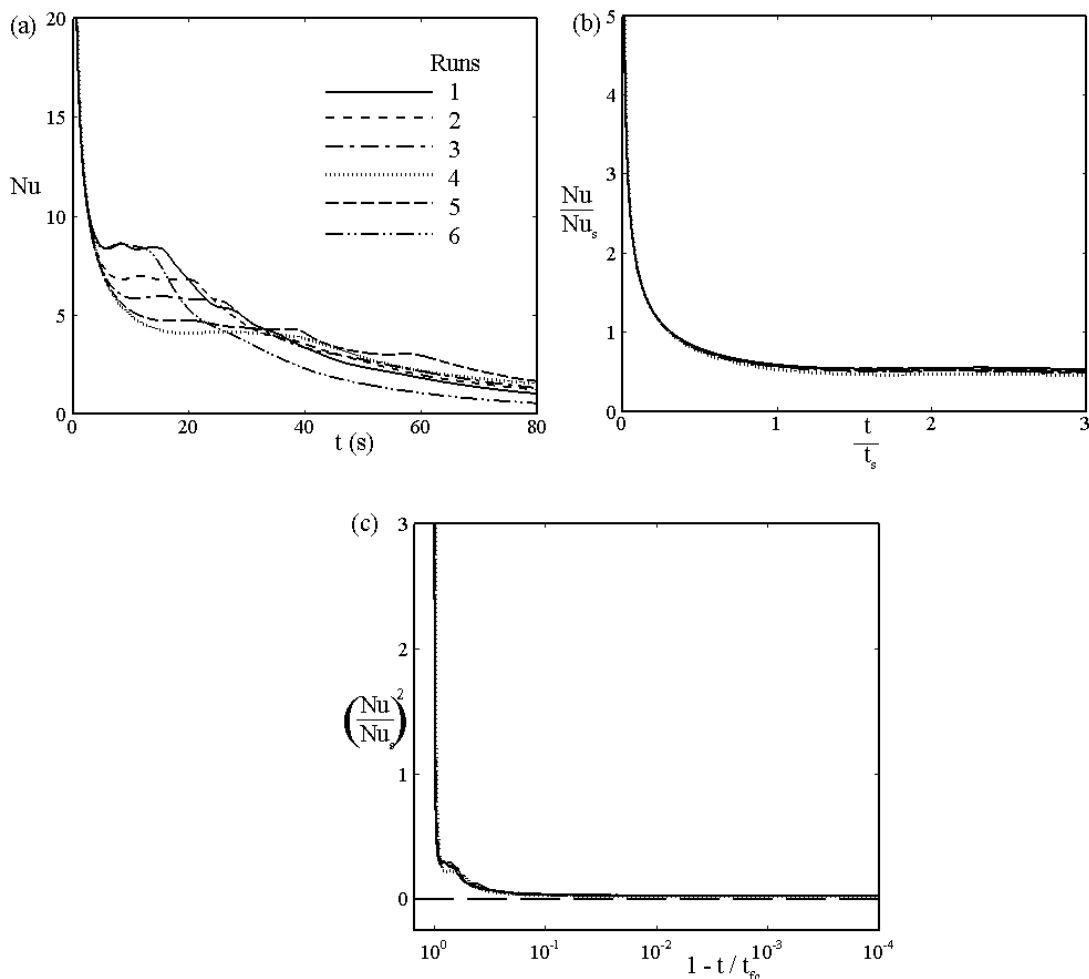
Figure 6.11 Time series of the Nusselt number calculated on the left inclined wall. (a) Plot of raw data; (b) Normalized Nusselt number versus normalized time; (c) Nusselt number at the cooling-down stage for six runs for sudden cooling.

To verify the cooling-down time scale, the average temperature inside the enclosure has been calculated with time. Figure 6.12 shows the time series of the

average temperature inside the cavity. Raw data of the time series of the average temperature for different Rayleigh numbers and aspect ratios have been plotted in Figure 6.12(a). It is anticipated that the variation of the temperature inside the enclosure depends significantly on the Rayleigh number and aspect ratio. The average temperature decreases with time for all parameters considered here. In Figure 6.12(b), the time is normalized with respect to the cooling-down time scale (6.12) and the temperature has been normalized by the temperature difference between the wall and the interior. We see that all curves of the temperature time series collapse at a single curve for different flow parameters. This confirms that the cooling-down time scale (6.12) is accurate.

Figure 6.12 Time series of the average temperature inside the enclosure. (a) Plot of raw data; (b) Normalized temperature versus normalized time at the cooling-down stage for six runs for sudden cooling.

6.6.2 Ramp cooling

Similar to the sudden cooling case, the cooling-down time is also determined by the heat flux through the natural convection boundary layer for the ramp temperature boundary condition.

Table 6.2 shows the full sets of parameters used for the numerical simulation to verify the scaling prediction. Runs 1-6 are in the regime in which the quasi-steady time is shorter than the ramp time and the flow is unstable; and runs 7-10 are in the regime in which the steady state time is longer than the ramp time and the boundary layer is in a stable condition.

Table 6.2 Values of *A* and *Ra* for 10 runs for ramp cooling.

Runs	A	Ra
1	0.5	7.2×10^6
2	0.5	5.8×10^6
3	0.5	3.6×10^6
4	0.5	7.2×10^5
5	1.0	7.2×10^5
6	0.2	7.2×10^5
7	0.5	1.0×10^5
8	0.5	6.0×10^4
9	0.5	3.0×10^4
10	0.5	1.0×10^4
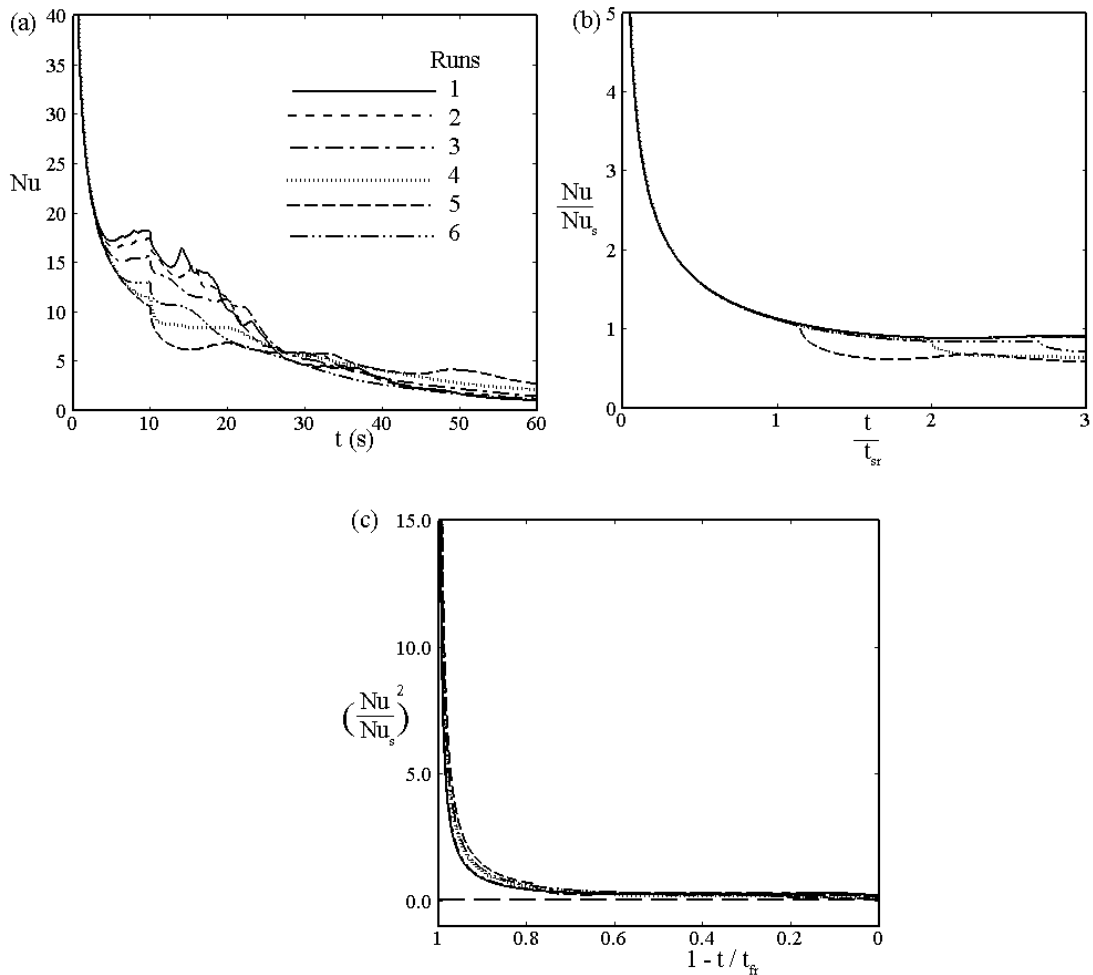
Figure 6.13 Time series of the Nusselt number calculated on the left inclined wall. (a) Plot of raw data; (b) Normalized Nusselt number versus normalized time; (c) Nusselt number at the cooling-down stage for six runs for ramp cooling.

The numerical results showing the dependence of the average Nusselt number, *Nu* on *Ra* and *A* at the boundary-layer development stage are presented in Figure 6.13. Figure 6.13(a) shows the raw data of the time series of the Nusselt number which has been calculated on the left inclined wall of the cavity. It is seen that initially the Nusselt number approaches infinity and decreases sharply until the quasi-steady state is reached. After the quasi-steady state time it increases very slowly until the ramp is finished. After the ramp finishes, the Nusselt number again decreases and approaches zero. We also see some oscillations in the Nusselt number plots. It is due to the unstable condition of the boundary layer. In Figure 6.13(b), the time has been normalized by the quasi-steady time (6.16) and the Nusselt number by the quasi-steady Nusselt number (6.22). We see that all lines lie together until the ramp is finished, which confirms the scaling relations (6.16) and (6.22).

The Nusselt number at the cooling-down time has been plotted in Figure 6.13(c). Again all lines fall together in a line for different flow parameters considered here which validates the scaling relation (6.36).
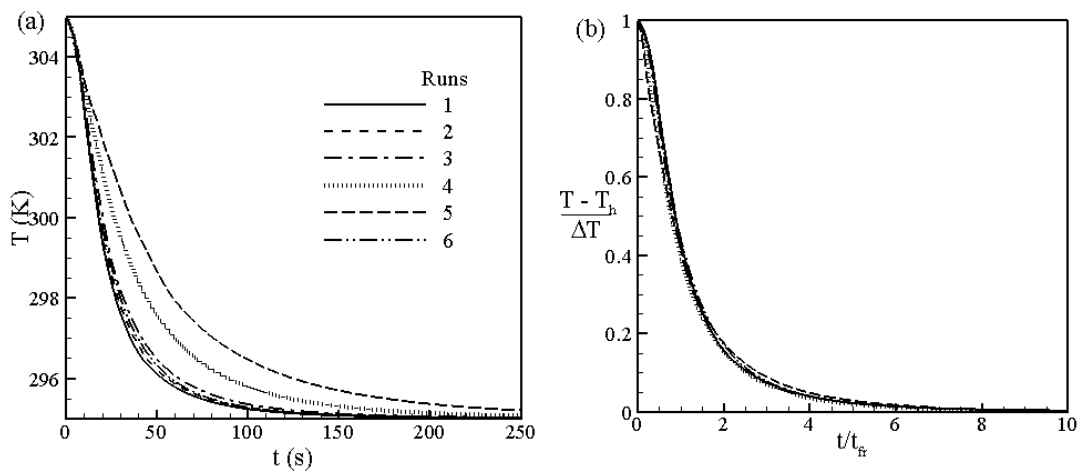
Figure 6.14 Time series of the average temperature inside the enclosure. (a) Plot of raw data; (b) Normalized temperature versus normalized time at the cooling-down stage for six runs for ramp cooling.

The raw data of the time series of the average temperature inside the enclosure has been plotted in Figure 6.14(a) for different Rayleigh numbers and aspect ratios. These parameters are in the flow regime in which the quasi-steady time is shorter than the ramp time. It is seen in this figure that the average temperature variation inside the

cavity depends strongly on the Rayleigh number and the aspect ratio. In Figure 6.14(b), the time is normalized with respect to the cooling-down time scale (6.32) and the temperature has been normalized by the temperature difference between the wall and inside the enclosure. We see that all temperature series fall onto a single curve for different flow parameters. This confirms that the cooling-down time scale (6.32) is accurate.
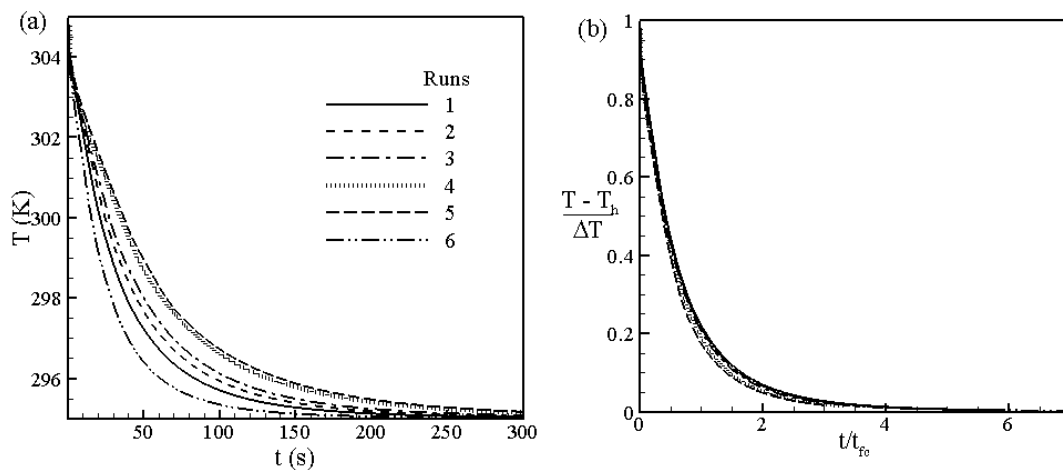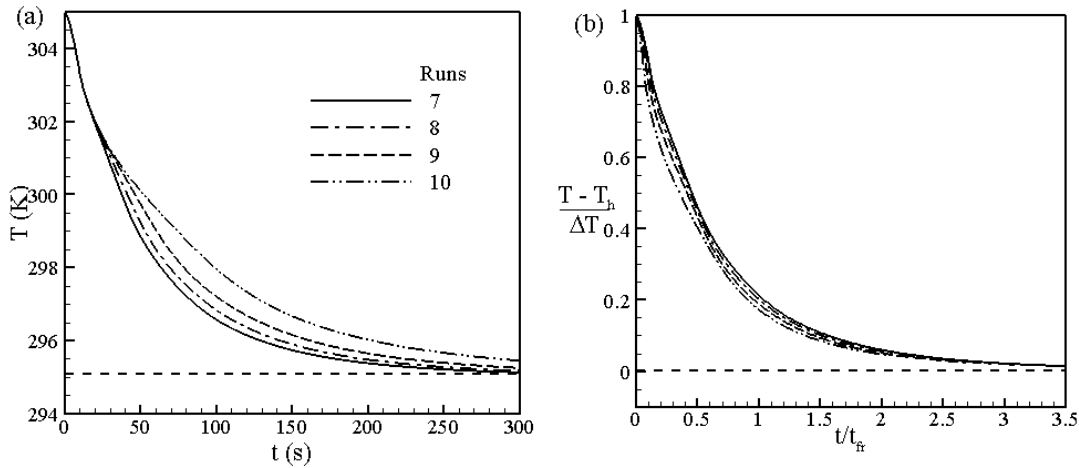

Figure 6.15 Time series of the average temperature inside the enclosure. (a) Plot of raw data; (b) Normalized temperature versus normalized time at the cooling-down stage for four runs for ramp cooling.

For the case in which the steady state time is longer than the ramp time, the cooling-down time scale is the same as that for the case of instantaneous cooling boundary condition. To verify the scaling relation (6.12), four different Rayleigh numbers have been chosen for the above regime. The raw data of the average temperature inside the enclosure has been depicted in Figure 6.15(a). In Figure 6.15(b), the time is normalized with respect to the cooling-down time scale (6.12) and the temperature is normalized with temperature difference. All curves for different Rayleigh numbers fall almost onto a single curve which confirms that the scaling relation (6.12) is accurate for the ramp boundary condition when the steady state time for the boundary layer is longer than the ramp time.

6.7 Summary

A set of scaling results have been developed for natural convection in an attic space and are verified by the numerical simulation for a fluid with a fixed Prandtl number (*Pr* = 0.72). The scaling relations of transient and steady state values of the velocity (u_s) and the thermal layer thickness (δ_T) and the steady state time scale (t_s) were established in Chapter 4. Those scaling results have been used directly to develop some further scaling (heat transfer, filling box time) for the attic space problem. A Nusselt number scale (Nu_s) during the boundary layer development stage is developed. The cooling-down time scale (t_{fc}) and the Nusselt number scale at the cooling-down stage are also achieved. Several possible flow regimes which were established in Chapter 4 are also discussed in this chapter with numerical results.

Furthermore, a temperature boundary condition of a ramp function applied to the inclined walls of the attic space is also investigated in this chapter. The boundary layer flow for this boundary condition depends on the comparison of the time at which the ramp cooling is completed with the time at which the boundary layer completes its growth. If the ramp time is long compared with the steady state time, the thermal boundary layer reaches a quasi-steady mode in which the growth of the layer is governed by the thermal balance between convection and conduction. On the other hand, if the ramp is completed before the thermal boundary layer becomes steady-state, the subsequent growth is governed by the balance between buoyancy and inertia, as for the case of instantaneous cooling. However, if the Rayleigh number exceeds the critical Rayleigh number then flow inside the boundary layer becomes unstable. The scaling results of the boundary layer development have been derived and discussed in Chapter 4. The scaling of heat transfer through the boundary layer into the enclosure and the cooling-down time scale for the enclosure have been developed in this chapter. The heat transfer scale at the cooling-down stage is also derived. Moreover, a discussion has been made regarding some important flow regimes developed in Chapter 4 with numerical results. The comparisons between the scaling predictions and the numerical simulations demonstrate that the scaling results agree very well with the numerical simulations

7. Natural convection in attics subject to periodic thermal forcing

From the literature review (see Chapter 1) it is seen that for the attic space problem previous research has been conducted for either the sudden heating or sudden cooling boundary condition on the sloping boundaries. Ramp heating and cooling temperature boundary conditions have been considered in the previous chapters (Chapter 5 and 6). In real situations, however, the attic space of buildings is subject to alternative heating and cooling over a diurnal cycle (see Figure 7.1). Therefore, the flow response and heat transfer in the attic space subject to a periodic thermal forcing are yet to be unveiled.
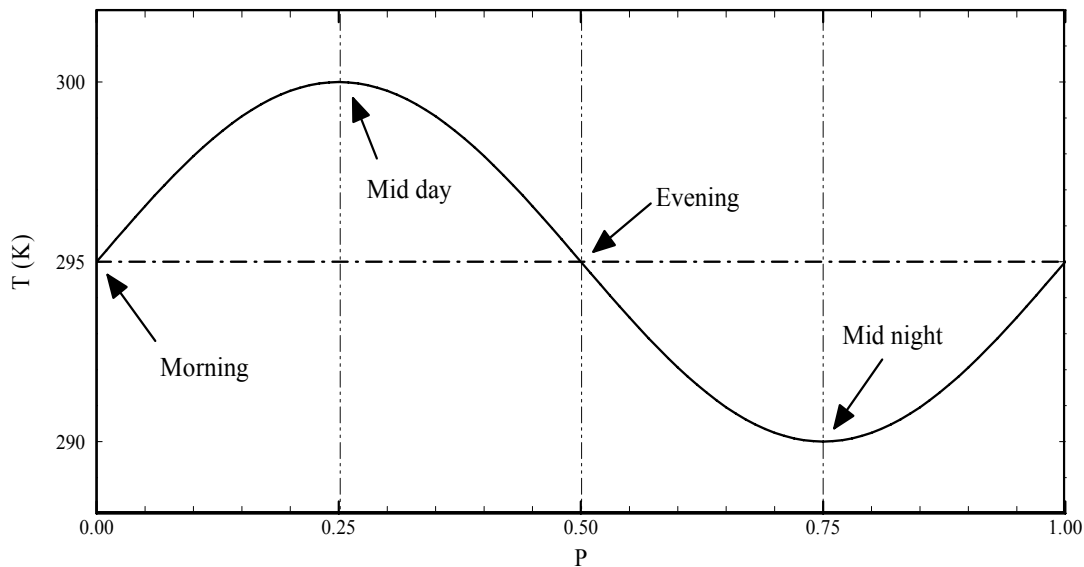
Figure 7.1 Temperature boundary condition on the incline walls of the enclosure.

In this chapter, numerical simulations of natural convection in an attic space subject to diurnal temperature condition on the sloping wall have been carried out. The effects of the aspect ratio and Rayleigh number on the fluid flow and heat transfer have been discussed in details as well as the formation of a pitchfork bifurcation of the flow at the symmetric line of the enclosure. Details of the numerical procedure can be found in chapter 2. However, grid and time step dependence tests for this periodic case are described in this chapter.

The physical system is sketched in Figure 7.2, which is an air-filled isosceles triangular cavity of variable aspect ratios. Here $2l$ is the length of the base or ceiling, T_0

is the temperature applied on the base, T_A is the amplitude of temperature fluctuation on the inclined surfaces, h is the height of the enclosure and P is the period of the thermal forcing.
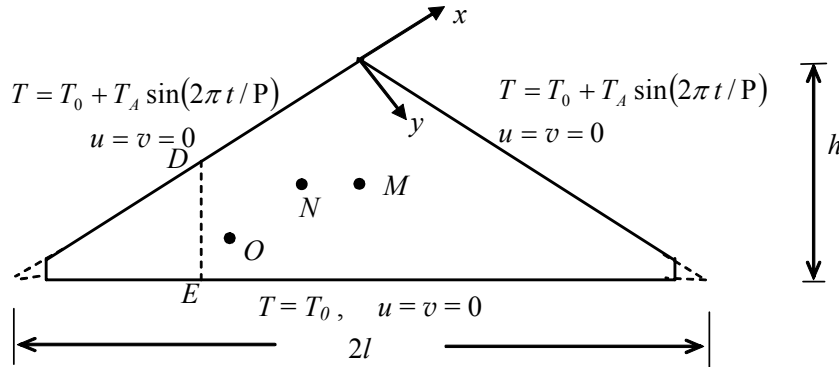
Figure 7.2 A schematic of the geometry and boundary conditions of the enclosure.

The boundary conditions for the present numerical simulations are also shown in Figure 7.2. Here, the temperature of the bottom wall of the cavity is fixed at $T = T_0$. A periodic temperature boundary condition is applied to the two inclined walls. The Rayleigh number for the periodic boundary condition has been defined based on the maximum temperature difference between the inclined surface and the bottom over a cycle.

$$Ra \sim \frac{2g\beta T_A h^3}{\kappa \nu}.$$

Three aspect ratios 0.2, 0.5 and 1.0, four Rayleigh numbers, 1.5×10^6, 7.2×10^5, 1.5×10^4, and 1.5×10^3, and a fixed Prandtl number 0.72 are considered in the present investigation. Based on the experimental observations of Flack (1980), which reported the critical Rayleigh number for the flow to become turbulent, we have chosen the maximum Rayleigh number, $Ra = 1.5\times10^6$ so that the flow stays in the laminar regime. It is understood that in real situations the Rayleigh number may be much higher than this and an appropriate turbulence model should be applied. This is beyond the scope of this study. In order to avoid the singularities at the tips in the numerical simulation, the tips are cut off by 5% and at the cutting points (refer to Figure 7.2) rigid non-slip and adiabatic vertical walls are assumed. We anticipate that this modification of the geometry will not alter the overall flow development significantly.

7.1 Selection of the physical period

The period is determined in consideration of the scaling predictions of Chapters 3, 4, 5 and 6 which have demonstrated that the time for the adjustment of the temperature in the thermal boundary layer is by far shorter than the thermal forcing period of 24 hours in field situations.

For sudden heating/cooling boundary conditions the steady state time scale for the boundary layer development from (5.2) is

$$t_s \sim \frac{(1+Pr)^{1/2}(1+A^2)^{1/2}}{ARa^{1/2}Pr^{1/2}}\left(\frac{h^2}{\kappa}\right),$$

(7.1)

and the heating-up or cooling-down time scale for the enclosure to be filled with hot or cold fluid under the same boundary conditions from (5.12) is

$$t_f \sim \frac{(1+Pr)^{1/4}}{A^{1/2}Ra^{1/4}Pr^{1/4}(1+A^2)^{1/4}}\left(\frac{h^2}{\kappa}\right), \quad \text{for } t_f > t_s$$

(7.2)

On the other hand, the quasi-steady time scale for ramp heating/cooling boundary condition of the boundary layer development for the case when the ramp time is longer than the quasi-steady time from (5.16) is

$$t_{sr} \sim \frac{(1+Pr)^{1/3}(1+A^2)^{1/3}}{A^{2/3}Ra^{1/3}Pr^{1/3}}\left(\frac{t_p}{h^2/\kappa}\right)^{1/3}\left(\frac{h^2}{\kappa}\right),$$

(7.3)

and the heating-up or cooling-down time scale of the enclosure under the same boundary conditions from (6.32) is

$$t_{fr} \sim \frac{\left[h(1+A^2)^{1/2}-Ax_1\right]^2}{A^{1/2}\kappa Ra^{1/4}(1+A^2)^{5/4}},$$

(7.4)

where x_1 is given by (6.26) as

$$\Rightarrow x_1 \sim L\left[1-\left(1-\frac{\kappa A^{1/2}Ra^{1/4}(1+A^2)^{1/4}}{h^2}t_p\right)^{1/2}\right].$$

(7.5)

However, if the cavity is filled with cold fluid before the ramp is finished then the filling up time is given by (6.34) as

$$t_{fq} \sim \frac{h^{8/7}t_p^{3/7}}{\kappa^{4/7}Ra^{1/7}A^{2/7}(1+A^2)^{1/7}}.$$

(7.6)

Table 7.1 Steady state and quasi-steady times for sudden and ramp boundary conditions respectively for different *A* and *Ra*.

Aspect ratio	Steady state time (t_s) for sudden heating/cooling		Quasi-steady time (t_{sr}) for ramp heating/cooling (t_p = 1000s)	
	$Ra = 1.5\times10^6$	$Ra = 7.2\times10^3$	$Ra = 1.5\times10^6$	$Ra = 7.2\times10^3$
A=0.2	8.15s	-	40.51s	-
A=0.5	2.54s	35.76s	18.62s	108.53s
A=1.0	2.26s	-	17.23s	-

Table 7.1 presents the scaling values of the steady and quasi-steady times for sudden and ramp heating/cooling boundary conditions respectively for different *A* and *Ra*. The highest Rayleigh number considered here for three different aspect ratio is *Ra* = 1.5×10⁶. It is noticed that the steady state times for the boundary layer for this Rayleigh number of *A* = 0.2, 0.5 and 1.0 are 8.1s, 2.54s and 2.26s respectively. However, for the lowest Rayleigh number, *Ra* = 7.2×10³ the steady state time for *A* = 0.5 is 35.76s. On the other hand, the quasi-steady time for the ramp temperature boundary condition depends on the length of the ramp. If we assume the ramp time to be 1000s then the quasi-steady times for these aspect ratios are 40.51s, 18.62s and 17.23s respectively and for the lowest Rayleigh number, *Ra* = 7.2×10³ the quasi-steady time for the aspect ratio *A*= 0.5 is 108.53s which is much shorter than the ramp time (1000s). If the ramp time is 200s the quasi-steady time of *A* = 0.5 for the lowest Rayleigh number considered here is 63.47s. Still the quasi-steady time is about half of the ramp time. Therefore, what happened between the quasi-steady time and the ramp time is, once the quasi-steady state time t_{sr} is reached, the boundary layer stops growing according to $\kappa^{1/2}t^{1/2}$ which is only valid for conductive boundary layers. The thermal boundary layer is in a quasi-steady mode with convection balancing conduction. Further increase of the heat input simply accelerates the flow to maintain the proper thermal balance. The thickness and the velocity scales during this quasi-steady mode is

$$\Rightarrow \delta_T \sim \frac{h\left(1+A^2\right)^{1/4}}{A^{1/2}Ra^{1/4}}\left(\frac{t_p}{t}\right)^{1/4}. \tag{7.7}$$

and

$$u \sim Ra^{1/2}\left(\frac{\kappa}{h}\right)\left(\frac{t}{t_p}\right)^{1/2}. \tag{7.8}$$

respectively. When the hot fluid travels through the boundary layer and reaches the top tip of the cavity then it has no choice but to move downward along the symmetry line of the cavity. In this way the cavity is filled up with hot fluid with a horizontal stratification of the thermal field.

However, during the cooling phase, the boundary layer is not stable for the Rayleigh numbers considered here. In that case initially a cold boundary layer develops adjacent to the inclined wall which is potentially unstable to the Rayleigh Bénard instability, which may manifest in a form of sinking plumes. These plumes mix up the cold fluid with the hot fluid inside the cavity until the end of the cooling phase.

Table 7.2 Heating-up/cooling-down times for sudden and ramp boundary conditions respectively for different *A* and *Ra*.

Aspect ratio	Filling-up time (t_f) for sudden heating/cooling		Filling-up time (t_{fr}) for ramp heating/cooling ($t_p = 1000s$)	
	$Ra = 1.5×10^6$	$Ra = 7.2×10^3$	$Ra = 1.5×10^6$	$Ra = 7.2×10^3$
A=0.2	83.24s	-	213.32s	-
A=0.5	42.39s	159.01s	145.07s	308.77s
A=1.0	31.61s	-	122.67s	-

Moreover, Table 7.2 shows the scaling values of the filling-up times for sudden and ramp heating/cooling boundary conditions for different *A* and *Ra*. It is seen that the heating-up or cooling-down times for the sudden heating/cooling boundary condition for $A = 0.5$ and $Ra = 1.5×10^6$ is 42.39s and for $Ra = 7.2×10^3$ and the same aspect ratio is 159.01s. For aspect ratios 0.2 and 1.0 the filling-up times are 83.24s and 31.61s respectively when $Ra = 1.5×10^6$. The filling-up times for ramp heating/cooling boundary conditions for $A = 0.5$ are 145.07s and 308.77s when $Ra = 1.5×10^6$ and $7.2×10^3$ respectively and $t_p = 1000s$. For two other aspect ratios, $A = 0.2$ and 1.0, the filling-up times are 213.32s and 122.67s respectively for $Ra = 1.5×10^6$. However, the filling-up time for ramp boundary conditions depends on the length of the ramp time. If the ramp time is 200s then the filling-up time for the lowest Rayleigh number considered here is 154.90s for $A = 0.5$. These times are very short when compared to the thermal forcing period of 24 hours in field situations. Therefore, the period of the thermal cycle may be considered as 400s or more based on the above discussions for the following numerical simulations. However, for a better understanding of the flow at

in the quasi-steady mode, we have chosen a thermal forcing period of 2000s for all the simulations.

7.2 Grid and time step dependence tests

Mesh and time step dependence tests have been carried out with three different meshes and three different time steps for each aspect ratio of A = 0.2, 0.5 and 1.0. The results of the mesh and time-step dependence tests are shown in Tables 7.3, 7.4 and 7.5, which show the temperature at three different positions in the cavity at specific times t = 0.75P when the flow is the most unstable.

Table 7.3 Parameters and results of mesh and time-step dependence test at t = 0.75P for A = 0.2 and Ra = 1.5×10^6.

Mesh Size	Time Step(s)	Temperature at different points in the cavity (K)		
		O	N	M
180 × 45	1.00	292.4748	292.6010	293.6372
280 × 70	0.75	292.4953	292.6086	293.6773
360 × 90	0.50	292.4987	292.61137	293.7017

It is seen in Tables 7.3, 7.4 and 7.5 that the variation of the calculated temperature among the three meshes with respect to T_A is very small (<1%). Based on these tests, any of the tested meshes would be sufficiently fine for resolving the flow. Therefore, mesh sizes of 360 × 90, 320 × 80 and 270 × 90 for A = 0.2, 0.5 and 1.0 respectively have been selected for the numerical simulations. The time step for the aspect ratios 0.2 and 0.5 is adopted as 0.5s and for the aspect ratio 1.0 is 0.75s.

Table 7.4 Parameters and results of mesh and time-step dependence test at t = 0.75P for A = 0.5 and Ra = 1.5×10^6.

Mesh Size	Time Step(s)	Temperature at different points in the cavity (K)		
		O	N	M
160 × 40	1.00	292.2819	292.3355	293.2779
240 × 60	0.75	292.3174	292.3501	293.2979
320 × 80	0.50	292.3346	292.3580	293.3059

Table 7.5 Parameters and results of mesh and time-step dependence test at *t* = 0.75P for
A = 1.0 and *Ra* = 1.5×10⁶.

Mesh Size	Time Step(s)	Temperature at different points in the cavity (K)		
		O	*N*	*M*
180 × 60	1.00	292.4279	292.4077	292.4598
270 × 90	0.75	292.2491	292.8421	292.2961
360 × 120	0.50	292.2521	292.8747	292.2925

7.3 Flow response to the periodic boundary condition

In this section, the flow response to the periodic thermal forcing and the heat transfer through the sloping boundary are discussed for the case with *A* = 0.5, *Pr* = 0.72 and *Ra* = 1.5×10⁶.

7.3.1 General flow response to diurnal heating and cooling

Since the initial flow is assumed to be isothermal and motionless, there is a start-up process of the flow response. In order to minimize the start-up effect, three full thermal forcing cycles are calculated in the numerical simulation before consideration of the flow. It is found that the start-up effect for the present case is almost negligible, and the flow response in the third cycle is identical to that in the previous cycle. In the following discussion, the results of the third cycle are presented.

Figure 7.3 shows snapshots of streamlines and the corresponding isotherms at different stages of the cycle. The flow and temperature structures, shown in Figure 7.3 at *t* = 2.00*P*, represent those at the beginning of the daytime heating process in the third thermal forcing cycle. At this time, the inclined surfaces and the bottom surface of the enclosure have the same temperature, but the temperature inside the enclosure is lower than the temperature on the boundaries due to the cooling effect in the previous thermal cycle. The residual temperature structure, which is formed in the previous cooling phase, is still present at *t* = 2.00*P*. The corresponding streamline contours at the same time show two circulating cells, and the temperature contours indicate stratification in the upper and lower section of the enclosure with two cold regions in the centre.
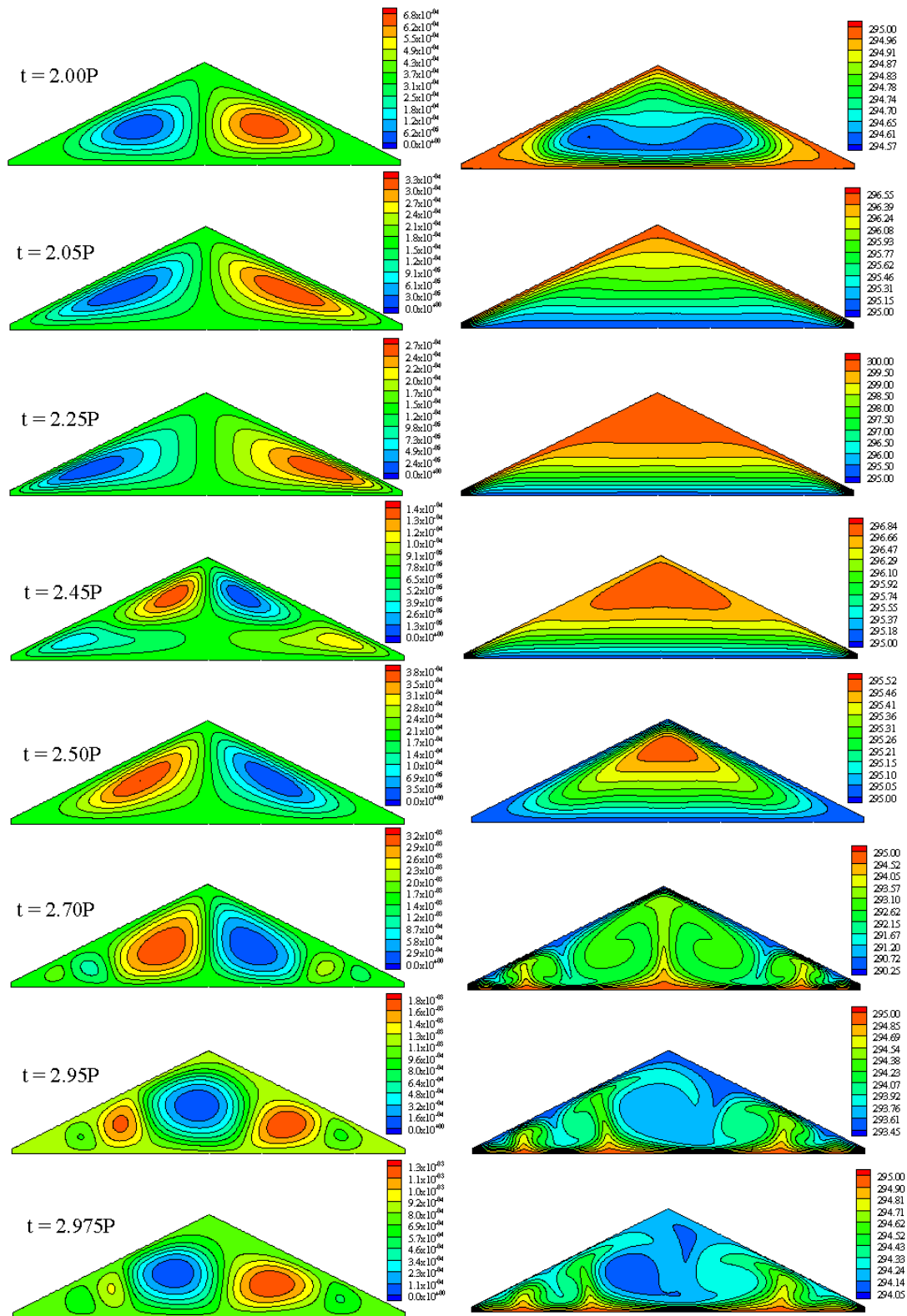
Figure 7.3 A series of snapshots of stream function and temperature contours of the third cycle at different times for *A* = 0.5 and *Ra* = 1.5×10⁶. Left: streamlines; right: isotherms.

As the upper surface temperature increases further, a distinct temperature stratification is established throughout the enclosure by the time *t* = 2.05*P* (see Figure

7.3). The streamlines at this stage indicate that the centers of the two circulating cells have shifted closer to the inclined surfaces, indicating a strong conduction effect near those boundaries. This phenomenon has been reported previously in Akinsete and Coleman (1982) and Asan and Namli (2000) for the daytime condition with constant heating at the upper surface or constant cooling at the bottom surface.

At $t = 2.25P$, the temperature on the inclined surfaces peaks. Subsequently, the temperature drops, representing a decreasing heating effect. Since the interior flow is stably stratified prior to $t = 2.25P$, the decrease of the temperature at the inclined surface results in a cooling event, appearing first at the top corner and expanding downwards as the surface temperature drops further. At $t = 2.45P$, two additional circulating cells have formed in the upper region of the enclosure, and the newly formed cells push the existing cells downwards. The corresponding temperature contours show two distinct regions, an expanding upper region responding to the cooling effect, and a shrinking lower region with stratification responding to the decreasing heating effect. By the time $t = 2.50P$, the daytime heating ceases; the lower stratified flow region has disappeared completely and the flow in the enclosure is dominated by the cooling effect. At this time, the top and the bottom surfaces again have the same temperature, but the interior temperature is higher than that on the boundaries.

As the upper inclined surface temperature drops below the bottom surface temperature ($t = 2.70P$, Figure 7.3), the cold-air layer under the inclined surfaces becomes unstable. At the same time, the hot-air layer above the bottom surface also becomes unstable. As a consequence, sinking cold-air plumes and rising hot-air plumes are visible in the isotherm contours and a cellular flow pattern is formed in the corresponding stream function contours. It is also noticeable that the flow is symmetric about the geometric symmetry plane at this time. However, as time increases the flow becomes asymmetric about the symmetric line (see isotherms at $t = 2.95P$). The large cell from the right hand side of the centreline, which is still growing, pushes the cell on the left of it towards the left tip. At the same time this large cell also changes its position and attempts to cross the centreline of the cavity and a small cell next to it moves into its position and grows.

At $t = 2.975P$, the large cell in the stream lines has crossed the centerline and the cell on the right of it grows and becomes as large as it is after a short time (for brevity figures not included). The flow is also asymmetric at this time. However, it

154

returns to a symmetric flow at the time $t = 3.00P$ which is the same as that at $t = 2.00P$, and similar temperature and flow structures to those at the beginning of the forcing cycle are formed. The above described flow development is repeated in the next cycle.
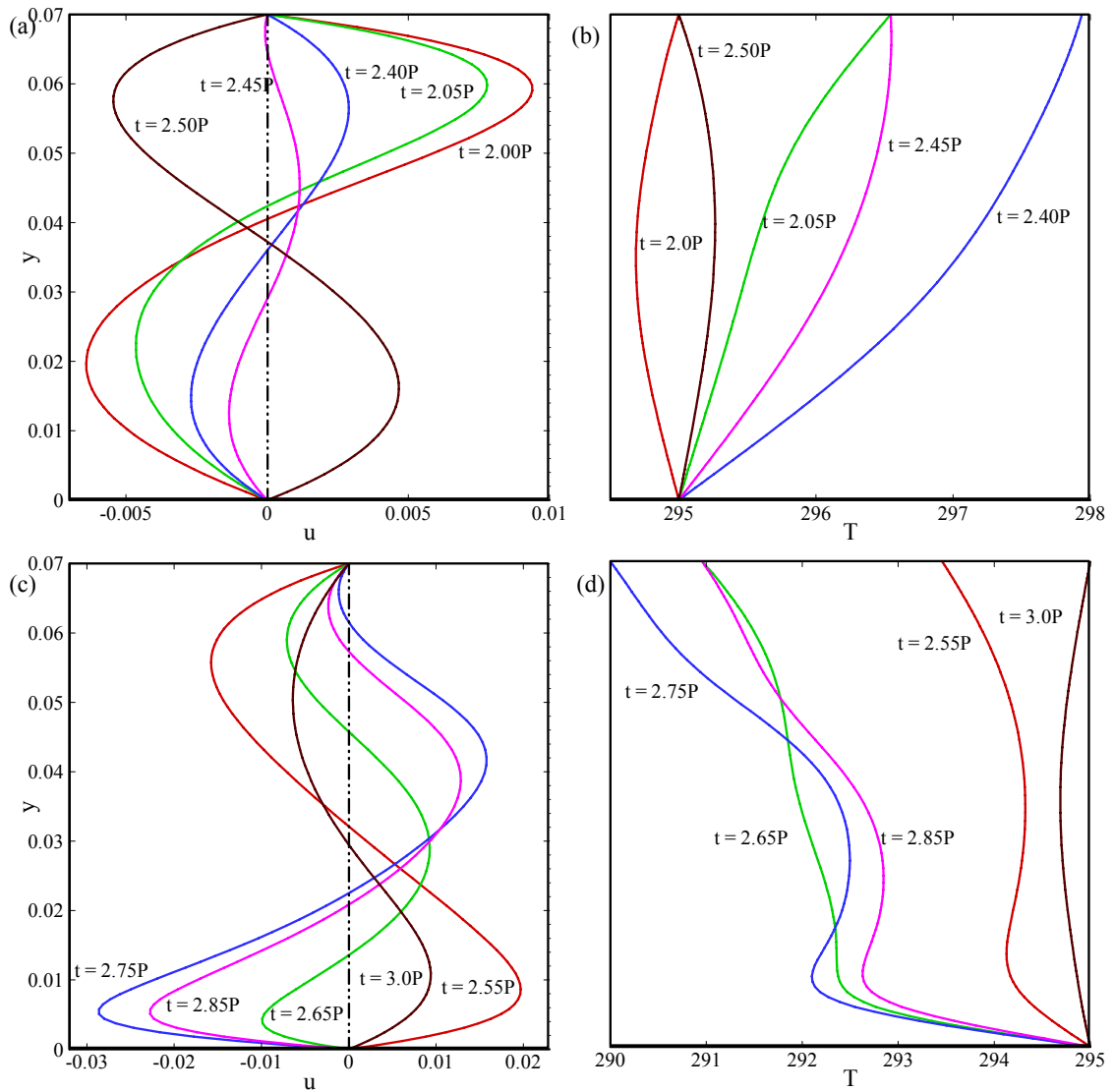
Figure7.4 Horizontal velocity profile (left) and temperature profile (right) along *DE* for *A* = 0.5 with *Ra* = 1.5×10^6.

The horizontal velocity profiles (velocity parallel to the bottom surface) and the corresponding temperature profiles evaluated along the line *DE* shown in Figure 7.2 at different time instances of the third thermal forcing cycle are depicted in Figure 7.4. At the beginning of the cycle ($t = 2.00P$) the velocity is the highest near the roof of the attic (see Figure 7.4a), which is the surface driving the flow. At the same time, the body of fluid residing outside the top wall layer moves fast toward the bottom tips to fill up

the gap. As time progresses the vertical velocity increases and the horizontal temperature decreases (see t = 2.05P). A three layer structure in the velocity field is found at t = 2.45P. At this time the top portion of the cavity is locally cooled and the bottom portion is still hot (see Figure 7.3). After that time the flow completely reverses at t = 2.50P. It is noted that at this time the horizontal velocity is lower than that at the beginning of the cycle despite that the temperatures on the sloping boundary and the ceiling are the same at both times (see Figure 7.4b). This is due to the fact that at the beginning of the cycle the flow is mainly dominated by convection as a result of the cooling effect in the second half of the previous thermal cycle. However, the flow is dominated by conduction at t = 2.50P as a result of the heating effect in the first half of the current thermal cycle.

As mentioned above, at the beginning of the cycle (t = 2.00P) the temperatures on the horizontal and inclined surfaces are the same as shown in Figure 7.4(b). However the temperature near the mid point of the profile line is lower than that at the surfaces by approximately 0.5K, which is consistent with the previous discussion of the flow field. Subsequently the temperature of the top surface increases (t = 2.05P) while the bottom surface temperature remains the same. It is noteworthy that the top surface reaches its peak temperature at t = 2.25P (for brevity the profile is not included). After this time the top surface temperature starts to decrease which can be seen at time t = 2.40P. By comparing the temperature profiles at t = 2.05P and t = 2.45P shown in Figure 7.4(b), it is clear that the temperatures at both the top and bottom surfaces are the same for these two time instances. However, different temperature structures are seen in the interior region. The same phenomenon has been found at the times t = 2.50P and t = 2.00P.

In Figure 7.4(c), the velocity profiles at the same location during the night-time cooling phase are displayed. In this phase the flow structure is more complicated. At t = 2.55P the velocity near the bottom surface is slightly higher than that near the top. Again a three layer structure of the velocity field appeared which is seen at t = 2.65P, 2.75P and 2.85P. The maximum velocity near the ceiling occurs at t = 2.75P when the cooling is at its maximum. After that it decreases and the flow reverses completely at t = 3.0P. The corresponding temperature profiles for the night-time condition are shown in Figure 7.4(d). It is seen that the temperature lines are not as smooth as those observed for the daytime condition. At t = 2.55P, the temperature near the bottom surface decreases first and then increases slowly with the height and again decreases

near the incline surface. This behaviour near the bottom surface is due to the presence of a rising plume. Similar behaviour has been seen for $t = 2.75P$ and $2.85P$. However, at $t = 2.65P$ it decreases slowly after rapidly decreasing near the bottom surface. At $t = 3.00P$ again the bottom and top surface temperatures are the same with a lower temperature in the interior region.

7.3.2 Heat transfer through the attic

The Nusselt number, which has practical significance, is calculated as follows:

$$Nu = \frac{h_{\text{eff}} h}{k},$$ (7.9)

where the heat transfer coefficient h_{eff} is defined by

$$h_{\text{eff}} = \frac{q}{T_A}.$$ (7.10)

Here q is the convective heat flux through a boundary. Since the bottom surface temperature is fixed at 295K and the sloping wall surface temperature cycles between 290K and 300K (refer to Figure 7.1), a zero temperature difference between the surfaces occurs twice in a cycle. Therefore, the amplitude of the temperature fluctuation (T_A) is chosen for calculating the heat transfer coefficient instead of a changing temperature difference, which would give an undefined value of the heat transfer coefficient at particular times.

Figure 7.5 shows the calculated average Nusselt number on the inclined and bottom surfaces of the cavity. The time histories of the calculated Nusselt number on the inclined surfaces exhibit certain significant features. Firstly, it shows a periodic behaviour in response to the periodic thermal forcing. Secondly within each cycle of the flow response, there is a time period with weak heat transfer and a period with intensive heat transfer. The weak heat transfer corresponds to the daytime condition when the flow is mainly dominated by conduction and the strong heat transfer corresponds to the night-time condition. At night, the boundary layers adjacent to the inclined walls and the bottom are unstable. Therefore, sinking and rising plumes are formed in the inclined and horizontal boundary layers. These plumes dominate the heat transfer through the sloping walls of the cavity. Finally the calculated maximum Nusselt number on sloping surfaces is 8.72, occurring during the night-time period,

whereas the maximum value during the day time is only 3.48, for the selected Rayleigh number and aspect ratio.

The corresponding Nusselt number calculated on the bottom surface shows similar behavior as that of top surfaces. Note that the Nusselt number calculated using (7.9) is based on the total heat flux across the surfaces. Since the surface area of the top surface is larger ($0.595m^2$) than the bottom surface ($0.532m^2$), therefore the total surface heat flux on the top surfaces will be lower than that of the bottom surface. However, the integral of the heat transfer rate for a cycle on both surfaces has been calculated and it is found that both are the same.
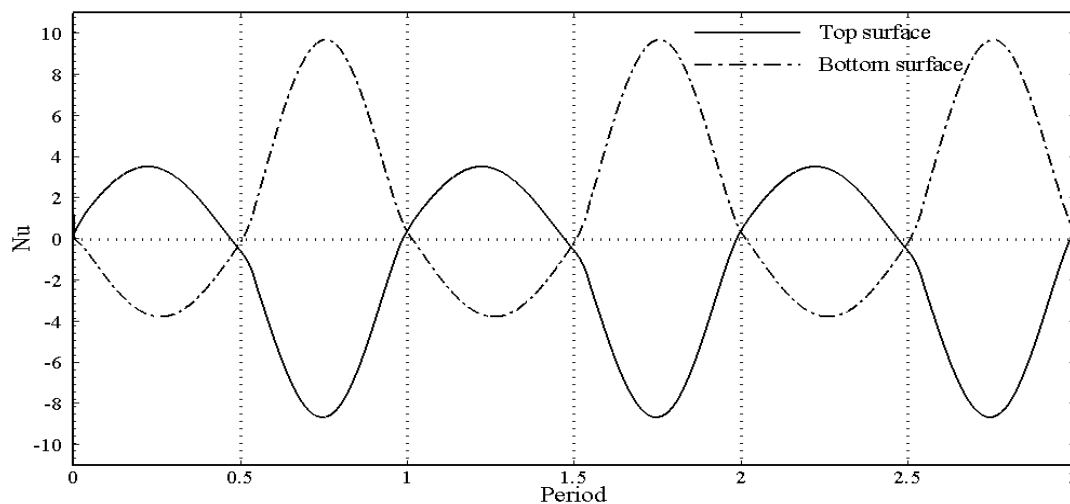
Figure 7.5 Average Nusselt number on the top and bottom surfaces of the cavity for three full cycles where $Ra = 1.5 \times 10^6$ and $A = 0.5$, $Pr = 0.72$.

7.3.3 Effect of the aspect ratio on the flow response

The flow responses to the periodic thermal forcing for the other two aspect ratios are shown in Figure 7.6 and 7.7, which are compared with the flow response for $A = 0.5$ shown in Figure 7.3. It is found that the aspect ratio of the enclosure has a great influence on the flow response as well as heat transfer. The residual effect of the previous cycle on the current cycle has been found similar for all aspect ratios (see at t $=2.0P$ in Figures 7.3, 7.6 and 7.7) and the flow and temperature structures during the heating process is qualitatively the same for $A = 1.0$ and $A = 0.2$ as those for $A = 0.5$ for $Ra = 1.5 \times 10^6$. However, during the cooling phase there are significant changes of flow and heat transfer among these aspect ratios. For the night-time the high velocity area of

these three aspect ratios exists between the two cells where the stream function gradient is higher. Therefore, the buoyancy drives the warm air upwards from the bottom of the geometry and at the same time the gravitational force acts on the cold air downwards from the top. This upward and downward movement can be seen in the temperature contours as a form of rising and sinking plumes.
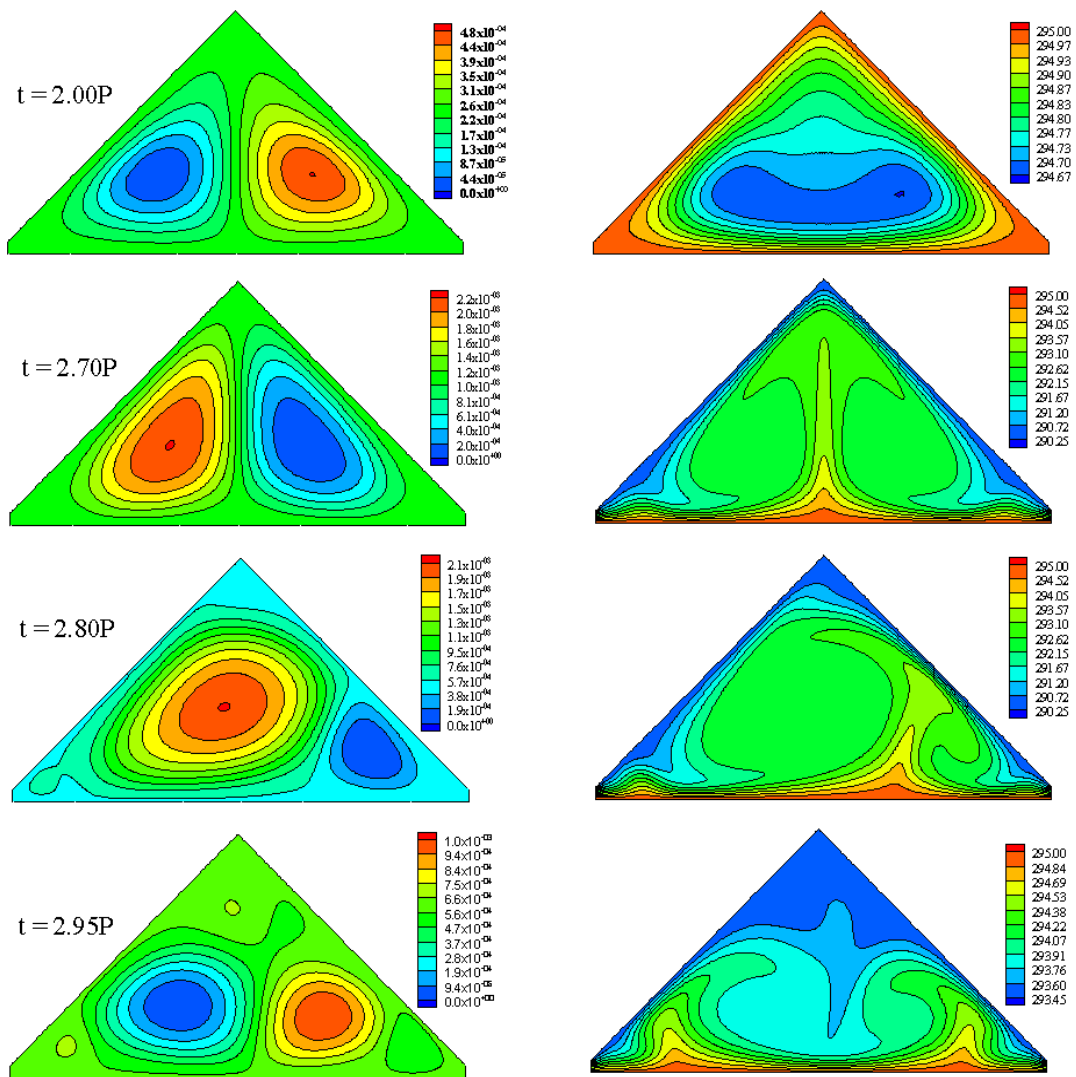
Figure 7.6 A series of snapshots of stream function and temperature contours of the third cycle at different times for $A = 1.0$ and $Ra = 1.5{\times}10^{6}$. Left: streamlines; right: isotherms.

It has been revealed that the flow remains symmetric about the geometrical centreline throughout the cycle for aspect ratio $A = 0.2$, whereas, it is asymmetric during the cooling phase for the other two aspect ratios for $Ra = 1.5{\times}10^{6}$. It is also

anticipated that the asymmetric solution is one of two possible mirror images of the solutions. Another noticeable variation with different aspect ratios is the formation of a circulation cell near the top of the enclosure. It is seen for $A = 1.0$ that there is an extra vortex (Figure 7.6 at $t = 2.95P$) on the top of the cavity, which is completely absent for $A = 0.5$ and $A = 0.2$. The flow and temperature fields for the smallest aspect ratio $A = 0.2$ are more complex, with several circulation cells on either side of the central line and many plumes alternately rising and falling throughout the domain, as seen in Figure 7.7. These cells and plumes are the result of flow instability described earlier.
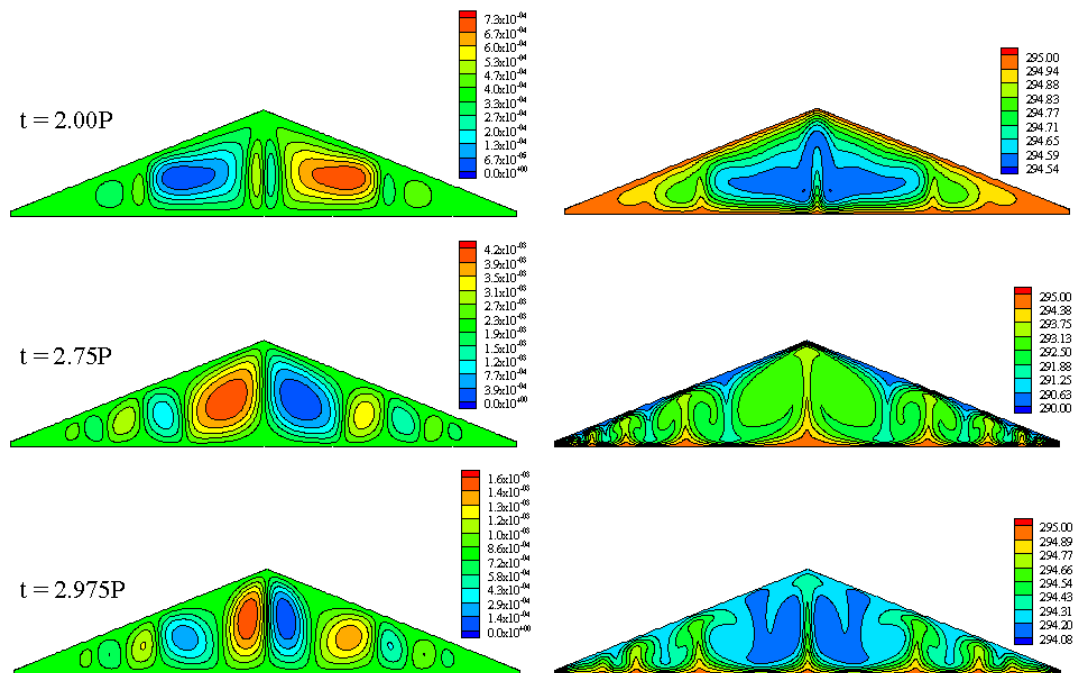
Figure 7.7 A series of snapshots of stream function and temperature contours of the third cycle at different times for $A = 0.2$ and $Ra = 1.5 \times 10^6$. Left: streamlines; right: isotherms.

Figure 7.8 illustrates the horizontal velocity and temperature profiles for aspect ratio $A = 1.0$ along the line DE as shown in Figure 7.2 for $Ra = 1.50 \times 10^6$. Since the flow is stable and stratified during the day (the heating phase), the structures of the velocity and temperature profiles are qualitatively the same as those for other aspect ratios.
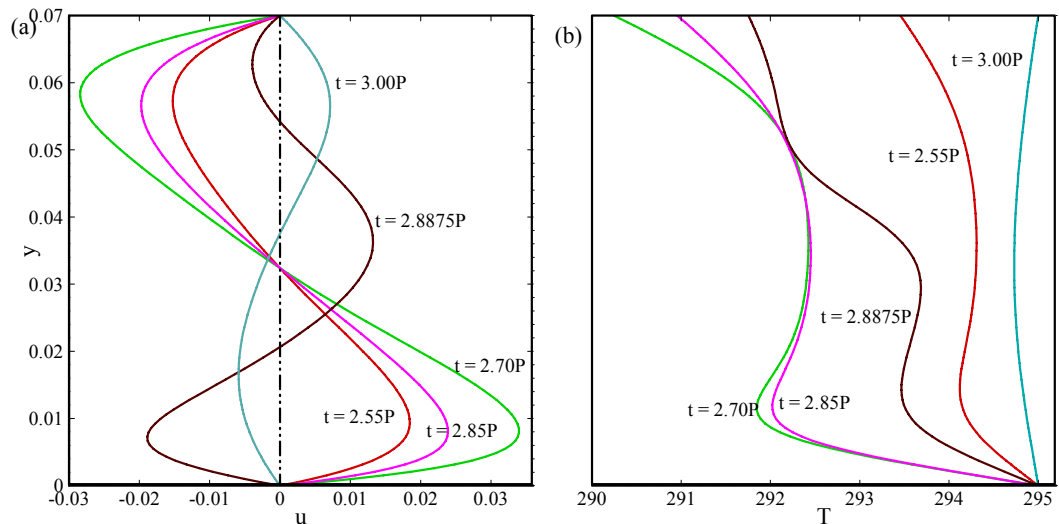
Figure 7.8 Horizontal velocity profile (left) and temperature profile (right) along *DE* for
A = 1.0 with *Ra* = 1.50×10⁶.

At the night-time the velocity and temperature profiles for *A* = 1.0 are more complicated than that for *A* = 0.5. As seen in Figure 7.8, at time *t* = 2.55P when the upper surface temperature is lower than the bottom surface, the velocity near the bottom surface is slightly higher than that near the inclined surfaces. After that the velocity increases near both the surfaces until *t* = 2.75P. Since a plume-type instability dominates the flow during the cooling phase and the flow has an asymmetric behaviour for a certain period of time, the horizontal velocity is in the same direction near both surfaces and is in an opposite direction in the middle (see *t* = 2.8875P). As the flow transits into the next thermal cycle, it becomes very weak. The corresponding temperature contours are plotted in Figure 7.8(b). It is seen that the temperature profiles near the bottom surface show a wave shaped for almost the whole cooling phase due to the rising plumes (see Figure 7.3). At the time *t* = 2.8875P, when three layers of the velocity structure is seen, the corresponding temperature profile also shows a wave structure.
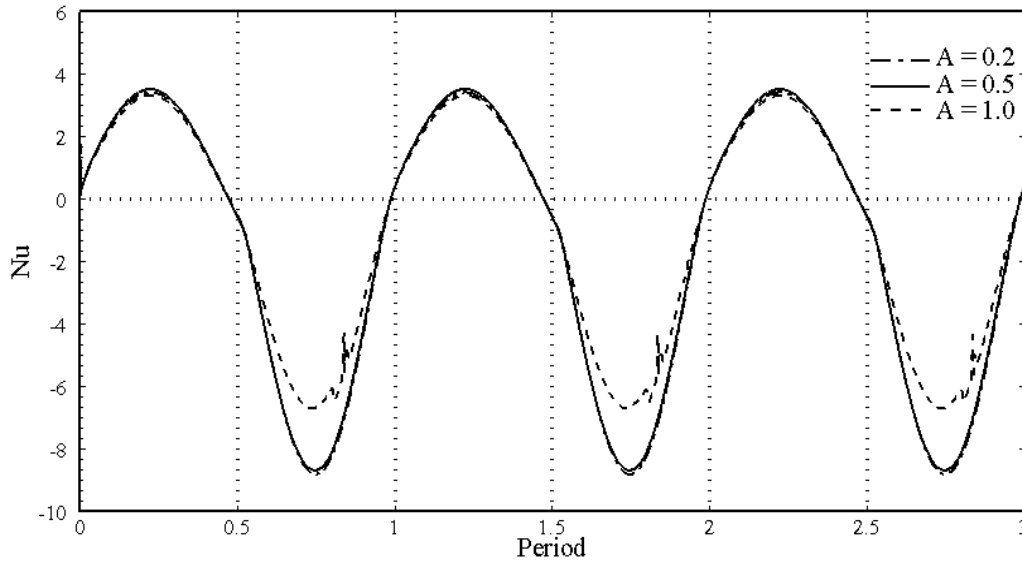
Figure 7.9 Comparison of the average Nusselt number of three aspect ratios for *Ra* = 1.5×10^6 and *Pr* =0.72.

Figure 7.9 shows the calculated average Nusselt number on the inclined surfaces of the cavity for three different aspect ratios. The time histories of the calculated Nusselt number exhibit certain common features. Within each cycle of the flow response, there is a time period with weak heat transfer and a period with intensive heat transfer for each aspect ratio. The weak heat transfer corresponds to the day time condition when the heat transfer is dominated by conduction and the strong heat transfer corresponds to the night-time condition when convection dominates the flows and the instabilities occur in the form of rising and sinking plumes. During the day time the heat transfer rate is almost the same for all three aspect ratios. However, at the night time the heat transfer rate for *A* =1.0 is much smaller than that for the other two aspect ratios, and there is a fluctuation of the Nusselt number for a certain period of time. This fluctuation is absent in the other two aspect ratios. This may be due to the fact that less convective cells are present in the streamlines for *A* = 1.0 than those for the other two aspect ratios. Moreover, the movement of the dominating cell for *A* = 1.0 is faster than those for other two. In addition to this, an extra cell appears on the top of the cavity for the aspect ratio *A* = 1.0. It is also noticed that there is not much difference in heat transfer for the aspect ratios *A* = 0.5 and 0.2. The highest average Nusselt numbers for *A* = 1.0, 0.5 and 0.2 are 6.55, 8.72 and 8.76 respectively.

7.3.4 Dependence of flow response and heat transfer on the Rayleigh number

Figure 7.10 shows snapshots of stream function and temperature contours for the aspect ratio 0.5 with three different Rayleigh numbers, $Ra = 1.5 \times 10^6$, 7.2×10^4 and 7.2×10^3. The contours for $Ra = 7.2 \times 10^5$ are qualitatively the same as for $Ra = 1.5 \times 10^6$. It is found that in the heating phase (i.e. when the upper wall temperature is higher than the temperature of the bottom) the flow structures are qualitatively similar for different Rayleigh numbers. However, in the cooling phase the flow behaviour is strongly dependent on the Rayleigh number. Stream function and temperature contours are presented at two different times, $t = 2.70P$ and $2.95P$ for each Rayleigh number in Figure 7.10. In the isotherms, rising and sinking plumes are visible for $Ra = 1.5 \times 10^6$ and 7.2×10^4 at both times. A cellular flow pattern is seen in the corresponding stream function contours for $Ra = 1.5 \times 10^6$. However, only two convective cells are present for $Ra = 7.2 \times 10^4$. If the Rayleigh number is decreased further ($Ra = 7.2 \times 10^3$), the flow becomes weaker. Only two cells are seen in the stream function contours and the temperature field is horizontally stratified (see the corresponding isotherms). At $t = 2.95P$, the flow seems to be asymmetric along the centre line for $Ra = 1.5 \times 10^6$. However, for the lower Rayleigh numbers the asymmetric behaviour is not visible.
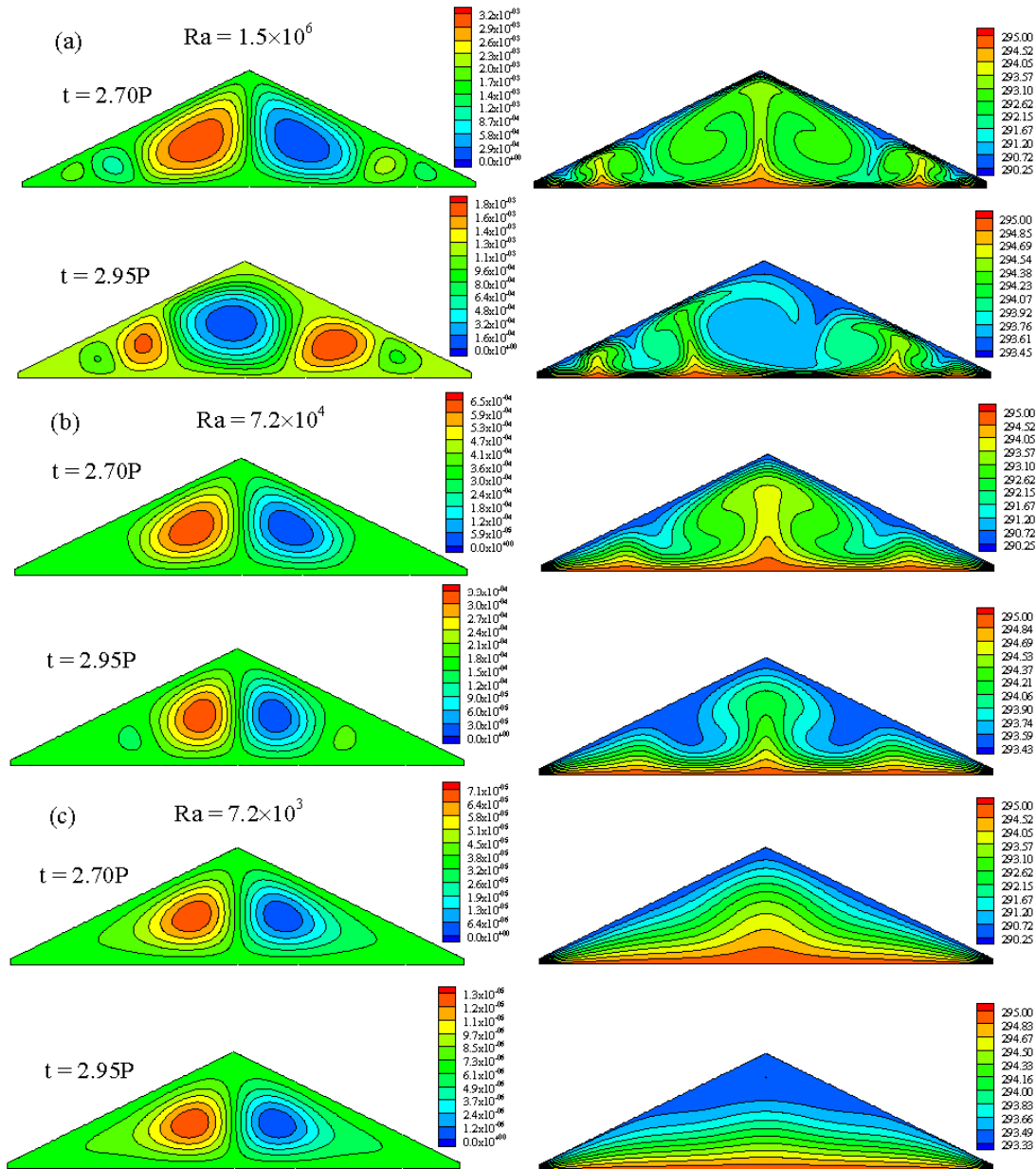
Figure 7.10 Snapshots of stream function contours (left) and isotherms (right) of the third cycle at different times and different Rayleigh numbers with fixed *A* = 0.5.

Figure 7.11 shows the comparison of the Nusselt number among four Rayleigh numbers for a fixed aspect ratio 0.5. It is seen clearly that during the heating phase the heat transfer rate is weaker, whereas it is much stronger in the cooling phase. With the increase of the Rayleigh number, the Nusselt number increases throughout the thermal cycle, but the rate of increase is much higher in the cooling phase compared to that in the heating phase. The maximum Nusselt number in the cooling phase for *Ra* = 1.5×10^6 is about 2.5 times of the maximum Nusselt number during the heating phase. It is

noticeable that for the lowest Rayleigh number $Ra = 1.5 \times 10^3$, the heat transfer rate during the heating and cooling phases are almost the same. The maximum Nusselt number for the four different Rayleigh numbers, $Ra = 1.5 \times 10^6$, 7.2×10^5, 7.2×10^4 and 7.2×10^3 for the aspect ratio 0.5 are 8.65, 7.34, 4.26 and 3.11 respectively.
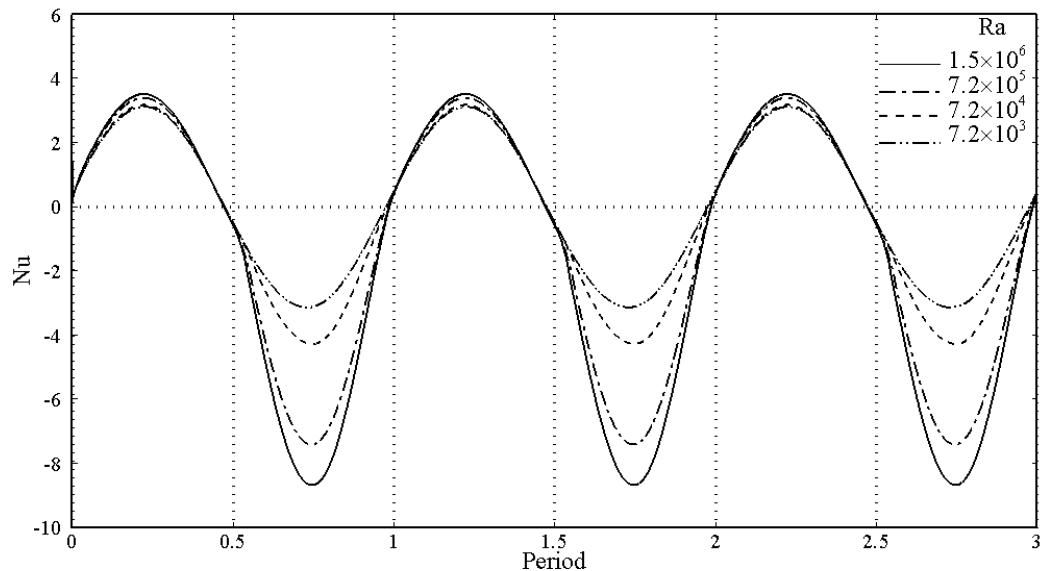
Figure 7.11 Comparison of the average Nusselt number of four Rayleigh numbers for *A* = 0.5 and *Pr* = 0.72

7.3.5 Transition between symmetric and asymmetric flows

The highest Rayleigh number considered in this study for the three aspect ratios is 1.5×10^6. Except for $A = 0.2$, the flow in the cavity for the other two aspect ratios is observed to undergo a supercritical pitchfork bifurcation for this Rayleigh number, in which case one of two possible mirror image asymmetric solutions is obtained. This asymmetric behaviour was first reported numerically and experimentally by Holtzman *et al.* (2000) in their study of the case of a sudden cooling boundary condition. If the flow is asymmetric, the horizontal velocity along the midplane of the isosceles triangle would be nonzero. Based on this hypothesis, Figure 7.12 illustrates the absolute value of maximum horizontal velocity along the geometric center line for $A = 1.0$ and 0.5. It is seen in this figure that, for both aspect ratios, the maximum horizontal velocity is zero up to approximately $t = 0.70P$ in each cycle, suggesting that the flow is symmetric during this time. However, after this time the maximum horizontal velocity starts to

increase, indicating that the flow becomes asymmetric. The asymmetry remains until shortly before the end of each cycle when the flow returns to symmetric again. The same asymmetric behaviour of the flow is seen for the Rayleigh number 7.2×10^5 for the aspect ratios 0.5 and 1.0.
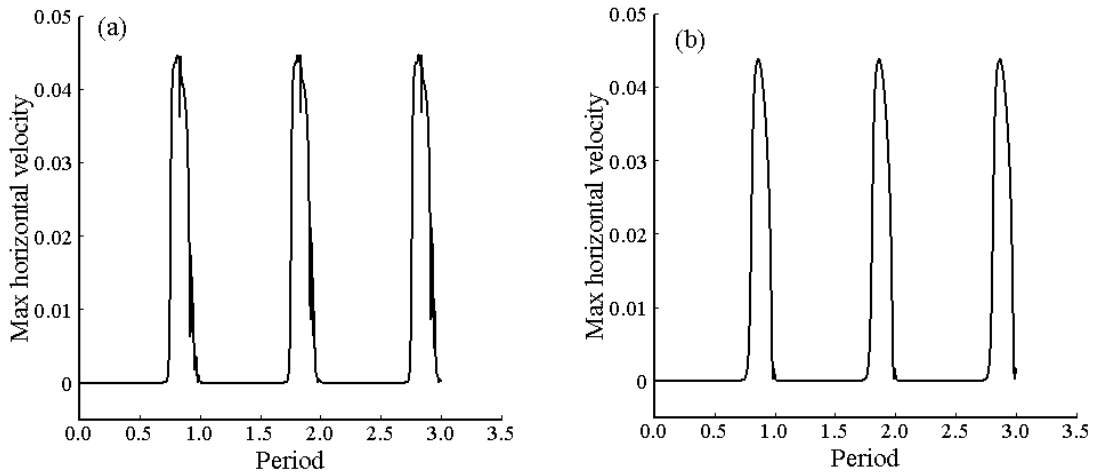
Figure 7.12 The maximum horizontal velocity along the symmetry line for (a) $A = 1.0$ and (b) $A = 0.5$ with $Ra = 1.5 \times 10^6$.

The same results have been found when the average Nusselt numbers obtained for both inclined surfaces are compared for the aspect ratios 1.0 and 0.5, which are shown in Figures 7.13 (a) and (b) respectively. It is seen that at about $t = 0.70P$, the calculated Nusselt numbers at the left and right inclined surfaces start to diverge, but later they meet again before the end of each cycle.
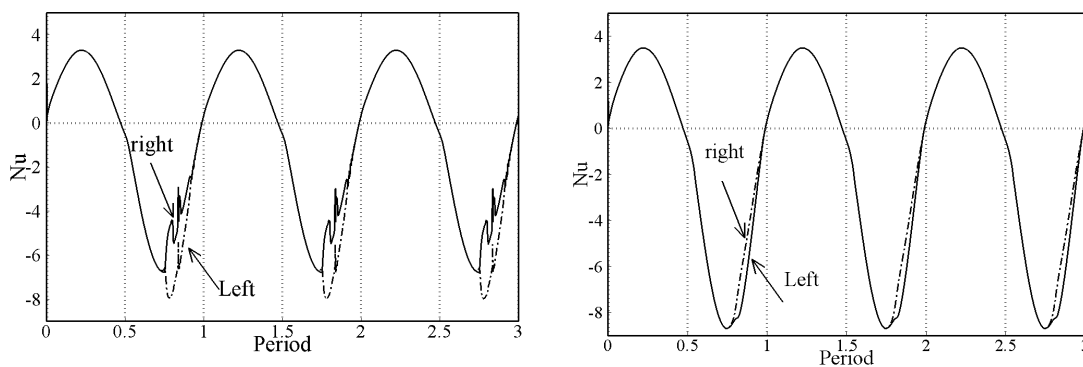
Figure 7.13 Comparison of the average Nusselt number on two inclined surfaces of the enclosure for (a) $A = 1.0$ and (b) $A = 0.5$ with $Ra = 1.5 \times 10^6$

7.4 Summary

Natural convection in an attic space subject to periodic thermal forcing has been described in this study based on numerical simulations. Three aspect ratios of A = 1.0, 0.5 and 0.2 with four Rayleigh numbers of Ra = $1.5{\times}10^6$, $7.2{\times}10^5$, $7.2{\times}10^4$ and $7.2{\times}10^3$ for each aspect ratio have been considered here. Many important features are revealed from the present numerical simulations. It is found that the flow response to the temperature variation on the external surface is fast, and thus the start-up effect is almost negligible. The occurrence of sinking cold-air plumes and rising hot-air plumes in the isotherm contours and the formation of cellular flow patterns in the stream function contours confirm the presence of the Rayleigh-Bénard type instability. It is also observed that the flow undergoes a transition between symmetry and asymmetry about the geometric symmetry plane over a diurnal cycle for the aspect ratios of A = 1.0 and 0.5 with the Rayleigh numbers $1.5{\times}10^6$ and $7.2{\times}10^5$. For all other cases the flow remains symmetric. A three-layer velocity structure has been found along the line at *DE* as shown in Figure 7.2 in both the daytime heating phase (due to local cooling effect in the upper sections of the inclined walls) and night-time cooling phase when the flow becomes asymmetric. Furthermore, the flow response in the daytime heating phase is weak, whereas the flow response in the night-time cooling phase, which is dominated by convection, is intensive. At lower Rayleigh numbers the flow becomes weaker for all aspect ratios, and no asymmetric flow behaviour has been noticed.

8. Conclusions

In this thesis, scaling and numerical analyses are employed to investigate transient natural convection in the boundary layer adjacent to an inclined flat plate and in an attic space under various forms of thermal forcing. Extensive scaling relations of the flow parameters have been derived for sudden and ramp heating/cooling boundary conditions and verified by numerical simulations. The major findings from the present study are summarized in this chapter and recommendations for future investigations are also made at the end of this chapter.

8.1 Summary of the research

8.1.1 Natural convection adjacent to an inclined plate

Natural convection adjacent to a heated inclined flat plate is examined by scaling analysis and verified by numerical simulations for air ($Pr = 0.72$) in Chapter 3. It is found that the flow development is mainly dominated by three distinct stages for the sudden heating boundary condition, i.e. the start-up stage, the transitional stage and the steady stage. The scaling relations are formed based on the established characteristic flow parameters of the maximum velocity inside the boundary layer (u_s), the time for the boundary layer to reach the steady state (t_s) and the thermal (δ_T) and viscous (δ_v) boundary layer thicknesses. Through comparisons of those scaling assumptions with the numerical simulations, it is found that the scaling results agree very well with the numerical simulations.

A temperature boundary condition of a ramp function which is applied on the inclined plate has also been investigated for the same problem. The boundary layer flow for this boundary condition depends on the comparison of the time at which the ramp heating is completed with the time at which the boundary layer completes its growth. If the ramp time is long compared with the steady state time, the thermal boundary layer reaches a quasi-steady mode in which the growth of the layer is governed by the thermal balance between convection and conduction. On the other hand, if the ramp is completed before the thermal boundary layer becomes steady, the subsequent growth is governed by the balance between buoyancy and inertia, as for the case of sudden heating. Several scaling relations have been established in this study,

which include the maximum velocity parallel to the inclined plate inside the boundary layer (u) at the transient stage and at the quasi-steady mode, the time for the boundary layer to reach the quasi-steady state (t_{sr}) and the thermal and viscous boundary layer thicknesses (δ_T and δ_v) at the transient stage and quasi-steady mode. The comparisons between the scaling relations and the numerical simulations demonstrate that the scaling results agree very well with the numerical simulations.

Natural convection adjacent to a cooled inclined flat plate is also examined by scaling analysis with numerical verification in Chapter 4. Two types of cooling boundary condition are considered: sudden cooling and ramp cooling. It is noticed that for sudden cooling, as soon as the cold temperature is applied to the inclined plate, a cold boundary layer is formed. This boundary layer is potentially unstable to Rayleigh-Bénard instability if the Rayleigh number exceeds a certain critical value. A prediction of the onset of instability has been achieved through scaling analysis. Different flow regimes for sudden cooling based on the Rayleigh number are developed and discussed with numerical results in this chapter. It is found that the scaling results agree very well with the numerical results.

Similarly to the sudden cooling case, the cooling boundary layer for the ramp cooling boundary condition is also unstable to the Rayleigh-Bénard instability if the Rayleigh number exceeds a certain critical value. The instability, which is governed by a local Rayleigh number across the boundary layer, may occur in different flow regimes classified based on the global Rayleigh number. The instability may set in before the quasi-steady time, after the quasi-steady time or after the ramp is finished if the ramp time is shorter than the steady state time. Several scaling relations have been established in this case including the onset time of instability for different flow regimes. The comparisons between the scaling relations and the numerical simulations also demonstrate that the scaling results agree very well with the numerical simulations.

8.1.2 Natural convection in an attic space

Natural convection in an attic space subject to heating on the inclined surfaces is examined by scaling analysis and verified by numerical simulations in Chapter 5. It is found that the flow is mainly dominated by four distinct stages for the sudden heating boundary condition, i.e. start-up stage, transitional stage, steady state stage of the boundary layer and heating-up stage of the entire cavity. A heat transfer scale, in the

form of a surface Nusselt number (Nu_s), at the boundary layer development stage is developed. The heating-up time (t_f) scale and the Nusselt number scale at the heating-up stage are also developed. The scaling results agree very well with the numerical simulations.

Furthermore, natural convection in an attic space subject to heating with a temperature boundary condition of a ramp function on the inclined walls has also been investigated in Chapter 5. Similarly to the sudden heating case, a heat transfer scale in the form of a Nusselt number (Nu_{sr} and Nu_{ins}), the heating-up time scale (t_{fr}) and the Nusselt number scale at the heating-up stage are also established. The comparisons between the scaling relations and the numerical simulations demonstrate that the scaling results agree very well with the numerical simulations.

A set of scaling results have also been developed for natural convection in an attic space subject to cooling on the inclined surfaces and are verified by numerical simulations in Chapter 6. The heat transfer through the sloping walls has been calculated in the form of a scaling relation during the boundary layer development. A time scale (t_{fc}) is established when the entire cavity is filled with cold fluid. The Nusselt number scale at the cooling-down time is also obtained. The scaling results agree very well with the numerical simulations.

In addition, cooling with a ramp temperature boundary condition applied to the inclined walls has also been investigated in this chapter. Like sudden cooling case, the scaling of heat transfer through the inclined surfaces and the cooling-down time scale for the enclosure have been developed in this chapter. The heat transfer scale at the cooling down stage is also derived. The comparisons between the scaling predictions and the numerical simulations demonstrate that the scaling results agree very well with the numerical simulations.

Natural convection in an attic space subject to periodic thermal forcing has been described in Chapter 7 based on numerical simulations. Three aspect ratios of $A = 1.0$, 0.5 and 0.2 with four Rayleigh numbers of $Ra = 1.5 \times 10^6$, 7.2×10^5, 7.2×10^4 and 7.2×10^3 are considered. Many important features are revealed from the present numerical simulations. It is found that the flow response to the temperature variation on the external surface is fast, and thus the start-up effect is almost negligible. The occurrence of sinking cold-air plumes and rising hot-air plumes observed in the isotherms and the formation of cellular flow patterns in the stream function contours confirm the presence

of the Rayleigh-Bénard type instability. It is also observed that the flow undergoes a transition between symmetry and asymmetry about the geometric symmetry plane over a diurnal cycle for the aspect ratios of $A = 1.0$ and 0.5 with Rayleigh numbers 1.5×10^6 and 7.2×10^5. For all other cases the flow remains symmetric. A three-layer velocity structure has been found in the enclosure in both the daytime heating phase and night-time cooling phase. Furthermore, the daytime responding flow is weak, whereas the night-time responding flow, which is dominated by convection, is intensive. For lower Rayleigh numbers the flow becomes weaker for these three aspect ratios and no asymmetric flow behaviour has been noticed.

8.2 Future studies

Significant progress regarding the transient natural convection boundary layer adjacent to an inclined flat plate and in an attic space has been achieved in this study. However, some new areas related to attic space are worth investigating in future studies.

In the attic space problem we assumed that the flow is two dimensional in this thesis. However, in real situation the flow may have some three dimensional effect which is worth further studying. Moreover, we used a sine function of the temperature to define the day-night temperature effect on the roof which is applicable for the east faces or west faces of buildings. But in reality, buildings are built with different faces. Therefore, the sun rays do not project at the same angle on the entire roof. A complex and more realistic temperature boundary condition may be defined for further studies. In addition, radiation effects need to be considered in future investigations.

Since the focus of this study was the attic space problem, we chose a single Prandtl number (0.72) for the verification of the scaling relation. We may extend this study by considering a wide range of Prandtl numbers which are less than or greater than unity. Moreover, scaling analysis has been performed for the sudden heating/cooling and ramp heating/cooling boundary conditions on the sloping walls of the attic space. A further investigation of the scaling analysis may include the diurnal (periodic) temperature boundary condition.

References

Akinsete, V. A. and Coleman, T. A. (1982), "Heat transfer by steady laminar free convection in triangular enclosures." *Int. J. Heat Mass Transfer* **25**: 991-998.

Asan, H. and Namli, L. (2000), "Laminar natural convection in a pitched roof of triangular cross-section: summer day boundary conditions." *Energy and Buildings* **33**: 69-73.

Asan, H. and Namli, L. (2001), "Numerical simulation of buoyant flow in a roof of triangular cross-section under winter day boundary conditions." *Energy and Buildings* **33**: 753-757.

Basak, T., Roy, S. and Trirumalesha, C. (2007), "Finite element analysis of natural convection in a triangular elclosure: Effects of various thermal boundary conditions." *Chemical Engineering Science* **62**: 2623-2640.

Batchelor, G. K. (1954), "Heat transfer by free convection across a closed cavity between vertical boundaries at different temperature." *Quart. Appl. Math.* **12**: 209-233.

Bejan, A. and Poulikakos, D. (1982), "Natural convection in an attic shaped space filled with porous material." *Trans. ASME C: J. Heat Transfer* **104**: 241-247.

Bodenschartz, E., Pesch, W. and Ahlers, G. (2000), "Recent developments in Rayleigh Benard convection." *Annu. Rev. Fluid Mech.* **32**: 709-778.

Catton, I. (1979), "Natural convection in enclosures". *Proc. 6th International Heat Transfer Conference, 1978*, Toronto.

Chandrasekhar, S. (1961). "Hydrodynamic and Hydromagnetic Stability", Dover.

Chen, C. C., Labhabi, A., Chang, H. C. and Kelly, R. E. (1991), "Spanwise pairing of finite-amplitude longitudinal vortex rolls in inclined free-convection boundary layers." *J. Fluid Mech.* **231**: 73-111.

Chen, T. S. and Tzuoo, K. L. (1982), "Vortex instability of free convection flow over horizontal and inclined surfaces." *Trans. ASME C: J. Heat Transfer* **104**: 637-643.

Chen, Y. M. and Pearlstein, A. J. (1989), "Stability of free-convection flows of variable-viscosity fluids in vertical and inclined slots." *J. Fluid Mech.* **198**: 513-541.

Cheng, K.C. and Kim, Y. M. (1988), "Flow visualization studies on vortex instability of natural convection flow over horizontal and slightly inclined constant-temperature plates." *Trans. ASME C: J. Heat Transfer* **110**: 608-615.

Drazin, P. G. and Reid, W. H. (1981). "Hydrodynamic Stability", Cambridge University Press.

Farrow, D. E. (2004), "Periodically forced natural convection over slowly varying topography." *J. Fluid Mech.* **508**: 1-21.

Farrow, D. E. and Patterson, J. C. (1993a), "On the response of a reservoir sidearm to diurnal heating and cooling." *J. Fluid Mech.* **246**: 143-161.

Farrow, D. E. and Patterson, J. C. (1993b), "On the stability of the near shore waters of a lake when subject to solar heating." *Intl J. Heat Mass Transfer* **36**: 89-100.

Farrow, D. E. and Patterson, J. C. (1994), "The daytime circulation and temperature structure in a reservoir sidearm." *Intl J. Heat Mass Transfer* **37**: 1957-1968.

Flack, R. D. (1980), "The experimental measurement of natural convection heat transfer in triangular enclosures heated or cooled from bellow." *ASME Journal of heat transfer* **102**: 770-772.

Gebhart, B., Jaluria, Y., Mahajan, R. L. and Sammakia, B. (1988). "Buoyancy-induced flows and transport". Hamisphere, Washington, DC.

Haaland, S. E. and Sparrow, E. M. (1973), "Vortex instability of natural convection flow on inclined surfaces." *Int. J. Heat Mass Transfer* **16**: 2355-2367.

Haese, P. M. and Teubner, M. D. (2002), "Heat exchange in an attic space." *Int. J. Heat Mass Transfer* **45**: 4925-4936.

Holtzman, G. A., Hill, R. W. and Ball, K. S. (2000), "Laminar natural convection in isosceles triangular enclosures heated from bellow and symmetrically cooled from above." *ASME Journal of heat transfer* **122**: 485-491.

Horsch, G. M. and Stefan, H. G. (1988a), "Convective circulation in littoral water due to surface cooling." *Limnol. Oceanogr.* **33**: 1068-1083.

Horsch, G. M. and Stefan, H. G. (1988b), "Cooling-induced natural convection in a triangular enclosure as a model for littoral circulation." *Coputational Methods in Water Resources, Elsevier, Amsterdam.* **1**: 307-312.

Horsch, G. M., Stefan, H. G. and Gavali, S. (1994), "Numerical simulation of cooling-induced convective currents on a littoral slope." *Intl J. Numer. Meth. Fluids* **19**: 105-134.

Hyun, J. M. (1994), "Unsteady buoyant convection in an enclosure." *Adv. Heat Transfe* **24**: 277-320.

Iyer, P. A. and Kelly, R. E. (1974), "The stability of the laminar free convection flow induced by a heated inclined plate." *Int. J. Heat Mass Transfer* **17**: 517-525.

Jones, D. R. (1973), "Free convection from a semi-infinite flat plate inclined at a small angle to the horizontal." *Quart. Jonrn. Mech. and Applied Math.* **XXVI**: 77-98.

Koca, A., Oztop, H. F. and Varol, Y. (2007), "The effects of Prandtl number on natural convection in triangular enclosures with localized heating from below." *Int. Comm. Heat Mass Transfer* **34**: 511-519.

Kurzweg, U. H. (1970), "Stability of natural convection within an inclined channel." *Trans. ASME C: J. Heat Transfer* **92**: 190-191.

Lei, C., Armfield, S. and Patterson, J. C. (2008), "Unsteady natural convection in a water-filled isosceles triangular enclosure heated from below." *Int. J. Heat Mass Transfer* **51**: 2637-2650.

Lei, C. and Patterson, J. C. (2002a), "Natural convection in a reservoir sidearm subject to solar radiation: A two dimensional simulation." *Numerical Heat Transfer, Part A.* **42**: 13-32.

Lei, C. and Patterson, J. C. (2002b), "Natural convection in a reservoir sidearm subject to solar radiation: experimental observations." *Exps. Fluids* **32**: 590-599.

Lei, C. and Patterson, J. C. (2002c), "Unsteady natural convection in a triangular enclosure induced by absorption of radiation." *J. Fluid Mech.* **460**: 181-209.

Lei, C. and Patterson, J. C. (2003a), "A direct stability analysis of a radiation-induced natural convection boundary layer in a shallow wedge." *J. Fluid Mech.* **480**: 161-184.

Lei, C. and Patterson, J. C. (2003b), "A direct three-dimensional simulation of radiation-induced natural convection in a shallow wedge." *Intl J. Heat Mass Transfer* **46**: 1183-1197.

Lei, C. and Patterson, J. C. (2005), "Unsteady natural convection in a triangular enclosure induced by surface cooling." *Intl. J. Heat and Fluid Flow* **26**: 307-321.

Lei, C. and Patterson, J. C. (2007), "A numerical simulation of natural convection in an isosceles triangular enclosure heated from bellow." *ANZIAM J.* **48**: C630-C644.

Leonard, B. P. and Mokhtari, S. (1990), "ULTRA-SHARP Nonoscillatory Convection Schemes for High-Speed Steady Multidimensional Flow." *NASA TM 1-2568 (ICOMP-90-12), NASA Lewis Research Center*.

Lin, W. and Armfield, S. W. (2005a), "Scaling laws for unsteady natural convection cooling of fluid with *Pr* < 1 in a vertical cylinder." *Phys. Rev. E* **72**: 016306.

Lin, W. and Armfield, S. W. (2005b), "Unsteady natural convection on an evenly heated vertical plate for *Pr* < 1." *Phys. Rev. E* **72**: 066309.

Lin, W., Armfield, S. W. and Patterson, J. C. (2007), "Cooling of a *Pr* < 1 fluid in a recangular container." *J. Fluid Mech.* **574**: 85-108.

Lin, W., Armfield, S. W. and Patterson, J. C. (2008), "Unsteady natural convection boundary-layer flow of a linearly-stratified fluid with *Pr* < 1 on an evenly heated semi-infinite vertical plate." *Int. J. Heat Mass Transfer* **51**: 327-343.

Lloyd, J. R. (1974), "Vortex wavelength in the transition flow adjacent to upward facing inclined isothermal surfaces". *Proc. 5th Intl Heat Transfer Conf.*

Lloyd, J. R. and Sparrow, E. M. (1970), "On the instability of natural convection flow on inclined plates." *J. Fluid Mech.* **42**: 465-470.

Nateghi, M. and Armfield, S. W. (2004), "Natural convection flow of air in an inclined open cavity." *ANZIAM J.* **45 (E)**: C870–C890.

Omri, A., Orfi, J. and Nasrallah, S. B. (2005), "Natural convection effect in solar stills." *Desalination* **183**: 173-178.

Ostrach, S. (1964). "Laminar flows with body forces, in theory of laminar flows". Princeton, Princeton Univ. Press.

Ostrach, S. (1972), "Natural convection in enclosures." *Adv. Heat Transfer* **8**: 161-227.

Ostrach, S. (1988), "Natural convection in enclosures." *Trans. ASME: J. Heat Transfer* **110**: 1175-1190.

Patterson, J. C. (1984), "Unsteady natural convection in a cavity with internal heating and cooling." *J. Fluid Mech.* **140**: 135-151.

Patterson, J. C. and Armfield, S. W. (1990), "Transient features of natural convections in a cavity." *J. Fluid Mech.* **219**: 469-497.

Patterson, J. C. and Imberger, J. (1980), "Unsteady natural convection in a rectangular cavity." *J. Fluid Mech.* **100**: 65-86.

Patterson, J. C., Lei, C., Armfield, S. W. and Lin, W. (2008), "Scaling of unsteady natural convection boundary layers with a non-instantaneous initiation." *Int. J. Therm. Sci.*: Submitted.

Poulikakos, D. and Bejan, A. (1983a), "The fluid dynamics of an attic space." *J. Fluid Mech.* **131**: 251-269.

Poulikakos, D. and Bejan, A. (1983b), "Natural convection experiments in a triangular enclosure." *Trans. ASME: J. Heat Transfer* **105**: 652-655.

Ridouane, E. H. and Campo, A. (2006), "Formation of a pitchfork bifurcation in thermal convection flow inside an isosceles triangular cavity." *Physics of Fluids* **18**: 074102.

Salmun, H. (1995a), "Convection patterns in a triangular domain." *Intl J. Heat Mass Transfer* **38**: 351-362.

Salmun, H. (1995b), "The stability of a single-cell steady-state solution in a triangular enclosure." *Int. J. Heat Mass Transfer* **18**: 363-369.

Schladow, S. G., Patterson, J. C. and Street, R. L. (1989), "Transient flow in a side-heated cavity at high Rayleigh number: A numerical study." *J. Fluid Mech.* **200**: 121-148.

Shaukatullah, H. and Gebhart, B. (1978), "An experimental investigation of natural convection flow on an inclined surface." *Intl J. Heat Mass Transfer* **21**: 1481-1490.

Sparrow, E. M. and Husar, R. B. (1969), "Longitudinal vortices in natural convection flow on inclined plates." *J. Fluid Mech.* **37**: 251-255.

Varol, Y., Koca, A. and Oztop, H. F. (2006a), "Natural convection in a triangular enclosure with flush mounted heater on the wall." *Int. Comm. Heat Mass Transfer* **33**: 951-958.

Varol, Y., Oztop, H. F. and Pop, I. (2008), "Natural convection flow in porous enclosures with heating and cooling on adjacent walls and divided by a triangular massive partition." *Int. Comm. Heat Mass Transfer* **35**: 476-491.

Varol, Y., Oztop, H. F. and Varol, A. (2006b), "Free convection in porous media filled right-angle triangular enclosures." *Int. Comm. Heat Mass Transfer* **33**: 1190-1197.

Varol, Y., Oztop, H. F. and Varol, A. (2007a), "Effects of thin fin on natural convection in porous triangular enclosures." *Int. J. Thermal Sci.* **46**: 1033-1045.

Varol, Y., Oztop, H. F. and Varol, A. (2007b), "Natural convection in porous triangular enclosures with a solid adiabatic fin attached to the horizontal wall." *Int. Comm. Heat Mass Transfer* **34**: 19-27.

Varol, Y., Oztop, H. F. and Yilmaz, T. (2007c), "Natural convection in triangular enclosures with protruding isothermal heater." *Int. J. Heat Mass Transfer* **50**: 2451-2462.

Zuercher, E. J., Jacobs, J. W. and Chen, C. F. (1998), "Experimental study of the stability of boundary-layer flow along a heated inclined plate." *J. Fluid Mech.* **367**: 1-25.